

PREPARATION OF FUNCTIONAL MATERIALS AND UTILIZATION OF RENEWABLE RESOURCES IN GREEN SOLVENTS

EDITED BY: Honglei Fan, Jinliang Song, Hongliang Liu, Zhenyu Sun and
Zongyu Wang

PUBLISHED IN: Frontiers in Chemistry





frontiers

Frontiers eBook Copyright Statement

The copyright in the text of individual articles in this eBook is the property of their respective authors or their respective institutions or funders. The copyright in graphics and images within each article may be subject to copyright of other parties. In both cases this is subject to a license granted to Frontiers.

The compilation of articles constituting this eBook is the property of Frontiers.

Each article within this eBook, and the eBook itself, are published under the most recent version of the Creative Commons CC-BY licence.

The version current at the date of publication of this eBook is CC-BY 4.0. If the CC-BY licence is updated, the licence granted by Frontiers is automatically updated to the new version.

When exercising any right under the CC-BY licence, Frontiers must be attributed as the original publisher of the article or eBook, as applicable.

Authors have the responsibility of ensuring that any graphics or other materials which are the property of others may be included in the CC-BY licence, but this should be checked before relying on the CC-BY licence to reproduce those materials. Any copyright notices relating to those materials must be complied with.

Copyright and source acknowledgement notices may not be removed and must be displayed in any copy, derivative work or partial copy which includes the elements in question.

All copyright, and all rights therein, are protected by national and international copyright laws. The above represents a summary only. For further information please read Frontiers' Conditions for Website Use and Copyright Statement, and the applicable CC-BY licence.

ISSN 1664-8714

ISBN 978-2-83250-879-4

DOI 10.3389/978-2-83250-879-4

About Frontiers

Frontiers is more than just an open-access publisher of scholarly articles: it is a pioneering approach to the world of academia, radically improving the way scholarly research is managed. The grand vision of Frontiers is a world where all people have an equal opportunity to seek, share and generate knowledge. Frontiers provides immediate and permanent online open access to all its publications, but this alone is not enough to realize our grand goals.

Frontiers Journal Series

The Frontiers Journal Series is a multi-tier and interdisciplinary set of open-access, online journals, promising a paradigm shift from the current review, selection and dissemination processes in academic publishing. All Frontiers journals are driven by researchers for researchers; therefore, they constitute a service to the scholarly community. At the same time, the Frontiers Journal Series operates on a revolutionary invention, the tiered publishing system, initially addressing specific communities of scholars, and gradually climbing up to broader public understanding, thus serving the interests of the lay society, too.

Dedication to Quality

Each Frontiers article is a landmark of the highest quality, thanks to genuinely collaborative interactions between authors and review editors, who include some of the world's best academicians. Research must be certified by peers before entering a stream of knowledge that may eventually reach the public - and shape society; therefore, Frontiers only applies the most rigorous and unbiased reviews.

Frontiers revolutionizes research publishing by freely delivering the most outstanding research, evaluated with no bias from both the academic and social point of view. By applying the most advanced information technologies, Frontiers is catapulting scholarly publishing into a new generation.

What are Frontiers Research Topics?

Frontiers Research Topics are very popular trademarks of the Frontiers Journals Series: they are collections of at least ten articles, all centered on a particular subject. With their unique mix of varied contributions from Original Research to Review Articles, Frontiers Research Topics unify the most influential researchers, the latest key findings and historical advances in a hot research area! Find out more on how to host your own Frontiers Research Topic or contribute to one as an author by contacting the Frontiers Editorial Office: frontiersin.org/about/contact

PREPARATION OF FUNCTIONAL MATERIALS AND UTILIZATION OF RENEWABLE RESOURCES IN GREEN SOLVENTS

Topic Editors:

Honglei Fan, Yantai University, China

Jinliang Song, Guangdong University of Technology, China

Hongliang Liu, Yantai University, China

Zhenyu Sun, Beijing University of Chemical Technology, China

Zongyu Wang, Oak Ridge National Laboratory (DOE), United States

Citation: Fan, H., Song, J., Liu, H., Sun, Z., Wang, Z., eds. (2022). Preparation of Functional Materials and Utilization of Renewable Resources in Green Solvents. Lausanne: Frontiers Media SA. doi: 10.3389/978-2-83250-879-4

Table of Contents

- 04 Editorial: Preparation of Functional Materials and Utilization of Renewable Resources in Green Solvents**
Honglei Fan, Jinliang Song, Hongliang Liu, Zhenyu Sun and Zongyu Wang
- 07 Catalytic Oxidative Cleavage of C(OH)-C Bonds in Lignin Model Compounds to Carboxylic Acids by $\text{Fe}(\text{NO}_3)_3 \cdot 9\text{H}_2\text{O}/\text{NaI}/\text{DMSO}$**
Xuerong Wang, Huilin Sun, Caicui Li, Shuijiao Niu, Yu Gao, Ying Chen, Tianwei Xu, Jinhui Wang and Huanjun Xu
- 16 A Novel Tannic Acid-Based Carbon-Supported Cobalt Catalyst for Transfer Hydrogenation of Biomass Derived Ethyl Levulinate**
Meng Wang, Xuefeng Yao, Yuxin Chen, Baodong Lin, Na Li, Keduan Zhi, Quansheng Liu and Huacong Zhou
- 28 A Novel and Highly Efficient Zr-Containing Catalyst Supported by Biomass-Derived Sodium Carboxymethyl Cellulose for Hydrogenation of Furfural**
Jianxiu Hao, Yafang Zhang, Tianyuan Zhang, Huacong Zhou, Quansheng Liu, Keduan Zhi, Na Li and Runxia He
- 37 Preparation of Pd Nanoparticles Stabilized by Modified Montmorillonite for Efficient Hydrodeoxygenation of Lignin-Derived Phenolic Compounds in Water**
Xuerong Wang, Chi Li, Xinyuan Guo, Zhichao Wang, Ruijing Cheng, Tianwei Xu, YiYing Li, Jinhui Wang and Huanjun Xu
- 45 Recent Progress of Photocatalysts Based on Tungsten and Related Metals for Nitrogen Reduction to Ammonia**
Xiangchao Hui, Lijun Wang, Zhibo Yao, Leiduan Hao and Zhenyu Sun
- 71 Tailoring the Catalytic Performance of Cu/SiO_2 for Hydrogenolysis of Biomass-Derived 5-Hydroxymethylfurfural to Renewable Fuels**
Hongyan Jia, Qing Lv, Qineng Xia, Wanpeng Hu and Yanqin Wang
- 81 Modifying the Conductive Properties of Poly(3,4-Ethylenedioxythiophene) Thin Films in Green Solvents**
Bin Hou, Chuao Ma, Sidi Li and Hongliang Liu
- 88 CH_4 Activation by PtX^+ ($\text{X} = \text{F}, \text{Cl}, \text{Br}, \text{I}$)**
Jin Zhao, Lingxi Qi, Wenzuo Li, Jianbo Cheng, Qingzhong Li and Shaoli Liu
- 100 Superwetting Membrane-Based strategy for High-Flux Enrichment of Ethanol From Ethanol/Water Mixture**
Zhongwei Wei, Shaoqing Zhang, Li Chang, Hongliang Liu and Lei Jiang
- 108 CO_2 -Assisted Fabrication of Silica Gel Adsorbent in Honeycomb Rotary Wheels for Air Dehumidification**
Junjie You, Junbo Qin, Chuanqing Du, Jianhua Fu and Siqing Cheng
- 115 Rational Design of Adhesives for Effective Underwater Bonding**
Sidi Li, Chuao Ma, Bin Hou and Hongliang Liu



OPEN ACCESS

EDITED AND REVIEWED BY

Florent Allais,
AgroParisTech Institut des Sciences et
Industries du Vivant et de
L'environnement, France

*CORRESPONDENCE

Honglei Fan,
fhl@ytu.edu.cn

SPECIALTY SECTION

This article was submitted to Green and
Sustainable Chemistry,
a section of the journal
Frontiers in Chemistry

RECEIVED 31 October 2022

ACCEPTED 03 November 2022

PUBLISHED 14 November 2022

CITATION

Fan H, Song J, Liu H, Sun Z and Wang Z
(2022), Editorial: Preparation of
functional materials and utilization of
renewable resources in green solvents.
Front. Chem. 10:1085405.
doi: 10.3389/fchem.2022.1085405

COPYRIGHT

© 2022 Fan, Song, Liu, Sun and Wang.
This is an open-access article
distributed under the terms of the
[Creative Commons Attribution License](#)
(CC BY). The use, distribution or
reproduction in other forums is
permitted, provided the original
author(s) and the copyright owner(s) are
credited and that the original
publication in this journal is cited, in
accordance with accepted academic
practice. No use, distribution or
reproduction is permitted which does
not comply with these terms.

Editorial: Preparation of functional materials and utilization of renewable resources in green solvents

Honglei Fan^{1*}, Jinliang Song², Hongliang Liu¹, Zhenyu Sun³ and
Zongyu Wang⁴

¹College of Chemistry and Chemical Engineering, Yantai University, Yantai, China, ²School of Chemical Engineering and Light Industry, Guangdong University of Technology, Guangzhou, China, ³College of Chemical Engineering, Beijing University of Chemical Technology, Beijing, China, ⁴Oak Ridge National Laboratory, Oak Ridge, TN, United States

KEYWORDS

green solvent, renewable resource, catalysis, functional materials, modification

Editorial on the Research Topic

Preparation of functional materials and utilization of renewable
resources in green solvents

The increasing consumption of toxic and non-renewable materials compels researchers to replace them with less dangerous, bio-based, and renewable materials. Moreover, legislative changes have implemented restrictions on the use of commonly employed dipolar aprotic solvents (e.g., dimethylformamide and *N*-methyl-2-pyrrolidinone) and ethers (e.g., 1,4-dioxane) (Jordan et al., 2022). Therefore, the employment of green solvents is an effective way to achieve sustainable development. To realize this, green solvents are regularly used nowadays and include water, alcohols, ionic liquids, deep eutectic solvents, and supercritical fluids. Green solvents are excellent solvents for a variety of chemical processes, for example, the preparation of functional materials, catalysis, and organic synthesis. Additionally, purification and extraction require large excesses of solvents and large amounts of energy. The utilization of green solvents may provide an economic and environmental way to realize environmental sustainability. This Research Topic highlights new research on the employment of green solvents in the preparation of functional materials and improvements in the catalytic efficiencies of important chemical reactions.

Green, task-specific solvents are advantageous in the fabrication of functional materials exhibiting controllable properties. Several studies in this Research Topic are related with this attractive aspect. Polymeric membrane fabrication should satisfy the principles of green chemistry since, generally, a wide range of toxic solvents are used for polymer dissolution and modification (Mehrabani et al., 2022). Hou et al. reviewed the modification of poly (3,4-ethylenedioxythiophene) (PEDOT) in green solvents. For example, alcoholic solvents could replace organic solvents like *N*-methyl-2-

pyrrolidone and pyridine to afford PEDOT almost consistent conductivities. High boiling point polar solvents generally increased the reaction time for forming longer polymer chains, allowing higher conductivities to be achieved. Biopolymers are excellent candidates for the fabrication of sustainable materials owing to their excellent availabilities, renewabilities, biodegradabilities, and biocompatibilities. Chemical modification is an appealing way to broaden the utilization of biopolymers (Ge et al., 2022). Li et al. designed adhesives for underwater use. As opposed to bonding in air, underwater bonding is quite challenging. Smart adhesives were explored and exhibited great potential in removing interfacial water and enhancing cohesion by using special functional groups. You et al. replaced sulfuric acid with a combination of carbon dioxide and water for the *in-situ* formation of acidic solutions, thereby rendering the fabrication process for porous silica gel green.

Solvents have a significant impact on reaction efficiencies (i.e., the activity and selectivity), which can be determined in numerous ways, such as the solubilities and stabilities of transient states (Hessel et al., 2022). In relation to this interesting aspect, Jia et al. prepared Cu/SiO₂ in different aqueous solutions. The as-prepared catalysts were synthesized using a hydrothermal method and showed high reaction selectivities due to high Cu dispersions, small particle sizes, and high proportions of metallic Cu⁰. Water, the most abundant and important solvent on earth, is cheap, green, readily available, and can be used to produce hydrogen or oxygen through electrolysis (Yu et al., 2022). Hui et al. reviewed the synthesis of ammonia by nitrogen photo-reduction over tungsten and the related metal semiconductors. For this transformation, water played dual roles as a hydrogen resource and a reaction medium, and the entire process was also promoted by water oxidation. Wang et al. developed a green process for the efficient hydrodeoxygenation of lignin-derived phenolic compounds in water. Using bio-alcohols as a hydrogen source can not only avoid risks related to high-pressure hydrogen, but can also improve the reaction efficiencies. Hao et al. enhanced the hydrogenation efficiency of furfural over a carboxymethyl cellulose zirconium-based catalyst by using isopropanol as the hydrogen source and the reaction solvent. Wang et al. adopted a similar strategy to promote the transfer-hydrogenation of biomass-derived ethyl levulinate. In addition, the transformation of small molecules like CH₄ could be realized by thermal, optical, and electrical methods. A numerical simulation of the transformation of CH₄ benefited the design of catalysts as well as optimization of the reaction process. Zhao et al. revealed a different mechanism for converting methane, exploiting the catalytic roles played by transition metal ions.

The separation of mixtures of miscible liquids is often a tedious and high energy-consumption process. Thus, it is still a major challenge to find an efficient and high-flux strategy. Wei et al. reported a superwetting membrane system to enrich bio-ethanol from water using a novel high-flux method. Excellent performance in obtaining concentrated ethanol was realized by synergistically regulating both the surface energy of the solid porous membrane, and the hydration between an additive inorganic potassium salt and water.

In this Research Topic, we have described recent developments and innovative technologies in the fabrication of functional materials. We have also discussed the performances of important catalytic transformations in green solvents, with the purpose of promoting the utilization of green solvents in related areas.

Author contributions

All authors listed have made a substantial, direct, and intellectual contribution to the work and approved it for publication.

Acknowledgments

The editors would like to thank the authors, co-authors, reviewers, and the Frontiers in Chemistry development team, whose efforts have led to the success of this Research Topic. The editors acknowledge support from the National Natural Science Foundation of China (grant numbers 21875265 and 22072157).

Conflict of interest

The authors declare that the research was conducted in the absence of any commercial or financial relationships that could be construed as a potential conflict of interest.

Publisher's note

All claims expressed in this article are solely those of the authors and do not necessarily represent those of their affiliated organizations, or those of the publisher, the editors and the reviewers. Any product that may be evaluated in this article, or claim that may be made by its manufacturer, is not guaranteed or endorsed by the publisher.

References

- Ge, W. J., Shuai, J. B., Wang, Y. Y., Zhaou, Y. X., and Wang, X. H. (2022). Progress on chemical modification of cellulose in "green" solvents. *Polym. Chem.* 13, 359–372. doi:10.1039/d1py00879j
- Hessel, V., Tran, N. N., Asrami, M. R., Tran, Q. D., Long, N. V., Escriba-Gelonch, M., et al. (2022). Sustainability of green solvents - Review and Perspective. *Green Chem.* 24, 410–437. doi:10.1039/d1gc03662a
- Jordan, A., Hall, C. G. J., Thorp, L. R., and Sneddon, H. F. (2022). Replacement of less-Preferred dipolar aprotic and Ethereal solvents in Synthetic organic chemistry with More sustainable Alternatives. *Chem. Rev.* 122, 6749–6794. doi:10.1021/acs.chemrev.1c00672
- Mehrabani, S. A. N., Vatanpour, V., and Koyuncu, I. (2022). Green solvents in polymeric membrane fabrication: A Review. *Sep. Purif. Technol.* 298, 121691. doi:10.1016/j.seppur.2022.121691
- Yu, Y. K., Fang, N., Chen, Z., Liu, D. X., Liu, Y. M., and He, M. Y. (2022). Greening Oxidation catalysis: Water as a solvent for efficient Alkene Epoxidation over a Titanosilicate/H₂O₂ system. *ACS Sustain. Chem. Eng.* 10, 11641–11654. doi:10.1021/acssuschemeng.2c03524



Catalytic Oxidative Cleavage of C(OH)-C Bonds in Lignin Model Compounds to Carboxylic Acids by $\text{Fe}(\text{NO}_3)_3 \cdot 9\text{H}_2\text{O}/\text{NaI}/\text{DMSO}$

Xuerong Wang^{1,2†}, Huilin Sun^{2†}, Caicui Li^{2†}, Shuijiao Niu³, Yu Gao⁴, Ying Chen², Tianwei Xu^{1,2*}, Jinhui Wang^{1,4*} and Huanjun Xu^{1,2*}

¹Key Laboratory of Child Cognition & Behavior Development of Hainan Province, Qiongtai Normal University, Haikou, China, ²School of Science, Qiongtai Normal University, Haikou, China, ³Shandong Institute for Food and Drug Control, Ji'nan, China, ⁴Department of Medicinal Chemistry and Natural Medicine Chemistry, College of Pharmacy, Harbin Medical University, Harbin, China

OPEN ACCESS

Edited by:

Jinliang Song,
Guangdong University of Technology,
China

Reviewed by:

Long Liu,
Hainan University, China
Xuan-Hui Ouyang,
Nanchang Hangkong University,
China

*Correspondence:

Tianwei Xu
27296930@qq.com
Jinhui Wang
15999290001@163.com
Huanjun Xu
15798946232@163.com

[†]These authors have contributed
equally to this work and share first
authorship

Specialty section:

This article was submitted to
Green and Sustainable Chemistry,
a section of the journal
Frontiers in Chemistry

Received: 01 May 2022

Accepted: 16 May 2022

Published: 01 July 2022

Citation:

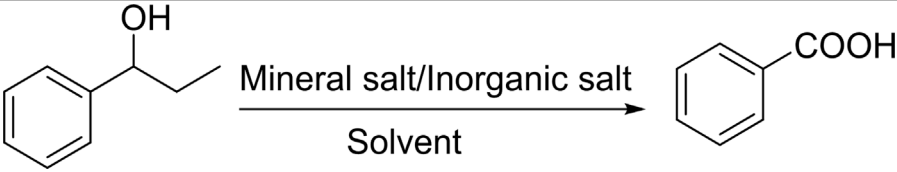
Wang X, Sun H, Li C, Niu S, Gao Y,
Chen Y, Xu T, Wang J and Xu H (2022)
Catalytic Oxidative Cleavage of C(OH)-
C Bonds in Lignin Model Compounds
to Carboxylic Acids by $\text{Fe}(\text{NO}_3)_3 \cdot 9\text{H}_2\text{O}/$
 NaI/DMSO .
Front. Chem. 10:933763.
doi: 10.3389/fchem.2022.933763

The secondary C(OH)-C bonds are abundant in biomass such as lignin and cellulose. Thus, selective cleavage of the C(OH)-C bonds into value chemicals attracted much attention. Molecular iodine has received considerable attention as an inexpensive and readily available catalyst to yield the corresponding products in excellent yields with high selectivity, but it is highly corrosive and toxic, making its use somewhat unattractive. In this study, I_2 was generated *in situ* from $\text{Fe}(\text{NO}_3)_3 \cdot 9\text{H}_2\text{O}/\text{NaI}$, which was further combined with $\text{Fe}(\text{NO}_3)_3 \cdot 9\text{H}_2\text{O}$ to catalyze the oxidation process. In the reaction, the H_2O molecule from the reaction and $\text{Fe}(\text{NO}_3)_3 \cdot 9\text{H}_2\text{O}$ attacked the phenylglyoxal to form benzaldehyde, which was further oxidized to benzoic acid. Aryl primary and secondary benzylic alcohols from lignin were successfully transformed into aryl carboxylic acids by $\text{Fe}(\text{NO}_3)_3 \cdot 9\text{H}_2\text{O}/\text{NaI}/\text{DMSO}$. The catalytic system was green and efficient, avoiding the usage of toxic and corrosive molecular I_2 . From the experiments, it was clear that the yield of the product from the substrates with an electron-donating group was higher than that of electron-withdrawing substituted substrates, which was similar to the aryl secondary alcohols. Aryl alkyl ketones were also successfully conducted by the $\text{Fe}(\text{NO}_3)_3 \cdot 9\text{H}_2\text{O}/\text{NaI}/\text{DMSO}$ catalytic system.

Keywords: catalytic oxidative cleavage, lignin model compounds, carboxylic acids, $\text{Fe}(\text{NO}_3)_3 \cdot 9\text{H}_2\text{O}/\text{NaI}/\text{DMSO}$, C(OH)-C bonds

INTRODUCTION

Lignin is the largest renewable source with a large number of aromatic units; thus, it could serve as a sustainable candidate feedstock for aromatic chemicals (Ohlrogge et al., 2009). Inspired by this, there are more efforts to selectively transform lignin into value-added chemicals, especially aromatic chemicals. In natural lignin, C(OH)-C bonds are widespread. Thus, it is an attractive strategy for selective cleavage and functionalization of C(OH)-C bonds for converting lignin into value-added chemical products, such as aryl carboxylic acid. Aryl carboxylic acid is very common in many structures of bioactive molecules and can be transformed to esters, amides, acid halides, and so on (Peng et al., 2016; Nicolaou et al., 2009; Liu et al., 2020). Although the C(OH)-C bonds in lignin have

TABLE 1 | Optimization of reaction conditions^a.


Entry	Mineral salt	Inorganic salt	Solvent	Yield (%) ^b
1	Fe(NO ₃) ₃ ·9H ₂ O	NaI	DMSO	67 ^c
2	Fe(NO ₃) ₃ ·9H ₂ O	NaI	DMSO	72 ^d
3	Fe(NO ₃) ₃ ·9H ₂ O	NaI	DMSO	83/0 ^e
4	Cu(NO ₃) ₂	NaI	DMSO	17
5	Co(NO ₃) ₂	NaI	DMSO	11
6	Fe(NO ₃) ₃ ·9H ₂ O	KI	DMSO	16
7	Fe(NO ₃) ₃ ·9H ₂ O	LiI	DMSO	65
8	Fe(NO ₃) ₃ ·9H ₂ O	NaCl	DMSO	56
10	Fe(NO ₃) ₃ ·9H ₂ O	NaBr	DMSO	27
11	Fe(NO ₃) ₃ ·9H ₂ O	NaI	DMF	12
12	Fe(NO ₃) ₃ ·9H ₂ O	NaI	NMP	15
13	Fe(NO ₃) ₃ ·9H ₂ O	NaI	Mesitylene	51
14	Fe(NO ₃) ₃ ·9H ₂ O	NaI	DMSO	8 ^f /81 ^g
15	Fe(NO ₃) ₃ ·9H ₂ O	NaI	DMSO	78 ^h
16	Fe(NO ₃) ₃ ·9H ₂ O	NaI	DMSO	82 ⁱ
17	Fe(NO ₃) ₃ ·9H ₂ O	—	DMSO	71 ^j

^aCondition: substrate (0.5 mmol), Fe(NO₃)₃·9H₂O (0.15 mmol), NaI (0.075 mmol), DMSO (2 ml), and air balloon, 130°C, 18 h.

^bIsolated yield.

^cSubstrate (0.5 mmol), Fe(NO₃)₃·9H₂O (0.1 mmol), NaI (0.05 mmol).

^dSubstrate (0.5 mmol), Fe(NO₃)₃·9H₂O (0.075 mmol), NaI (0.075 mmol).

^eUnder N₂.

^f12 h.

^g24 h.

^h120°C.

ⁱ140°C.

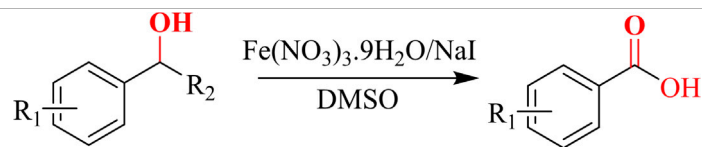
^jSubstrate (1 mmol), of I₂ (0.1 mmol), Fe(NO₃)₃·9H₂O (0.1 mmol), DMSO (2 ml), and O₂ (0.1 Mpa) 130°C, 12 h.

inherent kinetic inertness and thermodynamic stability, it is still very challenging for selective functionalization of these bonds.

In recent years, because molecular iodine possesses some advantages such as low in cost and easy to obtain, it has attracted considerable attention. More importantly, it is very efficient to make use as a powerful catalyst for various organic transformations with excellent yields and high selectivity under mild conditions, owing to its oxidation ability and Lewis acidity (Iida and Togo, 2006; Hazra et al., 2017). For example, Hazra's group has reported a metal-free catalytic system with iodine/NaOH, which could transform alcohols and aldehydes into carboxylic acids with excellent yield (Hazra et al., 2017). It is clear that I₂ is very useful in various types of organic reactions, but molecular iodine is highly corrosive and toxic, resulting in somewhat undesirable results in many reactions. Researchers conducted some excellent works to overcome the direct usage of I₂. Bailey et al. have reported that CuSO₄/NaI used in combination could be an *in situ* generation of I₂ (Mohan et al., 2006). Subsequently, another convenient system to generate I₂ *in situ* was reported by Tamin's group, which consisted of Fe(NO₃)₃·9H₂O/NaI, and the amount of I₂ generated *in situ* was measured by UV/Vis spectrophotometry (Rostami et al., 2009). Also, this group has applied this protocol

for trimethylsilylation and formylation of various alcohols catalyzed by I₂ generated *in situ* from Fe(NO₃)₃·9H₂O/NaI (Amin et al., 2011).

Moreover, iron is low in cost and toxicity and has rapidly developed in various fields (Martin and Suarez, 2002; Plietker and Dieskau, 2009; Czaplik et al., 2010). Compared with other transition metals, most of the iron species show low toxicity (Perutz, 1979). The oral permitted daily exposure limit of elemental iron is high at 13,000 Ug/day; thus, the application of elemental iron in the pharmaceutical and food industries is attractive (Bauer and Knölker, 2015). In recent years, iron-catalyzed oxidation reactions to pharmaceutical molecules have attracted significant attention. Also, Li' group reported a procedure of aerobic oxidative deoxygenation reactions that were catalyzed by iron (Li et al., 2018). In 2013, Ma's group have reported Fe(NO₃)₃·9H₂O/TEMPO/MCl (M = Na or K) oxidized corresponding alcohols to carbonyl compounds using O₂ or air as a terminal oxidant at room temperature (Jiang et al., 2016; Liu and Ma, 2013a; Liu and Ma, 2013b). Also, Xu and co-workers reported a strategy of I₂/Fe(NO₃)₃·9H₂O-catalyzed C–C bond cleavage of aryl alkyl ketones and secondary benzylic alcohols (Xu et al., 2018a). Notably, all these related research studies have confirmed that iron salts are efficient in catalytic oxidation reactions, but all the

TABLE 2 | Catalytic aerobic oxidation of secondary alcohols^a.

Entry	Substrate	Product/yield ^b
1		83
2		83
3		82
4		42
5		49
6		74
7		82
8		61

(Continued on following page)

TABLE 2 | (Continued) Catalytic aerobic oxidation of secondary alcohols^a.

9		74
10		23
11		74
12		75
13		57
14		88
15		76
16		80

(Continued on following page)

TABLE 2 | (Continued) Catalytic aerobic oxidation of secondary alcohols^a.

17	
18	

^aCondition: substrate (0.5 mmol), $\text{Fe}(\text{NO}_3)_3 \cdot 9\text{H}_2\text{O}$ (0.15 mmol), NaI (0.075 mmol), DMSO (2 ml), and air balloon, 130°C, 18 h.

^bIsolated yield.

catalytic systems need other types of co-oxidants to promote catalytic activity.

Inspired by those finding, we wish to report a facile and efficient approach for the oxidation of secondary C(OH)-C bonds in lignin to aryl carboxylic acid by using cheap and nontoxic $\text{Fe}(\text{NO}_3)_3$ and NaI as a catalyst, in which I_2 was generated *in situ* under the reaction, avoiding the usage of toxic and corrosive molecular I_2 . A variety of secondary and primary benzylic alcohols could be transformed into corresponding acids in moderate-to-excellent yields.

EXPERIMENTAL SECTION

Materials

All of the materials were purchased from Beijing Innochem Company and used as received.

Characterization

Other than the 9H-fluoren-9-ol, mass spectra were obtained on an SCIEX X500R QTOF high-resolution mass spectrometry instrument with negative ion mode. The 0.1 acetic acid/5 mM amine acetate in $\text{CH}_3\text{CN}/\text{H}_2\text{O}$ (20:80) was used as the eluent.

General Procedures for Aerobic Oxidation

Typical procedure: the desired amount of secondary alcohol substrate (0.5 mmol), $\text{Fe}(\text{NO}_3)_3 \cdot 9\text{H}_2\text{O}$ (0.15 mmol), NaI (0.075 mmol), and DMSO (2 ml) was added into a 25-ml reaction bottle. Then, the mixture was degassed three times with the oxygen balloon, and the reaction was held under 130°C for the desired time. After being acidified with 2 mol/L HCl (3 ml), the solution was extracted by ethyl acetate (5 ml) twice, and the organic phase was washed with saturated brine once and dried by Na_2SO_4 . The combined organic phase was removed from the solvent by a rotary evaporator. The desired product

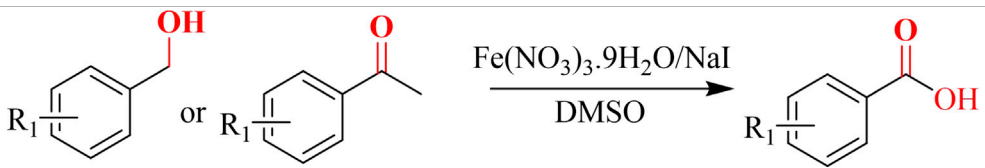
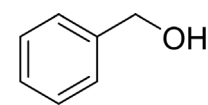
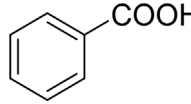
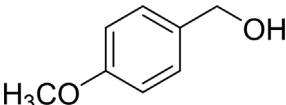
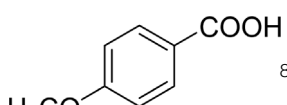
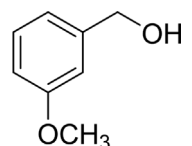
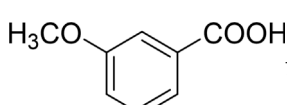
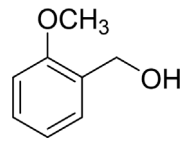
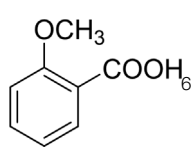
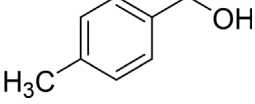
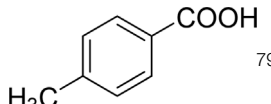
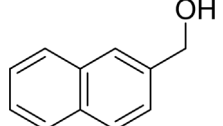
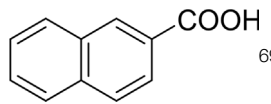
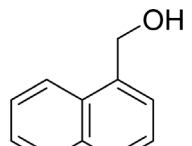
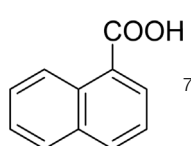
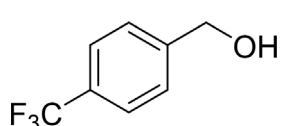
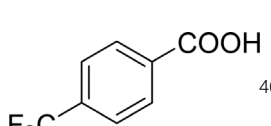
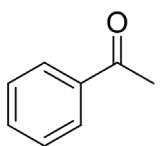
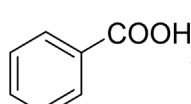
was obtained through column chromatography using ethyl acetate/petroleum ether as an eluent.

RESULTS AND DISCUSSION

Initially, 1-phenyl-1-propanol was taken as the model substrate to optimize the reaction conditions (Table 1). We tried to optimize the reaction with a suitable amount and ratio of $\text{Fe}(\text{NO}_3)_3 \cdot 9\text{H}_2\text{O}/\text{NaI}$; when the catalytic system consisted of 20 mol% of $\text{Fe}(\text{NO}_3)_3 \cdot 9\text{H}_2\text{O}$ and 10 mol% of NaI, the desired product could be successfully obtained with 67% yield in 18 h (Table 1, entry 1). When the loading of $\text{Fe}(\text{NO}_3)_3 \cdot 9\text{H}_2\text{O}$ was further increased to 30 mol% and NaI was increased to 15 mol%, the yield was sharply increased to 83% (Table 1, entry 2). But, while maintaining the loading of $\text{Fe}(\text{NO}_3)_3 \cdot 9\text{H}_2\text{O}$ at 30 mol%, the loading of NaI was further increased to 30 mol%, and then the benzoic acid was yielded at 72% (Table 1, entry 3). While other types of nitrate catalysts were used as catalyst, the yield of acid was lower than when the $\text{Fe}(\text{NO}_3)_3 \cdot 9\text{H}_2\text{O}$ was used as the catalyst (Table 1, entries 4–5). We also test other types of salts as the co-catalyst, such as LiI, KI, NaBr, or NaCl, but all those salts cannot offer a satisfactory yield of acid (Table 1, entries 6–10).

A series of solvents including DMF, NMP, and mesitylene were screened, and it was clearly shown that DMSO was the best solvent among them (Table 1, entries 11–13). When the reaction was conducted in the absence of oxygen, the yield of benzoic acid was not detected, but benzaldehyde was formed with a 65% yield (Table 1, entry 3). Then, we proceeded with the reaction under different temperatures and times, and it was found that the yield of the product was lower under 120°C (Table 1, entry 15). The yield of the desired product was not improved when the reaction temperature was increased to 140°C or the reaction time was increased to 24 h (Table 1, entries 14 and 16). More interestingly, when the reaction time was decreased to 12 h, the

TABLE 3 | Catalytic aerobic oxidation of primary alcohols and ketones^a.

		
Entry	Substrate	Product/yield ^b
1		 73
2		 80
3		 78
4		 69
5		 79
6		 69
7		 70
8		 46
9		 77

(Continued on following page)

TABLE 3 | (Continued) Catalytic aerobic oxidation of primary alcohols and ketones^a.

10			84
11			

^aCondition: substrate (0.5 mmol), $\text{Fe}(\text{NO}_3)_3 \cdot 9\text{H}_2\text{O}$ (0.15 mmol), NaI (0.075 mmol), DMSO (2 ml), and air balloon, 130°C, 18 h.

^bIsolated yield.

yield of acid was just 8%, and most of them was benzaldehyde, indicating that benzaldehyde was transformed to the desired product faster.

Thus, it was obvious that NaI (15 mol%)/ $\text{Fe}(\text{NO}_3)_3 \cdot 9\text{H}_2\text{O}$ (30 mol%) as the catalyst and DMSO as solvent under O_2 balloon at 130°C for 18 h could efficiently catalyze aerobic oxidation of alcohol. Subsequently, the standard reaction condition was chosen to explore the scope and generality of this protocol. The various aryl alkyl alcohols were further investigated, with the results shown in **Table 2**.

The aryl alkyl alcohols with different alkyl substituent groups on its β -position of the methyl group were then used as substrates, and all of the aryl alkyl alcohols could be oxidized to desired aryl carboxylic acids in moderate-to-good yields ranging from 42–83%. (**Table 2**, entries 1–5). Compared with phenyl-1-pentanol, 2-methyl-1-phenylpropanol with a steric hindrance group on the β -position was transformed into the desired product in 49% yield (**Table 2**, entry 5). A similar result was obtained from 1-phenyl-2-methyl-1-propanol (42%), which was also with a steric hindrance group in the same position.

In general, substrates with electron-donating or electron-withdrawing groups could be smoothly converted by this catalytic system, and the desired aryl carboxylic acids were obtained in moderate-to-good yields. 1-phenylethanol bearing electron-donating substituents such as 4- CH_3 and 4- OCH_3 were transformed to the corresponding benzoic acids in 74 and 74% isolated yields, respectively (**Table 2**, entries 6 and 9). The 3- OCH_3 and 2- OCH_3 substituted 1-phenylethanol gave corresponding benzoic acids in 82 and 61% isolated yields, respectively (**Table 2**, entries 7–8).

It is obvious that the product from the 2- OCH_3 substituted substrate is in a lower yield, which might be owing to the ortho-effect. 1-phenylethanol with strong electron-withdrawing groups (4- CF_3) could also afford the desired product in a low yield (23%) (**Table 2**, entry 10). In addition, the aryl alkyl alcohols bearing a p- or m-chloro substituent were also transformed into corresponding benzoic acid in moderate yields under standard conditions (**Table 2**, entries 11 and 12). However, like o- OCH_3

substituted 1-phenylethanol, the substrate bearing a chloro group in the ortho position was with lower reactivity, and the isolated yield of the product was 57% (**Table 2**, entry 13).

For 1-phenylethanol derivative with a phenyl substitute group on p-position (**Table 2**, entry 14), their catalytic oxidation of the substrate to the benzoic acid product resulted in excellent yield (88%). Meanwhile, the 1-(1-naphthyl) ethanol and 1-(2-naphthyl) ethanol also bear an aryl ring substitute with yields upto 80 and 76%, respectively (**Table 2**, entry 15 and 16). But the 9H-fluoren-9-ol, which was a representative diaryl secondary alcohol, could not be converted to the corresponding acid but to the corresponding ketone in a high yield (93%) (**Table 2**, entry 17). More interestingly, the important fragment of lignin (**Table 2**, entry 18) could be converted smoothly to the corresponding benzoic acid and phenol in moderate yield.

Then, various benzyl alcohols and aryl alkyl ketones also could be converted into carboxylic acids in moderate-to-good yields (45–84%) (**Table 3**, entries 1–8). For example, benzyl alcohols bearing electron-donating substituents such as 4- OCH_3 , 3- OCH_3 , and naphthyl alcohol substrates were smoothly oxidized to benzoic acid analogs in 69–80% isolated yields. Benzyl alcohols with an electron-withdrawing group (4- CF_3) could also afford the desired products in a low yield (46%). From the experiments, it was clear that the benzyl alcohols bearing the electron-donating substituent gave higher yields of products than substituted substrates bearing electron-withdrawing substituent, which was similar to the aryl secondary alcohols. Aryl alkyl ketones were also successfully conducted by the $\text{Fe}(\text{NO}_3)_3 \cdot 9\text{H}_2\text{O}$ /NaI/DMSO catalytic system (**Table 3**, entries 9–11).

Next, to gain insight into the mechanism of this oxygenation reaction, some control experiments were set up. Using phenylglyoxal instead of 1-phenyl-1-ethanol as the reactant, it was shown that the phenylglyoxal could be transformed to benzoic acid in 99% yield under standard conditions. Also, benzaldehyde was subjected as the substrate, and a quantitative yield of 99% was produced by benzoic acid under standard conditions. When the reaction

was conducted in the absence of NaI, the yield of benzoic acid was low to 56%, while no product was observed without $\text{Fe}(\text{NO}_3)_3 \cdot 9\text{H}_2\text{O}$. Also, while the reaction was carried out without oxygen, no benzoic acid was obtained, along with a 58% yield of benzaldehyde. From the previous results and the references (Xu et al., 2018a), we proposed a reaction mechanism as follows. Under the reaction condition, the 1-phenylethanol was first oxidized into acetophenone. Initially, I_2 was generated *in situ* from $\text{Fe}(\text{NO}_3)_3 \cdot 9\text{H}_2\text{O}/\text{NaI}$, and then acetophenone was transformed into α -iodoketone with the help of I_2 (Elmasry et al., 1998; Naimi-Jamal et al., 2009; Dressen et al., 2009; Martin et al., 2008). Then, α -iodoketone was oxidized into phenylglyoxal by DMSO and releases HI (Wu et al., 2016; Xiang et al., 2016; Wu and Natte, 2016; Xu et al., 2018b). With the Fe salt and H_2O molecule, the C–C bond was cleaved to give benzaldehyde and release a molecule of formic acid. Benzaldehyde can be oxidized into benzoic acid by the $\text{Fe}(\text{NO}_3)_3 \cdot 9\text{H}_2\text{O}/\text{NaI}/\text{DMSO}$ catalytic system (see **Supplementary Material**).

CONCLUSION

In summary, the $\text{Fe}(\text{NO}_3)_3 \cdot 9\text{H}_2\text{O}/\text{NaI}/\text{DMSO}$ catalytic system successfully transformed the aryl alcohols into the desired benzoic acids. In this catalyst system, I_2 was generated *in situ* from $\text{Fe}(\text{NO}_3)_3 \cdot 9\text{H}_2\text{O}/\text{NaI}$, which was further combined with $\text{Fe}(\text{NO}_3)_3 \cdot 9\text{H}_2\text{O}$ to catalyze the oxidation process. Compared with the $\text{Fe}(\text{NO}_3)_3 \cdot 9\text{H}_2\text{O}/\text{I}_2$ catalytic system, $\text{Fe}(\text{NO}_3)_3 \cdot 9\text{H}_2\text{O}/\text{NaI}/\text{DMSO}$ was found with a similar catalytic activity, avoiding direct usage of toxic and corrosive molecular I_2 . Aryl primary and secondary alcohols bearing an electron-donating substituent or electron-withdrawing substituent could be converted to the corresponding benzoic acid in moderate-to-high yields under standard conditions. Also, the represented lignin model compounds were all successfully transformed into the desired products. Fortunately, it was obvious that the catalytic system had great potential application in terms of

green process and technological innovation for the transformation of lignin.

DATA AVAILABILITY STATEMENT

The original contributions presented in the study are included in the article/**Supplementary Material**; further inquiries can be directed to the corresponding authors.

AUTHOR CONTRIBUTIONS

XW, HS, CL, YG, and YC: experimental operation and data collection; SN: the LC-MS data collection; JW: the conception and design of the study; JW and HX: article writing and revision; and TX: experimental data collection and analysis. All authors read and approved the submitted version.

FUNDING

This work was financially supported by the Hainan Provincial Natural Science Foundation of China (2019RC250 and 220QN281), National Science and Technology Major Project of the Ministry of Science and Technology of China (2018ZX09735005), National Natural Science Foundation of China (22165009), the Scientific Research Foundation of the Higher Education Institutions of Hainan Province (Hnky2021ZD-22), the Scientific Research Project of Qiongtai Normal University (qtyb201908), and the National Undergraduate Training Program for Innovation and Entrepreneurship (S202113811005, 202113811022).

SUPPLEMENTARY MATERIAL

The Supplementary Material for this article can be found online at: <https://www.frontiersin.org/articles/10.3389/fchem.2022.933763/full#supplementary-material>

REFERENCES

- Amin, R., Ardeshir, K., Heidari Ali, A.-N., and Zahra, T.-R. (2011). Formylation of Alcohol with Formic Acid under Solvent-free and Neutral Conditions Catalyzed by Free I_2 or I_2 Generated *In Situ* from $\text{Fe}(\text{NO}_3)_3 \cdot 9\text{H}_2\text{O}/\text{NaI}$. *Chin. J. Catal.* 32, 60–64. doi:10.1016/s1872-2067(10)60160-x
- Bauer, I., and Knölker, H.-J. (2015). Iron Catalysis in Organic Synthesis. *Chem. Rev.* 115, 3170–3387. doi:10.1021/cr500425u
- Czaplik, W. M., Mayer, M., Jacobi von Wangelin, A., and Wangelin, J. V. (2010). Iron-Catalyzed Reductive Aryl–Alkenyl Cross-Coupling Reactions. *ChemCatChem* 3, 135–138. doi:10.1002/cctc.201000276
- Dressen, M. H. C. L., Stumpel, J. E., Van de Kruijs, B. H. P., Meuldijk, J., Vekemans, J. A. J. M., and Hulshof, L. A. (2009). The Mechanism of the Oxidation of Benzyl Alcohol by iron(III)nitrate: Conventional versus Microwave Heating. *Green Chem.* 11, 60–64. doi:10.1039/B813030B
- Elmasry, M. A. A., Gaber, A., and Khater, E. M. H. (1998). Thermal Decomposition of Ni(II) and Fe(III) Nitrates and Their Mixture. *J. Therm. Anal. Calorim.* 52, 489–495. doi:10.1023/a:1010155203247
- Hazra, S., Deb, M., and Elias, A. J. (2017). Iodine Catalyzed Oxidation of Alcohols and Aldehydes to Carboxylic Acids in Water: a Metal-free Route to the Synthesis of Furandicarboxylic Acid and Terephthalic Acid. *Green Chem.* 19, 5548–5552. doi:10.1039/C7GC02802D
- Iida, S., and Togo, H. (2006). Direct and Facile Oxidative Conversion of Primary, Secondary, and Tertiary Amines to Their Corresponding Nitriles. *Synlett* 16, 2633–2635. doi:10.1055/s-2006-951491
- Jiang, X., Zhang, J., and Ma, S. (2016). Iron Catalysis for Room-Temperature Aerobic Oxidation of Alcohols to Carboxylic Acids. *J. Am. Chem. Soc.* 138, 8344–8347. doi:10.1021/jacs.6b03948
- Li, Y., Xu, N., Mei, G., Yun, Z., Zhao, Y., Lyu, J., et al. (2018). $\text{Fe}(\text{NO}_3)_3 \cdot 9\text{H}_2\text{O}$ -catalyzed Aerobic Oxidative Deoxygenation of Ketoximes and Aldoximes under Mild Conditions. *Can. J. Chem.* 96, 810–814. doi:10.1139/cjc-2017-0567
- Liu, J., and Ma, S. (2013b). Room Temperature $\text{Fe}(\text{NO}_3)_3 \cdot 9\text{H}_2\text{O}/\text{TEMPO}/\text{NaCl}$ -catalyzed Aerobic Oxidation of Homopropargylic Alcohols. *Tetrahedron* 2013 (69), 10161–10167. doi:10.1016/j.tet.2013.08.082
- Liu, J., and Ma, S. (2013a). Aerobic Oxidation of Indole Carbinols Using $\text{Fe}(\text{NO}_3)_3 \cdot 9\text{H}_2\text{O}/\text{TEMPO}/\text{NaCl}$ as Catalysts. *Org. Biomol. Chem.* 11, 4186–4193. doi:10.1039/C3OB40226F

- Liu, M., Zhang, Z., Yan, J., Liu, S., Liu, H., Liu, Z., et al. (2020). Aerobic Oxidative Cleavage and Esterification of C(OH)-C Bonds. *Chem* 6, 3288–3296. doi:10.1016/j.chempr.2020.09.006
- Martin, S. E., and Suarez, D. (2002). Catalytic Aerobic Oxidation of Alcohols by Fe(NO₃)₃-FeBr₃. *Tetrahedron Lett.* 43, 4475–4479. doi:10.1016/S0040-4039(02)00829-8
- Mohan, R. S., Bailey, A. D., Cherney, S. M., Anzalone, P. W., Anderson, E. D., and Ernat, J. J. (2006). A Convenient Method for *In Situ* Generation of I₂ Using CuSO₄/NaI and its Applications to the Deprotection of Acetals, Etherifications and Iodolactonizations. *Synlett* 2, 215–218. doi:10.1055/s-2005-923586
- Naimi-Jamal, M. R., Hamzeali, H., Mokhtari, J., Boy, J., and Kaupp, G. (2009). Sustainable Synthesis of Aldehydes, Ketones or Acids from Neat Alcohols Using Nitrogen Dioxide Gas, and Related Reactions. *ChemSusChem* 2, 83–88. doi:10.1002/cssc.200800193
- Nicolaou, K. C., Chen, J. S., Edmonds, D. J., and Estrada, A. A. (2009). Recent Advances in the Chemistry and Biology of Naturally Occurring Antibiotics. *Angew. Chem. Int. Ed.* 48, 660–719. doi:10.1002/anie.200801695
- Ohlrogge, J., Allen, D., Berguson, B., DellaPenna, D., Shachar-Hill, Y., and Stymne, S. (2009). Driving on Biomass. *Science* 324, 1019–1020. doi:10.1126/science.1171740
- Peng, J.-B., Qi, X., and Wu, X.-F. (2016). Visible Light-Induced Carbonylation Reactions with Organic Dyes as the Photosensitizers. *ChemSusChem* 9, 2279–2283. doi:10.1002/cssc.201600625
- Perutz, M. F. (1979). Regulation of Oxygen Affinity of Hemoglobin: Influence of Structure of the Globin on the Heme Iron. *Annu. Rev. Biochem.* 48, 327–386. doi:10.1146/annurev.bi.48.070179.001551
- Plietker, B., and Dieskau, A. (2009). The Reincarnation of the Hieber Anion [Fe(CO)₃(NO)] - - a New Venue in Nucleophilic Metal Catalysis. *Eur. J. Org. Chem.* 2009, 775–787. doi:10.1002/ejoc.200800893
- Rostami, A., Rahmati, S., and Khazaei, A. (2009). A Highly Efficient and Ecofriendly Procedure for Tetrahydropyranylation of Alcohols and Phenols in the Presence of *In-Situ* Generated I₂ under Heterogeneous and Neutral Conditions. *Monatsh. Chem.* 140, 663–667. doi:10.1007/s00706-009-0117-7
- Wu, X.-F., and Natte, K. (2016). The Applications of Dimethyl Sulfoxide as Reagent in Organic Synthesis. *Adv. Synth. Catal.* 358, 336–352. doi:10.1002/adsc.201501007
- Wu, X., Gao, Q., Geng, X., Zhang, J., Wu, Y.-d., and Wu, A.-x. (2016). Iodine-Promoted Oxidative Cross-Coupling of Unprotected Anilines with Methyl Ketones: A Site-Selective Direct C-H Bond Functionalization to C4-Dicarbonylation of Anilines. *Org. Lett.* 18, 2507–2510. doi:10.1021/acs.orglett.6b01162
- Xiang, J. C., Cheng, Y., Wang, M., Wu, Y. D., and Wu, A. (2016). XDirect Construction of 4-Hydroxybenzils via Para-Selective C-C Bond Coupling of Phenols and Aryl Methyl Ketones. *Lett. Org. Lett.* 18, 4360–4363. doi:10.1021/acs.orglett.6b02118
- Xu, L., Chen, Y., Shen, Z., Wang, Y., and Li, M. (2018a). I₂/Fe(NO₃)₃·9H₂O-catalyzed Oxidative Synthesis of Aryl Carboxylic Acids from Aryl Alkyl Ketones and Secondary Benzylic Alcohols. *Lett. Tetrahedron Lett.* 59, 4349–4354. doi:10.1016/j.tetlet.2018.10.060
- Xu, L., Wang, S., Chen, B., Li, M., Hu, X., Hu, B., et al. (2018b). Oxidative C-C Bond Cleavage for the Synthesis of Aryl Carboxylic Acids from Aryl Alkyl Ketones. *Synlett* 29, 1505–1509. doi:10.1055/s-0037-1609751

Conflict of Interest: The authors declare that the research was conducted in the absence of any commercial or financial relationships that could be construed as a potential conflict of interest.

Publisher's Note: All claims expressed in this article are solely those of the authors and do not necessarily represent those of their affiliated organizations, or those of the publisher, the editors, and the reviewers. Any product that may be evaluated in this article, or claim that may be made by its manufacturer, is not guaranteed or endorsed by the publisher.

Copyright © 2022 Wang, Sun, Li, Niu, Gao, Chen, Xu, Wang and Xu. This is an open-access article distributed under the terms of the Creative Commons Attribution License (CC BY). The use, distribution or reproduction in other forums is permitted, provided the original author(s) and the copyright owner(s) are credited and that the original publication in this journal is cited, in accordance with accepted academic practice. No use, distribution or reproduction is permitted which does not comply with these terms.



A Novel Tannic Acid-Based Carbon-Supported Cobalt Catalyst for Transfer Hydrogenation of Biomass Derived Ethyl Levulinate

Meng Wang, Xuefeng Yao, Yuxin Chen, Baodong Lin, Na Li, Keduan Zhi, Quansheng Liu and Huacong Zhou*

College of Chemical Engineering, Inner Mongolia University of Technology, Hohhot, China

OPEN ACCESS

Edited by:

Honglei Fan,
Institute of Chemistry (CAS), China

Reviewed by:

Feng Han,
Shandong Agricultural University,
China
Anlian Zhu,
Henan Normal University, China

*Correspondence:

Huacong Zhou
hczhou@imut.edu.cn

Specialty section:

This article was submitted to
Green and Sustainable Chemistry,
a section of the journal
Frontiers in Chemistry

Received: 08 June 2022

Accepted: 21 June 2022

Published: 11 July 2022

Citation:

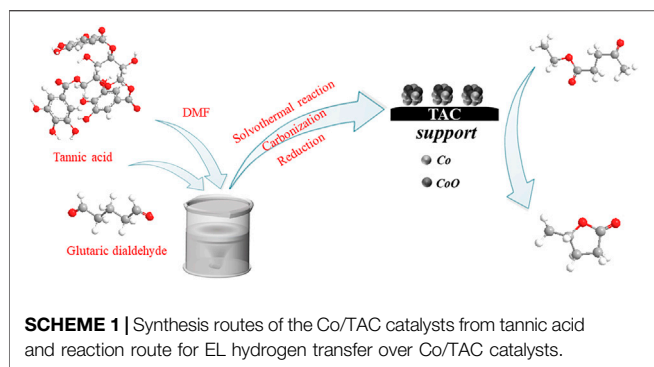
Wang M, Yao X, Chen Y, Lin B, Li N, Zhi K, Liu Q and Zhou H (2022) A Novel Tannic Acid-Based Carbon-Supported Cobalt Catalyst for Transfer Hydrogenation of Biomass Derived Ethyl Levulinate.
Front. Chem. 10:964128.
doi: 10.3389/fchem.2022.964128

The catalytic conversion of ethyl levulinate (EL) to γ -valerolactone (GVL) is an important intermediate reaction in the conversion and utilization of biomass resources. The development of novel and efficient catalysts is significantly important for this reaction. In this work, using the biomass-derived tannic acid as carbon precursor and the transition metal cobalt as active component, a novel tannic acid carbon supported cobalt catalyst (Co/TAC) was prepared by pyrolysis and subsequent hydrazine hydrate reduction method. The hydrogenation of EL and other carbonyl compounds by hydrogen transfer reaction was used to evaluate the performance of the catalysts. The effects of different preparation and reaction conditions on the performance of the catalysts were investigated, and the structures of the prepared catalysts were characterized in detail. The results showed that the carbonization temperature of the support had a significant effect on the activity of the catalyst for the reaction. Under the optimized conditions, the Co/TAC-900 catalyst obtained the highest GVL yield of 91.3% under relatively mild reaction conditions. Furthermore, the prepared catalyst also showed high efficiency for the hydrogenation of various ketone compounds with different structures. This work provides a new reference for the construction of the catalysts during the conversion of biomass and a potential pathway for the high-value utilization of tannin resource.

Keywords: biomass, tannic acid, carbon support, ethyl levulinate, hydrogen transfer, catalyst

INTRODUCTION

With the rapid development of human society, the demand for carbon resources and the consumption of fossil resources are increasing. It is the goal of human society to find renewable carbon resources and improve the utilization efficiency of carbon resources. Biomass, as an abundant, inexpensive and renewable organic carbon resource, is considered as an ideal substitute for traditional fossil resources (Li et al., 2017a; Xu et al., 2020a). A promising way to realize the utilization of biomass is the efficient catalytic conversion of biomass into fuels and platform chemicals. Ethyl levulinate (EL) is one of the most important biomass platform molecules that can be further converted into various high-value products (Tuck et al., 2012). γ -Valerolactone (GVL) is a useful chemical derived from lignocellulose and has the advantages of high stability, low toxicity and safe storage. Additionally, it can be used to produce liquid fuels,



polymers, intermediates in fine chemical production, and food additives, *etc.*, (Wang et al., 2013; Han et al., 2014; Liguori et al., 2015). Due to its potential applications, GVL is considered as a bridge linking biomass and valuable chemicals.

Hydrogenation of EL to GVL is one of the key reactions for the catalytic conversion of sustainable biomass into value-added chemicals. In the synthesis of GVL from biomass, the noble metal based catalysts are considered as excellent catalysts for the hydrogenation of EL to GVL with molecular hydrogen as the hydrogen source, and a variety of noble metal-based homogeneous catalysts such as Ru, Pd, Pt, Ir, Re, and Rh, *etc.*, have been reported for the conversion of EL to GVL. However, high-pressure hydrogen has considerable security risk. Additionally, the cost of noble metals is high and the resources are scarce, and ligand synthesis of homogeneous catalysts is complex and has poor recovery performance (Leitner, 2002; Manzer, 2004; Du et al., 2011; Yan et al., 2013a; Liu et al., 2013; Xin et al., 2014). In contrast, the synthesis of GVL from EL *via* the catalytic transfer hydrogenation (CTH), also known as Meerwein-Ponndorf-Verley (MPV) reaction, can realize the hydrogenation using liquid hydrogen such as isopropanol as the hydrogen source and non-noble metal based catalysts. Therefore, a series of non-noble metal based heterogeneous catalysts have been developed due to their superior performances (Gilkey and Xu, 2016; Osatiashtiani et al., 2017; Xu et al., 2020a), among which cobalt is an abundant metal with high availability and low price, and cobalt-based catalysts are widely used in the well-known Fischer-Tropsch synthesis and other hydrogenation reactions (Long et al., 2015; Osatiashtiani et al., 2017). Besides the metal active sites, the catalyst carrier has the function of supporting and dispersing metal active components. The supports reported in the literature for biomass transfer hydrogenation include Al_2O_3 (Long et al., 2015), zeolite (Obregón et al., 2014), SiO_2 (Ye et al., 2014) and carbon materials, *etc.* Carbon materials have attracted much attention due to their wide availability, high mechanical strength, and good chemical stability (Yan et al., 2013b). It is worth noting that biomass-based carbon has a wide range of sources and good physical and chemical properties, making it an environmentally friendly carbon material and an excellent choice as the candidate for catalyst support (Luo et al., 2015).

Tannic acid (TA) is a renewable and environmental friendly natural functional molecule with rich carbon content and functional groups such as gallic alcohol or catechol groups, which can be extracted from plant tissue. These advantages of TA contributed to its wide applications (MacDermid-Watts et al., 2021). For example, metal-tannin coordination polymers have been widely used as multifunctional platforms for functional surface engineering (Huang et al., 2018). There were also various researches on the use of tannic acid in adsorbent, cross-linking agents, coating materials, and modifying polymer surfaces (Rubentheren et al., 2015; Zhang et al., 2017). TA was also used in the preparation of catalysts. Since the phenolic hydroxyl groups in tannic acid have a strong chelating effect with metal ions, they can be used as ligands to coordinate with metal ions to prepare coordination catalysts. Many previous studies have demonstrated that tannic acid can coordinated with metal ions such as Zr, Hf, Ni, Fe, Cr, Cu, Rh, *etc.*, for furfural hydrogenation and photoelectric catalysis (Mao et al., 2012; Choudhary et al., 2017; Shi et al., 2018; Xu et al., 2020a). TA also has great potential in the preparation of metal/carbon composites due to its strong chelating ability with metal ions (Wang et al., 2020). Carbon materials are generally prepared from tannic acid by pyrolysis. There were some reports on the application of carbon supports produced by the pyrolysis of tannins for ORR, OER and HER electrocatalysts (Cao et al., 2020). The tannin-based carbon supported metal catalysts were used into the catalytic conversion of biomass. Varila et al. (Qin et al., 2019) reported the conversion of furfural to furfuryl alcohol with a Cu/Ni bimetallic catalyst supported by condensed tannin-based carbon foam, and achieved a high conversion of furfural at 503 K and 40 bar H_2 . Cobalt-based catalysts are excellent catalysts for biomass transfer hydrogenation using isopropanol as hydrogen source and solvent. Most of the reported supported catalysts prepared from cobalt and tannic acid were used for the hydrogenation of the halogenated aromatic or the degradation of dyes (Wang et al., 2020; Choi et al., 2021; Varila et al., 2021). To the best of our knowledge, the direct use of tannic acid derived carbon supported transition metal cobalt catalysts for the CTH reaction of EL has not been reported.

Herein, we prepared high-performance tannic acid carbon-supported cobalt catalyst by direct pyrolysis of TA and then hydrazine hydrate reduction method. The performance evaluation of the catalysts was carried out using the CTH reaction of EL to GVL (**Scheme 1**). The results showed that the carbonization temperature of the support had a significant effect on the catalytic activity, 94.3% conversion of EL and a GVL yield of 91.3% were achieved at the reaction temperature of 150°C for 5 h. Co^0 played a key role in the hydrogen transfer reaction and cooperated with the acid-base sites in the catalyst to promote the reaction. The prepared catalyst had a good catalytic performance for ketone compounds with different structures. This work is of great significance for the development of efficient catalysts in the catalytic conversion of biomass.

EXPERIMENTAL

Materials

Tannic acid (TA, 98%), glutaraldehyde solution (50%), ethyl levulinate (EL, 98%), isopropyl alcohol (iPrOH, 99.5%) were purchased from Beijing Innochem Technology Co. Ltd. Cobalt (II) chloride ($\text{CoCl}_2 \cdot 6\text{H}_2\text{O}$), glycol, sodium hydroxide were A.R. grade and provided by Tianjin Fengchuan Chemical Reagent Technology Co. Ltd. γ -Valerolactone (GVL, 99.5%) and decane were obtained from Beijing J&K Scientific Ltd.

Preparation of Carbon Support

The preparation of the carbon support using TA in this work was as follows. TA (1 mmol) was dissolved into DMF (20 ml) and stirred for 1.5 h at room temperature. Then, 25 ml 50% glutaraldehyde solution was added into tannic acid solution and stirred under room temperature for 30 min. The mixed solution was transferred to the PTFE lining of the hydrothermal reactor, and solvothermal reaction was carried out at 200°C for 3 h in a Muffle furnace. After solvothermal reaction, the viscous polymer was dried at 100°C and heated to the desired temperature (300–900°C) under nitrogen atmosphere at a heating rate of 10°C/min for 2 h. After being ground in agate mortar, the black powders were collected. The obtained TA-derived carbon support was denoted as TAC-T (T referred to the carbonization temperature).

Preparation of Catalysts

The Co/TAC-T catalysts were prepared by hydrazine hydrate reduction method. In a typical process, 1.0 g TAC and 3.0 g NaOH were added into the mixture of 20 ml water and 20 ml glycol in breaker A. 1.0 g $\text{CoCl}_2 \cdot 6\text{H}_2\text{O}$ was added into 20 ml glycol in breaker B and stirred for complete dissolution. Beaker A was placed in a water bath with magnetic stirring at 25°C and then 40 ml 80% (v/v) hydrazine hydrate was added to beaker A. The $\text{CoCl}_2 \cdot 6\text{H}_2\text{O}$ in beaker B was slowly dropped into beaker A with a separatory funnel solution and vigorously stirred for 3 h. The obtained solid precipitate was washed with distilled water until the pH was neutral and dried in vacuum at 80°C for 12 h.

Catalyst Characterization

Scanning electron microscope (SEM) measurements were performed on a Hitachi S-4800 scanning electron microscope operated at 15 kV. High resolution transmission electron microscope (HRTEM) images were obtained using a TEM JEOL-1011 with an accelerating voltage of 120 kV. The high-angle annular dark-field scanning TEM (HAADF-STEM) images were performed on a Talos F200X instrument. The specific surface area, pore volume and average pore diameter were measured on a 3H-2000PS2 type analyzer (Beishide instrument Co. Ltd.) by nitrogen adsorption-desorption method. Samples were pretreated for 8 h under vacuum at 250°C before testing. X-ray diffraction (XRD) patterns were recorded on XD8 Advance-Bruker AXS X-ray diffractometer using Cu-K α radiation ($\lambda = 0.1543$ nm) at 40 kV and 40 mA. The scanning speed was set to 30°/min ranging from 5° to 90°.

X-ray photoelectron spectroscopy (XPS) test was performed on an ESCALAB 250Xi spectrometer (Thermo Fisher Scientific) equipped with Al K α excitation source ($h\nu = 1486.6$ eV) and operating at 15 kV and 150 W. Calibration of binding energy by reference to C1 s signal (284.6 eV). Raman spectra at 120 cm^{-1} –4000 cm^{-1} ($\lambda = 532$ nm) were collected on a Renishaw inVia microscope. Temperature-programmed desorption of carbon dioxide (CO_2 -TPD) was performed on Micromeritics AutoChem II 2920. The samples were pretreated at 500°C for 1 h to remove physisorbed CO_2 by flowing helium at 100°C. The strongly adsorbed CO_2 was heated from room temperature to 800°C at a rate of 10°C/min for desorption under the flow of helium. The temperature-programmed desorption of ammonia (NH_3 -TPD) was performed on Micromeritics AutoChem II 2920. The samples were pretreated at 500°C for 1 h, and the physically adsorbed NH_3 was removed by He flowing at 100°C. Under helium flow, the strongly adsorbed NH_3 was heated from room temperature to 800°C at a rate of 10°C/min for desorption. The content of Co element in the Co/TAC catalyst was determined by inductively coupled plasma-optical atomic emission spectroscopy (ICP-AES) on Thermo Fisher Scientific iCAP 7000.

Catalytic Activity Test

The CTH reaction of EL and other ketones to produce the corresponding alcohol or its derivatives was carried out in a stainless steel closed reactor equipped with a polytetrafluoroethylene lining (15 ml in volume). In a typical reaction process, 1 mmol EL, 25–200 mg catalyst and 5 ml iPrOH were added to the lining. The reactor was sealed and purged with N_2 several times to remove air. Then, the reactor was filled with 0.1 MPa N_2 as a protective gas, and it was placed in an oil bath with magnetic stirring and reacted for 1–8 h at the temperature of 130–160°C. After the reaction, the reactor was rapidly cooled in an ice water bath, and the reaction solution and the catalyst were separated by centrifugation. The separated supernatant was analyzed by a gas chromatography (TECHCOMP GC7900) with flame ionization detector using decane as the internal standard. The identification of products and reactants was carried out on GC-MS (Agilent Technologies 7000D). The EL conversion, GVL yield and GVL selectivity were calculated using the following equations (Zhao et al., 2020):

$$\text{EL conversion (\%)} = \left(1 - \frac{\text{Residual mole of EL}}{\text{Initial mole of EL}} \right) \times 100\% \quad (1)$$

$$\text{GVL yield (\%)} = \frac{\text{Generated mole of GVL}}{\text{Initial mole of EL}} \times 100\% \quad (2)$$

$$\text{GVL selectivity (\%)} = \frac{\text{GVL yield}}{\text{EL conversion}} \quad (3)$$

$$\text{TOF (h}^{-1}\text{)} = \frac{\text{Conversion mole of EL}}{\text{Mole of Co catalyst} \times \text{Reaction time}} \quad (4)$$

In the reusability experiment, the catalyst was separated from the reaction system by centrifugation and washed three times with isopropanol, then used for the next cycle without other treatments. All experiments during the experiment have been

TABLE 1 | Catalytic performance of different catalysts in the conversion of EL to GVL.

Entry	Catalyst						
		Con. (%)	Yield (%)	Sel. (%)	S _{BET} ^a (m ² /g)	V _{total} ^b (cm ³ /g)	Pore size ^c (nm)
1	No catalyst	-	-	-			
2	TAC	-	-	-			
3	CoO	-	-	-			
4	CoCl ₂ 6H ₂ O	13.8	0.6	4.4			
5	Co-TAC-300	66.3	53.9	81.2	7.3	0.0123	2.8
6	Co-TAC-500	95.8	76.5	79.9	2.9	0.0116	3.8
7	Co-TAC-600	95.6	79	82.7	6.1	0.0135	3.1
8	Co-TAC-800	95.6	82.7	86.5	5.1	0.0188	2.7
9	Co-TAC-900	97.5	84.1	86.3	6.9	0.0194	2.5
10	Co/TAC-900-air ^d	22.3	2.5	11.1			

^aSpecific surface area was calculated with the BET, method from the adsorption branch of nitrogen sorption isotherm.

^bVolume of pores was estimated from single point adsorption total pore volume of pores.

^cAverage pore size was calculated with the Barrett–Joyner–Halenda (BJH) method from the adsorption branch of nitrogen sorption isotherm.

^dOxidation of the Co/TAC-900 catalyst at 250°C for 3 h under the air atmosphere in the tube furnace.

Reaction conditions: 5 ml iPrOH, 100 mg catalyst, 0.1 MPa N₂ 150°C, 3 h.

repeated at least twice. The quantitative analysis of reactants and products was repeated three times to ensure the accuracy of the data, and the average value was taken.

RESULTS AND DISCUSSION

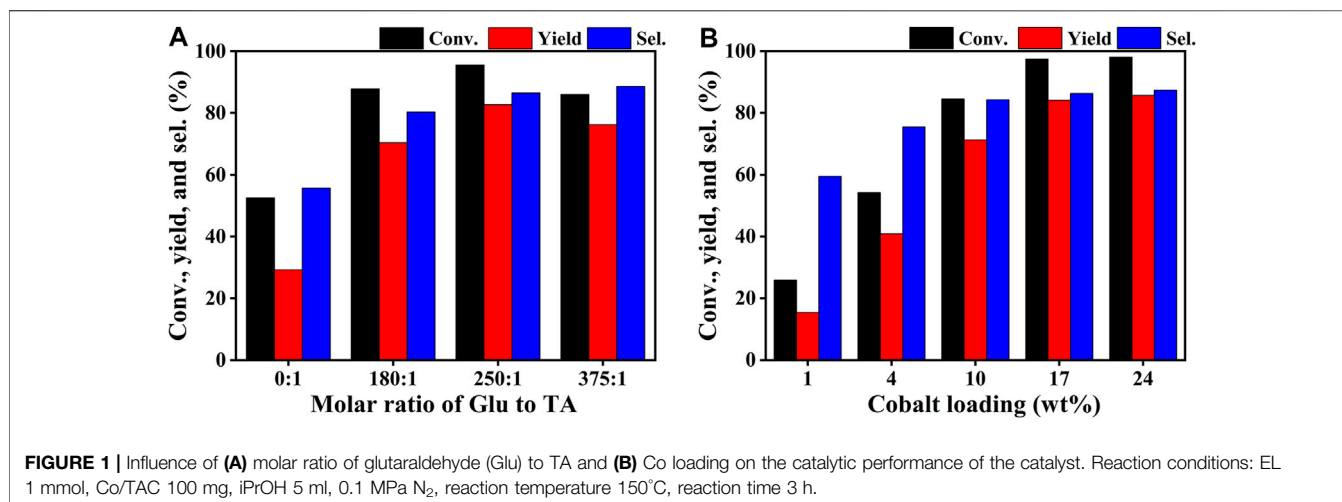
Activity of the Catalysts

The catalytic performance evaluation of the Co/TAC-T catalysts for the CTH reaction of EL to GVL was carried out. As can be seen from **Table 1**, the reaction cannot proceed without any catalyst (entry 1). In the cases of TAC, CoCl₂ 6H₂O alone, and pure CoO as catalysts, it was observed that the conversion of EL was quite low or nearly zero (**Table 1**, entries 2–4). Comparatively, the prepared catalysts showed different activities for the reaction (**Table 1**, entries 5–9). The performance of the Co/TAC-T catalysts was optimized by changing the preparation conditions. Three variables, the ratio of glutaraldehyde to TA, the carbonization temperature and the cobalt loading were investigated. As the carbonization temperature increasing, the conversion of EL and the yield of GVL increased, and the highest conversion and yield were obtained on Co/TAC-900 (**Table 1**, entries 5–9). The effects of the ratio of glutaraldehyde to TA and the cobalt loading were shown in **Figure 1**. The catalytic performance of the Co/TAC catalyst prepared under the ratio of glutaraldehyde to TA 250:1 was better than other catalysts (**Figure 1A**). Next, on the basis of TAC-900 as the catalyst carrier, the ratio of glutaraldehyde solution to TA 250:1, and carbonization temperature 900°C, the cobalt loading of the catalyst was optimized (**Figure 1B**). With the cobalt loading increasing, the catalyst activity increased significantly. Both the conversion of EL and the yield of GVL reached to the highest values when the cobalt loading came to 17 wt%. Further increasing the cobalt loading to 24 wt%, the

increasing of the activity was not obvious. Thus 17 wt% cobalt loading was selected for the follow-up researches. The above results showed that the carbonization temperature of the TA precursor had significant effects on the activity of the obtained catalysts. Therefore, the structure of the catalysts was analyzed through a series of characterizations in the following studies.

Catalyst Characterization

SEM was used to observe the surface morphology of the catalyst. As depicted in SEM images of Co/TAC-900 (**Figure 2A**), the catalyst exhibited uniform spheres with an average diameter of 0.35 μm. Characterizing the surface morphology of the spheres under high magnification, it could be seen that certain materials were covered on the spheres (**Figure 2B**). HRTEM proved that the spheres in the catalyst had a core-shell structure (**Figure 2C**). In order to give insights into the structures of the catalyst, HAADF-STEM images of Co/TAC-900 (**Figures 2D, E**) and the corresponding EDX mapping were conducted (**Figures 2F–I**). HAADF-STEM images showed that the spheres indeed had a core-shell structure, and the EDX mapping showed that cobalt element formed the core, and carbon element formed the shell structure. Besides, O elements existed in the catalyst, and the special distribution of O elements was mainly accompanied by the presence of Co element, indicating that partial cobalt might exist in the form of cobalt oxide, which would be discussed below. The specific surface area and pore size distribution of the Co/TAC-T catalysts were shown in **Table 1** (entries 5–9) and **Supplementary Figure S1**. The specific surface area and pore size of the catalysts at different carbonization temperatures had no significant difference, and there was no obvious change rule. The catalysts at different carbonization temperatures all presented a typical type IV curve with a H₃ hysteresis loop, indicating that the catalyst was a mesoporous material.



The crystal structure of the catalyst was characterized by XRD. As shown in **Figure 3**. The diffraction peaks at 25.6° and 43.5° of TAC-900 can be assigned to the C (002) and C (001) planes of amorphous carbon (Chen et al., 2021). Compared with the carrier, all the catalysts have obvious diffraction peaks of metallic Co (JCPDS database PDF#89-4308) at around 41.5°, 44.2°, and 47.3°, which were corresponded to the (100) (002), and (101) crystal lines of cubic cobalt, respectively (Xu et al., 2020b; Kong et al., 2021). In addition, no other crystalline forms of cobalt were found in the XRD pattern. This result proved that Co⁰ appeared after the reduction of hydrazine hydrate.

In order to analyze the chemical valence of Co species in the catalyst, XPS survey of Co/TAC-T was conducted. The results showed that the presence of Co, C and O elements in the catalyst (**Figure 4A**). The Co 2p_{3/2} XPS spectrum was fitted into three peaks at 778.8, 780.6, and 784.9 eV, respectively (**Figure 4B**), corresponding to the metallic Co, CoO and the satellite peak of CoO (Zhao et al., 2019). Cobalt species existed in the Co/TAC-900 catalyst mostly in the form of Co²⁺, and only a small fraction of Co⁰ existed. As shown in **Table 2**, the relative ratios of cobalt with different valences were analyzed by calculating the ratios of peak areas after peak fitting. The Co 2p peak fitting showed that the metal cobalt content was 16.8%. The ratio of metallic cobalt increased with the increasing of the pyrolysis temperature of the carbon support from 300°C to 900°C, and the higher content of metallic cobalt in the catalyst was beneficial to the activity of the prepared catalysts, which was consistent with the results in **Table 1**.

The structure of the catalyst was further investigated using Raman spectroscopy. As can be seen in **Figure 5**, the G band at 1592 cm⁻¹ and the D band at 1350 cm⁻¹ of the catalyst represent the in-plane vibrations of sp² carbon atoms and the defect-induced imperfect crystal structure, respectively (Chuang et al., 1976). The typical characteristic peaks for CoO appeared at 513 cm⁻¹ and 675 cm⁻¹ (Song et al., 2018; Liu et al., 2021), which also confirmed the existence of CoO. This result was consistent with the characterization of XPS. Therefore, cobalt species coexisted in the catalyst in the form of Co⁰ and CoO.

The acidity and basicity of the catalyst play a crucial role in the hydrogen transfer reaction (Song et al., 2015a; Li et al., 2018).

Therefore, the acidity and basicity of the catalysts were tested using NH₃-TPD and CO₂-TPD, respectively. The results were shown in **Supplementary Figure S2**. Co/TAC catalysts had acid and basic sites, the acidic sites were from Co²⁺, and the basic sites were from O²⁻ (Kong et al., 2021). With the increasing of the carbonization temperature, the desorption peak of the adsorbed gas moved to the high temperature area and the intensity decreased. It could be seen that the total contents of acidic and basic sites of Co/TAC-300, 500 were much stronger than that of Co/TAC-600, 800 and 900. This may be because the increasing of the carbonization temperature led to the change of the support structure and the destroy of the acidic and basic centers in the catalyst, resulting in the decreasing in the content of acidic and basic sites. The acidic and basic sites of Co/TAC-300, 500 were mainly weak to mediumly strong. The contents of the acidic and basic sites of Co/TAC-600, 800, and 900 tended to be stable without significant changes with the increasing of pyrolysis temperature. The quantitative calculation results of the TPD of the catalysts were shown in **Supplementary Tables S1, S2**. Among them, Co/TAC-900 had more strongly acidic sites but less strongly basic sites compared to Co/TAC-600, 800. The abundant strongly acidic sites may be one of the reasons for the high activity of this catalyst. It has been reported that stronger acid strength but weaker base strength was beneficial to transfer hydrogenation and could suppress side reactions (Song et al., 2015b).

Optimization of Reaction Conditions

In the subsequent studies, the effects of different reaction conditions were investigated to realize the high efficiency of the catalyst. The effects of catalyst dosage, reaction temperature and reaction time on the catalytic performance were studied using Co/TAC-900 as the catalyst prepared under the optimal preparation conditions **Figure 6**. As shown in (**Figure 6A**), with the increasing of the catalyst dosage from 25 to 100 mg corresponding to the molar percentage of Co/EL from 7 to 29%, both the conversion of EL and the yield of GVL increased significantly, and nearly total conversion of EL was achieved with GVL yield came to 84.1% under the catalyst dosage of 100 mg. Further increasing the catalyst dosage, the GVL yield had no obvious increasing and

even slightly decreased under excessive catalyst dosage. It may be because that too much catalyst increased the viscosity of the reaction solution and hindered the mass transfer during reaction. On the other hand, excessive catalyst dosage also resulted in the waste of the catalyst and the decreasing of utilization efficiency of the catalyst. The reaction temperature was a key factor affecting the catalytic performance of the catalyst (**Figure 6B**). The conversion of EL and the yield of GVL increased linearly with the increasing of the reaction temperature. When the reaction temperature was 150°C and the reaction time was 3 h, the conversion of EL and the yield of GVL reached to 97.5 and 84.1%, respectively. Further increasing the temperature, the conversion of EL and the yield of GVL decreased slightly, which might be due to the high temperature could affect the

microstructure of the catalyst or the adsorption of the substrate on the active sites of the catalyst. Interestingly, the catalyst also showed medium activity at 130°C, indicating that the catalyst could also catalyze the reaction of EL to GVL under milder conditions. It can be seen from (**Figure 6C**), the conversion of EL and the yield of GVL increased linearly with the extension of reaction time from 1 to 5 h, and the highest conversion and yield could reach to 94.3 and 91.3%, respectively.

Reusability of the Co/TAC-900

To examine the stability of the Co/TAC-900 catalyst during recycling, the catalyst was reused for five times. The results showed that conversion, yield and selectivity decreased gradually within five cycles (**Figure 7**). To further investigate the reasons for the

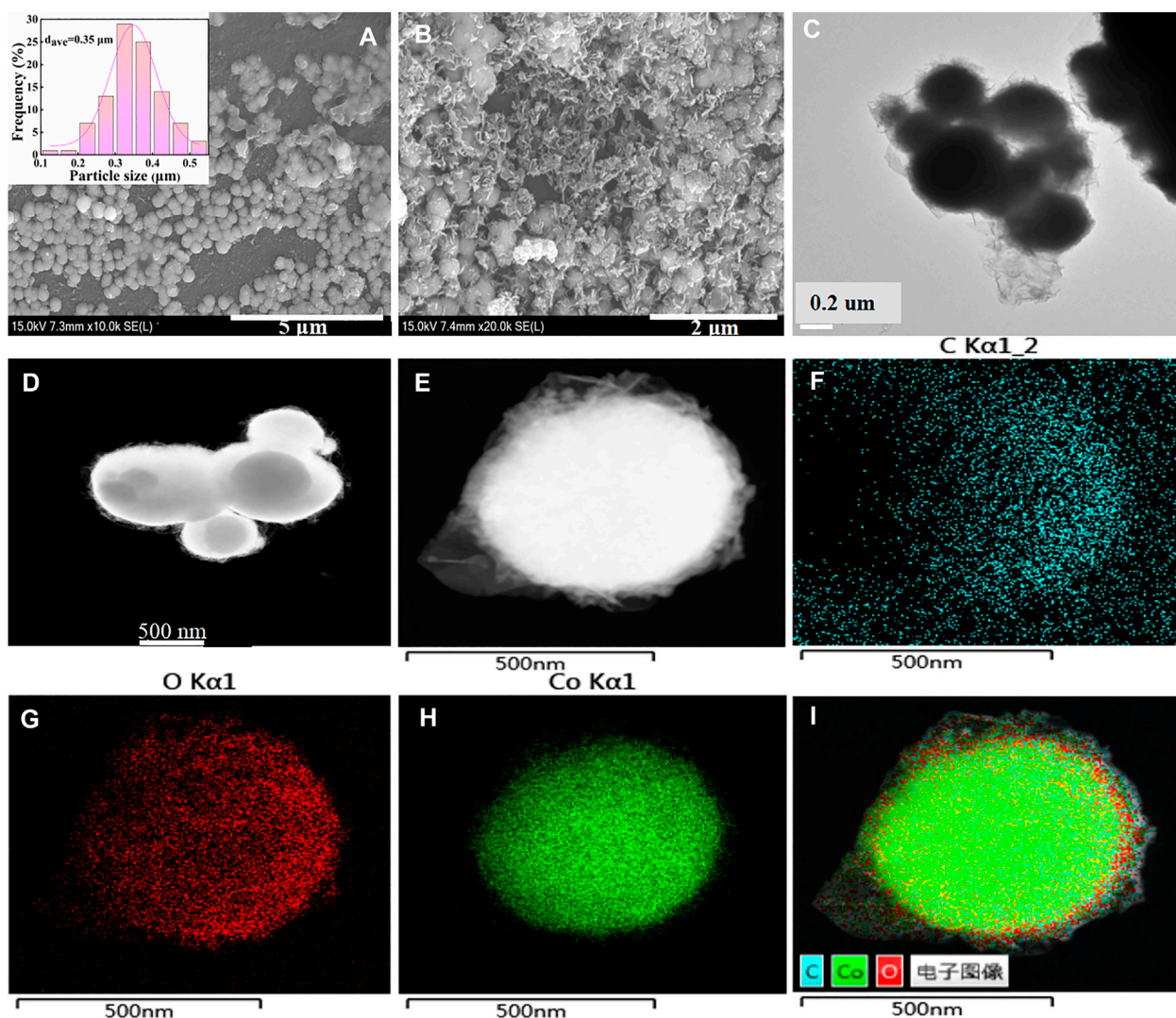
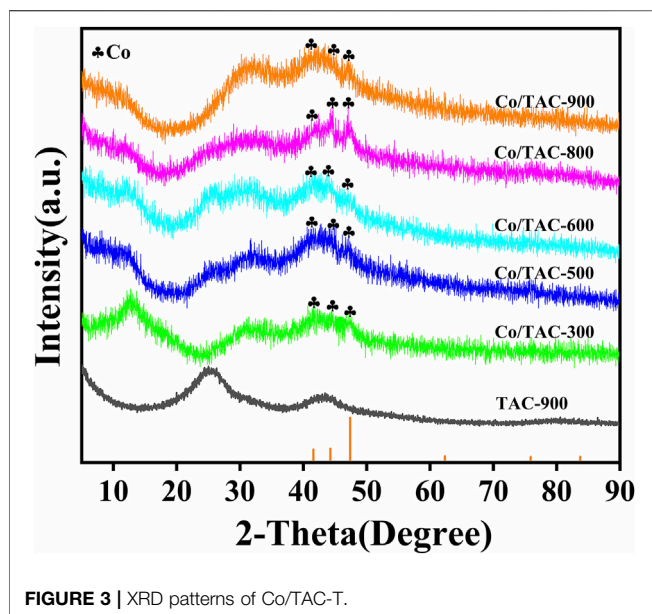
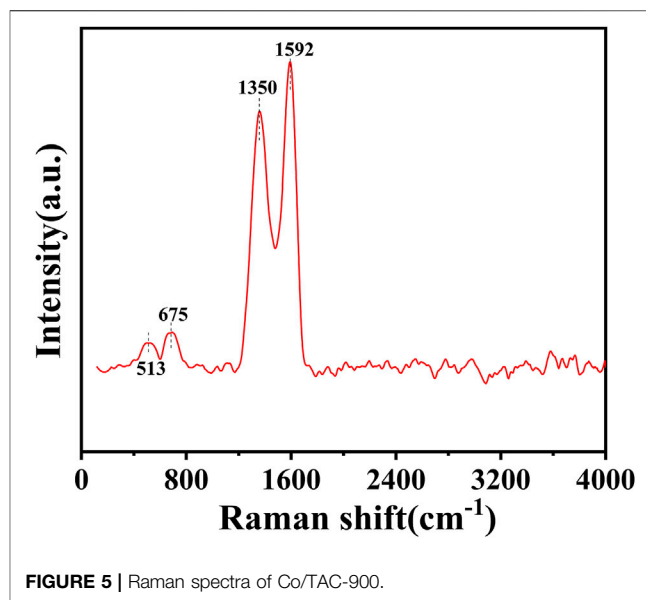


FIGURE 2 | (A) and (B) SEM images, (C) HRTEM image of Co/TAC-900, (D) and (E) HAADF-STEM images of Co/TAC-900, (F) C element, (G) O element, (H) Co element, (I) overlapping map of (F–H).



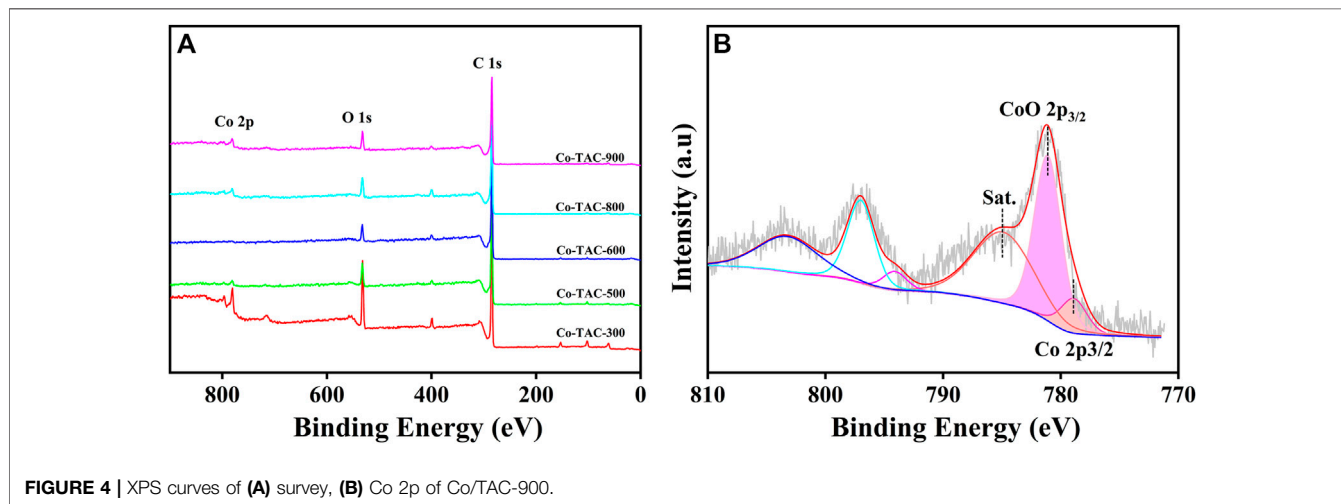
decrease in catalytic activity, the catalysts after five cycles were characterized and compared to the fresh catalyst. The results of ICP (**Supplementary Table S3**) showed that the cobalt content decreased from 17.0 to 7.7% after five cycles. Next, XPS was used to characterize whether the cobalt element's valence state of the catalyst changed after recycling, and the results were shown in **Supplementary Figure S3**. The results showed that the type of cobalt in the catalyst did not change after being recycled for 5 times, but the peak fitting results showed that the content of zero valent cobalt decreased from 16.8% (fresh catalyst) to 5.9% (recycled catalyst). Therefore, we speculated that the reason for the decrease in catalytic activity may be the loss of cobalt and the change of the chemical state of cobalt in the catalyst. This may be related to the structure of the carbon support. It was reported that when the cobalt at the active center was tightly bound to the N atom, the electron



distribution on the catalyst surface could be modulated, resulting in excellent stability of the catalyst. N-doping carbon supported cobalt catalysts were reported to be stable (Hasan et al., 2017; Xu et al., 2020b; Chen et al., 2022). It was speculated that the TAC-900 carbon support and the cobalt nanoparticles lacked strong interaction, leading to the easy leaching of cobalt and the changes in chemical state of cobalt. Subsequent studies aiming at increasing the stability of the Co/TAC-900 catalyst were conducted in our group, which will be discussed in another work.

Substrate Expansion

In order to investigate the catalytic performance of the catalyst for substrates with different structures, the Co/TAC-900 catalyst was used for the hydrogen transfer reaction of different ketone compounds, and the results were shown in **Table 3**. All ketone substrates could successfully undergo hydrogen transfer under different reaction



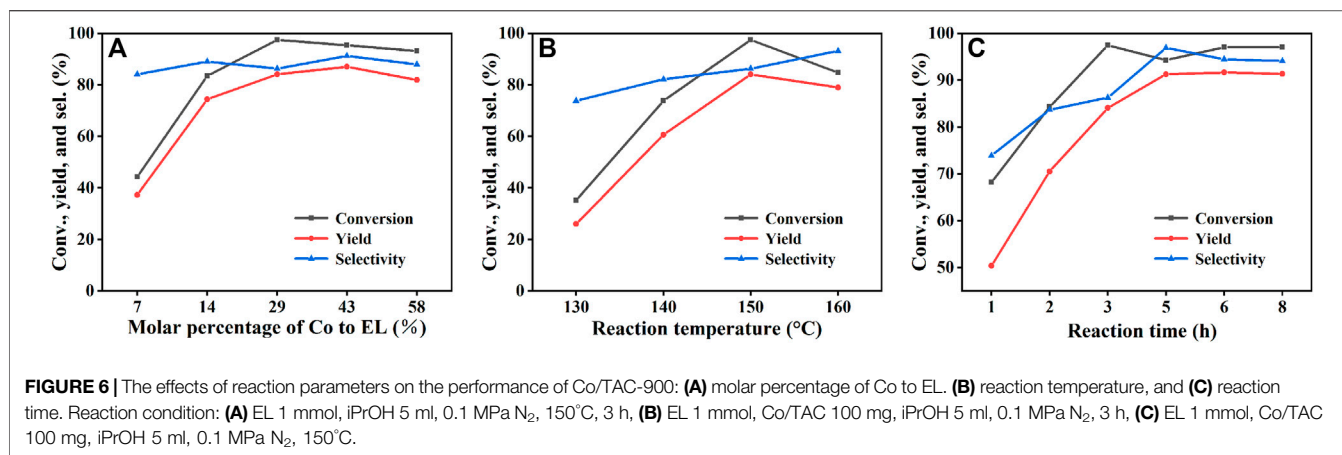
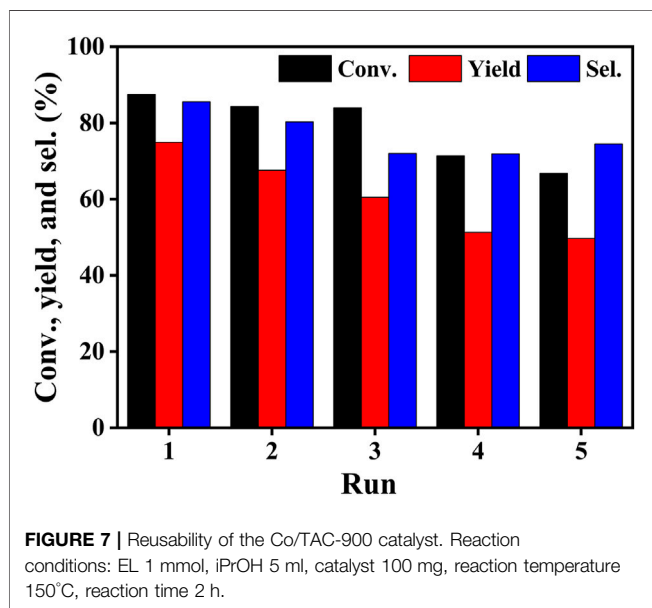


TABLE 2 | Contents of metallic Co and CoO in different Co/TAC-T catalysts.

Entry	Sample	Metallic Co % (778.5 eV)	CoO % (781.1 eV)
1	Co-TAC-300	10.43	89.57
2	Co-TAC-500	11.52	88.48
3	Co-TAC-600	11.61	88.39
4	Co-TAC-800	13.73	86.27
5	Co-TAC-900	16.83	83.17



temperatures, and the conversion of the substrates and the selectivity for the target products were higher than 90 and 95%, respectively. The results proved that Co/TAC-900 had certain universality for the transfer hydrogenation of different ketone substrates.

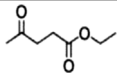
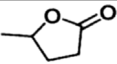
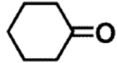
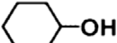
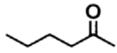
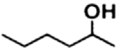
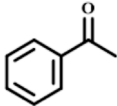
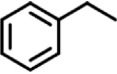
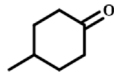
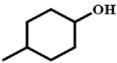
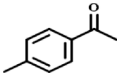
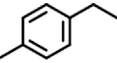
The catalytic performance of Co/TAC-900 was compared with other analogue catalysts for hydrogen transfer reactions (Supplementary Table S4). Compared with the catalysts that have

been reported in other literatures, the catalysts prepared in this work can obtain relatively high EL conversion and GVL yield under relatively mild conditions (150°C) with medium to higher TOF. In addition, the catalyst was prepared by using tannic acid as the precursor, which was renewable and had potential advantages in catalyst cost.

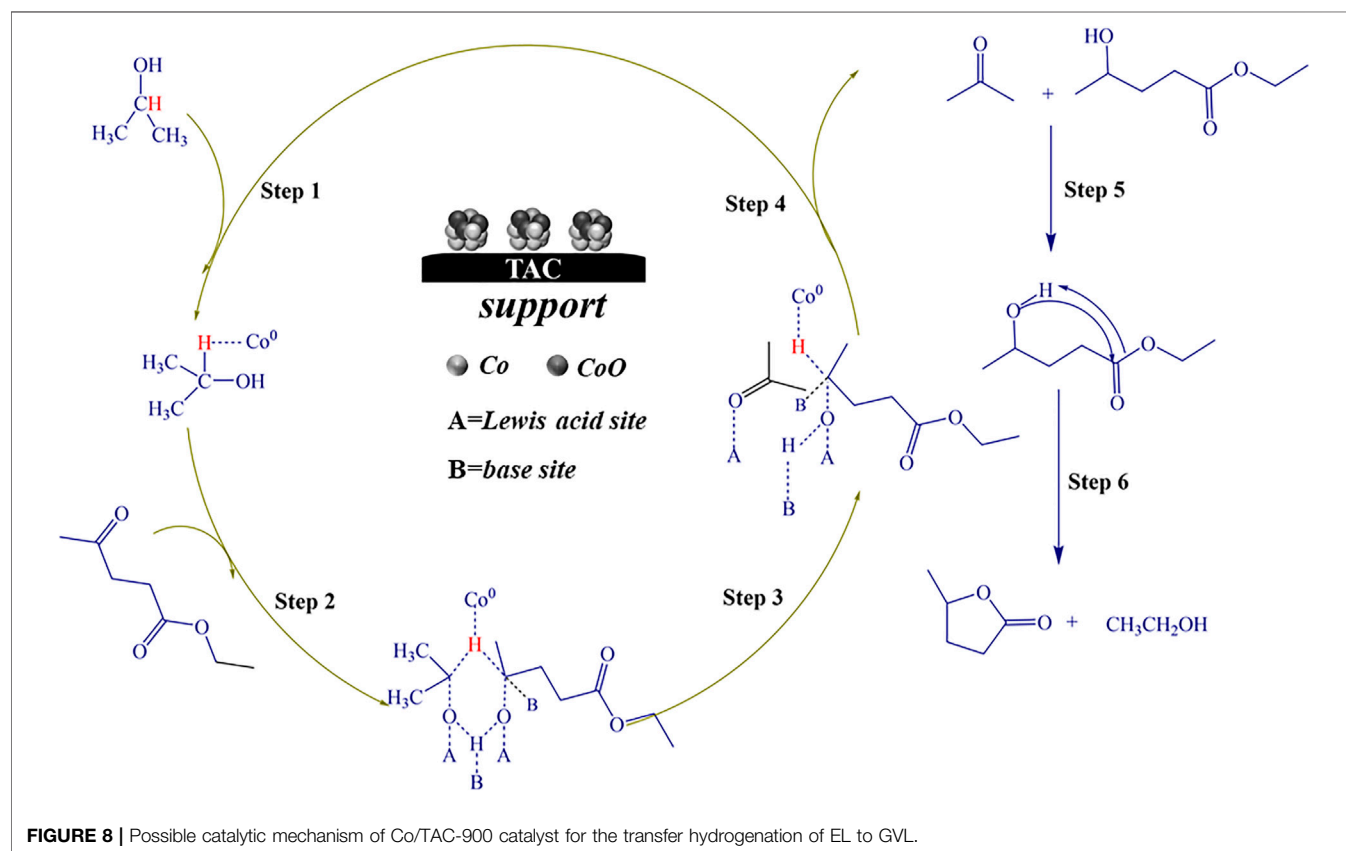
Possible Reaction Mechanism

Based on the experimental results and literature reports, the possible catalytic reaction mechanism of Co/TAC-900 catalyst for hydrogen transfer reaction was further discussed. The previous characterization results showed that cobalt species coexisted in the catalyst in the form of Co⁰ and CoO, and the two species cooperated to promote the hydrogen transfer reaction. In the Co/TAC-900 catalyst, CoO provided a Lewis acid-base pair active sites, where the Lewis acid sites were derived from the metal cation Co²⁺, and the basic sites were derived from O²⁻ (Jiang et al., 2020). In the hydrogen transfer reaction using isopropanol as the hydrogen source, the activation of hydrogen in isopropanol was an important step in the reaction process (Geboers et al., 2014). The energy of the 4s orbital in the ground state electron orbital arrangement of Co⁰ was lower than that of the 3d orbital, and electrons preferentially fill the 4s orbital, while the 3d orbital was not filled. So Co⁰ was more likely to accept electrons and easily adsorbed hydrogen in isopropanol to form Co-H bonds (Song et al., 2015b; Kaźmierczak et al., 2020; Kojima et al., 2021). To prove that Co⁰ plays a leading role in activating H in isopropanol, the Co/TAC-900 catalyst was oxidized in air at 250°C for 3 h. As a result, as shown in Table 1, entry 10, the catalyst activity after oxidation decreased significantly. To verify the cobalt states of the oxidized catalysts, we carried out XPS characterization for the oxidized catalysts, and the result was shown in Supplementary Figure S4. The result showed that Co⁰ nearly disappeared in the oxidized catalysts. Therefore, it could be concluded that Co⁰ played a critical role in the absorption and activation of isopropanol. Figure 8 showed the possible reaction mechanism of the catalyst for EL conversion. First, Co⁰ activated the hydrogen on the second carbon in isopropanol to form the Co-H bond. Secondly, the hydroxyl groups in isopropanol interacted with the acid-base sites (Co²⁺-O²⁻) on Co/TAC-900, making the hydroxyl groups activated and dissociated to the corresponding alkoxide (Song et al., 2015a; Li et al., 2017b). Meanwhile, the carbonyl group in EL

TABLE 3 | Co/TAC-900 catalyst catalyzed CTH reaction of ketones.

Entry	Substrate	Product	T (°C)	Time(h)	Conv. (%)	Yield (%)	Sel. (%)
1			150	5	94.3	91.3	96.9
2			120	15	>99	>99	>99
3			150	8	91.4	86.8	95.0
4			120	12	>99	>99	>99
5			120	12	>99	>99	>99
6			100	12	>99	>99	>99

Reaction condition: substrate 1 mmol, the molar percentage of Co/EL was 29%, iPrOH, 5 ml, 0.1 MPa, N₂.



could be adsorbed and activated by $\text{Co}^{2+}\text{-O}^{2-}$ on the catalyst. Then hydrogen transfer took place between the dissociated alcohol and the activated EL *via* a concerted process involving a six-link intermediate to form ethyl 4-hydroxypentanoate (4-HPE). Finally, the 4-HPE is converted into GVL through an intramolecular transesterification under the role of acidic sites in the catalyst. Isopropanol was converted into acetone after losing two hydrogen atoms.

CONCLUSION

In conclusion, a novel catalyst was prepared using renewable tannic acids derived carbon as the support and cobalt as the active metal. The effects of the preparation and the reaction conditions on the activity of the catalysts were systematically investigated. The results showed that the prepared catalyst (Co/TAC-900) had a core-shell structure, with cobalt as the core and carbon as the shell. Cobalt existed in the form of Co^0 and CoO . The pyrolysis temperature had significant influences on the activity of the catalyst *via* changing the acidic and basic properties of the catalyst. The prepared catalyst could fulfill the selective hydrogenation of various ketone compounds with high efficiency, indicating that it had wide substrate universality. The performance of the catalyst decreased during the recycling process, which was proved to be caused by the leaching of the cobalt and the decreasing of the Co^0 content in the catalyst. Mechanism analysis showed that Co^0 played a key role during the transfer hydrogenation reaction, and the catalytic reaction was finished by the combined action of Co^0 together with the acidic and basic sites in the catalyst. This work provides a novel reference for the construction of catalysts in the field of biomass conversion and a potential pathway for the high-value utilization of tannin acid resource.

REFERENCES

- Cao, Y., Liu, K., Wu, C., Zhang, H., and Zhang, Q. (2020). In Situ-formed Cobalt Embedded into N-Doped Carbon as Highly Efficient and Selective Catalysts for the Hydrogenation of Halogenated Nitrobenzenes under Mild Conditions. *Appl. Catal. A General* 592, 117434. doi:10.1016/j.apcata.2020.117434
- Chen, H., Xu, Q., Zhang, D., Liu, W., Liu, X., and Yin, D. (2021). Highly Efficient Synthesis of γ -valerolactone by Catalytic Conversion of Biomass-Derived Levulinic Esters over Support-free Mesoporous Ni. *Renew. Energy* 163, 1023–1032. doi:10.1016/j.renene.2020.09.023
- Chen, Y., Yao, X., Zhou, H., He, R., and Liu, Q. (2022). A Novel and Efficient N-Doping Carbon Supported Cobalt Catalyst Derived from the Fermentation Broth Solid Waste for the Hydrogenation of Ketones via Meerwein-Ponndorf-Verley Reaction. *Appl. Catal. A General* 630, 118436. doi:10.1016/j.apcata.2021.118436
- Choi, G. H., Nam, M. G., Kwak, S. J., Kim, S. H., Chang, H., Shin, C.-S., et al. (2021). Modularly Aromatic-Knit Graphitizable Phenolic Network as a Tailored Platform for Electrochemical Applications. *Energy Environ. Sci.* 14, 3203–3215. doi:10.1039/D1EE00402F
- Choudhary, B. C., Paul, D., Borse, A. U., and Garole, D. J. (2017). Recovery of Palladium from Secondary Waste Using Soluble Tannins Cross-Linked Lagerstroemia Speciosa Leaves Powder. *J. Chem. Technol. Biotechnol.* 92, 1667–1677. doi:10.1002/jctb.5163

DATA AVAILABILITY STATEMENT

The original contributions presented in the study are included in the article/**Supplementary Material**, further inquiries can be directed to the corresponding author.

AUTHOR CONTRIBUTIONS

The laboratory work, analysis of data and writing was carried out predominantly by MW. XY and YC helped in the design and review of data and interpretation. BL did supplementary experiment. NL, KZ, and QL provided experimental design ideas. All authors contributed to the final writing of the paper.

FUNDING

This work was supported by the National Natural Science Foundation of China (21968021, 21868020), Science and Technology Planning Project of Inner Mongolia Autonomous Region (2020GG0289), Program for Grassland Elite in Inner Mongolia, the Innovative and Entrepreneurial Talents Grassland Talents Engineering of Inner Mongolia (Q2017011), CAS “Light of West China” Program, Local Science and Technology Development Fund Projects Guided by the Central Government (2020ZY0010), and Major Science and Technology Projects of Inner Mongolia Autonomous Region (2021ZD0020).

SUPPLEMENTARY MATERIAL

The Supplementary Material for this article can be found online at: <https://www.frontiersin.org/articles/10.3389/fchem.2022.964128/full#supplementary-material>

- Chuang, T. J., Brundle, C. R., and Rice, D. W. (1976). Interpretation of the X-Ray Photoemission Spectra of Cobalt Oxides and Cobalt Oxide Surfaces. *Surf. Sci.* 59, 413–429. doi:10.1016/0039-6028(76)90026-1
- Du, X.-L., He, L., Zhao, S., Liu, Y.-M., Cao, Y., He, H.-Y., et al. (2011). Hydrogen-Independent Reductive Transformation of Carbohydrate Biomass into γ -Valerolactone and Pyrrolidone Derivatives with Supported Gold Catalysts. *Angew. Chem.* 123, 7961–7965. doi:10.1002/ange.201100102
- Geboers, J., Wang, X., De Carvalho, A. B., and Rinaldi, R. (2014). Densification of Biorefinery Schemes by H-Transfer with Raney Ni and 2-propanol: A Case Study of a Potential Avenue for Valorization of Alkyl Levulinates to Alkyl γ -hydroxypentanoates and γ -valerolactone. *J. Mol. Catal. A Chem.* 388–389, 106–115. doi:10.1016/j.molcata.2013.11.031
- Gilkey, M. J., and Xu, B. (2016). Heterogeneous Catalytic Transfer Hydrogenation as an Effective Pathway in Biomass Upgrading. *ACS Catal.* 6, 1420–1436. doi:10.1021/acscatal.5b02171
- Han, J., Sen, S. M., Alonso, D. M., Dumesic, J. A., and Maravelias, C. T. (2014). A Strategy for the Simultaneous Catalytic Conversion of Hemicellulose and Cellulose from Lignocellulosic Biomass to Liquid Transportation Fuels. *Green Chem.* 16, 653–661. doi:10.1039/C3GC41511B
- Hasan, Z., Ok, Y. S., Rinklebe, J., Tsang, Y. F., Cho, D.-W., and Song, H. (2017). N Doped Cobalt-Carbon Composite for Reduction of P-Nitrophenol and Pendimethalin. *J. Alloys Compd.* 703, 118–124. doi:10.1016/j.jallcom.2017.01.326

- Huang, H., Qin, J., Wang, G., Guo, Z., Yu, X., Zhao, Y., et al. (2018). Synthesis of Spiny Metal-Phenolic Coordination Crystals as a Sensing Platform for Sequence-specific Detection of Nucleic Acids. *CrystEngComm* 20, 7626–7630. doi:10.1039/C8CE01555D
- Jiang, S., Li, F., Huang, J., Wang, Y., Lu, S., Li, P., et al. (2020). Catalytic Transfer Hydrogenation of Furfural over Magnetic Carbon-Encapsulated CoO@C Catalyst. *ChemistrySelect* 5, 9883–9892. doi:10.1002/slct.202002269
- Kaźmierczak, K., Pinel, C., Lorient, S., Besson, M., Michel, C., and Perret, N. (2020). Supported Cobalt Catalysts for Acceptorless Alcohol Dehydrogenation. *ChemPlusChem* 85, 1315–1324. doi:10.1002/cplu.202000359
- Kojima, T., Koganezaki, T., Fujii, S., Kameoka, S., and Tsai, A.-P. (2021). Durability and Activity of Co₂YZ (Y = Mn or Fe, Z = Ga or Ge) Heusler Alloy Catalysts for Dehydrogenation of 2-propanol. *Catal. Sci. Technol.* 11, 4741–4748. doi:10.1039/D1CY00279A
- Kong, X., Geng, W., Li, W., Liu, L., Yan, X., Gong, L., et al. (2021). Co Encapsulated N-Doped Carbon Nanotubes as Robust Catalyst for Valorization of Levulinic Acid in Aqueous Media. *J. Energy Chem.* 52, 12–19. doi:10.1016/j.jechem.2020.04.050
- Leitner, W. (2002). Supercritical Carbon Dioxide as a Green Reaction Medium for Catalysis. *Acc. Chem. Res.* 35, 746–756. doi:10.1021/ar010070q
- Li, C., Xu, G., Zhai, Y., Liu, X., Ma, Y., and Zhang, Y. (2017). Hydrogenation of Biomass-Derived Ethyl Levulinate into γ -valerolactone by Activated Carbon Supported Bimetallic Ni and Fe Catalysts. *Fuel* 203, 23–31. doi:10.1016/j.fuel.2017.04.082
- Li, F., France, L. J., Cai, Z., Li, Y., Liu, S., Lou, H., et al. (2017). Catalytic Transfer Hydrogenation of Butyl Levulinate to γ -valerolactone over Zirconium Phosphates with Adjustable Lewis and Brønsted Acid Sites. *Appl. Catal. B Environ.* 214, 67–77. doi:10.1016/j.apcatb.2017.05.013
- Li, G., Yang, H., Zhang, H., Qi, Z., Chen, M., Hu, W., et al. (2018). Encapsulation of Nonprecious Metal into Ordered Mesoporous N-Doped Carbon for Efficient Quinoline Transfer Hydrogenation with Formic Acid. *ACS Catal.* 8, 8396–8405. doi:10.1021/acscatal.8b01404
- Liguori, F., Moreno-Marrocan, C., and Barbaro, P. (2015). Environmentally Friendly Synthesis of γ -Valerolactone by Direct Catalytic Conversion of Renewable Sources. *ACS Catal.* 5, 1882–1894. doi:10.1021/cs501922e
- Liu, L., Li, W., Qi, R., Zhu, Q., Li, J., Fang, Y., et al. (2021). Cobalt Encapsulated in N-doped G-rhaphene S-heet for O-ne-P-ot R-eductive A-mination to S-synthesize S-econdary A-mines. *Mol. Catal.* 505, 111504. doi:10.1016/j.mcat.2021.111504
- Liu, Q., Pu, Z., Asiri, A. M., Qusti, A. H., Al-Youbi, A. O., and Sun, X. (2013). One-step Solvothermal Synthesis of MoS₂/TiO₂ Nanocomposites with Enhanced Photocatalytic H₂ Production. *J. Nanopart. Res.* 15, 2057. doi:10.1007/s11051-013-2057-8
- Long, X., Sun, P., Li, Z., Lang, R., Xia, C., and Li, F. (2015). Magnetic Co/Al₂O₃ Catalyst Derived from Hydrotalcite for Hydrogenation of Levulinic Acid to γ -valerolactone. *Chin. J. Catal.* 36, 1512–1518. doi:10.1016/S1872-2067(15)60934-2
- Luo, J., Zhang, N., Lai, J., Liu, R., and Liu, X. (2015). Tannic Acid Functionalized Graphene Hydrogel for Entrapping Gold Nanoparticles with High Catalytic Performance toward Dye Reduction. *J. Hazard. Mater.* 300, 615–623. doi:10.1016/j.jhazmat.2015.07.079
- MacDermid-Watts, K., Pradhan, R., and Dutta, A. (2021). Catalytic Hydrothermal Carbonization Treatment of Biomass for Enhanced Activated Carbon: a Review. *Waste Biomass Valor* 12, 2171–2186. doi:10.1007/s12649-020-01134-x
- Manzer, L. E. (2004). Catalytic Synthesis of α -methylene- γ -valerolactone: a Biomass-Derived Acrylic Monomer. *Appl. Catal. A General* 272, 249–256. doi:10.1016/j.apcata.2004.05.048
- Mao, H., Liao, X., Zhang, W., and Shi, B. (2012). Recyclable Plant Tannin-Chelated Rh(III) Complex Catalysts for Aqueous-Organic Biphasic Hydrogenation of Quinoline. *J. Chem. Technol. Biotechnol.* 87, 1104–1110. doi:10.1002/jctb.3726
- Obregon, I., Corro, E., Izquierdo, U., Requies, J., and Arias, P. L. (2014). Levulinic Acid Hydrogenolysis on Al₂O₃-Based Ni-Cu Bimetallic Catalysts. *Chin. J. Catal.* 35, 656–662. doi:10.1016/S1872-2067(14)60051-6
- Osatiashiani, A., Lee, A. F., and Wilson, K. (2017). Recent Advances in the Production of γ -valerolactone from Biomass-Derived Feedstocks via Heterogeneous Catalytic Transfer Hydrogenation. *J. Chem. Technol. Biotechnol.* 92, 1125–1135. doi:10.1002/jctb.5213
- Qin, Q., Jang, H., Li, P., Yuan, B., Liu, X., and Cho, J. (2019). A Tannic Acid-Derived N-, P-Codoped Carbon-Supported Iron-Based Nanocomposite as an Advanced Trifunctional Electrocatalyst for the Overall Water Splitting Cells and Zinc-Air Batteries. *Adv. Energy Mat.* 9, 1803312. doi:10.1002/aenm.201803312
- Rubentheren, V., Ward, T. A., Chee, C. Y., and Tang, C. K. (2015). Processing and Analysis of Chitosan Nanocomposites Reinforced with Chitin Whiskers and Tannic Acid as a Crosslinker. *Carbohydr. Polym.* 115, 379–387. doi:10.1016/j.carbpol.2014.09.007
- Shi, Y., Yu, Y., Yu, Y., Huang, Y., Zhao, B., and Zhang, B. (2018). Boosting Photoelectrochemical Water Oxidation Activity and Stability of Mo-Doped BiVO₄ through the Uniform Assembly Coating of NiFe-Phenolic Networks. *ACS Energy Lett.* 3, 1648–1654. doi:10.1021/acscenergylett.8b00855
- Song, J., Wu, L., Zhou, B., Zhou, H., Fan, H., Yang, Y., et al. (2015). A New Porous Zr-Containing Catalyst with a Phenate Group: an Efficient Catalyst for the Catalytic Transfer Hydrogenation of Ethyl Levulinate to γ -valerolactone. *Green Chem.* 17, 1626–1632. doi:10.1039/C4GC02104E
- Song, J., Zhou, B., Zhou, H., Wu, L., Meng, Q., Liu, Z., et al. (2015). Porous Zirconium-Phytic Acid Hybrid: a Highly Efficient Catalyst for Meerwein-Ponndorf-Verley Reductions. *Angew. Chem. Int. Ed.* 54, 9399–9403. doi:10.1002/anie.201504001
- Song, T., Ren, P., Duan, Y., Wang, Z., Chen, X., and Yang, Y. (2018). Cobalt Nanocomposites on N-Doped Hierarchical Porous Carbon for Highly Selective Formation of Anilines and Imines from Nitroarenes. *Green Chem.* 20, 4629–4637. doi:10.1039/C8GC01374H
- Tuck, C. O., Pérez, E., Horváth, I. T., Sheldon, R. A., and Poliakov, M. (2012). Valorization of Biomass: Deriving More Value from Waste. *Sci.* 337, 695–699. doi:10.1126/science.1218930
- Varila, T., Mäkelä, E., Kupila, R., Romar, H., Hu, T., Karinen, R., et al. (2021). Conversion of Furfural to 2-methylfuran over CuNi Catalysts Supported on Biobased Carbon Foams. *Catal. Today* 367, 16–27. doi:10.1016/j.cattod.2020.10.027
- Wang, D., Hakim, S. H., Martin Alonso, D., and Dumesic, J. A. (2013). A Highly Selective Route to Linear Alpha Olefins from Biomass-Derived Lactones and Unsaturated Acids. *Chem. Commun.* 49, 7040–7042. doi:10.1039/C3CC43587C
- Wang, X., Hao, J., Deng, L., Zhao, H., Liu, Q., Li, N., et al. (2020). The Construction of Novel and Efficient Hafnium Catalysts Using Naturally Existing Tannic Acid for Meerwein-Ponndorf-Verley Reduction. *RSC Adv.* 10, 6944–6952. doi:10.1039/C9RA10317A
- Xin, J., Zhang, S., Yan, D., Ayodele, O., Lu, X., and Wang, J. (2014). Formation of C-C Bonds for the Production of Bio-Alkanes under Mild Conditions. *Green Chem.* 16, 3589–3595. doi:10.1039/C4GC00501E
- Xu, G., Liu, C., Hu, A., Wang, S., and Wang, H. (2020). A Novel Synthesis of Zirconium Tannate with High Stability: New Insight into the Structure of the Catalyst for Hydrogenation. *Appl. Catal. A General* 602, 117666. doi:10.1016/j.apcata.2020.117666
- Xu, L., Nie, R., Lyu, X., Wang, J., and Lu, X. (2020). Selective Hydrogenation of Furfural to Furfuryl Alcohol without External Hydrogen over N-Doped Carbon Confined Co Catalysts. *Fuel Process. Technol.* 197, 106205. doi:10.1016/j.fuproc.2019.106205
- Yan, K., Jarvis, C., Lafleur, T., Qiao, Y., and Xie, X. (2013). Novel Synthesis of Pd Nanoparticles for Hydrogenation of Biomass-Derived Platform Chemicals Showing Enhanced Catalytic Performance. *RSC Adv.* 3, 25865–25871. doi:10.1039/C3RA43619E
- Yan, K., Lafleur, T., and Liao, J. (2013). Facile Synthesis of Palladium Nanoparticles Supported on Multi-Walled Carbon Nanotube for Efficient Hydrogenation of Biomass-Derived Levulinic Acid. *J. Nanopart. Res.* 15, 1–7. doi:10.1007/s11051-013-1906-9
- Ye, F., Zhang, D., Xue, T., Wang, Y., and Guan, Y. (2014). Enhanced Hydrogenation of Ethyl Levulinate by Pd-AC Doped with Nb₂O₅. *Green Chem.* 16, 3951–3957. doi:10.1039/C4GC00972J
- Zhang, P., Wang, L., Yang, S., Schott, J. A., Liu, X., Mahurin, S. M., et al. (2017). Solid-state Synthesis of Ordered Mesoporous Carbon Catalysts via a Mechanochemical Assembly through Coordination Cross-Linking. *Nat. Commun.* 8, 1–10. doi:10.1038/ncomms15020

- Zhao, H., Hao, J., Ban, Y., Sha, Y., Zhou, H., Liu, Q., et al. (2019). Novel and Efficient Cobalt Catalysts Synthesized by One-step Solution Phase Reduction for the Conversion of Biomass Derived Ethyl Levulinate. *Catal. Today* 319, 145–154. doi:10.1016/j.cattod.2018.08.011
- Zhao, Y.-H., Huang, B.-C., Jiang, J., Xia, W.-J., Li, G.-F., Fan, N.-S., et al. (2020). Polyphenol-metal Network Derived Nanocomposite to Catalyze Peroxymonosulfate Decomposition for Dye Degradation. *Chemosphere* 244, 125577. doi:10.1016/j.chemosphere.2019.125577

Conflict of Interest: The authors declare that the research was conducted in the absence of any commercial or financial relationships that could be construed as a potential conflict of interest.

Publisher's Note: All claims expressed in this article are solely those of the authors and do not necessarily represent those of their affiliated organizations, or those of the publisher, the editors and the reviewers. Any product that may be evaluated in this article, or claim that may be made by its manufacturer, is not guaranteed or endorsed by the publisher.

Copyright © 2022 Wang, Yao, Chen, Lin, Li, Zhi, Liu and Zhou. This is an open-access article distributed under the terms of the Creative Commons Attribution License (CC BY). The use, distribution or reproduction in other forums is permitted, provided the original author(s) and the copyright owner(s) are credited and that the original publication in this journal is cited, in accordance with accepted academic practice. No use, distribution or reproduction is permitted which does not comply with these terms.



OPEN ACCESS

EDITED BY

Jinliang Song,
Guangdong University of Technology,
China

REVIEWED BY

Chao Xie,
South-Central University for
Nationalities, China
Haoran Wu,
Zhengzhou University, China

*CORRESPONDENCE

Jianxiu Hao,
hjsx2020@imut.edu.cn

SPECIALTY SECTION

This article was submitted to Green and Sustainable Chemistry, a section of the journal Frontiers in Chemistry

RECEIVED 10 June 2022

ACCEPTED 30 June 2022

PUBLISHED 22 July 2022

CITATION

Hao J, Zhang Y, Zhang T, Zhou H, Liu Q, Zhi K, Li N and He R (2022), A novel and highly efficient Zr-containing catalyst supported by biomass-derived sodium carboxymethyl cellulose for hydrogenation of furfural. *Front. Chem.* 10:966270. doi: 10.3389/fchem.2022.966270

COPYRIGHT

© 2022 Hao, Zhang, Zhang, Zhou, Liu, Zhi, Li and He. This is an open-access article distributed under the terms of the Creative Commons Attribution License (CC BY). The use, distribution or reproduction in other forums is permitted, provided the original author(s) and the copyright owner(s) are credited and that the original publication in this journal is cited, in accordance with accepted academic practice. No use, distribution or reproduction is permitted which does not comply with these terms.

A novel and highly efficient Zr-containing catalyst supported by biomass-derived sodium carboxymethyl cellulose for hydrogenation of furfural

Jianxiu Hao*, Yafang Zhang, Tianyuan Zhang, Huacong Zhou, Quansheng Liu, Keduan Zhi, Na Li and Runxia He

College of Chemical Engineering, Inner Mongolia University of Technology, Hohhot, NM, China

Functional use of biomass based on its structural properties is an efficient approach for the valuable utilization of biomass resources. In this work, carboxymethyl cellulose zirconium-based catalyst (Zr-CMC) was constructed by the coordination between the carboxylic groups in sodium carboxymethyl cellulose (CMC-Na) with transition metal Zr^{4+} . The prepared catalyst was applied into the synthesis of furfuryl alcohol (FAL) by catalytic transfer hydrogenation of biomass-derived furfural (FF) using isopropanol as hydrogen donor. Both the preparation conditions and the reaction conditions of Zr-CMC catalyst were investigated and optimized. The results showed that Zr-CMC was efficient for the reaction with the FF conversion, FAL yield and selectivity reaching to 92.5%, 91.5 %, and 99.0%, respectively, under the mild conditions (90°C). Meanwhile, the Zr-CMC catalyst could be reused at least for five times without obvious decrease in efficiency, indicating the catalyst had excellent stability. With the advantages of sustainable raw materials, high efficiency, and excellent stability, the prepared catalyst is potential for application in the field of biomass conversion.

KEYWORDS

sodium carboxymethyl cellulose, furfural, hydrogenation, catalyst, biomass

1 Introduction

As an important carbon source on Earth, biomass is abundant, renewable and can produce fuel and high-value chemicals through transformation. It is expected to replace or partially replace traditional fossil resources and reduce the dependence on fossil resources for human. The high-value utilization of biomass resources can improve the economy and utilization efficiency of carbon resources in biomass refining process, and the production of high-value chemicals from biomass or its derivatives is an effective way to improve the utilization efficiency of biomass resources (Li et al., 2016a). Among the various platform compounds from biomass, furfural is a valuable chemical derived from pentosan by hydrolyzing dehydration and cyclization reaction. Furfural can be used to produce

valuable chemicals such as furfuryl alcohol (FA), cyclopentanone (CLA), 2-methylfuran (2-MF) etcetera through hydrogenation (Wang et al., 2018a; Pirmoradi et al., 2020; Byun and Lee, 2021). Furfuryl alcohol is an important organic chemical raw material, mainly used in the production of furfural resin, furfuryl alcohol-urinal resin, phenolic resin and so on. It is also used to prepare fruit acid, plasticizer, solvent and rocket fuel. In addition, in the fields of dye, synthetic fiber, rubber, pesticides and casting and other industrial sectors, furfuryl alcohol is also widely used (Wang et al., 2018b; Campisi et al., 2020; Lee et al., 2020; Qiu et al., 2020).

For the hydrogenation of furfural to furfuryl alcohol, homogeneous catalysts are usually used, but the homogeneous catalysts are not easy to be recovered in the reaction system (Pasini et al., 2014; Panagiotopoulou et al., 2015). Meanwhile, the hydrogenation of furfural to furfural is mainly dependent on copper chromate and expensive precious metal catalyst (Li et al., 2022). Therefore, finding cheap and efficient heterogeneous catalyst is the key for the hydrogenation of furfural to furfuryl alcohol. With the development of heterogeneous catalytic technology, a variety of mono-metal based catalysts such as Zr, Cu, Ru, Ir, Co, Fe, Pd, Pt, etc. (Pang et al., 2014; Gong et al., 2019; Li et al., 2020; Qiu et al., 2020; Sohrabi et al., 2021; Valdebenito et al., 2021) and polymetallic catalysts such as Pt/Ge (Merlo et al., 2011), Cu/Fe (Yan and Chen, 2014), Cu/Mg/Al, etc. (Chen et al., 2018) have been developed, and the catalytic hydrogenation of furfural to alcohols or esters using hydrogen as hydrogen source was also reported (Mariscal et al., 2016). Although the hydrogenation efficiency of carbonyl compounds is improved by using the precious metals and gaseous hydrogen, the high cost of precious metals and the potential safety issue of gaseous hydrogen hinder the large-scale application of many catalysts.

Meerwein-Ponndorf-Verley (MPV) reduction is a common reaction for the catalytic hydrogenation of biomass derived aldehydes or carbonyls with secondary alcohols as hydrogen donors (Luo et al., 2014). Using alcohols as hydrogen source can not only avoid safety risks caused by high-pressure hydrogen, but also improve the economy of the hydrogenation of carbonyl compounds with relatively mild reaction conditions. The secondary alcohols play the role of both hydrogen donor and the reaction solvent for the catalytic hydrogenation of carbonyl compounds to produce high-value chemicals (Wright and Palkovits, 2012). The preparation of furfuryl alcohol by MPV reduction of furfural catalyzed by different heterogeneous metal catalysts (Han et al., 2015; Li et al., 2022) has been reported. Metal ion-organic ligand hybrid MPV catalysts are commonly used for the MPV reduction of furfural. The Zr-based catalysts such as UiO-66 (Qiu et al., 2020), Zr-DM (Hao et al., 2021), Zr-HAs (Sha et al., 2017), Zr-RSL (Hao et al., 2019) and Zr/Fe (Gu et al., 2020) showed good catalytic activity in the catalytic hydrogenation reaction using alcohols as hydrogen donors. The selection of ligands is important for the construction of metal ion-organic ligand hybrid MPV catalysts. Besides the pure

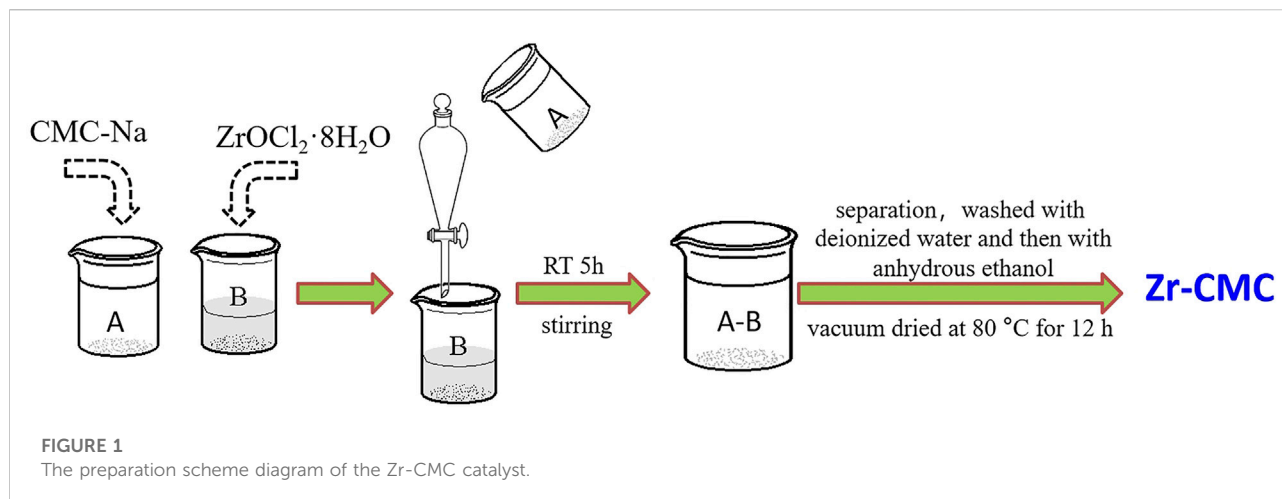
organic carboxylic acids, the natural macromolecules rich in organic carboxylic groups are also used in the construction of the MPV catalysts. In our previous work, the lignite derived humic acids and even lignite were used to construct Zr-containing MPV catalysts, and the prepared catalysts were proved to be highly efficient for the MPV reduction of various carbonyl compounds (Sha et al., 2017; Hao et al., 2019; Hao et al., 2021). Natural compounds rich in acidic carboxyl functional groups are natural functional molecules widely existing in nature (Luo et al., 2015). With the advantages of wide sources, low cost, renewable, etc., natural compounds are widely used in biological materials, catalytic materials, and other fields (Sahiner et al., 2015). Sodium carboxymethyl cellulose (CMC-Na) is a common anionic polymer compound derived from natural cellulose with abundant carboxylate groups in its structure. CMC-Na can be used as a ligand or carrier to construct a variety of metal catalysts. For example, carboxymethyl cellulose palladium (II) (CMC-PdII) catalyst was prepared by ion exchange between PdCl₂ aqueous solution and CMC-Na aqueous solution to catalyze the Suzuki-Miyaura and Mizoroki-heck coupling reaction (Xiao et al., 2015). The Fe₃O₄/CMC composite material was prepared by coprecipitating method with iron salt and CMC-Na. The Ni(0)-CMC-Na catalyst was obtained using the CMC-Na aqueous solution and the precursor NiCl₂·6H₂O, and the catalyst showed high efficiency for the hydrogenation of a variety of functionalized olefins at room temperature and moderate hydrogen pressures (Harrad et al., 2011). Based on the reported results, it is reasonable to speculate that CMC-Na could be applied into the construction of metal ion-organic ligand MPV catalyst for the conversion of furfural. However, to the best of our knowledge, there has been no report on the above idea.

In this work, a novel Zr-CMC catalyst was constructed using CMC-Na and Zr precursor as raw material *via* the interaction between the carboxylate groups in CMC-Na and transition metal Zr⁴⁺. The prepared catalyst was used for the catalytic transfer hydrogenation of furfural to furfuryl alcohol using isopropanol as hydrogen donor. The effects of the preparation conditions and the reaction conditions on the performance of the catalyst were studied. The structure and the reusability of the catalyst were investigated. This work can provide potential route for the exploration of efficient, cheap and green catalysts for biomass conversion and the efficient utilization of CMC biomass resources.

2 Experimental

2.1 Materials

Furfural (FF, 99%) (Furfural used in this work was freshly purchased and stored in the refrigerator (4°C). Before use, furfural was analyzed by GC to check its purity), furfuryl alcohol (FA, 98%) and ZrOCl₂·8H₂O (AR) were provided by



J&K Scientific Ltd. Isopropanol (AR), ethanol (AR), decane (AR) and other chemicals were obtained from Beijing Institute of Chemical Reagent. The sodium carboxymethyl cellulose was purchased from Tianjin Guangfu Fine Chemical Research Institute.

2.2 Catalyst preparation

Zr-based catalyst was prepared using sodium carboxymethyl cellulose (CMC-Na) and $\text{ZrOCl}_2 \cdot 8\text{H}_2\text{O}$ as the raw materials. In order to determine the appropriate ratio of sodium carboxymethyl cellulose and zirconium oxychloride octahydrate, a series of catalysts with different ratios were prepared, and their catalytic activity for hydrogenation of furfural was investigated under the same conditions, and then the appropriate ratio was selected. The mass ratios of sodium carboxymethyl cellulose and $\text{ZrOCl}_2 \cdot 8\text{H}_2\text{O}$ were 1:0.5, 1:1, 1:2, and 1:3, respectively.

Typical procedures were as follows (Figure 1): a certain amount of sodium carboxymethyl cellulose dissolved in 150 ml deionized water (solution A), heated and stirred in 60°C water bath to make it fully dissolved into transparent gel. At the same time, a certain amount of $\text{ZrOCl}_2 \cdot 8\text{H}_2\text{O}$ was proportionally weighed and dissolved in 50 ml deionized water (solution B). Pour the solution A into the separating funnel and slowly add it to the solution B, and stir the reaction system at room temperature for 5 h after dropping. The solution was then pumped and filtered or centrifuged ($\text{pH} = 2\text{--}3$), and washed with deionized water for at least seven times until pH neutralization. Rinse twice with anhydrous ethanol to remove the deionized water. Finally, the obtained solids were vacuum dried at 80°C for 12 h. The dried solids were ground thoroughly into powder form for subsequent use, denoted as Zr-CMC.

2.3 Catalyst characterization

Scanning electron microscopy (SEM) measurements were performed on a HITACHI SU8220 scanning electron microscope operated at 20 kV. Transmission electron microscopy (TEM) images were obtained using a TEM JEOL-1011 with an accelerating voltage of 120 kV. X-ray diffraction (XRD) was carried out via an XD8 Advance-Bruker AXS X-ray diffractometer using Cu-K α radiation ($\lambda = 0.1543 \text{ nm}$) and Ni filter scanning at two per minute ranging from 5° to 90°. The tube voltage was 40 kV, and the current was 40 mA. Fourier transform-infrared spectra (FT-IR) were obtained using a PerkinElmer spectrometer. The thermogravimetric (TG) analysis of the catalyst was performed using a thermogravimetric analysis system (Diamond TG/DTA6300, PerkinElmer Instruments) under N_2 atmosphere at the heating rate of 10°C min⁻¹. The specific surface area was calculated by the BET method, and mesopore volume was derived from the adsorption isotherm according to the Barrett-Joyner-Halenda (BJH) model. All calculations were based on the adsorption isothermals.

2.4 Reaction

2.4.1 Catalytic transfer hydrogenation of furfural over Zr-CMC

All the hydrogenation of furfural to furfuryl alcohol in this experiment was carried out in a stainless steel reactor. In the lining of the reaction kettle (15 ml), accurate weighing of reactant furfural (1 mmol) and isopropanol (5 ml) as hydrogen source and reaction solvent, as well as a certain amount of catalyst and decane as internal standard, using atmospheric pressure operation, the reaction kettle is sealed and placed in an oil bath with constant temperature heating magnetic stirring.

TABLE 1 Performances of Zr-CMC catalysts prepared under different mass ratios of CMC-Na to $\text{ZrOCl}_2 \cdot 8\text{H}_2\text{O}$.

Entry	Mass ratio of CMC-Na: $\text{ZrOCl}_2 \cdot 8\text{H}_2\text{O}$	Yield (%)	Conv. (%)	Sel. (%)
1	1:0.5	16.7	20.8	80.6
2	1:1	37.5	44.0	85.1
3	1:2	78.7	79.5	99.0
4	1:3	40.8	48.6	83.9

Reaction conditions: Furfural 1 mmol, isopropanol 5 ml, catalyst dosage 200 mg, reaction temperature 80°C, and reaction time 3 h.

After the reaction, remove the reactor quickly from the oil bath and place it in the mixture of ice water for rapid cooling. After cooling, the reaction solution is separated from the solid catalyst by centrifugation. The residue of reaction product and substrate can be quantitatively analyzed by gas chromatograph (TECHCOMP GC7900). The specific conditions of gas chromatography were as follows: hydrogen flame ion detector (FID), nitrogen as carrier gas, inlet temperature of 40°C, detection temperature of 230°C, set the heating program for furfural column temperature program, using area internal standard method for quantitative analysis of the reactant furfural and target product furfuryl alcohol, using decane as internal standard.

2.4.2 Catalyst heterogeneity and recycles

In order to check the heterogeneity of the catalysts, the solid catalysts were removed from the reaction mixture after reaction for certain time, and the supernatant was allowed to react to see if the product yield could further increase with the absence of the solid catalysts. In the reusability experiments, the catalyst was separated by centrifugation, washed with fresh isopropanol for three times, and then reused for the next run without further treatments.

3 Results and discussion

3.1 Studies of the preparation conditions of Zr-CMC catalyst

Table 1 showed the comparison of the activity of the catalysts prepared in different proportions. The results showed that with the increase of $\text{ZrOCl}_2 \cdot 8\text{H}_2\text{O}$ content, the conversion of furfural, the yield of furfuryl alcohol and the selectivity of the reaction increased gradually. When the mass ratio of CMC-Na to $\text{ZrOCl}_2 \cdot 8\text{H}_2\text{O}$ was 1:2, the activity of the prepared catalyst reached the highest, possibly because the carboxylic acid groups in CMC-Na and Zr^{4+} were completely combined at this ratio. With the further increase of the mass of $\text{ZrOCl}_2 \cdot 8\text{H}_2\text{O}$, the catalytic performance decreases, indicating that there is no excess carboxylic acid group in CMC-Na for the coordination of Zr^{4+} . It may be due to that when the mass ratio of

CMC-Na to $\text{ZrOCl}_2 \cdot 8\text{H}_2\text{O}$ is 1:3, the acidity of the solution increased, which may affect the coordination reaction between zirconium precursor and carboxylic acid in CMC-Na, leading to the low content of Zr in the catalyst. Besides, the precipitation amount obtained under this condition decreases. Therefore, from viewpoint of catalyst activity and the utilization efficiency of Zr precursor and CMC-Na, the best mass ratio of CMC-Na and $\text{ZrOCl}_2 \cdot 8\text{H}_2\text{O}$ in the preparation process is 1:2.

3.2 Structure characterization of the Zr-CMC catalyst

In order to better understand the structure and morphology characteristics of the prepared Zr-CMC catalyst, SEM, TEM, XRD, FTIR, TG, and BET were used to characterize it. Meanwhile, CMC-Na was also characterized by XRD, FTIR, and TG, and compared with the prepared Zr-CMC catalyst in structure. Firstly, the Zr content in the optimal catalyst was analyzed by ICP-OES, and the result showed that the Zr content in Zr-CMC (1:2) catalyst was around 20.5 wt%. As given in Figure 2, SEM and TEM showed that the Zr-CMC catalyst was composed of particles with no uniform shapes (Figures 2A,B). N_2 adsorption/desorption test showed that the Zr-CMC catalyst prepared was nonporous (Figure 2C), and the BET surface area was around 3 m^2/g . The low specific surface area may be caused by the dense structures formed by CMC-Na with Zr precursor and how to improve the surface area is under studying in our group. A strong X-ray diffraction peak was observed for the pure CMC-Na at about 21°, while a weak bulge peak was observed for the Zr-CMC catalyst at 20–30°, indicating that the prepared catalyst had no specific X-ray diffraction peak and had an amorphous structure (Figure 2D). The FTIR spectra of CMC-Na and the Zr-CMC catalyst were compared in Figure 2E. The FTIR spectra of CMC-Na showed that there were asymmetric and symmetric stretching vibration absorption peaks of the carboxyl functional groups at 1,591 and 1,456 cm^{-1} , respectively. In the FTIR spectra of Zr-CMC catalyst, the asymmetric and symmetric stretching vibration absorption peaks of the carboxyl functional groups were at 1,579 and 1,420 cm^{-1} , respectively. Compared with CMC-Na, the difference between the asymmetric and symmetric stretching

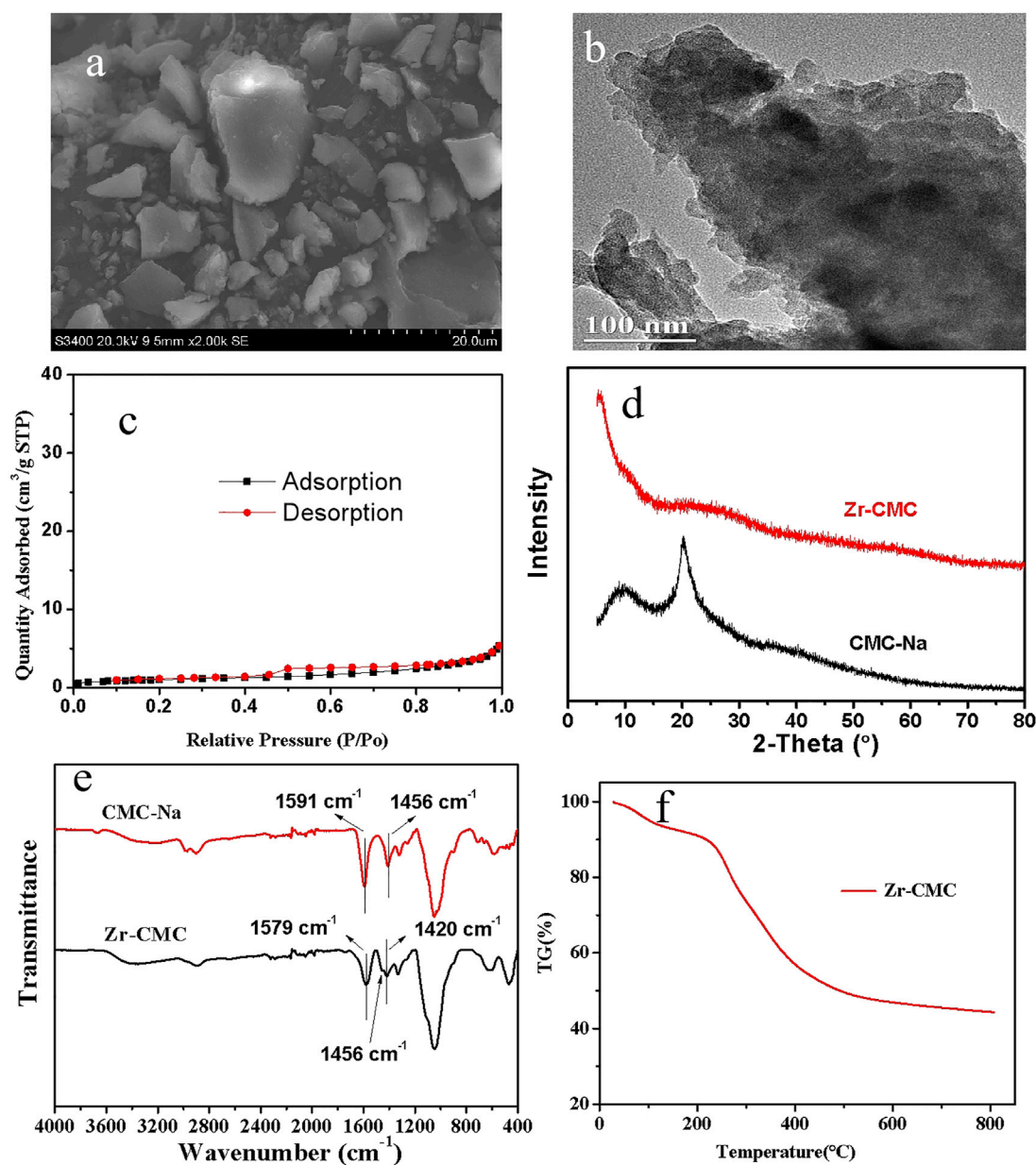


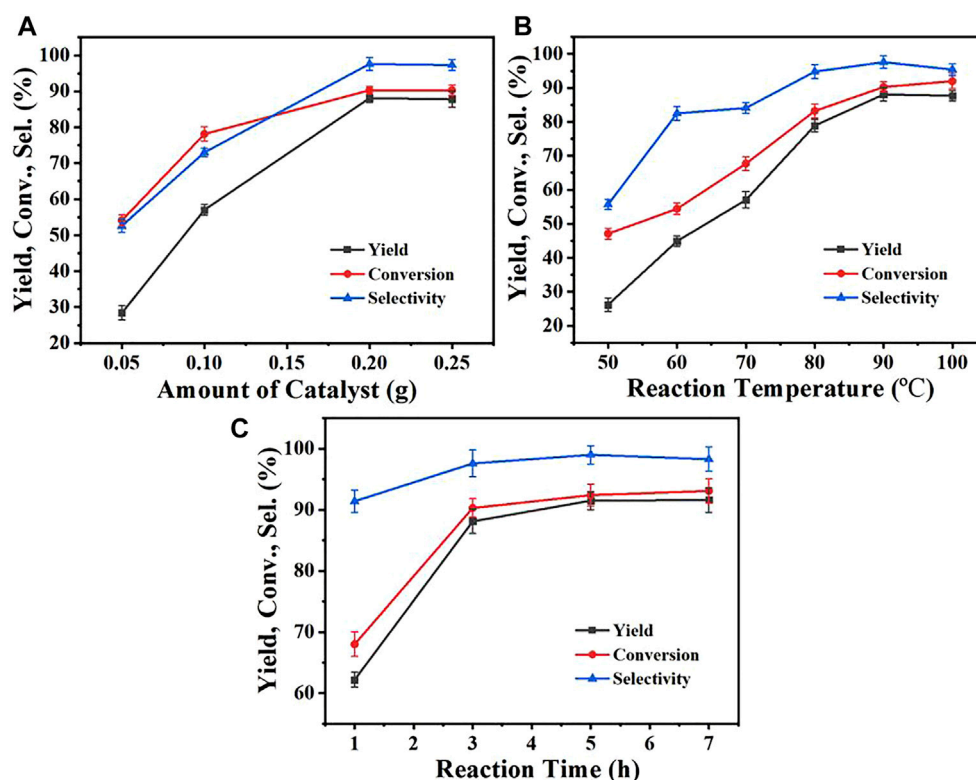
FIGURE 2

Characterization of the as-prepared Zr-CMC catalyst by SEM (A), TEM (B), N₂ adsorption-desorption (C), XRD pattern (D), FTIR spectra (E) and TG analysis (F).

vibration absorption peaks of the carboxyl functional groups in Zr-CMC catalyst changes from 135 cm⁻¹ to 159 cm⁻¹, and a new vibration absorption peak appears at 1,456 cm⁻¹. The above results indicate that zirconium is successfully combined with carboxyl functional groups (Song et al., 2015a). As shown in the figure (Figure 2F) for TG analysis, the prepared Zr-CMC catalyst begins to decompose at 300°C, while the reaction temperature is below 100°C. Therefore, the Zr-CMC catalyst is stable under the reaction temperature (Peng et al., 2012).

3.3 Studies of the reaction conditions

The important parameters influencing the performances of the catalysts were investigated, including the catalyst dosage, reaction temperature, and reaction time. Figure 2 showed the performances of the Zr-CMC catalyst under different conditions. As could be seen from Figure 3A, the conversion of furfural and the yield of furfuryl alcohol increased continually with the increasing of the catalyst dosage from 0.05 to 0.2 g. Under the

**FIGURE 3**

The influences of reaction parameters on the catalysts (A) Effect of the Zr-CMC catalyst dosage. (B) Effect of the reaction temperature. (C) Effect of the reaction time. Reaction conditions: Furfural (1 mmol), isopropanol (5 ml). (A) 90°C, 3 h (B) Catalyst 0.2 g, 3 h (C) Catalyst 0.2 g, 90°C.

catalyst dosage of 0.2 g, the conversion, yield and selectivity were 87.9%, 96.3 %, and 90.9%, respectively. However, the furfural conversion, furfuryl alcohol yield and reaction selectivity did not increase further when the amount of catalyst was increased to 0.25 g, which may be because the excessive amount of catalyst affected the mass transfer of catalyst in the reaction system. The above results indicate that 0.2 g dosage may be the appropriate catalyst dosage under the current reaction conditions, which can be used for further experimental studies. The effect of reaction temperature was shown in Figure 3B, and it was obvious that the reaction temperature had a significant influence on the performance of the Zr-CMC catalyst. Before 90°C, the furfural conversion and furfural alcohol yield increased significantly with the increase of temperature, reaching 90.9 % and 87.9%, respectively, under 90°C. However, as the temperature continued to rise, although the conversion continued to increase at a slower rate, the yield and selectivity declined slightly, presumably due to the formation of some by-products, which could be proved by the deep color of the reaction system under 100°C. Therefore, subsequent investigations were conducted at 90°C as the suitable temperature under the present reaction conditions. Under the above reaction conditions, the time-profile of the reaction was studied, as shown in Figure 3C. The conversion

of furfural and the yield of furfuryl alcohol increased significantly when the reaction time increased from 0.5 to 3 h. As the reaction time was extended to 6 h, the conversion and selectivity of the reactant increased slightly, which may be due to that the extension of the reaction time led to the formation of the condensation by-products of alcohol and aldehyde. This could be proved by the presence of some weak and unknown peaks during GC detect.

After studying the reaction condition, the performance of the prepared Zr-CMC catalyst was compared with other common Zr-based catalysts in the literatures (Table 2). The results showed that the activity of the prepared catalyst was comparable with many other catalysts under similar reaction conditions. The performance of the Zr-CMC catalyst was even superior to some catalyst in aspects of selectivity and TOF. Besides the high activity, the Zr-CMC catalyst possessed the advantages of biomass-derived and renewable raw ligands during preparation, making the Zr-CMC catalyst promising for potential application.

3.4 Reusability of Zr-CMC catalysts

Reusability and heterogeneity were important for the solid heterogeneous catalyst. The reusability of Zr-CMC catalyst showed

TABLE 2 Comparison of the prepared Zr-CMC catalyst with other Zr-based catalysts in literatures for the conversion of furfural into furfuryl alcohol using isopropanol as hydrogen donor^a.

Entry	Catalysts	Reaction conditions	C/%	Y/%	S/%	TOF/h ⁻¹	Refs.
1	Zr-CMC	90°C, 3 h	92.5	91.5	99.0	0.7	This work
2	Zr-TMSA	70°C, 5 h	93.6	89.5	95.6	0.4	Zhou et al. (2017)
3 ^b	ZrPN	100°C, 15 h	93.0	90.0	96.8	0.4	Li et al. (2016b)
4	Zr-HAs	50°C, 15 h	97.4	96.9	99.0	0.1	Sha et al. (2017)
5 ^c	Zr-PhyA	100°C, 2 h	99.3	99.3	100.0	0.8	Song et al. (2015b)
6	Zr-RSL (1:1)	90°C, 6 h	93.4	80.9	86.7	1.0	Hao et al. (2019)
7	Zr-SBA-15	90°C, 6 h	50.0	40.0	80.0	0.8	Iglesias et al. (2015)
8 ^d	Pd/Zr-BTC	20°C, 4 h (5bar)	98.4	98.4	100.0	—	Lestari et al. (2022)
9	Zr-HPAA	150°C, 1.5 h	98.0	96.0	97.9	—	Liu et al. (2019)

^aC, conversion of furfural; Y, yield of furfuryl alcohol; S, selectivity of FAL. The values of turnover frequency (TOF) were calculated by the mole of the product furfuryl alcohol/(mole of the active metals * reaction time).

^bZr-PN, organotriphosphate-zirconium hybrid.

^cZr-PhyA, Zr-phytic acid hybrid.

^dThe reaction uses H₂O as hydrogen source.

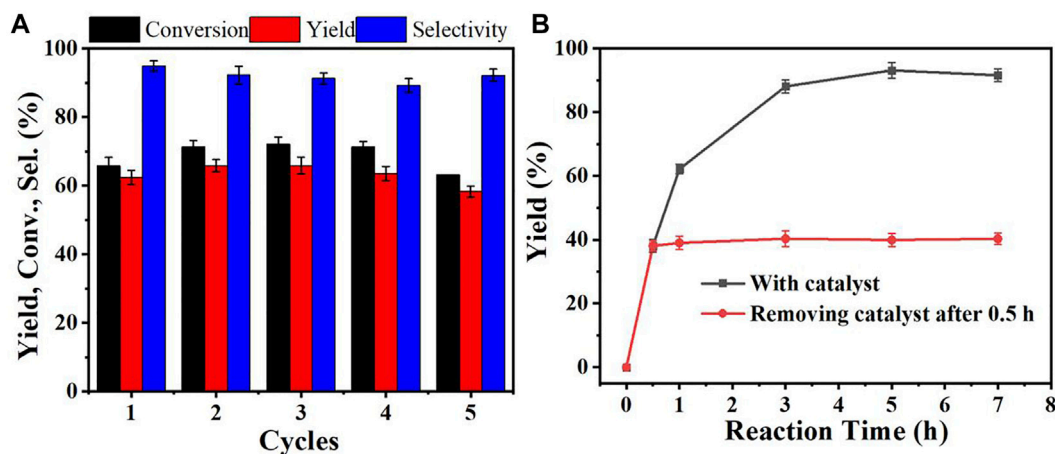


FIGURE 4

Reusability (A) and heterogeneity (B) of the prepared catalyst. Reaction conditions: Furfural 1 mmol, isopropanol 5 ml, Zr-CMC 0.2 g, reaction temperature 90°C, and reaction time 1 h (0.5 h for heterogeneity).

that the conversion, selectivity and product yield of the catalyst did not decrease significantly after repeated use for 5 times, indicating that the catalyst has good stability and can be reused (Figure 4A). The heterogeneity of Zr-CMC catalyst was also studied. The results showed that the reaction stopped after the catalyst was removed from the system, and no overflow of the active site of the catalyst was detected in the reaction solution, indicating that the catalyst was heterogeneous in the catalytic process (Figure 4B).

4 Conclusion

In summary, a route of using the sodium carboxymethyl cellulose (CMC-Na) from cellulose derivatives to construct Zr-

CMC catalyst was identified. The results of SEM and TEM showed that the catalyst was irregularly granular. TG results showed that the Zr-CMC catalyst has good thermal stability at the reaction temperature. FT-IR showed that Zr⁴⁺ was successfully coordinated with carboxyl group in CMC-Na. The XRD results showed that the prepared catalyst was amorphous. The reaction results showed that when the mass ratio of CMC-Na to ZrOCl₂·8H₂O was 1: 2, the reaction activity of the obtained catalyst was the highest. Under the condition of furfural 1 mmol, reaction temperature 90°C, catalyst 0.2 g, reaction time 5 h, the conversion of furfural, the selectivity and yield of furfuryl alcohol could be reached to 92.5%, 91.5 %, and 99.0%, respectively. The heterogeneity experiment showed that the catalyst was heterogeneous during the reaction, and the activity did not change significantly when the catalyst was recycled 5 times. On

the whole, the catalyst could be reused and had good stability. The proposed route in this work may find its potential applications in the field of biomass utilization with the advantages of high efficiency of the catalysts, broad applicability, and simple preparing processes.

Data availability statement

The original contributions presented in the study are included in the article/supplementary material, further inquiries can be directed to the corresponding author.

Author contributions

The laboratory work, analysis of data and writing was carried out predominantly by JH. HZ and NL helped in the design and review of data and interpretation. YZ and TZ did supplementary experiment. QL, KZ, and RH provided experimental design ideas. All authors contributed to the final writing of the paper.

Funding

This study was supported by the National Nature Science Foundation of China (21968021, 21868020, 21868021), Grassland

Talents Engineering of Inner Mongolia, CAS “Light of West China” Program, Local Science and Technology Development Fund Projects Guided by the Central Government (2020ZY0010), the Inner Mongolia Nature Science Foundation (2019MS02025), the Inner Mongolia Major Science and Technology Project (2021ZD0020), the Science and Research Projects of Inner Mongolia University of Technology (IMUT) (ZY202004 and BS2021018), and the Startup Fund for New Teachers of Inner Mongolia University of Technology (IMUT).

Conflict of interest

The authors declare that the research was conducted in the absence of any commercial or financial relationships that could be construed as a potential conflict of interest.

Publisher's note

All claims expressed in this article are solely those of the authors and do not necessarily represent those of their affiliated organizations, or those of the publisher, the editors and the reviewers. Any product that may be evaluated in this article, or claim that may be made by its manufacturer, is not guaranteed or endorsed by the publisher.

References

- Byun, M. Y., and Lee, M. S. (2021). Pt supported on hierarchical porous carbon for furfural hydrogenation. *J. Ind. Eng. Chem.* 104, 406–415. doi:10.1016/j.jiec.2021.08.038
- Campisi, S., Chan-Thaw, C. E., Chinchilla, L. E., Chutia, A., Botton, G. A., Mohammed, K. M. H., et al. (2020). Dual-site-mediated hydrogenation catalysis on Pd/NiO: Selective biomass transformation and maintenance of catalytic activity at low Pd loading. *ACS Catal.* 10, 5483–5492. doi:10.1021/acscatal.0c00414
- Chen, H., Ruan, H. H., Lu, X. L., Fu, J., Langrish, T., Lu, X. Y., et al. (2018). Efficient catalytic transfer hydrogenation of furfural to furfuryl alcohol in near-critical isopropanol over Cu/MgO-Al₂O₃ catalyst. *Mol. Catal.* 445, 94–101. doi:10.1016/j.mcat.2017.11.011
- Gong, W., Lin, Y., Chen, C., Al-Mamun, M., Lu, H. S., Wang, G., et al. (2019). Nitrogen-doped carbon nanotube confined Co–nx sites for selective hydrogenation of biomass-derived compounds. *Adv. Mat.* 31, 1808341. doi:10.1002/adma.201808341
- Gu, J., Zhang, J., Wang, Y., Li, D., Huang, H., Yuan, H., et al. (2020). Efficient transfer hydrogenation of biomass derived furfural and levulinic acid via magnetic zirconium nanoparticles: Experimental and kinetic study. *Ind. Crops Prod.* 145, 112133. doi:10.1016/j.indcrop.2020.112133
- Han, H. F., Zhang, S. F., Guo, Z. Q., Tong, H. B., and Wei, X. H. (2015). Three asymmetric guanidinato metal complexes: Synthesis, crystal structures and their use as pre-catalysts in the Meerwein–Ponndorf–Verley reduction. *Polyhedron* 99, 71–76. doi:10.1016/j.poly.2015.06.026
- Hao, J. X., Han, L. M., Liu, Q. S., Li, N., He, R., Zhi, K., et al. (2021). A general route of using lignite depolymerized derivatives for catalyst construction: Insights into the effects of the derivative structures and solvents. *ACS Omega* 6, 14926–14937. doi:10.1021/acsomega.1c00766
- Hao, J. X., Zhou, H. C., Liu, Q. S., Yu, X., Ma, X., et al. (2019). Facile use of lignite as robust organic ligands to construct Zr-based catalysts for the conversion of biomass derived carbonyl platforms into alcohols. *Fuel* 239, 1304–1314. doi:10.1016/j.fuel.2018.11.129
- Harrad, M. A., Valerga, P., Puerta, M. C., Houssini, I., Ali, M. A., Firdoussi, L. E., et al. (2011). Ni(0)-CMC-Na nickel colloids in sodium carboxymethyl-cellulose: Catalytic evaluation in hydrogenation reactions. *Molecules* 16, 367–372. doi:10.3390/molecules16010367
- Iglesias, J., Melero, J., Morales, G., Moreno, J., Segura, Y., Paniagua, M., et al. (2015). Zr-SBA-15 lewis acid catalyst: Activity in meerwein ponndorf verley reduction. *Catalysts* 5, 1911–1927. doi:10.3390/catal5041911
- Lee, J., Woo, J., Nguyen-Huy, C., Lee, M. S., Joo, S. H., An, K., et al. (2020). Highly dispersed Pd catalysts supported on various carbons for furfural hydrogenation. *Catal. Today* 350, 71–79. doi:10.1016/j.cattod.2019.06.032
- Lestari, W. W., Suharbiansah, R. S. R., Larasati, L., Rahmawati, F., Arrozi, U. S. F., Durini, S., et al. (2022). A zirconium(IV)-based metal-organic framework modified with ruthenium and palladium nanoparticles: Synthesis and catalytic performance for selective hydrogenation of furfural to furfuryl alcohol. *Chem. Pap.* doi:10.1007/s11696-022-02193-1
- Li, F., Jiang, S., Huang, J., Wang, Y., Lu, S., Li, C., et al. (2020). Catalytic transfer hydrogenation of furfural to furfuryl alcohol over a magnetic Fe₃O₄@C catalyst. *New J. Chem.* 44 (2), 478–486. doi:10.1039/c9nj04698d
- Li, H., He, J., Riisager, A., Saravanamurugan, S., Song, B. A., Yang, S., et al. (2016). Acid-base bifunctional zirconium N-alkyltriphosphate nanohybrid for hydrogen transfer of biomass-derived carboxides. *ACS Catal.* 6, 7722–7727. doi:10.1021/acscatal.6b02431
- Li, Y., Lv, G., Wang, Y., Deng, T., Wang, Y., Hou, X., et al. (2016). Synthesis of 2, 5-hexanedione from biomass resources using a highly efficient biphasic system. *ChemistrySelect* 1 (6), 1252–1255. doi:10.1002/slct.201600280
- Li, Z. F., Shen, Y., Zhang, Q., and Hu, T. L. (2022). Budget MOF-derived catalyst to realize full conversion from furfural to furfuryl alcohol. *Mol. Catal.* 518, 112092. doi:10.1016/j.mcat.2021.112092

- Liu, C., Xu, G. Z., Hu, A. Y., Xie, Y. D., and Wang, H. J. (2019). Porous zirconium hydroxyphosphonoacetate: Catalyst for conversion of furfural into furfuryl alcohol. *Chemistryselect* 4 (27), 8000–8006. doi:10.1002/slct.201901612
- Luo, H. Y., Consoli, D. F., Gunther, W. R., and Román-Leshkov, Y. (2014). Investigation of the reaction kinetics of isolated Lewis acid sites in Beta zeolites for the Meerwein–Ponndorf–Verley reduction of methyl levulinate to γ -valerolactone. *J. Catal.* 320, 198–207. doi:10.1016/j.jcat.2014.10.010
- Luo, J., Zhang, N., Lai, J., Liu, R., and Liu, X. (2015). Tannic acid functionalized graphene hydrogel for entrapping gold nanoparticles with high catalytic performance toward dye reduction. *J. Hazard. Mat.* 300, 615–623. doi:10.1016/j.jhazmat.2015.07.079
- Mariscal, R. M.-T. P., Ojeda, M., Sadaba, I., and Lopez Granados, M. (2016). Furfural: A renewable and versatile platform molecule for the synthesis of chemicals and fuels. *Energy Environ. Sci.* 9, 1144–1189. doi:10.1039/c5ee02666k
- Merlo, A. B., Vetere, V., Ramallo-López, J. M., Requejo, F. G., and Casella, M. L. (2011). Liquid-phase furfural hydrogenation employing silica-supported PtSn and PtGe catalysts prepared using surface organometallic chemistry on metals techniques. *Reac. Kinet. Mech. Cat.* 104 (2), 467–482. doi:10.1007/s11144-011-0374-4
- Paragiopoulou, P., Martin, N., and Vlachos, D. G. (2015). Liquid-Phase catalytic transfer hydrogenation of furfural over homogeneous lewis acid-Ru/C catalysts. *ChemSusChem* 8 (12), 2046–2054. doi:10.1002/cssc.201500212
- Pang, S. H., Love, N. E., and Medlin, J. W. (2014). Synergistic effects of alloying and thiolate modification in furfural hydrogenation over Cu-based catalysts. *J. Phys. Chem. Lett.* 5, 4110–4114. doi:10.1021/jz502153q
- Pasini, T., Lolli, A., Albonetti, S., Cavani, F., and Mella, M. (2014). Methanol as a clean and efficient H-transfer reactant for carbonyl reduction: Scope, limitations, and reaction mechanism. *J. Catal.* 317, 206–219. doi:10.1016/j.jcat.2014.06.023
- Peng, L., Zhang, J. L., Li, J. S., Han, B. X., Xue, Z. M., Yang, G. Y., et al. (2012). Surfactant-directed assembly of mesoporous metal-organic framework nanoplates in ionic liquids. *Chem. Commun.* 48, 8688. doi:10.1039/c2cc34416e
- Pirmoradi, M., Gulotty, R. J., and Kastner, J. R. (2020). Continuous hydroxyketone production from furfural using Pd-TiO₂ supported on activated carbon. *Catal. Sci. Technol.* 10, 7002–7015. doi:10.1039/d0cy01556c
- Qiu, M., Guo, T. M., Xi, R., Li, D. N., and Qi, X. H. (2020). Highly efficient catalytic transfer hydrogenation of biomass-derived furfural to furfuryl alcohol using UiO-66 without metal catalysts. *Appl. Catal. A General* 602, 117719. doi:10.1016/j.apcata.2020.117719
- Sahiner, N., Sagbas, S., and Aktas, N. (2015). Single step natural poly(tannic acid) particle preparation as multitasking biomaterial. *Mater. Sci. Eng. C* 49, 824–834. doi:10.1016/j.msec.2015.01.076
- Sha, Y. F., Xiao, Z. H., Zhou, H. C., Yang, K., Song, Y., Li, N., et al. (2017). Direct use of humic acid mixtures to construct efficient Zr-containing catalysts for Meerwein–Ponndorf–Verley reactions. *Green Chem.* 19 (20), 4829–4837. doi:10.1039/c7gc01925d
- Sohrabi, S., Abasabadi, R. K., Khodadadi, A. A., Mortazavi, Y., and Hoseinzadeh, A. (2021). In-situ one-step deposition of highly dispersed palladium nanoparticles into zirconium metal-organic framework for selective hydrogenation of furfural. *Mol. Catal.* 514, 111859. doi:10.1016/j.mcat.2021.111859
- Song, J. L., Wu, L. Q., Zhou, B. W., Zhou, H. C., Fan, H. L., Yang, Y. Y., et al. (2015). A new porous Zr-containing catalyst with a phenate group: An efficient catalyst for the catalytic transfer hydrogenation of ethyl levulinate to γ -valerolactone. *Green Chem.* 17, 1626–1632. doi:10.1039/c4gc02104e
- Song, J. L., Zhou, B. W., Zhou, H. C., Wu, L. Q., Meng, Q. L., Liu, Z. M., et al. (2015). Porous zirconiumphytic acid hybrid: A highly efficient catalyst for meerwein-ponndorf-verley reductions. *Angew. Chem. Int. Ed. Engl.* 54, 9531–9535. doi:10.1002/ange.201504001
- Valdebenito, G., Parra-Melipan, S., Lopez, V., Aranda, B., García, E., Vega, A., et al. (2021). Selective hydrogenation of furfural to furfuryl alcohol catalyzed by ruthenium complexes containing phosphorus-nitrogen ligands. *Appl. Organomet. Chem.* 35 (11), 6382. doi:10.1002/aoc.6382
- Wang, W., Villa, A., Kübel, C., Hahn, H., and Wang, D. (2018). Tailoring the 3D structure of Pd nanocatalysts supported on mesoporous carbon for furfural hydrogenation. *ChemNanoMat* 4, 1125–1132. doi:10.1002/cnma.201800308
- Wang, Y. T., Prinsen, P., Triantafyllidis, K. S., Karakoulia, S. A., Trikalitis, P. N., Yezep, A., et al. (2018). Comparative study of supported monometallic catalysts in the liquid-phase hydrogenation of furfural: Batch versus continuous flow. *ACS Sustain. Chem. Eng.* 6, 9831–9844. doi:10.1021/acssuschemeng.8b00984
- Wright, W. R., and Palkovits, R. (2012). Development of heterogeneous catalysts for the conversion of levulinic acid to gamma-valerolactone. *ChemSusChem* 5 (9), 1657–1667. doi:10.1002/cssc.201200111
- Xiao, J. L., Lu, Z. X., and Li, Y. Q. (2015). Carboxymethylcellulose-supported palladium nanoparticles generated *in situ* from palladium(II) carboxymethylcellulose as an efficient and reusable catalyst for ligand- and base-free Heck–Matsuda and Suzuki–Miyaura couplings. *Appl. Organomet. Chem.* 29 (9), 646–652. doi:10.1002/aoc.3346
- Yan, K., and Chen, A. (2014). Selective hydrogenation of furfural and levulinic acid to biofuels on the ecofriendly Cu–Fe catalyst. *Fuel* 115, 101–108. doi:10.1016/j.fuel.2013.06.042
- Zhou, H. C., Sha, Y. F., Xiao, Z. H., Li, L., Hao, J. M., Yang, K. L., et al. (2017). Using benzene carboxylic acids to prepare zirconium-based catalysts for the conversion of biomass-derived furfural. *Int. J. Coal Sci. Technol.* 5, 464–472. doi:10.1007/s40789-017-0181-2



Preparation of Pd Nanoparticles Stabilized by Modified Montmorillonite for Efficient Hydrodeoxygenation of Lignin-Derived Phenolic Compounds in Water

Xuerong Wang^{1,2†}, Chi Li^{2†}, Xinyuan Guo^{2†}, Zhichao Wang², Ruijing Cheng², Tianwei Xu¹, YiYing Li^{3*}, Jinhui Wang^{1,4*} and Huanjun Xu^{1,2*}

OPEN ACCESS

Edited by:

Jinliang Song,
Guangdong University of Technology,
China

Reviewed by:

Jianxiu Hao,
Inner Mongolia University of
Technology, China
Xin Huang,
China University of Geosciences,
China

*Correspondence:

YiYing Li
Liyiyiing_hy@163.com
Jinhui Wang
15999290001@163.com
Huanjun Xu
15798946232@163.com

[†]These authors have contributed
equally to this work and share first
authorship

Specialty section:

This article was submitted to
Green and Sustainable Chemistry,
a section of the journal
Frontiers in Chemistry

Received: 05 June 2022

Accepted: 13 June 2022

Published: 05 August 2022

Citation:

Wang X, Li C, Guo X, Wang Z,
Cheng R, Xu T, Li Y, Wang J and Xu H
(2022) Preparation of Pd Nanoparticles
Stabilized by Modified Montmorillonite
for Efficient Hydrodeoxygenation of
Lignin-Derived Phenolic Compounds
in Water.
Front. Chem. 10:961814.
doi: 10.3389/fchem.2022.961814

¹Key Laboratory of Child Cognition and Behavior Development of Hainan Province, Qiongtai Normal University, Haikou, China, ²School of Science, Qiongtai Normal University, Haikou, China, ³College of Basic Medicine and Life Sciences, Hainan Medical University, Haikou, China, ⁴Department of Medicinal Chemistry and Natural Medicine Chemistry, College of Pharmacy, Harbin Medical University, Harbin, China

Developing a new and efficient catalytic route for the production of alkanes by upgrading the aqueous phenolic biofuels still remains a challenge. Here, we designed and synthesized a bifunctional catalyst that uses natural montmorillonite (MMT) as support and combines metal active sites and Brönsted acid sites in the MMT via ion exchange and reduction roasting process. The catalytic activity of the as-synthesized Pd-MMT (H⁺) was evaluated by the hydrodeoxygenation (HDO) of a series of lignin-derived phenolic compounds in water. Our model reaction study reveals that the HDO of phenol undergoes an initial hydrogenation of aromatic rings to produce cyclohexanol and cyclohexanone, followed by the dehydration of cyclohexanol to provide intermediate cyclohexene and a final hydrogenation of cyclohexene to create a cyclohexane product. The combination of high metal catalytic activity and Brönsted acidity in Pd-MMT (H⁺) synergistically accelerated the HDO of phenol. Furthermore, good catalytic activity and recycling ability were also observed for other lignin-derived phenolic compounds.

Keywords: lignin model compound, modified montmorillonite, hydrodeoxygenation, cycloalkanes, biofuels

INTRODUCTION

The depletion of petroleum deposits and the increasing environmental concern regarding the burning of nonrenewable resources have diverted great attention toward recyclable resources. Biomass, therefore, is the best feedstock for the renewable production of biofuels, which could be a promising alternative to fossil fuels (Antar et al., 2021; Lee et al., 2021). Lignin is the second most abundant component of biomass, which is typically formed by methoxy-substituted phenylpropanoid units. After being processed by some technologies, it can be transformed into biofuels and special chemicals (Chio et al., 2019). The biofuels (most of those are phenols) decomposed from lignin are highly oxygenated, which, together with the unsaturated content of biofuels, leads to low oil quality problems, such as instability (Zakzeski et al., 2010; Saidi et al., 2014; Li et al., 2011; Ruiz et al., 2012; Jongerius et al., 2012; Ambursa et al., 2021).

Hydrodeoxygenation (HDO) is the most effective way to remove oxygen and some unsaturated content (Ambursa et al., 2021). Traditional catalysts for the HDO of biofuels are CoMo or NiMo sulfide, which have been widely used for industrial removal of sulfur, nitrogen, and oxygen from petroleum fuels (Zakzeski et al., 2010; Saidi et al., 2014; Li et al., 2011; Ruiz et al., 2012; Mortensena et al., 2011; Elliott, 2007; Liang et al., 2022). The disadvantage of the traditional catalysts includes sulfide contamination, coke formation, and deactivation caused by water. To overcome these shortcomings, researchers turned their attention to noble metals. The catalysts doped with noble metals showed better HDO activity and yield than traditional ones (Zhu et al., 2011; Lup et al., 2017; Lee et al., 2012). Meantime, various materials have been tested as support, such as ZrO₂ (Lup et al., 2017), Al₂O₃-SiO₂ (Lee et al., 2012), and Al₂O₃ (Bakhtyari et al., 2020). Recently, Zhao et al. (2009) reported an efficient difunctional catalytic system that combines carbon-supported noble metal catalysts and Brønsted acid (H₃PO₄) toward the HDO of lignin-derived phenolic fraction in water. This system has successfully hydrodeoxygenated phenol derivatives to produce cycloalkanes under a moderate condition (Zhao et al., 2009). However, this system used liquid H₃PO₄ as a Brønsted acid that is difficult to recover from the reaction mixture, harmful to the environment, and relatively corrosive to the reactor. Accordingly, some non-sulfide catalysts such as Pt/HY zeolite (Hong et al., 2010), Pt/HBeta (Zhu et al., 2011), Pt/C (Ohta et al., 2011), Ni-Nafion/SiO₂ (Zhao et al., 2010), and metal nanocatalysts combined with Brønsted acidic ionic liquids (ILs) (Yan et al., 2010) have been recently evaluated for the HDO of phenols.

It is well known that clays are widespread, easily available, low-cost, and environment-friendly chemical substances with a layered structure (Nagendrappa, 2011). For example, MMT is one of the most common smectite clays and a promising naturally abundant and non-toxic reinforcing material which can be used as one of the components for food, medicine, cosmetic, and healthcare recipients (Ali et al., 2021; Vaculíková et al., 2021). The layers of clay possess net negative charge that is neutralized by cations such as Na⁺, K⁺, and Ca²⁺, which occupy the interlamellar space of MMT. The interlamellar cations can be easily replaced by other cations or other molecules with desirable functions (Vaculíková et al., 2021; Bokade and Yadav, 2011; Tsagkalias et al., 2021). Liu and coworkers presented a Ru-ionic liquids/montmorillonite catalyst system, which was found to be highly efficient in the hydrogenation of benzene (Miao et al., 2006). The electrostatic and coordination forces between the metal and catalytic support are very strong, which results in a very stable catalyst. In some organic reactions, clays have also been modified to act as solid acid catalysts (Motokura et al., 2006; Motokura et al., 2007; Motokura et al., 2012). Kiyotomi Kaneda described a novel synthetic method in which MMT was used as a solid acid in the addition reactions of 1,3-dicarbonyl compounds to alkenes, and the recovered catalyst could be reused at least seven times without appreciable loss of activity and selectivity (Motokura et al., 2006). More importantly, the acidic sites in MMT could interact with the O atom in ether bonds (Hechelski et al., 2018).

Therefore, we are intrigued with the idea that combining proton (H⁺)-modified MMT and noble metal forms a bifunctional catalyst, Pd-MMT (H⁺). MMT endows the catalyst with natural properties, and meanwhile, noble metal nanoparticles and H⁺ loaded within the MMT afford high catalytic activity to the Pd-MMT (H⁺). We envisage that such a bifunctional catalyst will be highly efficient in the HDO of lignin-derived phenolic fraction in water.

In this work, the idea is introduced to take Na⁺-montmorillonite (Na⁺-MMT) as the representative clay, which first exchanged protons to get H⁺-MMT and then doped with noble metal ions, that is, Pd²⁺, Ru³⁺, and Pt²⁺. The metal-supported MMTs were finally calcined to get the difunctional catalysts, denoted as Pd-MMT (H⁺), Ru-MMT (H⁺), and Pt-MMT (H⁺), respectively. Among them, Pd-MMT (H⁺) showed excellent catalytic activity towards the hydrogenation of aromatic ring and subsequent dehydration reactions, leading to a high HDO product of lignin-derived phenolic compounds.

EXPERIMENT SECTION

Materials

Unless otherwise stated, all chemicals in this work were commercially available and used without further purification. The chemicals were phenol (Sinopharm, >99% GC assay); anisole (Sinopharm, >98% GC assay); 4-n-propylphenol (TCI, >99% GC assay); 4-ethylguaiaicol (Alfa Aesar, >98% GC assay); 4-hydroxy-3-methoxyphenylacetone (Alfa Aesar, >98% GC assay); guaiaicol (J&K, >98% GC assay); 4-allyl-2-methoxyphenol (Alfa Aesar, >98% GC assay); diphenyl ether (J&K, >98% GC assay); cyclohexanol (Alfa Aesar, >99% GC assay); cyclohexanone (Alfa Aesar, >99% GC assay); hydrogen (Hainan Analytical Instrument Company, >99.999%); Na⁺-montmorillonite (Zhejiang sanding Co., Ltd.); Pd (NO₃)₂·2H₂O; RuCl₃; Pt (NO₃)₂ (Aladdin); phenethoxybenzene; and penzyl phenyl ether (Innochem, >97% GC assay).

General Procedures for Aerobic Oxidation

The typical procedure was as follows: The desired amount of secondary alcohol substrate (0.5 mmol), Fe(NO₃)₃·9H₂O (0.15 mmol), NaI (0.075 mmol), and DMSO (2 ml) were added into a 25-ml reaction bottle. Then, the mixture was degassed three times with the oxygen balloon; the reaction took place under 130 °C for the desired time. After being acidified with 2 mol/L HCl (3 ml), the solution was extracted by ethyl acetate (5 ml) twice, and the organic phase was washed with saturated brine once and dried using Na₂SO₄. The combined organic phase was removed from the solvent by using a rotary evaporator. The desired product was obtained through column chromatography using ethyl acetate/petroleum ether as an eluent.

Synthesis of Catalysts

H⁺-MMT was prepared according to a previously reported ion exchange procedure^[25]. A mixture of Na⁺-MMT (3.0 g) and aqueous HCl (1 wt%, 200 ml) was stirred at 363 K for 24 h. A

slurry was obtained after centrifugation. The slurry was washed with abundant distilled water repeatedly, then with ethanol, and then it was dried at 343 K in a vacuum overnight. The residual solid was finally grinded to obtain a gray powder, which was named H^+ -MMT.

Pd -MMT (H^+) catalyst was prepared through a two-step procedure: First, 23.04 mg of palladium nitrate ($\text{Pd}(\text{NO}_3)_2 \cdot 2\text{H}_2\text{O}$) was dissolved in distilled water (15 ml), and H^+ -MMT (1 g) was then added. The mixture was stirred at room temperature for 12 h, centrifuged, washed with water thoroughly, and finally washed with ethanol. The Pd^{2+} -supported catalyst precursor was obtained after drying at 343 K in a vacuum overnight. In the second step, the catalyst precursor was reduced under H_2 atmosphere at 473 K for 3 h to obtain Pd -MMT (H^+). For comparison, Ru -MMT (H^+) Pt -MMT (H^+) and Pd -MMT (Na^+) were also prepared using a similar procedure in which RuCl_3 and $\text{Pt}(\text{NO}_3)_2$ were used as metal resources for Ru -MMT (H^+) and Pt -MMT (H^+), respectively and Na^+ -MMT was used as a support for Pd -MMT (Na^+). The metal loading content in Pd -MMT (H^+), Ru -MMT (H^+), Pt -MMT (H^+), and Pd -MMT (Na^+) was 0.45, 0.42, 0.42, and 0.43 wt%, respectively, as determined by ICP-AES.

Hydrodeoxygenation Reaction of Lignin Models

The HDO of lignin models was performed in a 15-ml stainless steel autoclave equipped with a magnetic stirrer. In a typical procedure, 2 mmol phenol, 40 mg catalyst, and 3 ml water are introduced into the reactor. The autoclave was first purged with H_2 (0.2 MPa) three times to remove the air in it and then charged with 5 MPa H_2 at room temperature. The autoclave was heated and maintained at the desired temperature (473 K or 493 K) for 1 h, and then stirred at 1,000 rpm. After a suitable reaction time, the reactor was cooled with ice water to quench the reaction. Conversion and yield were analyzed by using ethylbenzene as an internal standard. The organic phase was extracted from the mixture three times by ethyl acetate, and the combined organic phases were analyzed by an Agilent 6890 gas chromatograph equipped with an HP-INNOWax capillary column and an FID.

Characterization

Powder X-ray diffraction (XRD) patterns were recorded on a Rigaku D/max-2500 X-ray diffractometer using $\text{Cu K}\alpha$ radiation ($\lambda = 0.15406 \text{ nm}$). The tube voltage was 40 kV, and the current was 200 mA. The X-ray photoelectron spectroscopy (XPS) data were obtained by using an ESCALab 220i-XL electron spectrometer from VG Scientific using 300 W $\text{Al K}\alpha$ radiation. The base pressure was about 3×10^{-9} mbar. The binding energies were referenced to the C1s line at 284.9 eV from adventitious carbon. The specific surface area of the samples was determined by the N_2 adsorption technique (Quantachrome Autosorb-1). The samples were degassed at 473 K for 3 h, and adsorption-desorption isotherms were measured at 77 K. The structural properties were characterized by transmission electron microscopy (TEM, JEOL JEM-2100F). The temperature programmed desorption (TPD) of ammonia was analyzed by using the Micromeritics AutoChem 2590 HP chemisorption

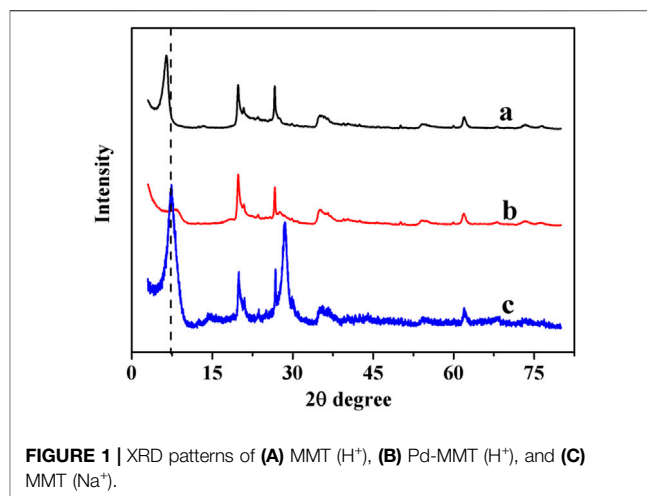


FIGURE 1 | XRD patterns of (A) MMT (H^+), (B) Pd -MMT (H^+), and (C) MMT (Na^+).

RESULTS AND DISCUSSION

Figure 1 shows the XRD patterns of MMT (H^+), Pd -MMT (H^+), and MMT (Na^+). The pattern of MMT (H^+) became weak and shifted slightly to a lower value, implying that after being treated with HCl , the space between interlayers of MMT widened; however, the lamellar structure of MMT remained. No notable diffractive peaks of Pd or PdO appeared in the pattern of Pd -MMT (H^+) compared with that of MMT (H^+). However, it was observed that the intensity of the peak at $2\theta = 9.6$ was attenuated after Pd nanoparticles were loaded on the MMT (H^+), indicating that the Pd nanoparticles were highly dispersed within the MMT (H^+) support. All peaks of MMT (H^+) were maintained after loading Pd nanoparticles, suggesting that the layered structure of MMT (H^+) support was not destroyed, as confirmed by XRD measurement. The interlayer distance of the MMT (H^+) was determined by subtracting the c dimension of the silicate sheet (9.6 \AA) from the observed (001) values in the XRD spectrum (Motokura et al., 2012). Normally, the interlayer distance was enlarged by the added Pd nanoparticles that entered the layers of MMT (H^+). However, the interlayer distance value was found to decrease in this work, as reflected by the increased 2θ value of the (001) peak (**Figure 1**). This can be ascribed to the lost water in MMT that was removed after the reduction roasting treatment, which was in accordance with Toshhide Baba's research (Motokura et al., 2012).

The chemical states of Pd before and after reduction roasting were characterized by XPS, and the results are shown in **Figure 2**. In spite of the interference of the Mg in the natural MMT, the XPS spectrum could be resolved fairly well with two spin-orbit-split doublets from two chemically different Pd entities and the Mg (KLL) peak for the Pd -MMT (H^+) before reduction roasting (**Figure 2A**). The peak binding energies of 336.5 eV ($\text{Pd } 3d_{5/2}$)

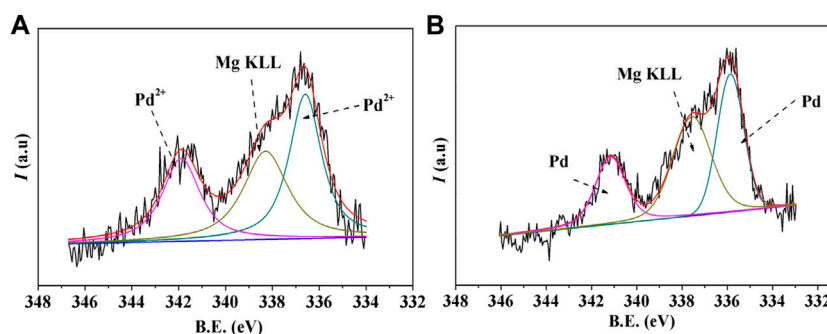


FIGURE 2 | XPS spectra of the Pd 3d spectrum of Pd-MMT (H^+) catalyst **(A)** before and **(B)** after reduction roasting.

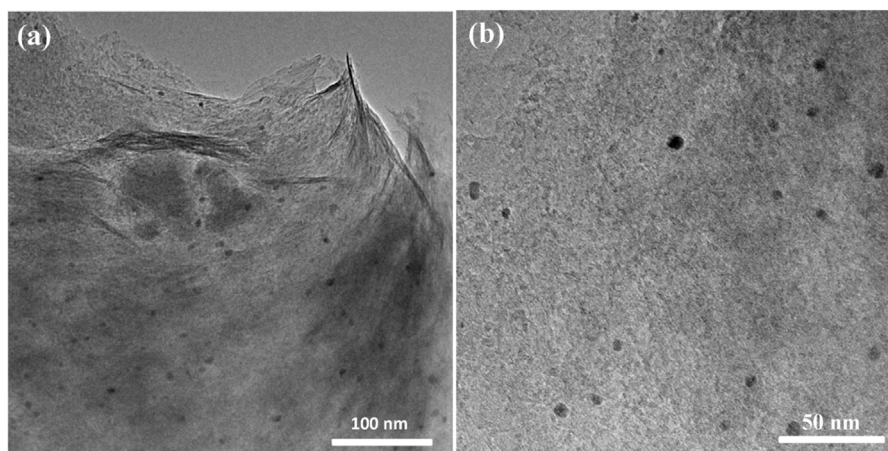


FIGURE 3 | TEM images of Pd-MMT (H^+).

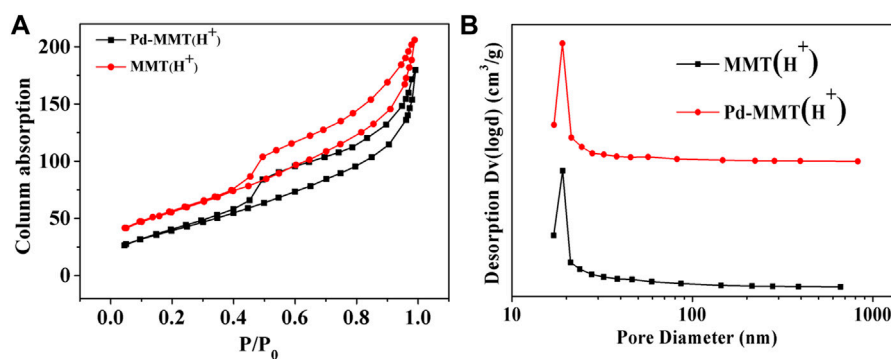


FIGURE 4 | **(A)** N_2 adsorption-desorption isotherms of MMT (H^+) and Pd-MMT (H^+); **(B)** Corresponding Barrett-Joyner-Halenda (BJH) pore size distribution curve determined from the desorption branch.

and 341.9 eV ($Pd\ 3d_{3/2}$) correspond to the Pd^{2+} ion. After the reduction roasting, the peak binding energies were changed to 335.8 eV ($Pd\ 3d_{5/2}$) and 341.1 eV ($Pd\ 3d_{3/2}$), respectively, which illustrates that the Pd^{2+} ions have been successfully transformed into Pd^0 nanoparticles.

The size and distribution of Pd nanoparticles have been observed by TEM images. It was shown that these spherical nanoparticles were uniformly dispersed within the MMT matrix with an average diameter of about 5–7 nm (**Figure 3A**). In the meantime, few Pd nanoparticles with a diameter close to 10 nm

TABLE 1 | Textural properties of MMT (Na⁺), MMT (H⁺) and Pd-MMT (H⁺).

Sample	SSA _{BET} (m ² g ⁻¹)	Pore size (nm)	V _{total} (cm ³ g ⁻¹)
MMT (Na ⁺)	6	/	0.016
MMT (H ⁺)	200	19.071	0.288
Pd-MMT (H ⁺)	148	19.021	0.260

SSA_{BET}, total BET specific surface area; V_{total}, total pore volume.

can also be observed, which was described as the presence of Pd nanoparticles on the outer surface of the MMT rather than inside the pores (Borah and Dutta, 2013).

The porosity nature of MMT (Na⁺), MMT (H⁺), and Pd-MMT (H⁺) was measured by the N₂ adsorption-desorption isotherm at 77 K. **Figure 4A** shows the typical type IV adsorption-desorption isotherm with a H₁ hysteresis loop at P/Po = 0.4–0.9, indicative of a mesoporous structure (Xu et al., 2014). The pore size distribution curves calculated by the BJH method are shown in **Figure 4B**. The Brunauer–Emmett–Teller (BET) surface area, BJH pore sizes, and pore volumes were summarized in **Table 1**. The BET surface area of MMT (H⁺) and Pd-MMT (H⁺) (as determined from the desorption branch of the curve) was 200 and 148 m² g⁻¹, respectively, indicating that the BET surface area of MMT after being treated with HCl was significantly increased (**Table 1** and **Supplementary Figure S4**). Meanwhile, after being treated with HCl, the BJH pore size distribution sharply increased to 19.071 nm, while the differential volumes versus pore diameter plot indicated relatively narrow pore size distributions.

It was notable that the BET surface area of Pd-MMT (H⁺) decreased, which might have resulted from the decrease in the distance between layers under high-temperature reduction roasting treatment. But after loading Pd nanoparticles, the isotherm shape was preserved and the BJH pore size distribution was not changed notably, indicating that the incorporated Pd nanoparticles did not block or alter the pore structure. The pore size was larger than 19 nm, which was ascribed to the dealumination of MMT during acidification (Pablo et al., 1998). The specific surface area and the pore diameter, as well as the pore size distribution of MMT, were changed after treatment with HCl. Those tuned properties of MMT make it act as an excellent “Host” for Pd⁰-nanoparticles.

The acidity of MMT (Na⁺) and MMT (H⁺) was estimated by NH₃-TPD profiles (**Supplementary Figure S5**). MMT (Na⁺) only showed the strong peak that appeared at a high temperature of 450–650°C; meanwhile, the peaks of MMT (H⁺) appeared at 100–250°C and 450–650°C, respectively. It is evident that a new type of acidic site was produced in this acidification process (Ramesh et al., 2015). After acidification, there were still some Na⁺, K⁺, and Ca²⁺ ions remaining. The exchange of Pd²⁺ with MMT (H⁺) might be in an adsorption and exchange process, and as such, we predicted that there are some protons (H⁺) remaining in the Pd-MMT (H⁺).

Catalytic Performance of Pd-MMT (H⁺)

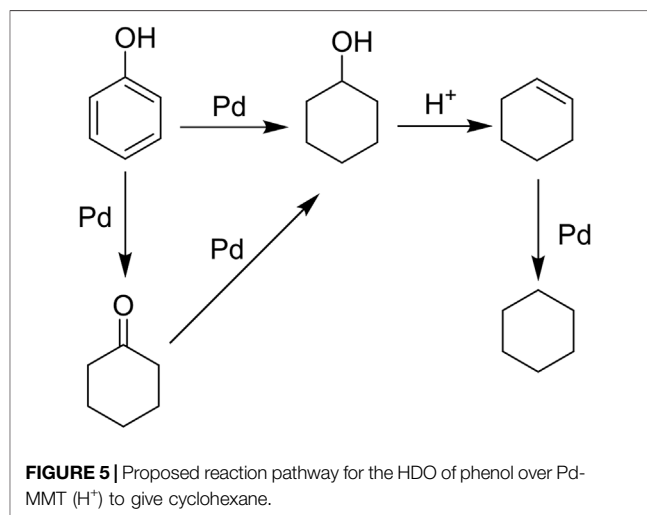
To evaluate the catalytic performance of the synthesized Pd-MMT (H⁺), the HDO of a model compound, phenol, was chosen as the probe reaction. The reactions were performed at 473 K, 5.0 MPa

TABLE 2 | HDO of phenol in aqueous media^{ab}.

Catalyst	Conversion (%)	Yield (%)
MMT (H ⁺)	0	0 (cyclohexane)
Pd-MMT (Na ⁺)	100	38 (cyclohexanol); 56 (cyclohexanone)
Pd-MMT (H ⁺)	100	99 (cyclohexane)

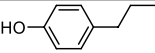
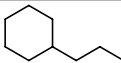
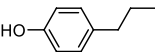
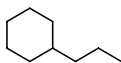
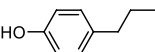
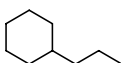
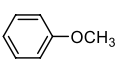
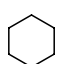
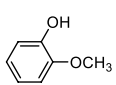
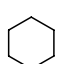
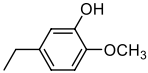
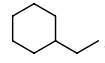
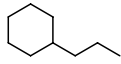
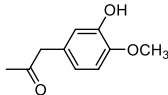
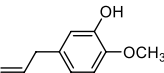
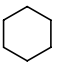
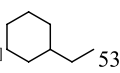
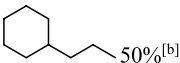
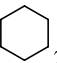
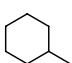
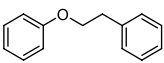
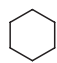
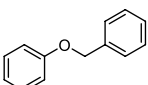
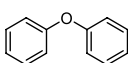
^aReaction conditions: phenol 188 mg (2 mmol), catalyst 40 mg, H₂O (3 ml), P(H₂) = 5.0 MPa, T = 473 K, t = 2 h.

^bConversion was determined by gas chromatography (GC).



H₂, and the reaction time was 2 h. The experimental results are shown in **Table 2**. No products were obtained when Pd was absent in the catalyst (**Table 2**, entry 1). The appearance of Pd nanoparticles in Pd-MMT (Na⁺) led to a complete conversion of phenol to afford 38% cyclohexanol and 56% cyclohexanone products (**Table 2**, entry 2). In contrast, a 99% product of cyclohexane was observed when Pd-MMT (H⁺) was used as catalyst (**Table 2**, entry 3). These results indicated that the HDO of phenol may undergo two reduction steps: phenol may be first hydrogenated to cyclohexanone and cyclohexanol catalyzed by Pd nanoparticles. Herein, we cannot rule out the possibility that phenol was first reduced to cyclohexanone and the intermediate cyclohexanone was further hydrogenated to cyclohexanol. In the second step, cyclohexanol was further hydrogenated to produce cyclohexane that was catalyzed by the H⁺ acidity of Pd-MMT (H⁺) (**Figure 5**). This process was in accordance with Zhao's report that phenol did not undergo direct hydrogenolysis to benzene and that only a combination of metal sites and Brønsted acid resulted in the HDO of phenolic compounds to alkanes (Zhao et al., 2010). Although carbon-supported platinum catalyst was also successful in catalyzing the HDO of phenols, the lack of hydronium ions required a high temperature of 553 K (Ohta et al., 2011). Obviously, the dehydration of cyclohexanol was accelerated by Brønsted acid sites on the Pd-MMT (H⁺) that significantly decreased the reaction temperature. The overall reaction pathway for the HDO of phenol to cyclohexane involves an initial Pd-catalyzed hydrogenation of the aromatic

TABLE 3 | HDO of several lignin-derived compound models^a.

Entry	Lignin models	Catalyst	Conversion (%)	Cycloalkanes yield (%)
1		Pd-MMT (H ⁺)	100	 99% ^[a]
2		Pt-MMT (H ⁺)	100	 99% ^[a]
3		Ru-MMT (H ⁺)	100	 97% ^[a]
4		Pd-MMT (H ⁺)	100	 77% ^[b]
5		Pd-MMT (H ⁺)	100	 49% ^[b]
6		Pd-MMT (H ⁺)	100	 73% ^[b]  56% ^[b] 
7		Pd-MMT (H ⁺)	100	 18% ^[c]  53% ^[c]
8	 50% ^[b]	Pd-MMT (H ⁺)	100	 29% ^[a]  46%
9		Pd-MMT (H ⁺)	100	 85% ^[a]
10		Pd-MMT (H ⁺)	100	cc 29% ^a 46%
11		Pd-MMT (H ⁺)	100	85% ^a

^aReaction conditions: phenols (2 mmol), catalyst (40 mg), H₂O (3.0 ml), P(H₂) = 5.0 MPa, T = 473 K; t = 2 h.^bT = 493 K, t = 8 h.^cT = 473 K, t = 4 h.

ring, a subsequent acid-catalyzed dehydration of cyclohexanol, and a final Pd-catalyzed hydrogenation of the cyclohexene to afford the cyclohexane product. A tentative mechanism for Pd-MMT (H⁺) hydrodeoxygenated lignin-derived phenolic compounds in water is as follows: The phenol was hydrogenated to cyclohexanone, and then the cyclohexanone was reduced to cyclohexanol. After that, the cyclohexanol was dehydrated to the cyclohexene, which was further reduced to cyclohexane (Figure 5).

In addition to phenol, several important lignin-derived products were also successfully converted to their corresponding cycloalkanes (Table 3). Hydrogenation of

these lignin-derived compounds leads to a variety of products. For instance, 4-propylphenol was transformed to n-propylcyclohexane in a high yield of 99% (Table 3, entry 1). Apart from Pd-MMT (H⁺), we attempted the HDO of 4-propylphenol with Pt-MMT (H⁺) and Ru-MMT (H⁺), respectively, and found that both Pt-MMT (H⁺) and Ru-MMT (H⁺) (Supplementary Figures S1, S2) can also efficiently catalyze the HDO reaction with a yield larger than 97% (Table 3, entry 2 and 3). However, anisole (Table 3, entry 4) and guaiacols (Table 3, entries 5–8) provided relatively low cycloalkane yield which varied from

50% to 73%, although a higher temperature (493 K) and a longer reaction time (8 h) were applied. This indicates that the methoxy group is unfavorable for the HDO to obtain a cycloalkane product.

Furthermore, the bifunctional catalyst could be effectively applied in representational dimeric lignin models, such as phenethoxybenzene, benzyloxybenzene, and diphenyl ether (Table 3, entries 9–11). The total yield of cycloalkanes was between 71% and 85%. Among them, phenethoxybenzene with the most abundant linkage in lignin (β -O-4, 55% in lignin) was converted to 18% cyclohexane and 53% ethylcyclohexane at 473 K and 5 MPa H_2 during 4 h reaction time. Benzyloxybenzene possessing α -O-4 linkage in lignin (8% in lignin) was also converted with a 29% yield of cyclohexane and a 46% yield of methylcyclohexane during a 2 h reaction. Diphenyl ether with 4-O-5 linkage was converted to cyclohexane with a yield of 85% at 473 K and 5 MPa H_2 . These results reveal that Pd-MMT (H^+) not only easily depolymerized the linkages of representational lignin models but also further efficiently hydrogenated those to afford cycloalkanes.

The reusability of the Pd-MMT (H^+) catalyst was investigated by the hydrogenation of 4-n-propylphenol. In each cycle, Pd-MMT (H^+) was removed by centrifugation and then rinsed with 4-n-propylphenol. After drying, the catalyst was reused for the next run. The conversion of 4-n-propylphenol is 100, 100, 100, 98, and 98%, respectively, and the yield of n-propylcyclohexane is 99, 99, 99, 95, and 94%, respectively. Moreover, no Pd species were observed in the aqueous solution and organic solution detected by ICP. It was indicated that the Pd-MMT (H^+) can be reused at least five times without significant loss of activity in the fifth run. Under the same reaction conditions, we performed the model reaction only using 1/5 dosage of Pd-MMT (H^+) as a catalyst. A conversion rate of about 76% was reached. The reusability of this reaction was detected five times and the conversion was 75, 74, 72, 74, and 71%, respectively. These results indicate that Pd-MMT (H^+) possesses good reusability for the HDO of lignin model compounds. The morphology of Pd-MMT (H^+) was also examined by TEM observation after five recycles. It was found that the size of Pd nanoparticles slightly increased (Supplementary Figure S3), which might result in the slight decline in the conversion and yield of the HDO of the lignin model compound.

CONCLUSION

In summary, we designed and prepared a bifunctional catalyst that combined Brønsted acid sites and metal active sites (Pd, Pt, and Ru) in montmorillonite (MMT) as support. The as-synthesized bifunctional Pd-MMT (H^+) was characterized by XRD, XPS, TEM, and N_2 adsorption-desorption isotherms. The catalytic performance of the Pd-MMT (H^+) was evaluated by the

hydrodeoxygenation (HDO) of lignin-derived phenolic compounds. As for the model reaction, the aromatic rings of phenol were hydrogenated to produce cyclohexanone and cyclohexanol catalyzed by Pd (0) nanoparticles, followed by the dehydration of cyclohexanol that was catalyzed by Brønsted acid in the Pd-MMT (H^+) and further Pd (0)-catalyzed hydrogenation of cyclohexene to cyclohexane. The combination of Pd (0) nanoparticles and Brønsted acid in Pd-MMT (H^+) accelerated the HDO process of phenol. This bifunctional Pd-MMT (H^+) was also successfully applied to a series of lignin-derived phenolic compounds and exhibited good catalytic and recycle ability. This new approach may provide an efficient and economical route for upgrading lignin-derived phenolic oils to transportation biofuels.

DATA AVAILABILITY STATEMENT

The original contributions presented in the study are included in the article/Supplementary Material; further inquiries can be directed to the corresponding authors.

AUTHOR CONTRIBUTIONS

XW, CL, XG, and ZW: experimental operation and data collection; JW: the conception and design of the study; TW, JW and HX: manuscript writing and revision; RC and YL: experimental data collection and analysis. All authors read and approved the submitted version.

FUNDING

This work was financially supported by the Hainan Provincial Natural Science Foundation of China (2019RC250, 220QN281, and 521NS0786), the National Science and Technology Major Project of the Ministry of Science and Technology of China (2018ZX09735005), the National Natural Science Foundation of China (22165009), the Scientific Research Foundation of the Higher Education Institutions of Hainan Province (Hnky2021ZD-22), and the National Undergraduate Training Program for Innovation and Entrepreneurship (202113811007, S202113811005, S202113811006, and 202113811022).

SUPPLEMENTARY MATERIAL

The Supplementary Material for this article can be found online at: <https://www.frontiersin.org/articles/10.3389/fchem.2022.961814/full#supplementary-material>

REFERENCES

Ali, I., Kon'kova, T., Kasianov, V., Rysev, A., Panglisch, S., Mbianda, X. Y., et al. (2021). Preparation and Characterization of Nano-Structured

Modified Montmorillonite for Dioxidine Antibacterial Drug Removal in Water. *J. Mol. Liq.* 331, 115770. doi:10.1016/j.molliq.2021.115770

Ambursa, M. M., Juan, J. C., Yahaya, Y., Taufiq-Yap, Y. H., Lin, Y.-C., and Lee, H. V. (2021). A Review on Catalytic Hydrodeoxygenation of Lignin to

- Transportation Fuels by Using Nickel-Based Catalysts. *Renew. Sustain. Energy Rev.* 138, 110667. doi:10.1016/j.rser.2020.110667
- Antar, M., Lyu, D., Nazari, M., Shah, A., Zhou, X., and Smith, D. L. (2021). Biomass for a Sustainable Bioeconomy: An Overview of World Biomass Production and Utilization. *Renew. Sustain. Energy Rev.* 139, 110691. doi:10.1016/j.rser.2020.110691
- Bakhtyari, A., Rahimpour, M. R., and Raeissi, S. (2020). Cobalt-molybdenum Catalysts for the Hydrodeoxygenation of Cyclohexanone. *Renew. Energy* 150, 443–455. doi:10.1016/j.renene.2019.12.119
- Bokade, V. V., and Yadav, G. D. (2011). Heteropolyacid Supported on Montmorillonite Catalyst for Dehydration of Dilute Bio-Ethanol. *Appl. Clay Sci.* 53, 263–271. doi:10.1016/j.clay.2011.03.006
- Borah, B. J., and Dutta, D. K. (2013). *In Situ* Stabilization of Pd0-Nanoparticles into the Nanopores of Modified Montmorillonite: Efficient Heterogeneous Catalysts for Heck and Sonogashira Coupling Reactions. *J. Mol. Catal. A Chem.* 366, 202–209. doi:10.1016/j.molcata.2012.09.024
- Cañizares, P., De Lucas, A., Valverde, J. L., and Dorado, F. (1998). n-Butane Hydroisomerization over Pd/HZSM-5 Catalysts. 1. Palladium Loaded by Impregnation. *Ind. Eng. Chem. Res.* 37, 2592–2600. doi:10.1021/ie970923b
- Chio, C., Sain, M., and Qin, W. (2019). Lignin Utilization: A Review of Lignin Depolymerization from Various Aspects. *Renew. Sustain. Energy Rev.* 107, 232–249. doi:10.1016/j.rser.2019.03.008
- Elliott, D. C. (2007). Historical Developments in Hydroprocessing Bio-Oils. *Energy Fuels* 21, 1792–1815. doi:10.1021/ef070044u
- Hechelski, M., Ghinet, A., Louvel, B., Dufrénoy-Benoît Rigo, P., Rigo, B., Daïch, A., et al. (2018). From Conventional Lewis Acids to Heterogeneous Montmorillonite K10: Eco-Friendly Plant-Based Catalysts Used as Green Lewis Acids. *ChemSusChem* 11, 1249–1277. doi:10.1002/cssc.201702435
- Hong, D.-Y., Miller, S. J., Agrawal, P. K., and Jones, C. W. (2010). Hydrodeoxygenation and Coupling of Aqueous Phenolics over Bifunctional Zeolite-Supported Metal Catalysts. *Chem. Commun.* 46, 1038–1040. doi:10.1039/b918209h
- Jongerius, A. L., Jastrzebski, R., Bruijninx, P. C. A., and Weckhuysen, B. M. (2012). CoMo Sulfide-Catalyzed Hydrodeoxygenation of Lignin Model Compounds: An Extended Reaction Network for the Conversion of Monomeric and Dimeric Substrates. *J. Catal.* 285, 315–323. doi:10.1016/j.jcat.2011.10.006
- Kay Lup, A. N., Abnisa, F., Wan Daud, W. M. A., and Aroua, M. K. (2017). A Review on Reactivity and Stability of Heterogeneous Metal Catalysts for Deoxygenation of Bio-Oil Model Compounds. *J. Industrial Eng. Chem.* 56, 1–34. doi:10.1016/j.jiec.2017.06.049
- Lee, C. R., Yoon, J. S., Suh, Y.-W., Choi, J.-W., Ha, J.-M., Suh, D. J., et al. (2012). Catalytic Roles of Metals and Supports on Hydrodeoxygenation of Lignin Monomer Guaiacol. *Catal. Commun.* 17, 54–58. doi:10.1016/j.catcom.2011.10.011
- Lee, C. S., Conradie, A. V., and Lester, E. (2021). Review of Supercritical Water Gasification with Lignocellulosic Real Biomass as the Feedstocks: Process Parameters, Biomass Composition, Catalyst Development, Reactor Design and its Challenges. *Chem. Eng. J.* 415, 128837. doi:10.1016/j.cej.2021.128837
- Li, K., Wang, R., and Chen, J. (2011). Hydrodeoxygenation of Anisole over Silica-Supported Ni2P, MoP, and NiMoP Catalysts. *Energy Fuels* 25, 854–863. doi:10.1021/ef101258j
- Liang, J., Wu, M., Zhang, Z., Wang, H., Huang, T., Zhao, L., et al. (2022). Constructing a Superior Co-mo HDS Catalyst from a Crystalline Precursor Separated from the Impregnating Solution. *Catal. Sci. Technol.* 12, 2278–2288. doi:10.1039/d2cy00083k
- Miao, S., Liu, Z., Han, B., Huang, J., Sun, Z., Zhang, J., et al. (2006). Ru Nanoparticles Immobilized on Montmorillonite by Ionic Liquids: a Highly Efficient Heterogeneous Catalyst for the Hydrogenation of Benzene. *Angew. Chem.* 118, 272–275. doi:10.1002/ange.200502632
- Mortensen, P. M., Grunwaldt, J.-D., Jensen, P. A., Knudsen, K. G., and Jensen, A. D. (2011). A Review of Catalytic Upgrading of Bio-Oil to Engine Fuels. *Appl. Catal. A General* 407, 1–19. doi:10.1016/j.apcata.2011.08.046
- Motokura, K., Fujita, N., Mori, K., Mizugaki, T., Ebitani, K., and Kaneda, K. (2006). Brønsted Acid Mediated Heterogeneous Addition Reaction of 1,3-Dicarbonyl Compounds to Alkenes and Alcohols. *Angew. Chem. Int. Ed.* 45, 2605–2609. doi:10.1016/j.jcat.2011.03.030
- Motokura, K., Matsunaga, S., Noda, H., Miyaji, A., and Baba, T. (2012). Water-Accelerated Allylsilylation of Alkenes Using a Proton-Exchanged Montmorillonite Catalyst. *ACS Catal.* 2, 1942–1946. doi:10.1021/cs300261b
- Motokura, K., Nakagiri, N., Mizugaki, T., Ebitani, K., and Kaneda, K. (2007). Nucleophilic Substitution Reactions of Alcohols with Use of Montmorillonite Catalysts as Solid Brønsted Acids. *J. Org. Chem.* 72, 6006–6015. doi:10.1021/jo70416w
- Nagendrappa, G. (2011). Organic Synthesis Using Clay and Clay-Supported Catalysts. *Appl. Clay Sci.* 53, 106–138. doi:10.1016/j.clay.2010.09.016
- Obireddy, S. R., Subbarao, S. M. C., Venkata, K. R. K. S., and Lai, W. F. (2021). Development and Characterization of Montmorillonite-Based Hybrid Materials for pH-Responsive Drug Delivery. *Chemistryselect* 6, 1466–1470. doi:10.1002/slct.202004711
- Ohta, H., Kobayashi, H., Hara, K., and Fukuoka, A. (2011). Hydrodeoxygenation of Phenols as Lignin Models under Acid-free Conditions with Carbon-Supported Platinum Catalysts. *Chem. Commun.* 47, 12209–12211. doi:10.1039/c1cc14859a
- Ramesh, S., Prakash, B. S., and Bhat, Y. S. (2015). Nanoporous Montmorillonite Catalyzed Condensation Reactions under Microwave Irradiation: a Green Approach. *Cocat* 2, 51–57. doi:10.2174/221333720201150225123821
- Ruiz, P. E., Frederick, B. G., De Sisto, W. J., Austin, R. N., Radovic, L. R., Leiva, K., et al. (2012). Guaiacol Hydrodeoxygenation on MoS2 Catalysts: Influence of Activated Carbon Supports. *Catal. Commun.* 27, 44–48. doi:10.1016/j.catcom.2012.06.021
- Saidi, M., Samimi, F., Karimipourfard, D., Nimmanwudipong, T., Gates, B. C., and Rahimpour, M. R. (2014). Upgrading of Lignin-Derived Bio-Oils by Catalytic Hydrodeoxygenation. *Energy Environ. Sci.* 7, 103–129. doi:10.1039/c3ee43081b
- Tsakgalias, I. S., Loukidi, A., Chatzimichailidou, S., Salmas, C. E., Giannakas, A. E., and Achilias, D. S. (2021). Effect of Na- and Organo-Modified Montmorillonite/Essential Oil Nanohybrids on the Kinetics of the *In Situ* Radical Polymerization of Styrene. *Nanomaterials* 11, 474. doi:10.3390/nano11020474
- Vaculíková, L., Valovičová, V., Plevová, E., Napruszewska, B. D., Duraczynska, D., Karcz, R., et al. (2021). Synthesis, Characterization and Catalytic Activity of Cryptomelane/montmorillonite Composites. *Appl. Clay Sci.* 202, 105977. doi:10.1016/j.clay.2021.105977
- Xu, H., Wang, K., Zhang, H., Hao, L., Xu, J., and Liu, Z. (2014). Ionic Liquid Modified Montmorillonite-Supported Ru Nanoparticles: Highly Efficient Heterogeneous Catalysts for the Hydrodeoxygenation of Phenolic Compounds to Cycloalkanes. *Catal. Sci. Technol.* 4, 2658–2663. doi:10.1039/c4cy00250d
- Yan, N., Yuan, Y., Dykeman, R., Kou, Y., and Dyson, P. J. (2010). Hydrodeoxygenation of Lignin-Derived Phenols into Alkanes by Using Nanoparticle Catalysts Combined with Brønsted Acidic Ionic Liquids. *Angew. Chem. Int. Ed.* 49, 5549–5553. doi:10.1002/anie.201001531
- Zakzeski, J., Bruijninx, P. C. A., Jongerius, A. L., and Weckhuysen, B. M. (2010). The Catalytic Valorization of Lignin for the Production of Renewable Chemicals. *Chem. Rev.* 110, 3552–3599. doi:10.1021/cr900354u
- Zhao, C., Kou, Y., Lemonidou, A. A., Li, X., and Lercher, J. A. (2009). Highly Selective Catalytic Conversion of Phenolic Bio-Oil to Alkanes. *Angew. Chem. Int. Ed.* 48, 3987–3990. doi:10.1002/anie.200900404
- Zhao, C., Kou, Y., Lemonidou, A. A., Li, X., and Lercher, J. A. (2010). Hydrodeoxygenation of Bio-Derived Phenols to Hydrocarbons Using RANEY Ni and Nafion/SiO2 catalysts. *Chem. Commun.* 46, 412–414. doi:10.1039/b916822b
- Zhu, X., Lobban, L. L., Mallinson, R. G., and Resasco, D. E. (2011). Bifunctional Transalkylation and Hydrodeoxygenation of Anisole over a Pt/HBeta Catalyst. *J. Catal.* 281, 21–29. doi:10.1016/j.jcat.2011.03.030

Conflict of Interest: The authors declare that the research was conducted in the absence of any commercial or financial relationships that could be construed as a potential conflict of interest.

Publisher's Note: All claims expressed in this article are solely those of the authors and do not necessarily represent those of their affiliated organizations, or those of the publisher, the editors, and the reviewers. Any product that may be evaluated in this article, or claim that may be made by its manufacturer, is not guaranteed or endorsed by the publisher.

Copyright © 2022 Wang, Li, Guo, Wang, Cheng, Xu, Li, Wang and Xu. This is an open-access article distributed under the terms of the Creative Commons Attribution License (CC BY). The use, distribution or reproduction in other forums is permitted, provided the original author(s) and the copyright owner(s) are credited and that the original publication in this journal is cited, in accordance with accepted academic practice. No use, distribution or reproduction is permitted which does not comply with these terms.



OPEN ACCESS

EDITED BY

Tiancheng Mu,
Renmin University of China, China

REVIEWED BY

Baowen Zhou,
Shanghai Jiao Tong University, China
Tianbin Wu,
Institute of Chemistry (CAS), China

*CORRESPONDENCE

Leiduan Hao,
haoled@mail.buct.edu.cn
Zhenyu Sun,
sunzy@mail.buct.edu.cn

SPECIALTY SECTION

This article was submitted to Green and Sustainable Chemistry, a section of the journal Frontiers in Chemistry

RECEIVED 25 June 2022

ACCEPTED 15 July 2022

PUBLISHED 22 August 2022

CITATION

Hui X, Wang L, Yao Z, Hao L and Sun Z (2022), Recent progress of photocatalysts based on tungsten and related metals for nitrogen reduction to ammonia.
Front. Chem. 10:978078.
doi: 10.3389/fchem.2022.978078

COPYRIGHT

© 2022 Hui, Wang, Yao, Hao and Sun. This is an open-access article distributed under the terms of the [Creative Commons Attribution License \(CC BY\)](#). The use, distribution or reproduction in other forums is permitted, provided the original author(s) and the copyright owner(s) are credited and that the original publication in this journal is cited, in accordance with accepted academic practice. No use, distribution or reproduction is permitted which does not comply with these terms.

Recent progress of photocatalysts based on tungsten and related metals for nitrogen reduction to ammonia

Xiangchao Hui, Lijun Wang, Zhibo Yao, Leiduan Hao* and Zhenyu Sun*

State Key Laboratory of Organic-Inorganic Composites, College of Chemical Engineering, Beijing University of Chemical Technology, Beijing, China

Photocatalytic nitrogen reduction reaction (NRR) to ammonia holds a great promise for substituting the traditional energy-intensive Haber–Bosch process, which entails sunlight as an inexhaustible resource and water as a hydrogen source under mild conditions. Remarkable progress has been achieved regarding the activation and solar conversion of N_2 to NH_3 with the rapid development of emerging photocatalysts, but it still suffers from low efficiency. A comprehensive review on photocatalysts covering tungsten and related metals as well as their broad ranges of alloys and compounds is lacking. This article aims to summarize recent advances in this regard, focusing on the strategies to enhance the photocatalytic performance of tungsten and related metal semiconductors for the NRR. The fundamentals of solar-to- NH_3 photocatalysis, reaction pathways, and NH_3 quantification methods are presented, and the concomitant challenges are also revealed. Finally, we cast insights into the future development of sustainable NH_3 production, and highlight some potential directions for further research in this vibrant field.

KEYWORDS

photocatalysis, nitrogen reduction, ammonia synthesis, tungsten, semiconductor

1 Introduction

As the cornerstone of modern civilization, ammonia (NH_3) is an incontrovertible raw material for modern industry and agriculture, which plays a crucial role in human survival and economic growth. Moreover, due to its high hydrogen content (17.7 wt%), gravimetric energy density (3 kWh kg^{-1}) and easy liquification (-33°C under atmospheric pressure), NH_3 also serves as a useful commodity for chemicals used in industries and as a carbon-free clean energy carrier (Guo and Chen, 2017). NH_3 is by far predominantly fabricated via the energy- and capital-intensive Haber-Bosch process requiring extreme reaction conditions of $300\text{--}500^\circ\text{C}$ and $15\text{--}25 \text{ MPa}$, which gives rise to excessive consumption of feedstocks and consequently high CO_2 emissions. Therefore, exploring and developing renewable, environment-friendly, and green routes to yield NH_3 is desirable. Photocatalytic N_2 fixation is perceived as an alternative sustainable

strategy for facile, cost-effective ammonia production using water and nitrogen gas under ambient conditions. There is enormous, acknowledged and untapped potential in this emerging field. Considering that nitrogen reduction reaction (NRR) coupled with water oxidation is a thermodynamically uphill reaction, solar energy is hence crucial to induce incoming photons generating electronic charge carriers to initiate the catalytic reaction. Since the pioneering research by Schrauzer and co-workers embarked on the photocatalytic reduction of N_2 to NH_3 by employing TiO_2 -based photocatalysts (Schrauzer and Guth, 1977), explorative efforts in this sector have been exerted to develop novel photocatalysts with high efficiency, especially in recent years (Schrauzer and Guth, 2002). The initial attempts are currently expanded to widen the scope of investigated materials and their modifications, as well as effective strategies of tuning crystalline phase, surface defects, heteroatom doping, surface modification and/or heterostructure construction for enhancing photocatalytic performances. The photochemical process underpins the terms of selectivity, efficiency, and low operational cost for the production of NH_3 toward the practical implementation at relatively ambient conditions using solar energy. Despite the huge potentials, the photocatalytic NH_3 production still falls far short of the ideal of being commercialized, which results from weak adsorption/activation of the nonpolar $N\equiv N$ triple bond of N_2 (941 kJ mol^{-1}), inefficient light absorption, and poor photo-induced charge separation (Shen et al., 2021).

Design and development of efficient photocatalysts hold the key to achieve improved performance of photocatalytic NRR. To date, several prior articles (Chen et al., 2018; Shi et al., 2019; Shuai Zhang et al., 2019; Huang et al., 2020; Chen-Xuan Xu et al., 2021; Lee et al., 2021; Shen et al., 2021; Tong Xu et al., 2021) have outlined the recent advancements of photoreduction of N_2 to NH_3 and photocatalysts engineering strategies. Transition metals, especially the early transition metals (e.g., tungsten, molybdenum, vanadium etc.), which possess both empty orbitals and abundant d -orbital electrons as well as suitable bandgap energies, could activate dinitrogen molecules through σ -donation/ π -backdonation effects, showing huge potential for applications as photocatalysts for photocatalytic NRR. However, few reviews, to the best of our knowledge, have hitherto summarized tungsten and related metals photocatalysts together with a specific focus on strategies to enhance their performances. This review elaborated the state-of-the-art understanding of the basic principles of NRR photocatalysis, reaction mechanisms, thermodynamic limits, and enforceable protocols involved in the overall photochemical processes. We comprehensively discuss recent progress over semiconductors containing tungsten (W), molybdenum (Mo), cobalt (Co), vanadium (V), tantalum (Ta), niobium (Nb), rhenium (Re), zirconium (Zr), hafnium (Hf), and their major advantages as to

photocatalysis activity. Furthermore, we emphasize several strategies to improve the photocatalytic performance and also highlight the challenges and future directions for sustainable NH_3 production.

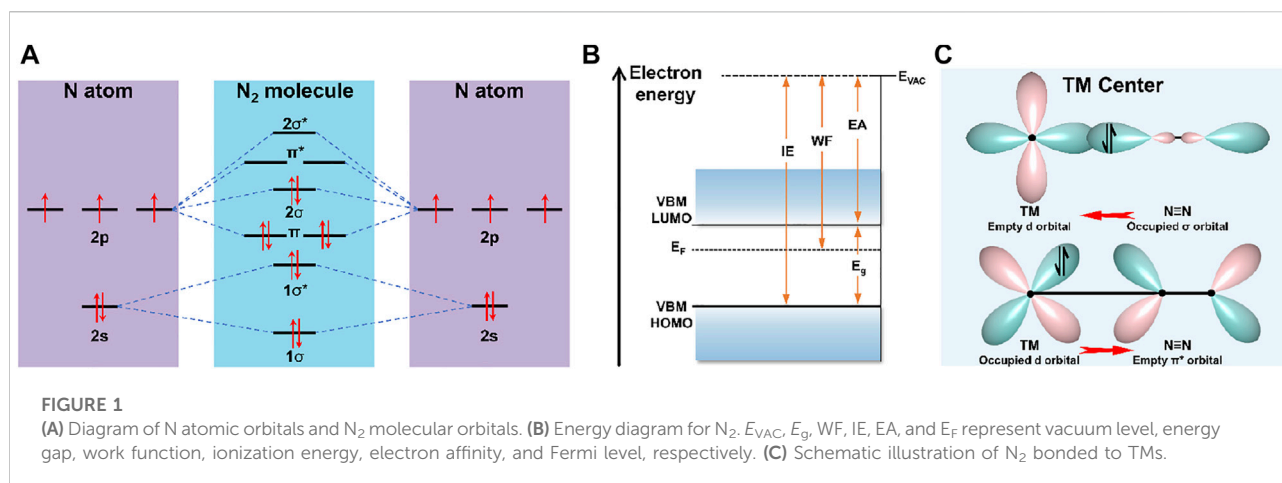
2 Fundamentals for photochemical NRR

2.1 Properties of N_2 molecules

Molecular dinitrogen possesses a triple bond between the nitrogen atoms and a non-bonding pair of electrons on each atom. Atomic nitrogen has 5 valence electrons and 4 valence orbitals ($2s$, $2p_x$, $2p_y$, and $2p_z$), whereas hybridization of the s - p atomic orbitals of N_2 consists of four bonding orbitals (two σ and two π orbitals) and four antibonding orbitals (two σ^* and two π^* orbitals). The electrons from the π and 2σ orbitals are shared to form $N\equiv N$ bond leaving these from $1\sigma^*$ and 1σ orbitals the non-bonding electron pairs (Figure 1A) (Kitano et al., 2012). Hence, the large energy gap of 10.82 eV between the highest occupied molecular orbital (HOMO) and lowest unoccupied molecular orbital (LUMO) seriously hinders electron injection into N_2 antibonding orbitals (Jia and Quadrelli, 2014). A strong $N\equiv N$ bond energy (945 kJ mol^{-1}) and first-bond breaking energy (410 kJ mol^{-1}) render N_2 molecules extremely thermodynamically stable (Gambarotta and Scott, 2004), meanwhile, N_2 molecules are chemically inert by virtue of high ionization energy of 15.85 eV and negative electron affinity of -1.9 eV (Figure 1B). Therefore, adsorption and dissociation of N_2 with weak polarizability and lacking dipole moment are widely regarded to be the rate-determining steps of NRR (Guo et al., 2018; Liang Yang et al., 2020; Yi-Fei Zhang et al., 2020). Both computational and experimental works have demonstrated that transition metal-based materials interact strongly with N_2 through the formation of N-metal bonds, thanks to the empty d orbitals in the transition metals (TMs) accepting the lone pair electrons of N_2 and back donating d - p electrons into the anti-binding orbitals of N_2 based on an “acceptance-donation” protocol, whereby the triple bond can be weakened and activated to facilitate the bond dissociation (Figure 1C). Some advances have demonstrated the incomparable advantages of d block compounds, but this realm remains elusive.

2.2 Principles and mechanisms of photochemical NRR to NH_3

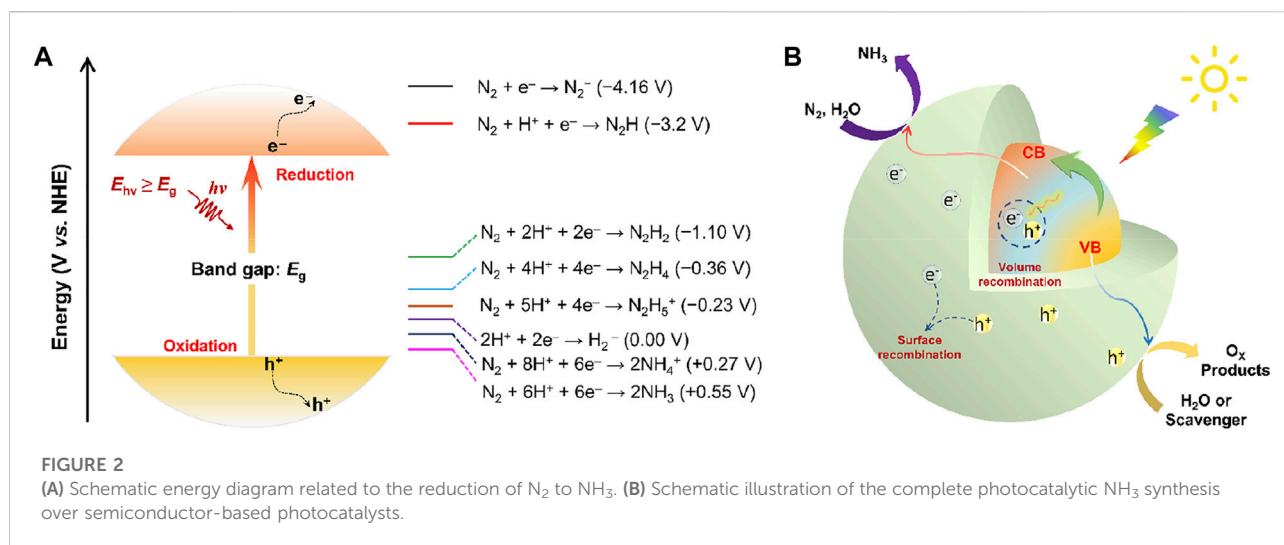
Ideally, photocatalytic NRR into NH_3 involves transfer of 6 protons and 6 electrons, which is a strong endothermic reaction with stoichiometric O_2 production formed by water oxidation (overall reaction: $N_2(g) + 3H_2O(l) \leftrightarrow 2NH_3(g) + 3/2O_2(g)$,



$\Delta G = +7.03$ eV) (Medford and Hatzell, 2017). The photochemical NRR requires a potential of at least 1.17 eV per electron (Comer and Medford, 2018), which is initiated by the absorption of photons with an energy higher than the energy bandgap (E_g) of a semiconductor photocatalyst to generate photoexcited electron-hole pairs and an energy >1.17 eV demanded for the overall NH₃ production (Figure 2A). Upon photo-irradiation with sufficient energy supply, electrons (e^-) leap into the conduction band (CB) with simultaneous generation of holes (h^+) at valence band (VB), thus triggering the reduction of N₂ to NH₃ with photo-excited electrons and water oxidation with created holes (Linsebigler et al., 1995). The photoinduced separation of charge carriers is the prerequisite for all semiconductor photocatalysis. However, the migration and separation of photoexcited electron-hole pairs to the semiconductor surface active sites to participate in the redox reactions competes with their recombination in the bulk and on the surface. Eventually, the reaction products desorb from the photocatalyst surface and are transferred to the medium to close the cycle (Figure 2B). Note that the NRR is an uphill reaction. As a consequence, the CB and VB positions of a photocatalyst must bestride the reduction potential of N₂/N₂H (−3.2 V vs. normal hydrogen electrode, NHE), while the top of VB must be beyond the oxidation potential of H₂O/O₂ (+1.23 V vs. NHE). Satisfying both of the above requirements with a singular conventional semiconductor seems to be incompatible, which is unfavorable for harvesting most of the light across the solar spectrum. Since a considerable number of electron-hole pairs recombine inside or on the surface of the catalyst with a rather fast kinetics rate (Zhang et al., 2012), or dissipate in the form of heat or light energy, thus resulting in a decrease of reaction efficiency. Accordingly, most of the reported catalysts for photocatalytic NH₃ production still suffer from low light utilization, fast

recombination of photoexcited electron-hole pairs, poor N₂ adsorption/activation, and sluggish electron-to-N₂ transfer kinetics, hobbling the overall solar-to-ammonia conversion efficiency. Additionally, the insufficient stability of the photocatalysts is another serious issue. Many semiconductors could undergo photo-corrosion upon light irradiation, which can be induced by the photo-generated electrons or holes, thus leading to degradation of NRR performance and inhibiting the long-time photocatalytic ammonia synthesis.

The current well-established mechanisms for photocatalytic NRR can be roughly divided into the following: dissociative, associative or enzymatic pathways as shown in Figure 3 (van der Ham et al., 2014; Hao Li et al., 2016; Shipman and Symes, 2017). For the dissociative pathway, the breaking of the N≡N bond precedes the hydrogenation process, followed by the stepwise protonation of the adsorbed nitrogen atoms to form NH₃, analogous to the reaction mechanism of the industrial Haber-Bosch process (Garden and Skulason, 2015), which is however unfavorable for N₂ photoreduction to NH₃ resulting from the large external energy input required for the cleavage of the N≡N triple bond (Shipman and Symes, 2017). According to the different hydrogenation sequences, the associative N₂ reduction mechanism follows either distal pathway or alternating pathway. In the distal associative pathway, the nitrogen atom far from the adsorption site is protonated successively before generating the first NH₃ molecule, leaving another N atom to yield the second NH₃ molecule. Conversely, in the alternate pathway, the hydrogenation reaction occurs alternately at two nitrogen atoms, each of which could react with injected electrons and protons, forming key intermediates such as metal-bound diazene (HN = NH) and reaction byproducts such as N₂H₄ (Bo et al., 2021). As for the enzymatic pathway, the 2 N atoms of the nitrogen molecule are simultaneously adsorbed by the



active center of the catalyst, anchored on the catalyst surface via the “side-on” configuration, and then hydrogenated (Hinnemann and Norskov, 2006; Xiao-Fei Li et al., 2016). The proposal that gained the widest support was that photocatalytic NH_3 synthesis follows associative pathways, during which the adsorption and activation of N_2 and then the transfer of photogenerated electrons from the photocatalyst to N_2 provide a lower reaction energy barrier for the dissociation of $N \equiv N$ triple bonds (Montoya et al., 2015). The activation of N_2 involves the formation of a coordinate bond with the active site proceeded on a catalytic surface, and the subsequent electron transfer and protonation are the keys to weakening the $N \equiv N$ bonding energy (Jacobsen et al., 2001). Different mechanisms have been proposed, but deep mechanistic understanding of NRR that may vary for distinct catalytic systems remains to be further explored.

2.3 Thermodynamic limits of photocatalytic NRR to NH_3

Due to the proton-electron transfer of multiple intermediates resulting in sluggish reaction kinetics, the thermodynamic constraints relying on the reaction intermediates and the overall and half-reaction thermodynamics independent of the photocatalysts play the decisive role in the photocatalytic NRR process (Table 1). Despite the overall reaction of NH_3 production via N_2 reduction in water ($N_2(g) + 6H^+ + 6e^- \leftrightarrow 2NH_3(g)$, $E^0 = +0.55$ V vs. NHE) is more thermodynamically feasible than the competing hydrogen evolution reaction (HER) by water reduction, HER is more likely to occur with fewer electrons, decreasing the selectivity toward NH_3 . Besides, the more negative potentials for the intermediate reactions, such

TABLE 1 Thermodynamic potentials of hydrogenation reactions related to the whole nitrogen fixation pathways.

Reaction equilibrium	E^0	Ref.	Eqn.
$N_2(g) + 3H_2O(l) \leftrightarrow 2NH_3(g) + 3/2O_2(g)$	-1.137 V vs. SHE (pH 0)	Hochman et al. (2020)	1
$2H^+ + 2e^- \leftrightarrow H_2(g)$	0 V vs. SHE (pH 0)	Shi et al. (2020a)	2
$3H_2O(l) \leftrightarrow 3/2O_2(g) + 6H^+ + 6e^-$	+1.23 V vs. NHE (pH 0)	Hochman et al. (2020)	3
$N_2(g) + 6H^+ + 6e^- \leftrightarrow 2NH_3(aq)$	+0.092 V vs. RHE	Lindley et al. (2016)	4
$N_2(g) + 6e^- \leftrightarrow N_2^{2-}(aq)$	-4.16 V vs. NHE or -3.37 V vs. RHE (pH 14)	Shi et al. (2020b)	5
$N_2(g) + 6H^+ + 6e^- \leftrightarrow 2NH_3(g)$	+0.55 V vs. NHE (pH 0)	Bazhenova and Shilov, (1995)	6
$N_2 + 8H^+ + 8e^- \leftrightarrow 2NH_4^+$	+0.27 V vs. NHE (pH 0)	Chen et al. (2018)	7
$N_2(g) + H^+ + e^- \leftrightarrow N_2H$	-3.20 V vs. RHE	Shi et al. (2020a)	8
$N_2 + 2H^+ + 2e^- \leftrightarrow N_2H_2(g)$	-1.10 vs. RHE	Shi et al. (2020a)	9
$N_2 + 4H^+ + 4e^- \leftrightarrow N_2H_4(g)$	-0.36 V vs. RHE	Shi et al. (2020a)	10
$N_2H_2(g) + 2H^+ + 2e^- \leftrightarrow N_2H_4(aq)$	0.529 vs. RHE	Fu et al. (2022)	12
$N_2H_4(aq) + 2H^+ + 2e^- \leftrightarrow 2NH_3(aq)$	0.939 vs. RHE	Fu et al. (2022)	13
$N_2(g) + 6H_2O \leftrightarrow 2NO_3^- + 12H^+ + 10e^-$	+1.24 V vs. NHE	Yifu Chen et al. (2020)	14

as -4.2 V (vs. RHE) for one-electron activation to form surface-bound N_2 and -3.2 V (vs. RHE) for first proton-coupled one-electron hydrogenation of N_2 (Zhu et al., 2013; Shi et al., 2020a; Huang et al., 2020), are beyond the photocatalysis capability of most semiconductors without active sites.

The initial chemisorption and activation of N_2 could trigger the formation of different kinds of species in the subsequent reactions owing to multiple complicated electrons transferred hydrogenation procedures and the presence of reactive oxygen species by water oxidation half-reaction, such as oxygen, hydroxyl radicals $\cdot OH$ ($2H_2O + 4h^+ \rightarrow O_2 + 4H^+$, $E^0 = 0.81$ V vs. NHE at pH 7 or $H_2O + h^+ \rightarrow OH + H^+$, $E^0 = 2.32$ V vs. NHE at pH 7) (Sun et al., 2018). Adversely, the formed O_2 further captures electrons in the CB to suppress the NH_3 photosynthesis (Shiraishi et al., 2018; Sun et al., 2018), and the strong oxidation agents $\cdot OH$ can also further generate nitrite or nitrate from the generated NH_3 by photooxidation, which are detrimental to N_2 photoreduction to NH_3 . Because of its weaker interaction with the surface O atom caused by vacancies or doping, metal is further less firmly bound to O following the release of one H atom from adsorbed H_2O^* onto the surface O atom, thus two OH^* bonded at the neighboring catalytic sites are easily coupled forming peroxide $H_2O_2^*$ preferentially adsorbed at active sites, thereafter poisoning the photocatalyst (Liu et al., 2012). The oxidation half-reaction products also oxidize the photogenerated NH_3 to HNO_3 , leading to a decrease in the NH_3 yield. Yang et al. (2021) transformed the N_2 disproportionation reaction into a complete reductive nitrogen photofixation by introducing Au nanoparticles into Fe-TiO₂ to effectively decompose H_2O_2 . Some neglected N_2 fixation products (e.g., N_2H_4 , NO_2^- , and NO_3^- , etc.) as essential chemicals should be noted (Table 1, Eqs. 10 and 14), in which N_2H_4 as a by-product from aforementioned associative alternating pathways has also been detected in the same research (Schrauzer and Guth, 2002; Xiao-Fei Li et al., 2016). Li et al. (Hao Li et al., 2016) discovered that N_2H_4 was quickly generated over the BiOCl nanosheets exposed with (010) facets and then gradually disappeared to produce NH_3 , which strongly supports the alternative mechanism. In terms of thermodynamic potentials (Table 1, Eqs. 9 and 12), N_2H_4 is more prone to be transformed to NH_3 from surface- N_2H_4 intermediates due to its much weaker N–N single bond. Similar to the hydrogenation pathway to NH_3 , dissociated adsorbed N_2 molecule is oxidized to the intermediate of metastable NO^* by photogenerated h^+ , followed by further oxidation with O_2 and H_2O from the reaction media, by which N_2 is converted to nitrate and nitrite through continuous photooxidation reactions (Comer and Medford, 2018). The previously reported N_2 photoreduction products are either NH_4^+ or NO_3^- (Liu et al., 2019; Dong Zhang et al., 2022), simultaneous coproduction of NH_4^+ and NO_3^- through simultaneous reduction and oxidation of N_2 in pure water,

which was demonstrated to occur spontaneously in aqueous solutions (Ren et al., 2020). Another critical aspect in NH_3 production via photochemical N_2 reduction is that some key reaction intermediates are instrumental in NH_3 conversion. Zhao et al. (2022) established a redox pathway with a lower kinetic barrier for NH_3 photosynthesis, in which N_2 and O_2 can be trapped at the oxygen vacancies in ultrathin two-dimensional (2D) CuCo metal-organic frameworks (MOFs) to generate *NO and further be reduced to NH_3 by visible light. Although the desired NH_3 conversion and selectivity are swayed by these competing reactions, some by-products also play imperative roles in industrial production and living needs.

The addition of sacrificial agents (typically electron donors such as sulfites, amines, humic acid, ascorbic acid, and alcohols) with oxidation potentials lower than water appeases the requirement for oxidizing ability in some SC photocatalysts, further suppressing electron-hole pair recombination (Shen et al., 2020). On the other hand, the overall production rate of NH_3 is kinetically balanced by the hole consumption rate on the photocatalyst since electrons and holes are generated in pairs under illumination. Organic alcohols with an α -H adjacent to the OH group(s)-to wit, methanol, ethanol, 2-propanol, ethylene glycol, and so forth, can react with holes in VB to accelerate the production of electrons and liberation of protons (Chen et al., 2015). Among them, methanol is demonstrated to be more appropriate and efficient than other hole sacrificial reagents. Methanol not only loses electrons more easily to consume the accumulated holes due to its lower HOMO (Zhao et al., 2015), but also promotes the solubility of N_2 , which could act as a proton donor and partial electron donor for subsequent reduction reactions (Li et al., 2018). However, methanol as the sacrificial agent could be oxidized to form carbonyl-containing compounds (e.g., aldehyde or ketone) and finally CO_2 , which might interfere with product detection and quantification. The N_2 fixation reaction can also be facilitated by $^*CO_2^-$ produced from the oxidation process of methanol (Swain et al., 2020). Cao and co-workers (Cao et al., 2018) found that the- CO_2^- intermediates transformed from methanol or absorbed CO_2 affected the nitrogen fixation due to their strongly reducing ability ($E_{CO_2^-/CO_2} = 1.8$ V) ($5N_2 + 2CO_2^- + 4H_2O \rightarrow 2NH_3 + 2CO_2 + 2OH^-$) (Dimitrijevic et al., 2011). It should be noted that the NH_3 formation mechanism in such sacrificial systems should be taken with great caution, the target scavenger should be chosen carefully.

2.4 Protocols, evaluation, and detection methods in photocatalytic NRR

Despite the great strides toward photon-driven ammonia production that have been taken, unified rules and standards in this fledgling field should be formulated to ensure the authority and accuracy, by which the impetus imparted forcefully

contribute to advance of the sustainable technology. Since the low NH_3 yield (ppb/ppm level) and ubiquitous contaminants plague experimental practices (Gao et al., 2018; Tang and Qiao, 2019; Zhao et al., 2019), establishing a uniform protocol for rigorous experiments preceding the detection and quantification of NH_3 are noncontroversial. Therefore, to clarify the source of NH_3 and ensure data reproducibility, various contamination sources from the environment, latex gloves, human respiration, stable deionized water, photochemical reactor, or the used feed gas, even NH_3 or amine groups unintentionally introduced by catalysts, should be ruled out to avoid overestimation of the NH_3 concentration (Bai et al., 2017; Zhao et al., 2021). The photocatalysts, photoreaction set-up and all its components as well as sample tubing should be thoroughly rinsed with fresh ultrapure water and properly stored. Particular emphasis should be put on the NO_x contaminants derived from N-containing chemicals, protic solvents, or supply gas, which are easily reduced to NH_3 (Xue Chen et al., 2020; Li et al., 2022a; Feng Wang et al., 2022; Xu et al., 2022). To account for the reliability and repeatability of photoactivity, it is strongly recommended to use reported rigorous experimental protocols (Andersen et al., 2019; Tang and Qiao, 2019; Choi et al., 2020; Shen et al., 2021), which clearly list experimental methods, gas purification, blank and control experiments, especially the isotopic labeling experiments. The $^{14}\text{N}_2$ and $^{15}\text{N}_2$ feed gases should be pre-purified to remove any possible NO_x or NH_3 to eliminate uncertainty and even false positives of catalytic data (Zhao et al., 2020; Hui et al., 2022; Yuting Wang et al., 2022).

However, controversy exists as to how to obtain reliable detection and quantification of NH_3 and NH_4^+ , which severely hampered the growth of this field. Fortunately, the development of measuring techniques further pushed the advance of NH_3 evaluation. Currently, detection and quantification of NH_3 could be mainly divided into five methods, including spectrophotometric/colorimetric assays using indophenol blue or Nessler's reagent, ion chromatography (IC), ion-selective electrode (ISE), fluorescence, and ^1H -NMR spectroscopy methods (Gao et al., 2018; Zhao et al., 2019). These methods are methodologically sound and get concordant precise results for NH_3 determination in water systems (Mansingh et al., 2021). However, each of these methods has both advantages and limits for measuring NH_3 . Colorimetric assays are widely available with benefits of good sensitivity, fine accuracy ($0\text{--}500\ \mu\text{g}_{\text{NH}_3}\ \text{L}^{-1}$), and low cost (Zhao et al., 2019). The pH, solvent used, presence of certain metal ions, sacrificial agents and their oxides, and nitrogen-containing chemicals can all adversely increase the amount of NH_3 detected by the coloration methods (Gao et al., 2018). IC is recommended for NH_3 quantification given its reproducible, precise results with a wider range of NH_3 estimation, superior efficiency

and selectivity, and good stability, but it still suffers from the disadvantage that certain sacrificial agents affect the separation efficiency of the cation-exchange column. NMR spectroscopy, mass spectroscopy, and enzyme assays are also employed as supplementary measures to eliminate the possible false-positive results, the first of which, even quantitatively, could not prove the origin of all ammonia generated. For consistency and scientific rigor, the concentration of NH_3 detected should be cross-checked with two or more different quantitative methods, even conducted in *in-situ* and continuous monitoring processes for reliable evidences from an unimpeachable source.

Given the lack of the standard photocatalytic reaction systems used in conventional laboratory tests (Ziegenbalg et al., 2021), it is therefore necessary to pay particular attention to various vital details during the assessment of photocatalytic nitrogen fixation. Figure 4 presents the effect of important experimental parameters on the observed catalytic performance for photo-driven NH_3 production. An objective and meaningful comparison of photocatalytic NH_3 synthesis performance among different groups is heavily reliant on a set of standard experimental conditions (e.g., light source intensity, irradiation wavelength range, photocatalyst dosage, reaction solution volume, reactor type, reaction temperature and pressure, etc.). Many technical aspects especially the light source are often missing or not stated in sufficient details. Standardization of reactor design is desirable, thereby minimizing the impact of geometry. Reported performance evaluation is primarily based on NH_3 yield, apparent quantum yield/efficiency (AQY/AQE) and turnover frequency (TOF). However, mass-based performance metrics (e.g., $\mu\text{mol h}^{-1}\text{g}^{-1}$) are insufficient because photocatalytic activity is not necessarily proportional to the catalyst mass (Kramm et al., 2019; Huimin Liu et al., 2021). Similarly, AQY/AQE is often used to evaluate the photocatalytic activity under monochromatic light excitation of the same specific wavelength, which is closely related to the wavelength of incident photons and the intrinsic properties of the materials, since photocatalysts generally behave differently on absorption coefficients and photocatalytic activities at each irradiation wavelength (Yuhua Wang et al., 2019). TOF differs as well in terms of the active centers. Solar-to- NH_3 -yield (SAY)/solar-to- NH_3 (STA) efficiency can be universally used as the practical standard for comparison, which is determined by a solar simulator (AM 1.5G) with an irradiance of $100\ \text{mW cm}^{-2}$. With more regard to normalizing evaluation systems, solar-to- NH_3 energy conversion (SEC) efficiency is suggested to objectively compare the catalytic activity of different materials and assay the future industrialization opportunities (targeted SEC $\approx 10\%$) (Rong Zhang et al., 2019; Ziegenbalg et al., 2021).

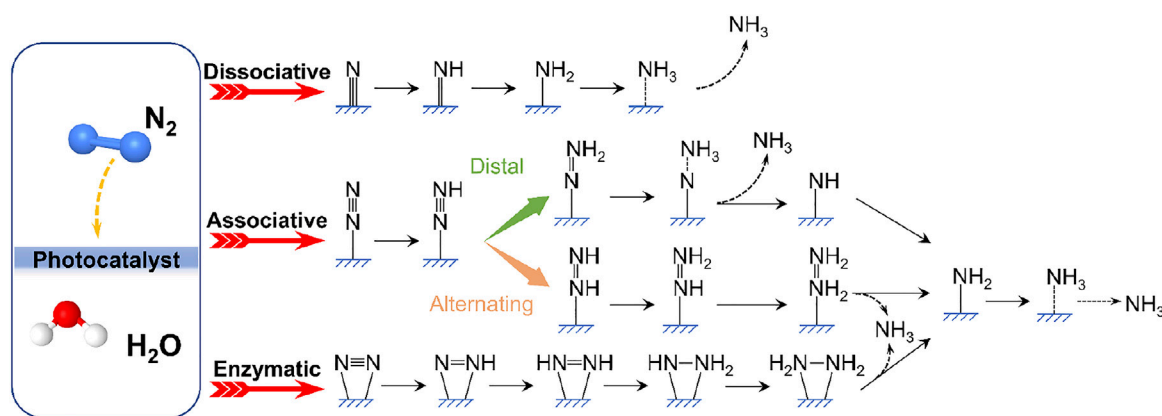


FIGURE 3

Schematic representation of possible pathways for N_2 fixation to NH_3 on catalyst surfaces.

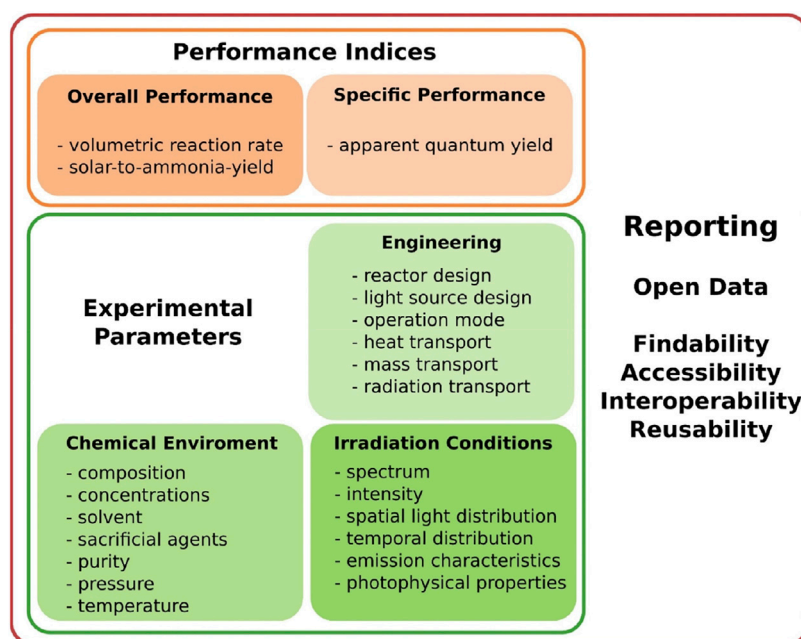


FIGURE 4

Guidelines for experiment normalization to rule out the impact of various parameters that influence the overall and specific performance indices. Reproduced from ref. (Ziegenbalg et al., 2021). With permission from the John Wiley and Sons.

3 Tungsten-based and related photocatalysts for NRR

3.1 Metal oxide-based photocatalysts

3.1.1 Tungsten oxides

Tungsten oxides, commonly denoted as $WO_{3-x} \cdot nH_2O$ ($x < 1$, $n = 0-2$), are somewhat distorted in their crystal structure made

up of perovskite units, rather not perfect octahedral, with bandgap energies ranging from 2.4 to 2.8 eV depending on their stoichiometries, crystalline structure and density of defects (Zheng et al., 2011; Sun et al., 2019). Tungsten trioxide (WO_3) is the most popular semiconductor among all tungsten oxides because of its exceptional chromic properties and mixed polymorphs, which manifest in rich and diverse structures (Girish Kumar and Koteswara Rao, 2015; Yin and Asakura, 2019;

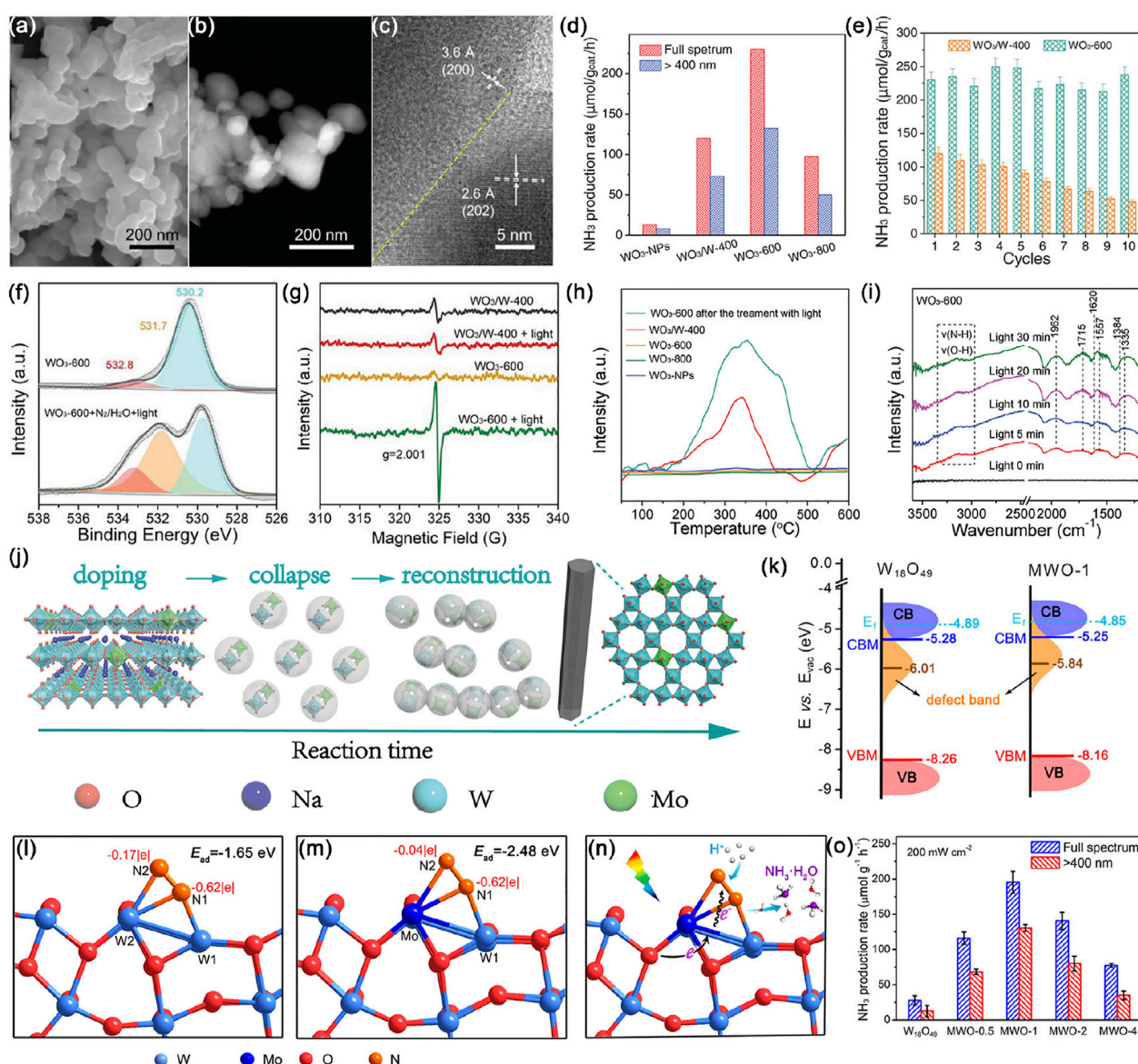


FIGURE 5

(A) Scanning electron microscopy (SEM) image, (B) high-angle annular dark-field scanning transmission electron microscopy (HAADF-STEM) image, and (C) high-resolution TEM (HRTEM) image of WO_3 -600. (D) Photocatalytic NH_3 production rates over WO_3 -NPs, WO_3/W -400, WO_3 -600, and WO_3 -800. (E) NH_3 production rates for WO_3 -600 and WO_3/W -400 over the course of ten rounds of successive reactions. (F) Quasi *in situ* XPS spectra of O 1s in WO_3 -600 before and after treatment. (G) *In situ* ESR spectra of WO_3/W -400 and WO_3 -600 before and after light irradiation. (H) N_2 -TPD profiles of WO_3/W -400, WO_3 -600, WO_3 -800, WO_3 -NPs, and WO_3 -600 after the treatment with light. (I) *In situ* DRIFT spectra recorded during the photocatalytic N_2 fixation over WO_3 -600. Reproduced from Hou et al. (2019) with permission from the John Wiley and Sons. (J) Schematic illustration of the generation of Mo doped h- WO_3 crystalline nanowires. Reproduced from Mao et al. (2020) with permission from the John Wiley and Sons. (K) Schematic illustration of the electronic band structures of $\text{W}_{18}\text{O}_{49}$ and 1 mol% Mo-doped $\text{W}_{18}\text{O}_{49}$ ultrathin nanowires. Optimized adsorption configurations of N_2 molecules and their corresponding charge distribution on the surface of (L) $\text{W}_{18}\text{O}_{49}$ and (M) Mo-doped $\text{W}_{18}\text{O}_{49}$. (N) Scheme for photocatalytic N_2 reduction over Mo-doped $\text{W}_{18}\text{O}_{49}$. (O) Photocatalytic ammonia production rates by $\text{W}_{18}\text{O}_{49}$, MWO-0.5, MWO-1, MWO-2, and MWO-4 UTNWs in the first 2 h. Reproduced from Ning Zhang et al. (2018) with permission from American Chemical Society.

Cheng and Zhang, 2020). Among different structures of WO_3 , the monoclinic phase is a preferred photocatalyst with the most relatively thermodynamically stable configuration than orthorhombic and hexagonal phases, while triclinic and cubic

crystal structures rarely get attention (Zheng et al., 2011; Girish Kumar and Koteswara Rao, 2015; Fan et al., 2021). Hou et al. (Hou et al., 2019) developed a facile method to prepare monoclinic WO_3 via thermal treatment of nanoporous metals,

wherein nanoporous WO₃-600 was composed of connected grains rather than a single grain, containing abundant grain boundaries (GBs) (Figures 5A–C). Impressively, WO₃-600 showed excellent performance for photocatalytic NRR with an NH₃ yield rate as high as 230 $\mu\text{mol g}_{\text{cat}}^{-1} \text{h}^{-1}$ without any sacrificial agents at room temperature, 17 times higher than that for WO₃ nanoparticles (WO₃-NPs) without GBs (Figure 5D). Moreover, almost 100% of initial activity was maintained even after ten successive reaction rounds over WO₃-600 (Figure 5E). Quasi *in situ* XPS and *in situ* electron spin resonance (ESR) measurements have been employed to verify the pivotal role of GBs in inducing a large number of operando OV_s under light irradiation (Figures 5F,G). These operando OV_s served as highly active sites for efficient adsorption and activation of N₂, which have been confirmed by temperature-programmed desorption of N₂ (N₂-TPD) (Figure 5H), directly contributing to easier delivery of photoexcited electrons to adsorbates through metal-oxygen covalency. Then N₂H* intermediates coupled with protons were observed by *in situ* diffuse reflectance infrared Fourier transform (DRIFT) (Figure 5I). As shown in Figure 5J, sub-5-nm-sized nanowires of hexagonal tungsten oxide (*h*-WO₃) via a dopant replacement-driven molten salt method also turned out to be excellent photocatalysts with a high NH₃ production rate of 370 $\mu\text{mol g}^{-1} \text{h}^{-1}$, benefiting from unique features of the Mo-doped ultrathin hexagonal structure, thus facilitating carrier separation and dissociation of N₂ molecules (Mao et al., 2020). Tailoring the morphology of WO₃ is not only a rational route to investigate the relationship between the microstructure and photocatalytic performances, but also a feasible approach for fabricating highly photoactive nanomaterials.

Since the lattice of WO₃ withstands a considerable loss of oxygen content, the resulting nonstoichiometric tungsten suboxides (WO_{3-x}) compositions such as W₂₀O₅₈, W₁₈O₄₉ and W₂₄O₆₈, have suitable bandgap energy, and tunable electronic band structure, charge redistribution, as well as existence of mixed-valence W ions benefiting different degrees of oxygen deficiency in their structures (Song et al., 2015; Sun et al., 2019; Yin and Asakura, 2019; Meng Yang et al., 2020). To accommodate the large energy band of N₂, Zhang et al. (Congmin Zhang et al., 2018) used a solvothermal method to fabricate defect-rich W₁₈O₄₉ ultrathin nanowires doped with Mo, where Mo dopants shifted defect-band center up toward the Fermi level (E_F), thereby harvesting more photon energy to provide adequate energetic electrons for N₂ reduction (Figure 5K). Moreover, the Mo–O covalent bond facilitated the separation and transfer of photogenerated charges from coordinatively unsaturated Mo sites to N₂ adsorbates, while the formation of the Mo–W bond can effectively enhance the molecular polarization of chemisorbed N₂ as a reactive dual-active center, resulting in better activation (Figures 5L, N). The as-prepared 1 mol% Mo-doped W₁₈O₄₉ sample showed

enhanced photocatalytic performance with an NH₃ generation rate of 195.5 $\mu\text{mol g}^{-1} \text{h}^{-1}$ and STA efficiency of 0.028% under simulated sunlight (Figure 5O). Analogously, Mn²⁺ ions were introduced to replace W sites in the W₁₈O₄₉ lattice, which not only acted as chemisorption and activation centers for N₂ and H₂O molecules, but also facilitated the separation and migration of photogenerated charges (Ying et al., 2019). Tailoring surface oxygen vacancies and doping of tungsten oxides with heteroatoms are effective strategies to increase the number of active sites for N₂ chemisorption (Mingli Zhang et al., 2020).

3.1.2 Molybdenum trioxides

Molybdenum in the same transition metal group with tungsten shares some similar chemical properties, where a non-stoichiometric form MoO_{3-x}, analogous to WO_{3-x}, exhibits prodigious potential for solar-driven photocatalysis due to its strong OV_s-induced localized surface plasmon resonance (LSPR) absorption in visible-near infrared (vis-NIR) region (Yehuan Li et al., 2019; Zheng Wang et al., 2019; Qiu et al., 2021; Li et al., 2022b). Bai et al. (Bai et al., 2022) synthesized Schottky-barrier-free MoO_{3-x} spheres via a facile aerosol-spray method for plasmon-driven photochemical N₂ fixation to NH₃, which features metal-like free charge carriers with the Fermi level above the bottom of the defect band and the defect band located closely to the conduction band (Figures 6A,B). The MoO_{3-x} spheres treated at 350 °C delivered an NH₃ production rate of 435.57 $\mu\text{mol h}^{-1} \text{g}^{-1}$ in 20 vol% methanol aqueous solution under full-spectrum Xe lamp illumination, with an AQE of 1.24% at 808 nm and 1.12% at 1,064 nm and a STA efficiency of 0.057% in pure water under simulated sunlight (Figures 6C,D). Both the measured AQEs and the corresponding wavelengths under NIR region are among the highest values to date. Specifically, the OV_s enable a perfect functional combination of rich active sites for N₂ absorption with broad-spectrum plasmon-induced hot electrons and empty states in the defect band within the MoO_{3-x} spheres, which facilitates the multi-electron reduction-oxidation (red-ox) reactions involved in photocatalytic N₂ reduction. With the Schottky-barrier-free characteristic, the hot electrons moved freely in the defect-induced electronic states and the conduction band reduced those adsorbed and activated N₂ molecules trapped at the OV_s to produce NH₃, as illustrated in Figure 6B. The defective MoO_{3-x} has been exploited as matrix support to valorize rare earth La single-atom catalysts (SACs) via simple Lewis acid-base interactions due to their well-defined surface structure and high degree of anisotropy (Liu et al., 2022). The density functional theory (DFT) calculations revealed that a La single atom theoretically tends to occupy terminal OV_s and coordinate with 2-coordinated O site (Mo–O–Mo, O_{2c}) to form O_{2c}–La–O_{2c} coordination. Moreover, the role of La atoms on O_{2c}–La–O_{2c} site was further clarified, which pumps energetic electrons from their unsaturated 5d orbitals into the $\pi^* 2p$ orbital of the adsorbed N₂, boosting N₂ adsorption and activation. Isolated atomically dispersed La atoms anchored on MoO_{3-x}

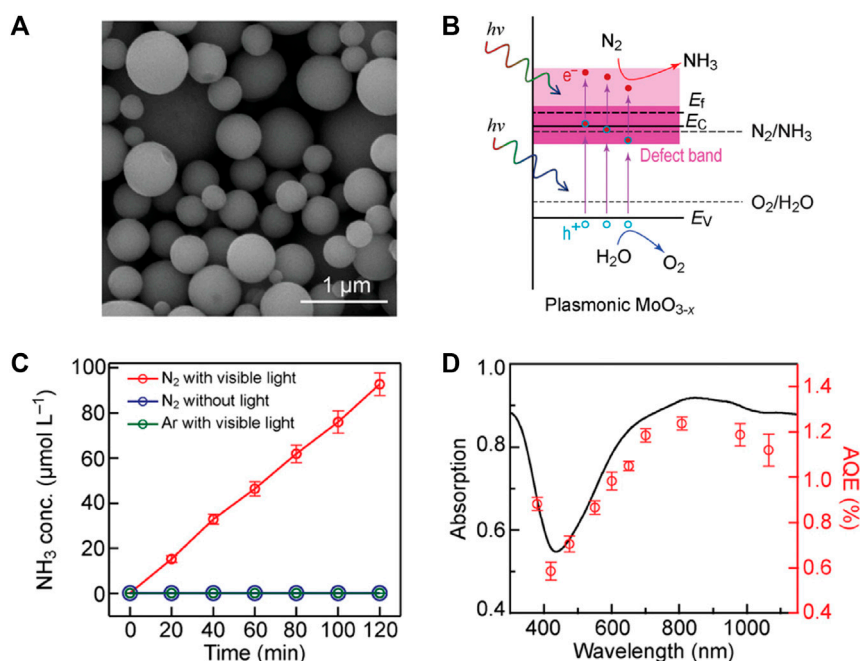


FIGURE 6

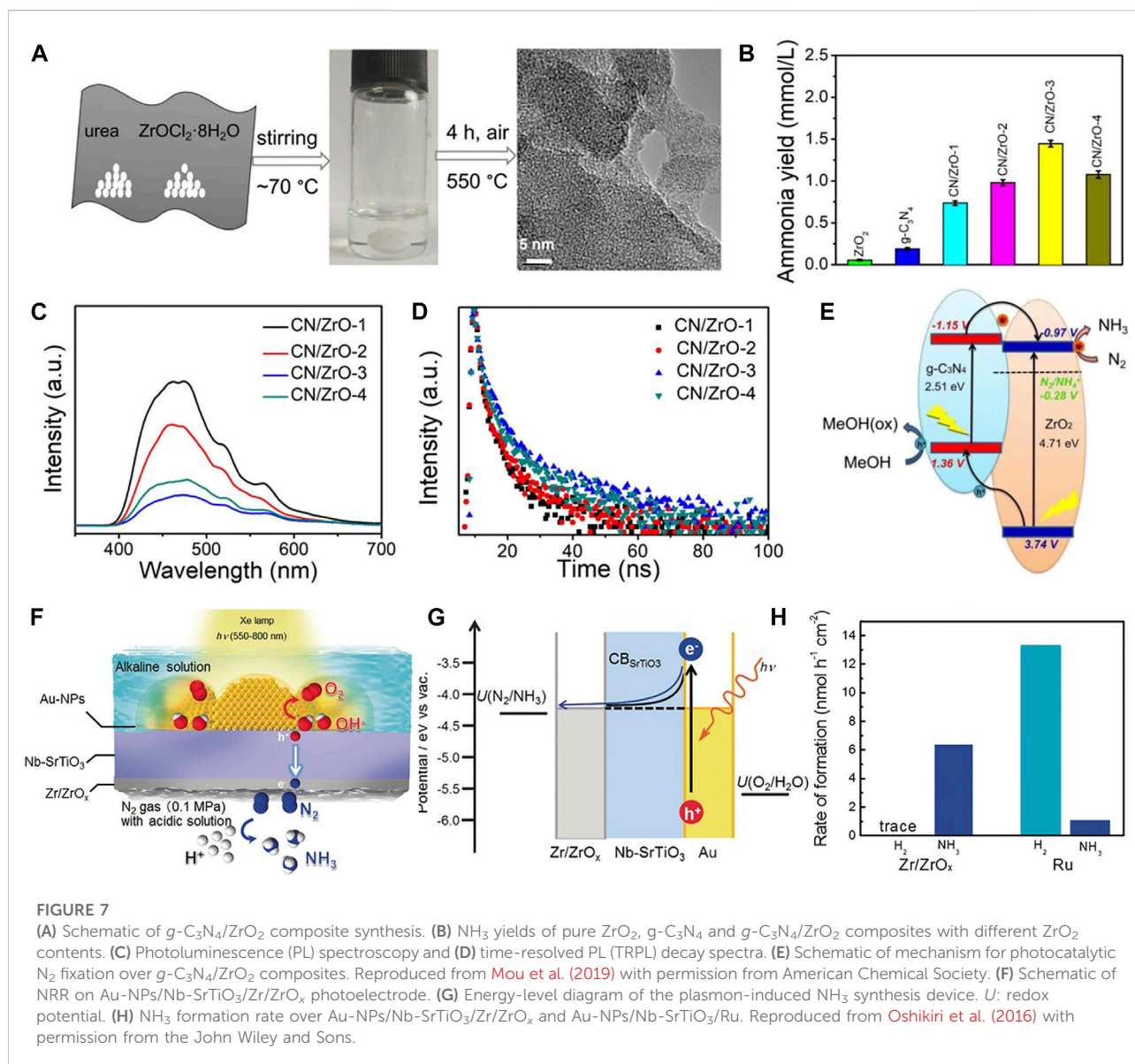
(A) SEM image of the MoO_{3-x} spheres prepared at 350°C. (B) Schematics illustrating the band structures of the plasmonic MoO_{3-x} photocatalyst. (C) Photocatalytic NH₃ production under different conditions and (D) AQE at different wavelengths over the MoO_{3-x} spheres. The light absorption spectrum is plotted for comparison. Reproduced from Bai et al. (2022) with permission from the John Wiley and Sons.

support were observed by the aberration-corrected HAADF-STEM and corresponding rainbow-colored images. The O_{2c}-La-O_{2c} configuration close to two oxygen coordination environment was further verified by X-ray absorption fine structure (XAFS), by which La-La bond cannot be distinctly observed in La/MoO_{3-x}. La/MoO_{3-x} possess an NH₃ production rate of 209.0 μmol h⁻¹ g⁻¹ without any hole scavenger under visible light, nearly 10 times that of the support. Enhanced adsorption of nitrogen and the symmetric alternative pathway following a side-on bridging adsorption configuration have been corroborated by *in situ* FT-IR spectra with the combination of DFT calculations, thus La single atoms substantially amplify the activation of N₂ toward successive hydrogenation, while lowering the formation energy barrier for *NNH → *NHNH process.

3.1.3 Mixed valence cobalt oxides

Cobalt, one of the earth-abundant first row transition metals, has gained tremendous attention for photocatalytic N₂ reduction and conversion due to its eligibility for N₂ dissociation and tunable activity (Chu et al., 2019; Gao et al., 2019), whereas its oxides with mixed-valence states of Co species have poor photostability due to photo-corrosion arising from half oxidation reaction. Combination of CoO_x with 2D carbon material supports have been rationally

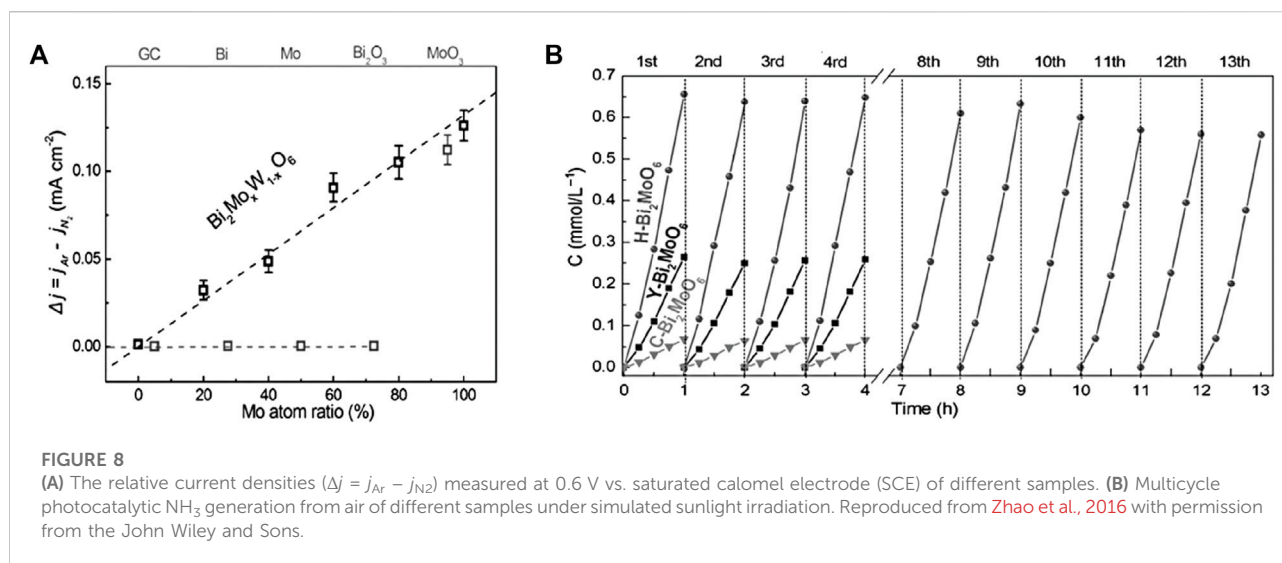
explored to optimize their electronic structures and tailor the active site density (Ahmed et al., 2019; Chu et al., 2019; Zhi-Yuan Wang et al., 2020; Lu et al., 2022). For example, Liu et al. (Yuxin Liu et al., 2021) fabricated CoO_x quantum dots anchored on porous graphdiyne (GDY) (GDY@CoO_xQD) to construct highly efficient and robust catalysts via a facile *in-situ* growth strategy for photocatalytic NRR. The composite photocatalysts featured with superlative activity and stability under various conditions as a result of strong quantum effect and a highly compatible synergistic effect. The three-dimensional configurations of the self-supported GDY@CoO_xQD nanosheet array and uniformly dispersed CoO_xQD on the porous GDY surface were confirmed by SEM and HRTEM, respectively. An average NH₃ yield rate of 46 independent experiments over the GDY@CoO_xQD in 0.1 M Na₂SO₄ aqueous solution (pH 7) up to 19,583 μmol g⁻¹ h⁻¹ was attained, exceeding most reported catalysts. Equally importantly, the six different batches exhibited long-term stability of 10 h with nearly constant NH₃ yield rates. By comparing the Co XPS results of CoO_xQDs on different supported carbon materials and the XANES of GDY@CoO_xQD before and after the reaction, it was concluded that the mixed-valence states of Co (Co³⁺ and Co²⁺) played a pivotal role in enhancing the reaction activity.



As revealed by the DFT calculations, the introduction of GDY and the coexistence of $\text{Co}^{2+}/\text{Co}^{3+}$ could facilitate the electron transfer to form a strong $d\text{-}\pi^*$ (unocc) antibonding orbital interaction above E_F and $d\text{-}\pi^*$ (occ) bonding orbital interaction below E_F . This is beneficial for weakening the bond order and bond strength of $\text{N}\equiv\text{N}$ bond.

Lu et al. (2022) also reported that different cobalt oxide species were responsible for innate active properties, resulting in a synergistic effect on the two half reactions with reduction and oxidation spatially separated at CoO and Co_3O_4 , respectively. The CoO- Co_3O_4 mixed-oxide (CoO dominated) composites on reduced graphene oxide (RGO) manifested a remarkable NH_3 formation efficiency of

$89.1 \mu\text{mol g}^{-1} \text{h}^{-1}$, over 14 times that of each single component. Furthermore, the photoreaction-induced cation oxidation (CoO to Co_3O_4) was reduceable/recyclable by photo-reactivating the non-active Co_3O_4 back to the active CoO at room temperature, thus leading to well-maintained NRR activity after six cycles of operation. As indicated by XANES, XPS, and HRTEM measurements, the compositions were completely transformed into Co_3O_4 during the 8 h of NRR and converted back to dominant CoO after the reactivation. The component CoO in the composite entailed deep-red-light absorbing defect states, which hindered carrier recombination. The band structure of CoO/ Co_3O_4 formed a direct Z-scheme heterojunction, in



which the electrons at the CB of CoO reduced N_2 molecules and the holes at the VB and defect energy levels of Co_3O_4 oxidized H_2O molecules.

3.1.4 Other transition metal oxides

Non-noble metal oxides have gained tremendous expectations as promising alternative NRR catalysts primarily owing to their high chemical stability, ease of synthesis, and minimization of noble metals consumption (Liang Yang et al., 2020; Gao et al., 2022; Zhen Zhao et al., 2022). Only a few metal oxides such as VO_2 (Haiguang Zhang et al., 2019), Ta_2O_5 (Fu et al., 2019), Nb_2O_5 (Han et al., 2018; Kong et al., 2019), NbO_2 (Huang et al., 2019), and ZrO_2 (Xu et al., 2020) have been reported for electrocatalytic NRR. However, these metal oxides suffer from large band gap, poor light absorption capacity toward visible light, low quantum efficiency, and fast recombination rate of photogenerated excitons, restricting their applications in photocatalytic NRR. The insulating material ZrO_2 with a band gap of ~ 5.0 eV (Xu and Schoonen, 2000) can absorb ultrahigh UV light (Gaggero et al., 2021). In addition, it possesses high mechanical strength, non-toxicity, and corrosion resistance. Intensive research has been concentrated on engineering and visible photosensitization of high band gap oxides based on Zr elements of the fourth subgroup (Oshikiri et al., 2016; Caiting Feng et al., 2022). Theoretical calculations revealed that the adsorption energy of N (ΔN^*) is much lower than that of H on the ZrO_2 surface in the aqueous photocatalytic NRR process. This suggests that ZrO_2 preferentially adsorbs N atoms and baffles the reduction of H_2O to H_2 (Skúlason et al., 2012; Tao et al., 2019). Mou et al. (Mou et al., 2019) demonstrated photocatalytic NRR to NH_3 based on amorphous ZrO_2 in association with $g\text{-C}_3\text{N}_4$ as a visible light harvester. The

$g\text{-C}_3\text{N}_4/\text{ZrO}_2$ lamellar composites were constructed by a simple one-step pyrolysis of the deep eutectic solvent $\text{ZrOCl}_2 \cdot 8\text{H}_2\text{O}/\text{urea}$ (Figure 7A). The composites imparted an optimal NH_3 yield rate of $1,446 \mu\text{mol L}^{-1} \text{h}^{-1}$ under visible light illumination, noticeably outperforming each individual counterpart (Figure 7B). The introduction of amorphous ZrO_2 restrained the hydrogen generation and facilitated N_2 reduction. A synergy between amorphous ZrO_2 and $g\text{-C}_3\text{N}_4$ was created contributing to the rapid photoproduced electron-hole pair separation and transfer (Figures 7C–E). ^{15}N isotope analysis verified the contamination-free N_2 photofixation in this work. Similarly, Oshikiri and co-workers designed a multi-component photocatalytic system of Au-NPs/ $\text{Nb-SrTiO}_3/\text{Zr}/\text{ZrO}_x$. The composite was shown to have high affinity to NH_3 . Plasmonic-induced charge separation happened at the Au/ SrTiO_3 interface, thereby allowing occurrence of oxidation reactions on gold nanocrystals and N_2 reduction on the ZrO_x/Zr coating (Figures 7F,G). Figure 7H shows the large interface of ZrO_x/Zr and Nb-SrTiO_3 affording high selectivity and efficiency for NH_3 synthesis owing to the advantage of a stronger binding of ZrO_x/Zr to N atoms relative to H atoms compared to Ru.

3.2 Oxometallate-based photocatalysts

3.2.1 Bismuth-based oxometallates

Among various polyoxometallates, bismuth-based compounds such as Bi_2WO_6 , Bi_2MoO_6 of Aurivillius structure, and BiVO_4 of Scheelite structure, are another class of oxides of interest because of their considerable chemical stability, up-shifted VB resulting from hybridization between Bi 6s and O 2p states and narrow band gaps,

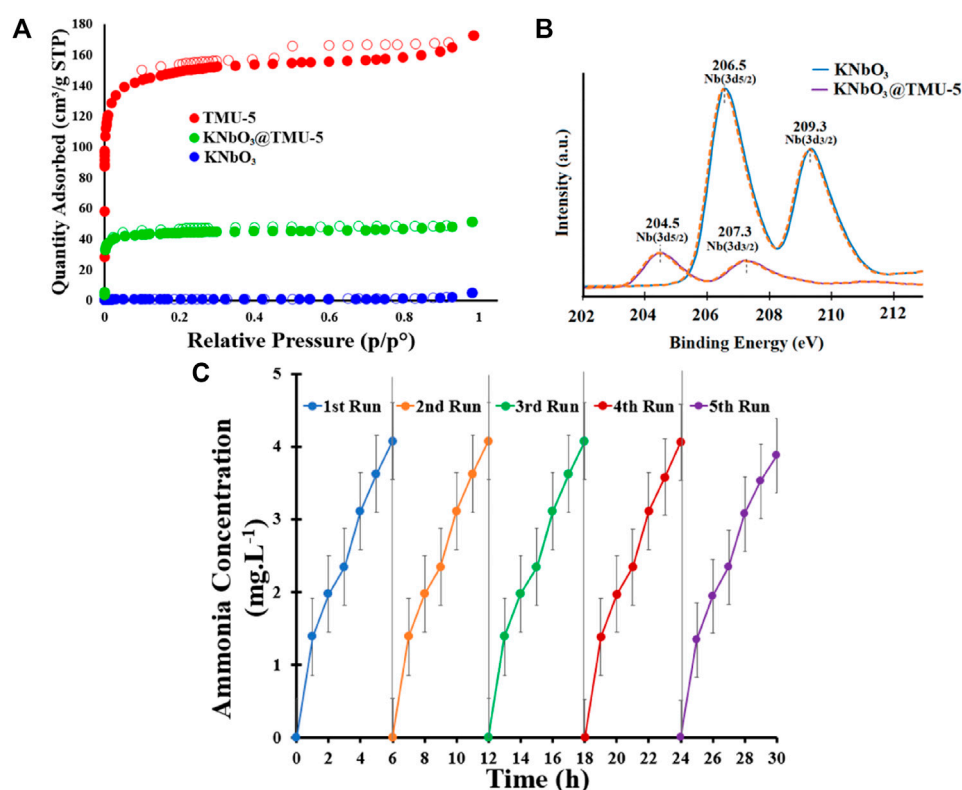


FIGURE 9

(A) N₂ adsorption/desorption isotherms for the KNbO₃@TMU-5 composite and its components. (B) Core-level XPS scans of Nb atoms of KNbO₃ and KNbO₃@TMU-5. (C) NH₃ concentration versus cycling test on KNbO₃@TMU-5. Reproduced from Chamack et al. (2022) with permission from American Chemical Society.

together with their similar layered crystal structures complementary for charge separation and transfer (Zhang et al., 2011; Hao et al., 2020; Wenjie Liu et al., 2020; Utomo et al., 2022). Besides, the hybridization of Bi 6s and O 2p levels accounts for their largely dispersed VB, benefiting the migration of photoinduced holes and thus improving the oxidative reactions (Huang et al., 2020). Bi₂WO₆ consists of accumulated layers of discontinuous [Bi₂O₂]²⁺ and octahedral [WO₄]²⁻ sheets, and Bi₂MoO₆ is composed of [MoO₂]²⁺ layers and [Bi₂O₂]²⁺ layers, while BiVO₄ features with a monoclinic crystal system comprising BiO₈ and VO₄ groups (Cooper et al., 2014; Dai et al., 2016; Zhu et al., 2022). Nevertheless, the potentially high NRR activities are profoundly impeded by their intrinsic shortcomings, such as the photo-corrosion susceptibility for Bi₂WO₆, the limited light absorption in the ultraviolet region for Bi₂MoO₆, the poor water oxidation kinetics and slow mobility of photo-excited charge carriers for BiVO₄ (Girish Kumar and Koteswara Rao, 2015; Xin Liu et al., 2020). Also, they suffer from limited interaction with nitrogen and weak reducing ability as the CB is not sufficiently negative (Hao et al., 2020). To alleviate these

problems, heteroatom doping (Meng et al., 2019; Lin Liu et al., 2021), control of facet exposure (Zhang et al., 2021), defect engineering (Haitao Li et al., 2021; Libo Wang et al., 2021; Cai Feng et al., 2022; Guoan Wang et al., 2022), heterostructure construction (Fei et al., 2019; Shende et al., 2019; Xue et al., 2019; Vesali-Kermani et al., 2020a; Chao Liu et al., 2020; Xuerui Zhang et al., 2022), morphology modification (Ning Zhang et al., 2018; Zhou et al., 2019; Sun et al., 2020; Bao et al., 2021), and regulation of internal electric fields (Lv et al., 2018) have been employed to improve the photocatalytic efficiency of N₂-to-NH₃ conversion.

Hao et al. (2016) doped Bi₂WO₆ with different ratios of Mo, combined with exposed edge unsaturated Mo atoms as the active center for N₂ adsorption, activation and photocatalytic reduction (Figure 8A). Benefiting from exposed active sites, narrower bandgap, and ultrasmall subunits in Bi₂MoO₆ system (H-Bi₂MoO₆), N₂ molecules from air were transformed into NH₃ with an NH₃ evolution rate of 1.3 mmol g⁻¹ h⁻¹ under simulated sunlight illumination, ≈9.5 times higher than bare Bi₂MoO₆ (Figure 8B). In another work, Wang et al.

demonstrated creation of enriched surface OV's via surface-layer Br doping into Bi_2MoO_6 (BMO) which boosted photocatalytic NRR activity owing to enhanced chemisorption of N_2 molecules, enlarged surface area, improved photogenerated charge separation and transfer efficiencies (Lin Wang et al., 2022). The as-made hierarchical BMO microspheres comprised small nanosheets, in which two Br replaced one MoO_4^{2-} with OH coordination balancing the crystal structure. DFT simulation indicated that Br doping promoted the formation of surface OV's at adjacent Bi, thus inducing the fabrication of the surface/internal homojunction to enhance the photogenerated charge separation. Addition of methanol as an electron donor (eliminating holes) further accelerated the generation of NH_3 with a rate of $4.77 \mu\text{mol h}^{-1}$. The BMO showed no decrease in photocatalytic activity after five consecutive runs, manifesting its high stability, while the low stability of BMO80 in pure water indicates photogenerated hole oxidation induced by Br loss and OV reduction. Exposing different crystal facets provides enhanced spatial separation of photogenerated electrons and holes between different crystal facets. For instance, Zhang et al. (Zhang et al., 2021) controlled the growth of (040) and (110) facets of single-crystal BiVO_4 by adjusting pH, and studied the correlation of facet ratios of BiVO_4 crystals with photocatalytic NRR performance. They found that the activity was linearly dependent on the ratio of exposed $S_{(040)}/S_{(110)}$. Separation of space charges was boosted by *in-situ* photo-deposition of Ag NPs and MnO_x selectively loaded on the respective (040) and (110) planes. This enabled creation of a built-in electric field (BIEF) between (040)/(110) facets. Based on the results of active sites and DFT calculations, the cycle of oxygen vacancy- $\text{V}^{4+}/\text{V}^{5+}$ in the (040) facets was inferred to be the exact active site for photocatalytic NH_3 synthesis. V^{4+} was proposed to enhance chemisorption of N_2 while V^{5+} behaved as an electron transfer bridge, and the photogenerated electrons trapped in OV's provided driving force for NRR.

3.2.2 Polymetallic oxides

Most ternary metal oxides first used for photocatalytic nitrogen fixation are titanate or Bi-based oxide systems (Chen et al., 2018; Huang et al., 2020). Higher conversion efficiency for mingled transition metal composite oxides such as Sb_2MoO_6 (Mousavi et al., 2022), SrMoO_4 (Luo et al., 2019), LaCoO_3 (Haiguang Zhang et al., 2019), CoFe_2O_4 (Zheng et al., 2020), $\text{Ni}_3\text{V}_2\text{O}_8$ (Vesali-Kermani et al., 2020b), KNbO_3 (Xing et al., 2019; Xing et al., 2020; Chamack et al., 2022), LiNbO_3 (Xiazhang Li et al., 2020), have been reported compared to corresponding monometallic oxides. Most mixed metal oxides are perovskite oxide compounds with wide bandgaps (Zejian Wang et al., 2021). To overcome the large band gap issue, exotic element doping, noble metal loading, and coupling with other semiconductors can be applied to broaden the light absorption range. For instance, doping of SrMoO_4 with Fe simultaneously introduced defect states and Fe-Mo-O active centers acting as

the active sites for N_2 adsorption, which minimized bandgaps to extend the absorption edge (Luo et al., 2019). As the doping concentration increased, the intrinsic bandgap became narrowed, enabling utilization of visible light. However, the excess doped heteroatoms could act as recombination sites for photoproduced charge carriers, as reflected that the normalized photocurrent transient decreased with that of NH_3 yield at higher doping concentrations.

Niobates have emerged as a research hotspot because of their sufficiently negative CB potential endowing photogenerated electrons with strong reducibility and their spontaneous polarization nature promoting surface charge separation (Chen et al., 2019; Chao Liu et al., 2020; Nunes et al., 2020). Chen et al. (2021a) demonstrated the synergy effect between Bi_2S_3 and $\text{KTa}_{0.75}\text{Nb}_{0.25}\text{O}_3$ (KTN) under simulated sunlight irradiation and the simultaneous action of light and ultrasonic irradiation. The hybrid displayed high piezo-photocatalytic performance with an NH_3 production rate reaching $581 \mu\text{mol L}^{-1} \text{g}^{-1} \text{h}^{-1}$. All samples depended on $\text{KTa}_{0.75}\text{Nb}_{0.25}\text{O}_3$ to provide the photo/piezogenerated electrons for promoting spatial charge separation, which likely played a dominant role for nitrogen fixation. A pioneering study that coupled conventional KNbO_3 with photoactive MOFs was conducted by Chamack et al. (Chamack et al., 2022). Introduction of $([\text{Zn}(\text{OBA}) (\text{BPDH})_{0.5}]_n \cdot 1.5\text{DMF})$ (TMU-5) enhanced the photocatalytic performance owing to the porosity, high surface area, and higher density of negative charges on Nb sites observed by N_2 adsorption/desorption isotherms and XPS scans, respectively (Figures 9A,B). In addition, $\text{KNbO}_3@\text{TMU-5}$ also exhibited good stability during the five-cycle test (Figure 9C).

3.2.3 Polyoxometalates

Polyoxometalates (POMs) are a class of discrete inorganic polynuclear anionic molecular metal-oxo clusters composed of cations and polyoxometalate polyanions linked together by shared oxygen atoms to form closed 3-dimensional frameworks. Corner-sharing metal oxide polyhedra (MO_x , $x = 4, 5$, and 6) are the basic building blocks, where M usually represents V, Nb, Mo, W, and Ta in high oxidation states (Yin et al., 2018; Gu et al., 2021; Horn et al., 2021). Semiconductor-like POMs or their constituent hybrids are considered as prodigious photocatalytic materials for NRR due to the following reasons: 1) the reversible gain or loss of a specific number of electrons and diverse active sites furnishing the reversible redox capability and modifiable stability; 2) the preponderance of POMs as an electron "reservoir"; 3) the well-defined HOMO-LUMO gap contributing to oxygen (ligand)-to-metal charge transfer; 4) definite particle sizes and dimensions together with the maintenance of structural intactness (Xiao-Hong Li et al., 2019; Xin Wang et al., 2020; Gu et al., 2021; Horn et al., 2021; Yuan Feng et al., 2022). Xiao et al. (Xiao et al., 2018) successfully covalently bonded the polyacid cluster

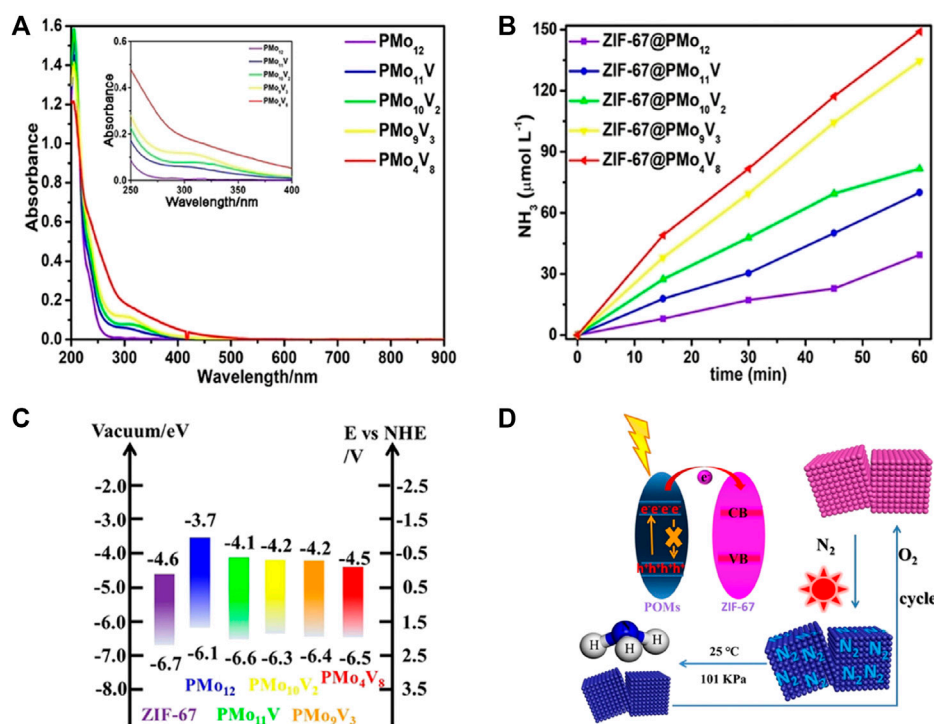


FIGURE 10

(A) UV/Vis absorption spectra of various V-substituted POMs. (B) NH_3 yield as a function of reaction time on various ZIF-67/POMs hybrids. (C) Energy levels and (D) electron-transfer mechanism for ZIF-67/POMs hybrids. Reproduced from Hongda Li et al. (2020) with permission from the John Wiley and Sons.

$[\text{H}_4\text{SiO}_4\text{W}_{12}]$ (SiW_{12}) to KOH-modified carbonitride graphite nanosheets through a phosphate bridging strategy. This allowed a rapid transfer of photogenerated electrons. The polyacid anion in POMs was suggested to function as an effective binder and electron transport chain, enhancing the interaction with the carrier and electron transport. Cyclic voltammograms of 30- $\text{SiW}_{12}/\text{K-C}_3\text{N}_4$ showed that a reversible two-electron redox reaction occurred at -0.06 V and -0.36 V, implying that 30- $\text{SiW}_{12}/\text{K-C}_3\text{N}_4$ could act as good containers of electrons and protons to provide protons for the N_2 reduction. Integration of porous zeolitic imidazolate framework-67 (ZIF-67) (to enhance N_2 adsorption) with various TM-substituted POMs ($\text{PMo}_{12-x}\text{V}_x$, $x = 1, 2, 3, 8$) (to supply multiple electrons), was investigated by Li et al. (Xiao-Hong Li et al., 2020). The light absorption of POMs was intensified to red shift by introducing V into POMs caused by the difference in the number of V hyperchromic effects (Figure 10A). The photocatalytic N_2 reduction activity increased with increasing the number of V atoms with stronger redox ability than Mo (Figure 10B). The ZIF-67/POM composites attained higher catalytic performance than that of ZIF and POMs alone with the highest N_2 fixation efficiency reaching $149.0 \mu\text{mol L}^{-1} \text{h}^{-1}$ and a STA efficiency of up to 0.032% for ZIF-67/ PMo_8V_4 . POMs not only improved the

utilization of light energy but also easily excited electrons under light conditions to participate in the catalytic process (Figure 10C). Reduced POMs could be regenerated to form oxidized POMs in the presence of oxidants (such as O_2), enabling a complete self-healing and circulatory system (Figure 10D).

Given the solubility of POM, there are recycling problems with environmental pollution. To overcome this issue, some strategies have been developed to reinforce its stability during NRR, including adhesive (Tianyu Wang et al., 2020), coupling with MOFs (Tianyu Wang et al., 2021), and interfacial interaction (Yuan Feng et al., 2022). For example, Su et al. (2022) fabricated SiW_{12} encapsulated Cr-MOFs (MIL-101(Cr)) hybrids, which were applied to N_2 photocatalysis affording an NH_3 yield rate of $75.56 \mu\text{mol h}^{-1} \text{g}^{-1}$, about 10 times that of $\text{Na}_4\text{SiW}_{12}\text{O}_{40}$. SiW_{12} of polyoxometalates was supposed to be the active center, which could be regulated to locate in different cavities of MIL-101(Cr) by controlling the synthesis method. This enhanced the separation efficiency of photoexcited electron-hole pairs. The N_2 reduction activity and photocatalyst structure did not change much after 5 cycles. The cooperative effect between the porous MIL-101(Cr) and SiW_{12} was hypothesized to boost the nitrogen fixation efficiency.

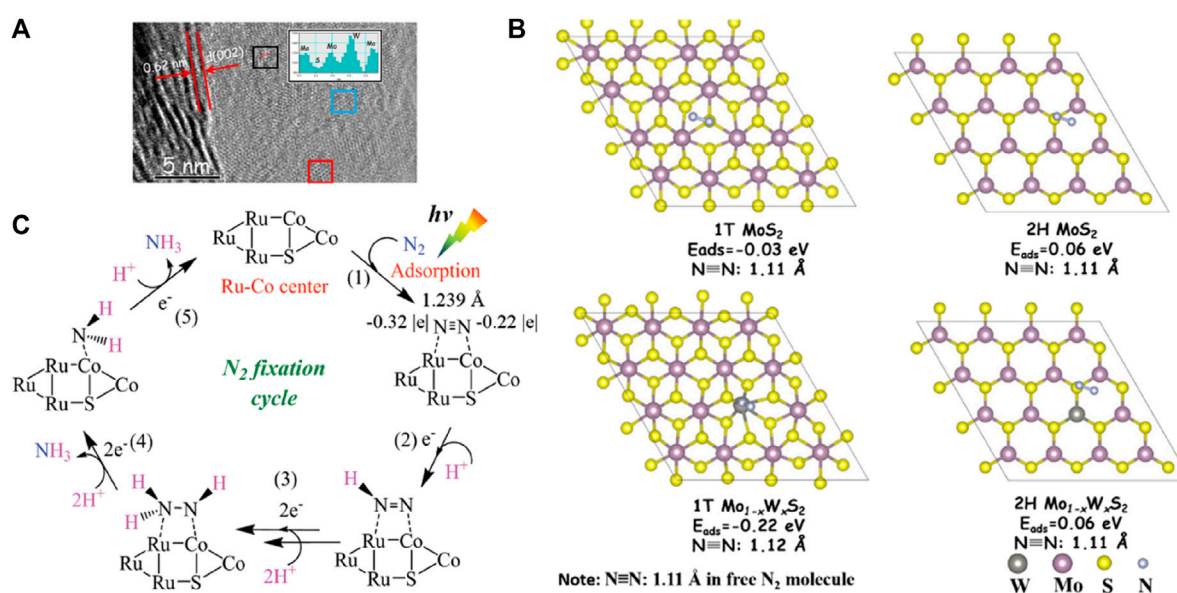


FIGURE 11

(A) HRTEM image of MWS-2 nanosheets. The red and blue squares represent the 2H and 1T structures, respectively; (B) Different adsorption energies of N_2 molecules on 1T MoS_2 , 1T $Mo_{1-x}W_xS_2$, 2H MoS_2 , and 2H $Mo_{1-x}W_xS_2$. Reproduced from Qin et al. (2021) with permission from American Chemical Society. (C) Proposed NRR reaction schemes on Ru-SV-CoS/CN. Reproduced from Yuan et al. (2020) with permission from the John Wiley and Sons.

3.3 Transition metal chalcogenides

Transition metal chalcogenides (TMDs) have attracted heightened research interest for photocatalytic NRR primarily owing to their outstanding optical properties (wide spectral response range), relative nontoxicity, liquid media stability, superior electronic mobility, and intrinsic catalytic activity (Sun et al., 2018; Lei et al., 2020; Shen et al., 2020; Shen et al., 2021). Sun et al. (2017) presented the trion-induced NRR on ultrathin sulfur-vacancies (SVs)-rich 2D MoS_2 , where photoexcited electron-hole pairs combined the doping-induced charges to form trions, bound multiple electrons and located around the Mo sites in MoS_2 , which lowered thermodynamic barriers and favored the simultaneous six-electron transfer to produce NH_3 . N_2 molecules were prone to be absorbed at the SV sites and activated by the electron-rich species to form NH_3 over the SV-tuned ultrathin MoS_2 . A quasi-stable NH_3 evolution rate of $325 \mu\text{mol g}^{-1} \text{h}^{-1}$ was attained without using any sacrificial agent or cocatalyst. Qin and coworkers employed a simple one-step hydrothermal method to prepare ultrathin alloyed $Mo_{1-x}W_xS_2$ nanosheets with tunable hexagonal (2H)/trigonal (1T) phase ratios using $Na_2MoO_4 \cdot 2H_2O$, $Na_2WO_4 \cdot 2H_2O$, and thiourea as Mo, W, and S precursors, respectively. Phase engineering and appropriate W doping markedly boosted the N_2 photoreduction efficiency. As shown in Figures 11A, the alloys maintained a layer structure during the hydrothermal

process, and the 1T, 2H, and polymorph structural domains were also observed in the alloyed $Mo_{1-x}W_xS_2$ nanosheets. The alloyed $Mo_{1-x}W_xS_2$ nanosheets with a 1T phase concentration of 33.6% and Mo/W of 0.68:0.32 (MWS-2) were found to reach the maximal N_2 fixation rate of about $111 \mu\text{mol g}^{-1} \text{h}^{-1}$ under visible light, 3.7 (or 3)-fold higher than that of pristine MoS_2 (or WS_2). DFT calculations revealed that N_2 had the highest negative adsorption energy on 1T $Mo_{1-x}W_xS_2$ compared to that on 1T MoS_2 , 2H MoS_2 , and 2H $Mo_{1-x}W_xS_2$ (Figure 11B). Meanwhile, *in situ* N_2 absorption XANES techniques interpreted the energy shift on the peaks of the Mo *K*-edge as the ascending valence states of Mo, and that of W *L*-edge as a higher electron density state in W 5*d* orbitals, resulting in the migration of many electrons from Mo to W. Based on theoretical calculations and photochemical experiments, W doping and the 2H/1T structure were supposed to synergistically enhance the N_2 adsorption. Binary and ternary metal sulfide-based composites were shown to facilitate photocatalytic NH_3 synthesis via intimate heterointerfaces to diminish charge recombination (Dong Liu et al., 2021). Reported systems in this regard include $MoS_2/C\text{-}ZnO$ (Xing et al., 2018), $C_3N_4/MoS_2/Mn_3O_4$ (Gui Li et al., 2021), $WS_2@TiO_2$ (Shi et al., 2020b), and $MoS_2/MgIn_2S_4$ (Swain et al., 2020).

Sparked by the nitrogenase MoFe-based protein, the reduction of N_2 on Fe single-atom-modified MoS_2 nanosheet photocatalyst was first theoretically predicted by Azofra et al.

(Azofra et al., 2017). Following this, various photocatalyst systems entailing Fe supported on MoS₂ have emerged. As an example, Zheng et al. (Zheng et al., 2021) developed Fe-decorated 2D MoS₂ photocatalysts [Fe-S₂-Mo] mimicking FeMoco in nature for NH₃ synthesis. A solar-to-NH₃ energy-conversion efficiency of 0.24% at 270°C was achieved, representing the highest efficiency among all reported photocatalytic systems thus far. The HAADF-STEM images and simulation results jointly supported that Fe atoms were favorably situated on the atop sites of Mo rather than substituted Mo sites to form inorganic Fe-S₂-Mo motifs analogous [Fe-S₂-Mo] unit in FeMoco. Theoretical calculations suggested that the HOMO and LUMO orbitals were concentrated on the edge of single-layered MoS₂ (sMoS₂) with relatively low electron delocalization, indicating the active edge sites of sMoS₂. Fe doping distinctly improved their LUMO orbital delocalization degree. Further *in situ* attenuated total reflection FTIR and the energy plots revealed that the NRR on Fe₁ over [Fe-S₂-Mo] followed an alternating pathway, showing similarity for both non-biological and biological processes regarding NRR mechanism. Excited electrons could be transferred from the VB to the CB of sMoS₂ via the conductive Fe-S₂-Mo motifs and reside on the Fe atom during the photoexcitation process to enter into the anti-bonding orbital of an adsorbed N₂ molecule, which thus facilitated the hydrogenation reaction of N₂ for ammonia production. Similarly, a biomimetic “MoFe cofactor” (the Fe³⁺/Fe²⁺ and Mo⁶⁺/Mo⁴⁺ redox couples) was introduced in MoTe₂ nanosheets to facilitate the transport and separation of photo-generated charge carriers by one-electron and two-electron redox reactions with 15 times longer photocarrier lifetime after Fe doping and about 11 times higher NH₃ production rate of Fe-doped MoTe₂ than that of pure MoTe₂ (Hongda Li et al., 2020). An enzymatic-analogous N₂-fixation mechanism was also demonstrated on a bimetallic Ru-Co center at Ru/CoS_x interface on g-C₃N₄ sheets by Ru deposition near CoS_x induced by S vacancies (Figure 11C). The side-on bridging of N₂ on under-coordinated Ru-Co center at Ru/CoS_x interface led to high polarization and strong activation of N₂, resulting in an AQE of 1.28% at 400 nm and a STA efficiency of 0.042% for NH₃ production in pure water.

3.4 Biomimetic photocatalysts

Biological nitrogen fixation has advantages of low energy consumption and high NH₃ yield, while multiple adenosine 5'-triphosphate (ATP) hydrolysis electron transfer steps are required per reduced N₂ molecule, resulting in modest overall reaction kinetics and slow NH₃ synthesis rate. Under such circumstance, exploration of biomimetic systems of molecular analogs to simulate and optimize this process has gained a tremendous interest in scientific community (Meng et al., 2021). Taking advantage of iron molybdenum sulfide

chalcogels, Kanatzidis et al. (Banerjee et al., 2015) proposed a nitrogen-fixing biomimetic system by replacing MoFe-based proteins, which is the active site of nitrogenase, with Fe₂Mo₆S₈ chalcogel interconnected through [Sn₂S₆]⁴⁻ ligands (Figure 12A). Featuring strong visible-light-absorbing, high spatial density of active sites, and multielectron transformations, the chalcogel-based amorphous framework could effectively convert N₂ to NH₃ in aqueous media under light illumination. Although its turnover number (TON) was not appealing, this study proved that cluster compounds analogous to nitrogenase can confer cogent catalysis and better stability than nitrogenase. Brown et al. (Brown et al., 2016) employed CdS to photosensitize MoFe proteins by harvesting light energy to replace ATP hydrolysis to drive the enzymatic N₂ fixation, with peak NH₃ production rates of 315 ± 55 nmol NH₃ mg_(MoFe protein)⁻¹ min⁻¹ at a TOF of 75 min⁻¹ (Figures 12B,C). N₂ reduction persisted for up to 5 h under constant illumination with a TON of 1.1 × 10⁴ mol NH₃ mol_(MoFe protein)⁻¹. This study indicates that bio-nanocomposites can function as photocatalysts for solar-powered generation of NH₃ with TOF comparable to nitrogenase. Inspired by the above works, Liu et al. (Liu et al., 2016) designed a redox-active FeMoS-FeS-SnS chalcogel system consisting of Fe₂Mo₆S₈(SPh)₃ and Fe₃S₄ biomimetic clusters linked by Sn₂S₆ to reduce N₂ to NH₃ (Figure 12D). All FeMoS-M-SnS chalcogels constructed by replacing Fe₄S₄ clusters with redox-inert ions Sb³⁺, Sn⁴⁺, Zn²⁺, exhibited effective NRR performance. FeMoS with FeS clusters was observed to strengthen NH₃ production over FeMoS alone and Fe₄S₄-only chalcogel (FeS-SnS) and provided higher efficiency than that of [Mo₂Fe₆S₈(SPh)₃]-containing chalcogels. Therefore, Fe was believed to be more conducive than Mo for N₂ binding (Figure 12E). The active sites in the Fe-containing sulfide clusters were considered to differ (i.e., based mainly on Fe) from that in the nitrogenase enzymes (based on both Mo and Fe). Quantitative isotope labeling and *in situ* DRIFTS corroborated the origin of detected NH₃ from N₂ (Figure 12F).

3.5 Metal-organic frameworks (MOFs)

MOFs are micro-mesoporous hybrid materials composed of metal ion nodes connected with organic linkers together or clusters and organic frameworks. Similar excitation characteristics of electron-hole pairs endow MOFs and their derivatives with intriguing semiconductor-like properties in various photochemical reactions (Hu et al., 2022). High microporosity and diverse functionalities enable the introduction of defined and highly exposed metal nodes onto the larger surfaces to promote or catalyze targeted reactions (Hao et al., 2021; Lin Wang et al., 2022). Especially, these exposed coordinatively unsaturated metal sites not only contribute to higher catalytic activities, but also behave as Lewis acid sites to

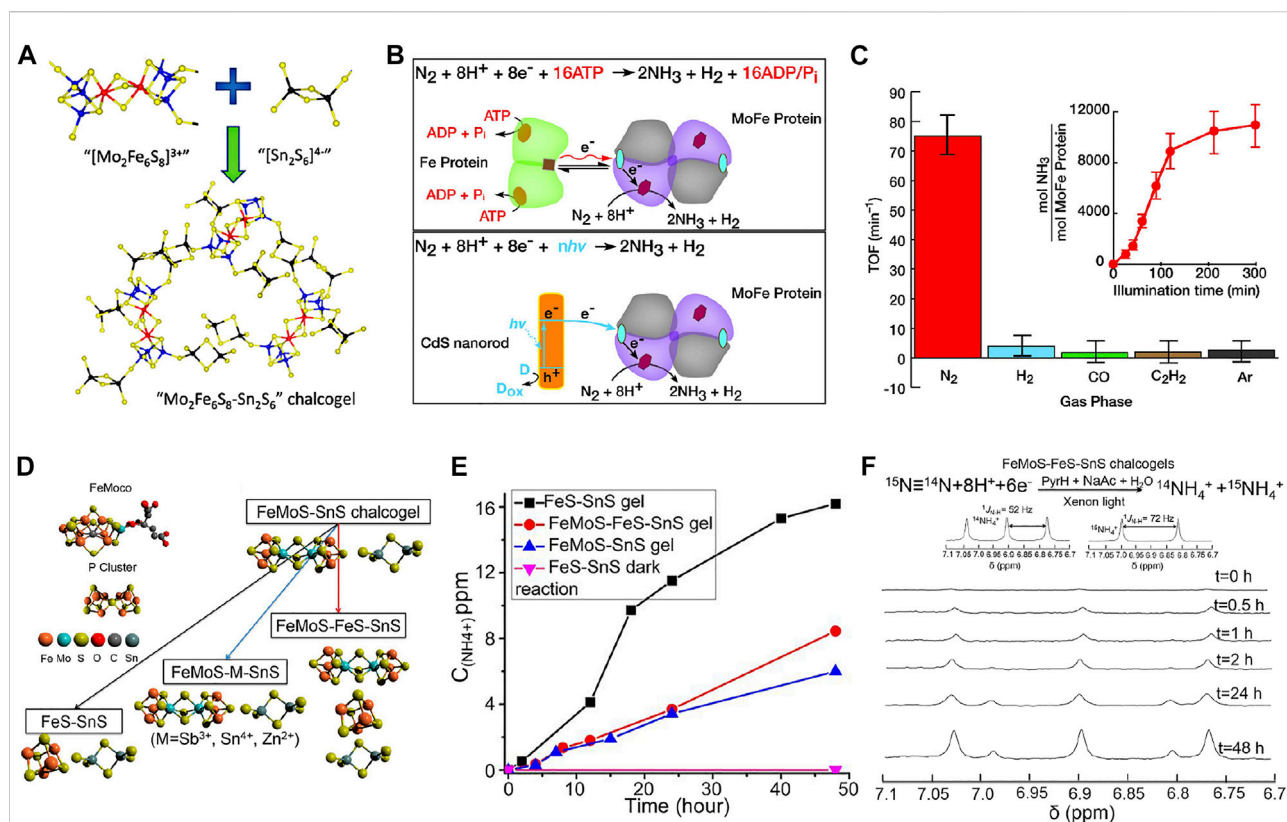
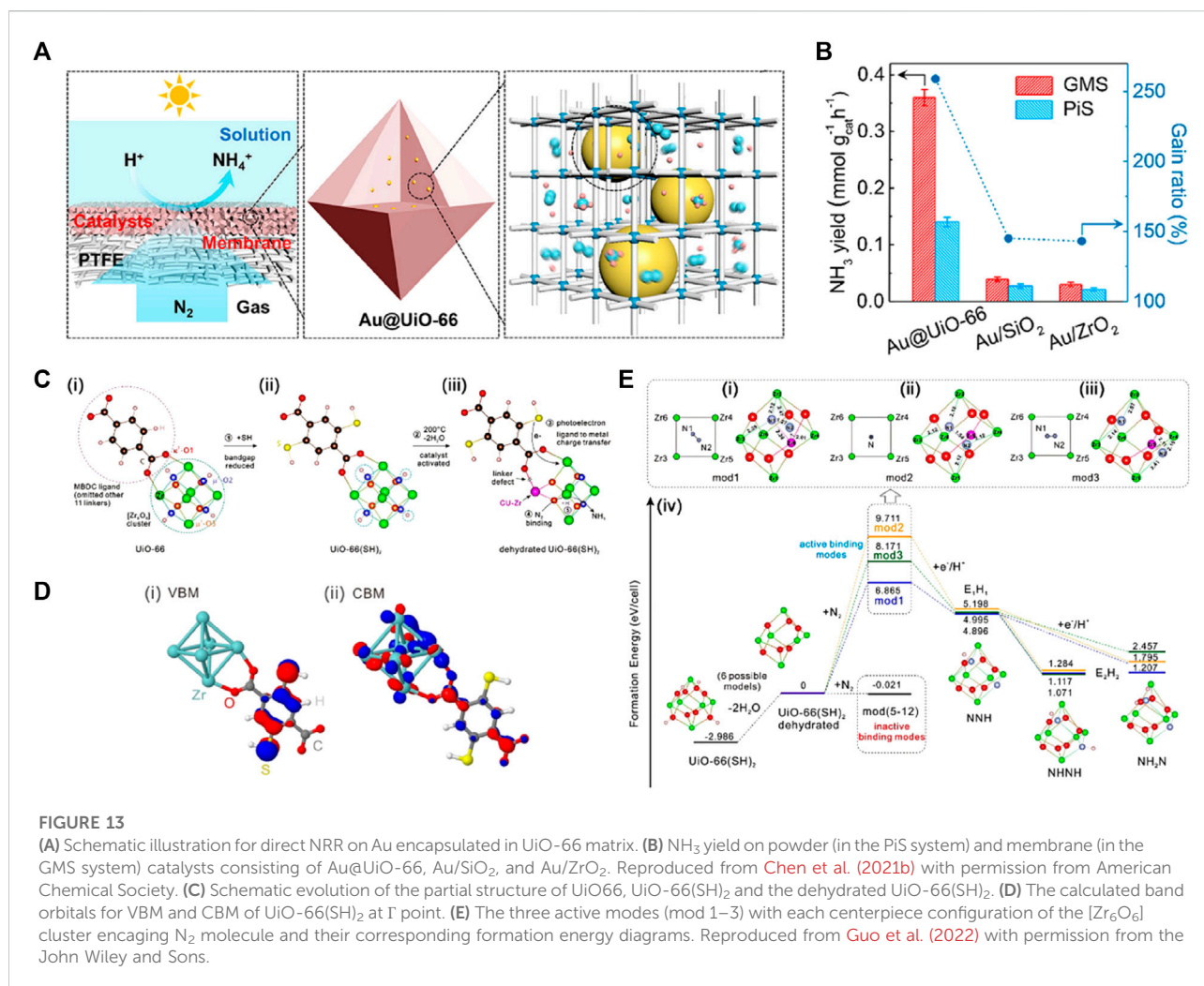


FIGURE 12

(A) Schematic of synthesis of Mo₂Fe₆S₈-Sn₂S₆ biomimetic chalcogel (FeMoS-chalcogel) (Mo in blue; Fe in red; S in yellow; Sn in black). Reproduced from Banerjee et al. (2015) with permission from American Chemical Society. (B) Reaction scheme for photocatalytic NRR to NH₃ by nitrogenase (top) and the CdS:MoFe protein biohybrids (below). (C) Photocatalytic NRR to NH₃ on CdS:MoFe protein biohybrids under a 100% N₂ atmosphere, 10% of either H₂, CO, or C₂H₂ in a bulk phase of 90% N₂. Reproduced from Brown et al. (2016) with permission from American Association for the Advancement of Science. (D) Model structures of the FeMo cofactor and P cluster, and the synthetic routes towards the assembly of different chalcogels. (E) Comparisons of photocatalytic NRR performance for different biomimetic chalcogels. (F) Isotope labeling experiment results detected by NMR. Reproduced from Liu et al. (2016) with permission from National Academy of Sciences of the United States of America.

withdraw *p* electrons from N₂ molecules and weaken the N≡N triple-bonds, accounting for photochemical N₂ reduction (Fu et al., 2022). Chen et al. (2021b) exploited gas-permeable MOF substrates (i.e., UiO-66) to not only serve as a stable matrix to confine the surface-clean gold nanoparticles (AuNPs) with high dispersity, but also ensure the accessibility of these AuNPs to both N₂ molecules and (hydrated) protons (Figure 13A), enabling direct plasmonic NRR with high efficiency. The porosity of the MOF matrix facilitated mass transport of reactants and products, promoting the total reaction rate (Chen et al., 2022; Guanhua Zhang et al., 2022). Accordingly, the NH₃ evolution rates on porous Au@MOFs particles were superior to those of nonporous particles at the specially designed gas-membrane-solution (GMS) reaction interface, and the GMS system was better than the powder-in-solution (PiS) system (Figure 13B). In another work, Guo et al. (Guo et al., 2022) investigated the [Zr₆O₆] cluster effect and the leading role of photoelectrons over the protonation of nitrogen by using an

N-free dehydrated Zr-based MOF, UiO-66(SH)₂ (Figure 13C). The UV/Vis diffuse reflectance spectrum combined with theory studies suggested that the introduction of thiol groups (-SH) caused an absorption edge of UiO-66(SH)₂ deep into the visible region. The hopping process of the photoelectron from VB to the unoccupied Zr-4d orbitals is dominated by the ligand-to-metal charge transfer (LMCT) (Figure 13D). The dehydration opened a "gate" for the entry of N₂ molecules into the [Zr₆O₆] cluster, of which three active cage modes strongly bound with N₂ molecules and drive the cleavage of N≡N bond by the photoelectrons (Figure 13E). However, most MOF-related photocatalysts focused either on the coordination environment around the metal nodes, or the role of photosensitive ligands or single transition metals (Hu et al., 2022). Gao and co-authors presented photo-excited cluster defects and linker defects to revamp the photocatalytic NRR performance of UiO-66 (Gao et al., 2021). They show the performance under alternate UV-Vis and visible light irradiation and after subsequent post-



synthetic ligand exchange (PSE) process. Compared to UV-Vis light, the performance of the second test under visible light did not improve. After the PSE process that repaired linker defects instead of cluster defects, activity was restored under UV-Vis light. This demonstrated that photo-induced defects can only be created by UV light, where linker defects played a critical role in improving the performance due to the Zr nodes with unsaturated coordination induced by linker defects being more conducive to photo-driven NH_3 synthesis.

Designing and constructing photocatalysts with bimetallic active centers is an effective way for nitrogen photofixation (Zhen Zhao et al., 2022). An et al. (An et al., 2021) designed a series of modularized UiO-66-based MOFs, U(Zr-Hf)-X, with bimetallic Zr-Hf nodes and functionalized ligands, and demonstrated a tandem ligand-to-metal-to-metal electron transfer (LMMET) pathway. By independently manipulating the Zr/Hf molar ratio and substituent group of TPA, the optimal U (0.5Hf)-2SH (metal nodes: 0.5Zr: 0.5Hf; linkers:

TPA-2SH) yielded an NH_3 production rate up to $116.1 \mu\text{mol h}^{-1} \text{g}^{-1}$ under visible light. This was attributed to the broadening of the absorption spectrum to visible light by -2SH modification according to combined experiment-theory results. Although these results suggested that the synergistic effect of bimetallic Zr-Hf nodes was favorable for NRR performance, it is uncertain whether the TPA-2SH ligand contributed to charge transfer mechanism. The proposed NRR pathway of U (0.5Hf)-2SH was explored. The one-step two-photon excitation path strides across the uphill process of the electron transfer from TPA-2SH ligands to metal nodes in UiO-66. The Hf species served as an electron buffer tank to optimize the electron transfer, while the Zr species acted as the catalytic active site due to the difference in electrode potentials between Zr-O and Hf-O clusters. Meanwhile, Zr-dominated π -backbonding mechanism weakened the $\text{N}\equiv\text{N}$ bond in absorbed N_2 molecules via the electron transfer synergy to generate NH_3 . Nonetheless, research on photocatalytic NRR using MOFs is relatively rare, the existing MOF-based photocatalysts have still

an exemplary significance regarding constructing other visible-light-driven MOF-based NRR photocatalysts.

4 Conclusions and future remarks

The photocatalytic NRR is an appealing alternative to the current industrial thermocatalytic Haber-Bosch process for NH_3 production. It only requires solar energy and water, rendering the process environmentally friendly and highly sustainable. With a general awareness of emphasizing on green chemistry and sustainable development, this field is bound to have a significant and far-reaching impact on how humans understand and engage in the nitrogen cycle. Despite recent progresses that have been achieved in the field of photocatalytic NH_3 synthesis, it is still in its infancy. A comparable conversion efficiency to the century-old Haber-Bosch process remains unsolved, especially on how to accentuate N_2 activation and accelerate the kinetics of electron transfer to N_2 . Continuous efforts in the design and development of nontoxic, efficient, stable and low-cost catalysts minimizing the consumption of noble metals have obtained some positive advancements. Tungsten and related metal-based materials have shown enormous accolades as photocatalysts for NRR. However, there still remain many challenges to be addressed as follows:

- 1) The intrinsic mechanism and kinetic control of nitrogen fixation are still ambiguous and complex, warranting further investigations. Because of the complex multi-electron reactions involved and the presence of various intermediate species, combination of multiple accurate analytical methods and advanced characterization techniques are required. It is essential to develop *in-situ* techniques to study the adsorption structure of N_2 and key intermediates on the surface of catalytic materials, providing useful information on the catalytic active center and its dynamic evolution during the reaction process.
- 2) Various environmental factors (such as cation effect, electric field effect, pH, hydrophobicity, and actual active site, *etc.*) (Zhou et al., 2022) can profoundly affect the photocatalytic NRR process. It is thus necessary to explore and clarify the synergistic effect among the semiconductor photocatalysts and mixed solvent systems to further reveal the multi-effects of collaborative catalytic mechanism.
- 3) Equally importantly, the cooperative mechanisms among heterostructure, element doping and interaction between components and role of each individual strategy in N_2 photocatalysis remain to be elucidated. It is necessary to comprehensively use various design and control strategies of catalysts to combine element doping, defect construction, and structural design to increase active sites, suppress the recombination of photogenerated carriers, and enhance the adsorption and activation of nitrogen molecules in the NRR process.
- 4) Efficient utilization of solar energy is the focus of interest in photocatalysis. However, the utilization of light in the NIR and the far-infrared region above 1,000 nm for NRR photocatalysis is poor. To facilitate the practical utilization of NRR photocatalysis, the design of suitable photocatalysts for wide-range light harvest from ultraviolet to near-infrared regions is important. This may be realized by integration with NIR and even far-infrared responsive materials such as dye molecules and black phosphorus (Zhang et al., 2017), narrow band gap NIR harvesters as well as materials having surface plasmon resonance effect.
- 5) The extensive use of sacrificial agents leads to additional costs, which deteriorate the overall affordability of the environment. Therefore, some cheap sacrificial agents at this stage, such as starch, biomass, plastics, wastewater, *etc.*, could also be developed as sacrificial agents to further reduce the cost of large-scale application of N_2 photocatalysis.
- 6) The attained SCE of N_2 photoreduction is still less than 1%, far below the minimum standard of 10% needed to realize industrialization, and the stability during the reaction process is however still much below the requirements for long-term practical applications.
- 7) The photostability of semiconductor catalysts is another adverse issue that deserves much attention. The surfaces of many *n*-type and *p*-type semiconductors (such as sulphides) are susceptible to decomposition by photogenerated holes or electrons, decreasing the lifetimes of the photocatalysts. To address this issue, strategies such as coating with a second phase, surface passivation and functionalization and incorporation with cocatalysts can be employed (Sun et al., 2018).

To date, major endeavors in materials engineering toward N_2 photocatalysis have been made on traditional semiconductors. Some emerging photocatalytic materials such as MOFs and covalent organic frameworks (COFs) have not been fully explored for photocatalytic N_2 reduction. Meanwhile, the design of cation defects and further combined defects and investigation of their roles in MOFs in N_2 reduction are rarely conducted, which deserves further studies. To synergistically promote N_2 photocatalysis, integration of multiple design strategies (e.g., defect engineering and other modification strategies such as creation of Z-scheme heterostructures to separate ammonia production and water oxidation sites in space) is preferred. Additionally, combination of material engineering and external fields (e.g., microwaves, mechanical stress, temperature gradient, electric field, magnetic field, and coupled fields) is another promising strategy to further boost photocatalytic N_2 reduction reactions.

Current research focuses mainly on the microstructure design of materials and the improvement of photocatalytic performance, while less attention was paid on the development of photocatalytic devices suitable for future applications and reliable

cost accounting. The bridge between laboratory research and practical application development is crucial. To better understand the conditions required to reach practical industrial applications, we should compare photocatalytic NRR with current industrial Haber-Bosch reactions from various perspectives, such as reaction temperature and pressure, ammonia/nitrate output, pollution, etc. In an actual photoreactor, N_2 would be separated from the air using standard cryogenic separation or membrane processes and would need to be recovered and recycled for cost reasons. Current Photocatalytic NRR is more carried out in aqueous solutions, which means that liquid-phase products can be directly obtained to produce liquid fertilizers that can be directly used and sold, but the subsequent separation of catalysts will further increase the energy cost of the entire process. Even if the final product is anhydrous ammonia for fuel feedstock, the purification of low concentrations of NH_3 from the N_2 stream adds to the energy-consuming step. Therefore, how to achieve higher product concentrations in flowing gas setups is an important target of this particular approach. From another point of view, this idea guides us to no longer pay attention to the NH_3 yield as an indicator, but to focus on the integration of upstream synthesis and downstream applications to reduce energy consumption and pollution in the entire production process, to achieve the final goal of “carbon neutrality” faster.

Author contributions

All authors listed have made a substantial, direct, and intellectual contribution to the work and approved it for publication.

References

- Ahmed, M. I., Chen, S., Ren, W., Chen, X., and Zhao, C. (2019). Synergistic bimetallic $CoFe_2O_4$ clusters supported on graphene for ambient electrocatalytic reduction of nitrogen to ammonia. *Chem. Commun.* 55 (81), 12184–12187. doi:10.1039/C9CC05684J
- An, K., Ren, H., Yang, D., Zhao, Z., Gao, Y., Chen, Y., et al. (2021). Nitrogenase-inspired bimetallic metal organic frameworks for visible-light-driven nitrogen fixation. *Appl. Catal. B Environ.* 292, 120167. doi:10.1016/j.apcatb.2021.120167
- Andersen, S. Z., Colic, V., Yang, S., Schwalbe, J. A., Nielander, A. C., McEnaney, J. M., et al. (2019). A rigorous electrochemical ammonia synthesis protocol with quantitative isotope measurements. *Nature* 570 (7762), 504–508. doi:10.1038/s41586-019-1260-x
- Azofra, L. M., Sun, C., Cavallo, L., and MacFarlane, D. R. (2017). Feasibility of N_2 binding and reduction to ammonia on Fe-deposited MoS_2 2D sheets: A DFT study. *Chem. Eur. J.* 23 (34), 8275–8279. doi:10.1002/chem.201701113
- Bai, J., Chen, X., Xi, Z. Y., Wang, X., Li, Q., Hu, S. Z., et al. (2017). Influence of solvothermal post-treatment on photochemical nitrogen conversion to ammonia with $g-C_3N_4$ Catalyst. *Acta Phys.-Chim. Sin.* 33 (3), 611–619. doi:10.3866/pku.Whxb201611102
- Bai, H., Lam, S. H., Yang, J., Cheng, X., Li, S., Jiang, R., et al. (2022). A Schottky-barrier-free plasmonic semiconductor photocatalyst for nitrogen fixation in a “one-stone-two-birds” manner. *Adv. Mat.* 34 (2), 2104226. doi:10.1002/adma.202104226
- Banerjee, A., Yuhas, B. D., Margulies, E. A., Zhang, Y., Shim, Y., Wasielewski, M. R., et al. (2015). Photochemical nitrogen conversion to ammonia in ambient conditions with $FeMoS$ -chalcogenides. *J. Am. Chem. Soc.* 137 (5), 2030–2034. doi:10.1021/ja512491v
- Bao, L., Yuan, Y.-j., Zhang, H., Zhang, X., and Xu, G. (2021). Understanding the hierarchical behavior of Bi_2WO_6 with enhanced photocatalytic nitrogen fixation activity. *Dalton Trans.* 50 (21), 7427–7432. doi:10.1039/D1DT00762A
- Bazhenova, T. A., and Shilov, A. E. (1995). Nitrogen fixation in solution. *Coord. Chem. Rev.* 144, 69–145. doi:10.1016/0010-8545(95)01139-G
- Bo, Y., Wang, H., Lin, Y., Yang, T., Ye, R., Li, Y., et al. (2021). Altering hydrogenation pathways in photocatalytic nitrogen fixation by tuning local electronic structure of oxygen vacancy with dopant. *Angew. Chem. Int. Ed.* 60 (29), 16085–16092. doi:10.1002/anie.202104001
- Brown, K. A., Harris, D. F., Wilker, M. B., Rasmussen, A., Khadka, N., Hamby, H., et al. (2016). Light-driven dinitrogen reduction catalyzed by a CdS : Nitrogenase $MoFe$ protein biohybrid. *Science* 352 (6284), 448–450. doi:10.1126/science.aaf2091
- Cai Feng, C., Wu, P., Li, Q., Liu, J., Wang, D., Liu, B., et al. (2022). Amorphization and defect engineering in constructing ternary composite $Ag/PW_{10}V_2/am-TiO_{2-x}$ for enhanced photocatalytic nitrogen fixation. *New J. Chem.* 46 (4), 1731–1740. doi:10.1039/D1NJ05917C
- Caiting Feng, C., Liu, J., Li, Q., Ji, L., Wu, P., Yuan, X., et al. (2022). Fabricating $Ag/PW_{12}/Zr-mTiO_2$ composite via doping and interface engineering: An efficient catalyst with bifunctionality in photo- and electro-driven nitrogen reduction reactions. *Adv. Sustain. Syst.* 6 (1), 2100307. doi:10.1002/adsu.202100307
- Cao, S., Chen, H., Jiang, F., and Wang, X. (2018). Nitrogen photofixation by ultrathin amine-functionalized graphitic carbon nitride nanosheets as a gaseous product from thermal polymerization of urea. *Appl. Catal. B Environ.* 224, 222–229. doi:10.1016/j.apcatb.2017.10.028

Funding

This work was supported by the National Natural Science Foundation of China (No. 21972010) and the Beijing Natural Science Foundation (No. 2192039).

Conflict of interest

The authors declare that the research was conducted in the absence of any commercial or financial relationships that could be construed as a potential conflict of interest.

Publisher's note

All claims expressed in this article are solely those of the authors and do not necessarily represent those of their affiliated organizations, or those of the publisher, the editors and the reviewers. Any product that may be evaluated in this article, or claim that may be made by its manufacturer, is not guaranteed or endorsed by the publisher.

Supplementary material

The Supplementary Material for this article can be found online at: <https://www.frontiersin.org/articles/10.3389/fchem.2022.978078/full#supplementary-material>

- Chamack, M., Ifires, M., Akbar Razavi, S. A., Morsali, A., Addad, A., Larimi, A., et al. (2022). Photocatalytic performance of perovskite and metal-organic framework hybrid material for the reduction of N_2 to ammonia. *Inorg. Chem.* 61 (3), 1735–1744. doi:10.1021/acs.inorgchem.1c03622
- Chao Liu, C., Zhang, Q., Hou, W., and Zou, Z. (2020). 2D titanium/niobium metal oxide-based materials for photocatalytic application. *Sol. RRL* 4 (9), 2000070. doi:10.1002/solr.202000070
- Chen, W. T., Chan, A., Al-Azri, Z. H. N., Dosado, A. G., Nadeem, M. A., Sun-Waterhouse, D., et al. (2015). Effect of TiO_2 polymorph and alcohol sacrificial agent on the activity of Au/ TiO_2 photocatalysts for H_2 production in alcohol–water mixtures. *J. Catal.* 329, 499–513. doi:10.1016/j.jcat.2015.06.014
- Chen, X., Li, N., Kong, Z., Ong, W.-J., and Zhao, X. (2018). Photocatalytic fixation of nitrogen to ammonia: State-of-the-art advancements and future prospects. *Mat. Horiz.* 5 (1), 9–27. doi:10.1039/c7mh00557a
- Chen, F., Huang, H., Guo, L., Zhang, Y., and Ma, T. (2019). The role of polarization in photocatalysis. *Angew. Chem. Int. Ed.* 58 (30), 10061–10073. doi:10.1002/anie.201901361
- Chen, L., Dai, X., Li, X., Wang, J., Chen, H., Hu, X., et al. (2021a). A novel $Bi_2S_3/KTa_{0.75}Nb_{0.25}O_3$ nanocomposite with high efficiency for photocatalytic and piezocatalytic N_2 fixation. *J. Mat. Chem. A* 9 (22), 13344–13354. doi:10.1039/D1TA02270A
- Chen, L., Hao, Y.-C., Guo, Y., Zhang, Q., Li, J., Gao, W.-Y., et al. (2021b). Metal-organic framework membranes encapsulating gold nanoparticles for direct plasmonic photocatalytic nitrogen fixation. *J. Am. Chem. Soc.* 143 (15), 5727–5736. doi:10.1021/jacs.0c13342
- Chen, C., Sun, M., Wang, K., and Li, Y. (2022). Dual-metal single-atomic catalyst: The challenge in synthesis, characterization, and mechanistic investigation for electrocatalysis. *SmartMat.* doi:10.1002/smm2.1085
- Chen-Xuan Xu, C. X., Huang, J. D., and Ma, J. M. (2021). Green, cheap and rechargeable Al–Ni battery with efficient N_2 fixation. *Rare Met.* 40 (1), 1–2. doi:10.1007/s12598-020-01626-8
- Cheng, Q., and Zhang, G.-K. (2020). Enhanced photocatalytic performance of tungsten-based photocatalysts for degradation of volatile organic compounds: A review. *Tungsten* 2 (3), 240–250. doi:10.1007/s42864-020-00055-5
- Choi, J., Suryanto, B. H. R., Wang, D., Du, H. L., Hodgetts, R. Y., Ferrero Vallana, F. M., et al. (2020). Identification and elimination of false positives in electrochemical nitrogen reduction studies. *Nat. Commun.* 11 (1), 5546. doi:10.1038/s41467-020-19130-z
- Chu, K., Liu, Y.-p., Li, Y.-b., Zhang, H., and Tian, Y. (2019). Efficient electrocatalytic N_2 reduction on CoO quantum dots. *J. Mat. Chem. A* 7 (9), 4389–4394. doi:10.1039/C9TA00016j
- Comer, B. M., and Medford, A. J. (2018). Analysis of photocatalytic nitrogen fixation on rutile TiO_2 (110). *ACS Sustain. Chem. Eng.* 6 (4), 4648–4660. doi:10.1021/acssuschemeng.7b03652
- Congmin Zhang, C., Chen, G., Lv, C., Yao, Y., Xu, Y., Jin, X., et al. (2018). Enabling nitrogen fixation on Bi_2WO_6 photocatalyst by c-PAN surface decoration. *ACS Sustain. Chem. Eng.* 6 (9), 11190–11195. doi:10.1021/acssuschemeng.8b02236
- Cooper, J. K., Gul, S., Toma, F. M., Chen, L., Glans, P.-A., Guo, J., et al. (2014). Electronic structure of monoclinic $BiVO_4$. *Chem. Mat.* 26 (18), 5365–5373. doi:10.1021/cm5025074
- Dai, Z., Qin, F., Zhao, H., Ding, J., Liu, Y., Chen, R., et al. (2016). Crystal defect engineering of Aurivillius Bi_2MoO_6 by Ce doping for increased reactive species production in photocatalysis. *ACS Catal.* 6 (5), 3180–3192. doi:10.1021/acscatal.6b00490
- Dimitrijevic, N. M., Vijayan, B. K., Poluektov, O. G., Rajh, T., Gray, K. A., He, H., et al. (2011). Role of water and carbonates in photocatalytic transformation of CO_2 to CH_4 on titania. *J. Am. Chem. Soc.* 133 (11), 3964–3971. doi:10.1021/ja108791u
- Dong Liu, D., Chen, S., Li, R., and Peng, T. (2021). Review of Z-scheme heterojunctions for photocatalytic energy conversion. *Acta Phys. -Chim. Sin.* 37 (6), 2010017. doi:10.3866/pku.Whxb202010017
- Dong Zhang, D., Li, Y., Li, Y., and Zhan, S. (2022). Towards single-atom photocatalysts for future carbon-neutral application. *SmartMat.* doi:10.1002/smm2.1095
- Fan, Y. S., Xi, X. L., Liu, Y. S., Nie, Z.-R., Zhao, L. Y., Zhang, Q. H., et al. (2021). Regulation of morphology and visible light-driven photocatalysis of WO_3 nanostructures by changing pH. *Rare Met.* 40 (7), 1738–1745. doi:10.1007/s12598-020-01490-6
- Fei, T., Yu, L., Liu, Z., Song, Y., Xu, F., Mo, Z., et al. (2019). Graphene quantum dots modified flower like Bi_2WO_6 for enhanced photocatalytic nitrogen fixation. *J. Colloid Interface Sci.* 557, 498–505. doi:10.1016/j.jcis.2019.09.011
- Feng Wang, F., Ding, Q., Bai, Y., Bai, H., Wang, S., Fan, W., et al. (2022). Fabrication of an amorphous metal oxide/p- $BiVO_4$ photocathode: Understanding the role of entropy for reducing nitrate to ammonia. *Inorg. Chem. Front.* 9 (4), 805–813. doi:10.1039/D1QI01472B
- Fu, W., Zhuang, P., OliverLam Chee, M., Dong, P., Ye, M., Shen, J., et al. (2019). Oxygen vacancies in Ta_2O_5 nanorods for highly efficient electrocatalytic N_2 reduction to NH_3 under ambient conditions. *ACS Sustain. Chem. Eng.* 7 (10), 9622–9628. doi:10.1021/acssuschemeng.9b01178
- Fu, Y., Liao, Y., Li, P., Li, H., Jiang, S., Huang, H., et al. (2022). Layer structured materials for ambient nitrogen fixation. *Coord. Chem. Rev.* 460, 214468. doi:10.1016/j.ccr.2022.214468
- Gaggero, E., Calza, P., Cerrato, E., and Paganini, M. C. (2021). Cerium-europium- and erbium-modified ZnO and ZrO_2 for photocatalytic water treatment applications: A review. *Catalysts* 11 (12), 1520. doi:10.3390/catal11121520
- Gambarotta, S., and Scott, J. (2004). Multimetallic cooperative activation of N_2 . *Angew. Chem. Int. Ed.* 43 (40), 5298–5308. doi:10.1002/anie.200301669
- Gao, X., Wen, Y., Qu, D., An, L., Luan, S., Jiang, W., et al. (2018). Interference effect of alcohol on Nessler's reagent in photocatalytic nitrogen fixation. *ACS Sustain. Chem. Eng.* 6 (4), 5342–5348. doi:10.1021/acssuschemeng.8b00110
- Gao, Y., Han, Z., Hong, S., Wu, T., Li, X., Qiu, J., et al. (2019). ZIF-67-derived cobalt/nitrogen-doped carbon composites for efficient electrocatalytic N_2 reduction. *ACS Appl. Energy Mat.* 2 (8), 6071–6077. doi:10.1021/acsaem.9b01135
- Gao, W., Li, X., Zhang, X., Su, S., Luo, S., Huang, R., et al. (2021). Photocatalytic nitrogen fixation of metal–organic frameworks (MOFs) excited by ultraviolet light: Insights into the nitrogen fixation mechanism of missing metal cluster or linker defects. *Nanoscale* 13 (16), 7801–7809. doi:10.1039/D1NR00697E
- Gao, Y., Xia, Q., Hao, L., Robertson, A. W., and Sun, Z. (2022). Design of porous core–shell manganese oxides to boost electrocatalytic dinitrogen reduction. *ACS Sustain. Chem. Eng.* 10 (3), 1316–1322. doi:10.1021/acssuschemeng.1c07824
- Garden, A. L., and Skúlason, E. (2015). The mechanism of industrial ammonia synthesis revisited: Calculations of the role of the associative mechanism. *J. Phys. Chem. C* 119 (47), 26554–26559. doi:10.1021/acs.jpcc.5b08508
- Girish Kumar, S., and Koteswara Rao, K. S. R. (2015). Tungsten-based nanomaterials (WO_3 & Bi_2WO_6): Modifications related to charge carrier transfer mechanisms and photocatalytic applications. *Appl. Surf. Sci.* 355, 939–958. doi:10.1016/j.apsusc.2015.07.003
- Gu, J., Chen, W., Shan, G. G., Li, G., Sun, C., Wang, X. L., et al. (2021). The roles of polyoxometalates in photocatalytic reduction of carbon dioxide. *Mat. Today Energy* 21, 100760. doi:10.1016/j.mtener.2021.100760
- Guanhua Zhang, G., Yuan, X., Xie, B., Meng, Y., Ni, Z., Xia, S., et al. (2022). S vacancies act as a bridge to promote electron injection from Z-scheme heterojunction to nitrogen molecule for photocatalytic ammonia synthesis. *Chem. Eng. J.* 433, 133670. doi:10.1016/j.cej.2021.133670
- Gui Li, G., Yang, W., Gao, S., Shen, Q., Xue, J., Chen, K., et al. (2021). Creation of rich oxygen vacancies in bismuth molybdate nanosheets to boost the photocatalytic nitrogen fixation performance under visible light illumination. *Chem. Eng. J.* 404, 127115. doi:10.1016/j.cej.2020.127115
- Guo, B., Cheng, X., Tang, Y., Guo, W., Deng, S., Wu, L., et al. (2022). Dehydrated $UO_2-66(SH)_2$: The Zr–O Cluster and its photocatalytic role mimicking the biological nitrogen fixation. *Angew. Chem. Int. Ed. Engl.* 61 (13), e202117244. doi:10.1002/anie.202117244
- Guo, C. X., Ran, J., Vasileff, A., and Qiao, S. Z. (2018). Rational design of electrocatalysts and photo(electro)catalysts for nitrogen reduction to ammonia (NH_3) under ambient conditions. *Energy Environ. Sci.* 11 (1), 45–56. doi:10.1039/C7EE02220D
- Guo, J., and Chen, P. (2017). Catalyst: NH_3 as an energy carrier. *Chem* 3 (5), 709–712. doi:10.1016/j.chempr.2017.10.004
- Guan Wang, G., Huo, T., Deng, Q., Yu, F., Xia, Y., Li, H., et al. (2022). Surface-layer bromine doping enhanced generation of surface oxygen vacancies in bismuth molybdate for efficient photocatalytic nitrogen fixation. *Appl. Catal. B Environ.* 310, 121319. doi:10.1016/j.apcatb.2022.121319
- Hai Guang Zhang, H., Li, X., Su, H., Chen, X., Zuo, S., Yan, X., et al. (2019). Sol–gel synthesis of upconversion perovskite/attapulgite heterostructures for photocatalytic fixation of nitrogen. *J. Sol-Gel Sci. Technol.* 92 (1), 154–162. doi:10.1007/s10971-019-05071-7
- Haitao Li, H., Liu, Y., Liu, Y., Wang, L., Tang, R., Deng, P., et al. (2021). Efficient visible light driven ammonia synthesis on sandwich structured $C_3N_4/MoS_2/Mn_3O_4$ catalyst. *Appl. Catal. B Environ.* 281, 119476. doi:10.1016/j.apcatb.2020.119476
- Han, J., Liu, Z., Ma, Y., Cui, G., Xie, F., Wang, F., et al. (2018). Ambient N_2 fixation to NH_3 at ambient conditions: Using Nb_2O_5 nanofiber as a high-performance electrocatalyst. *Nano Energy* 52, 264–270. doi:10.1016/j.nanoen.2018.07.045
- Hao Li, H., Shang, J., Shi, J., Zhao, K., and Zhang, L. (2016). Facet-dependent solar ammonia synthesis of $BiOCl$ nanosheets via a proton-assisted electron transfer pathway. *Nanoscale* 8 (4), 1986–1993. doi:10.1039/C5NR07380D

- Hao, Y., Dong, X., Zhai, S., Ma, H., Wang, X., Zhang, X., et al. (2016). Hydrogenated bismuth molybdate nanoframe for efficient sunlight-driven nitrogen fixation from air. *Chem. Eur. J.* 22 (52), 18722–18728. doi:10.1002/chem.201604510
- Hao, Q., Liu, C., Jia, G., Wang, Y., Arandiyani, H., Wei, W., et al. (2020). Catalytic reduction of nitrogen to produce ammonia by bismuth-based catalysts: State of the art and future prospects. *Mat. Horiz.* 7 (4), 1014–1029. doi:10.1039/C9MH01668F
- Hao, L., Xia, Q., Zhang, Q., Masa, J., and Sun, Z. (2021). Improving the performance of metal-organic frameworks for thermo-catalytic CO₂ conversion: Strategies and perspectives. *Chin. J. Catal.* 42 (11), 1903–1920. doi:10.1016/S1872-2067(21)63841-X
- Hinnemann, B., and Nørskov, J. K. (2006). Catalysis by enzymes: The biological ammonia synthesis. *Top. Catal.* 37 (1), 55–70. doi:10.1007/s11244-006-0002-0
- Hochman, G., Goldman, A. S., Felder, F. A., Mayer, J. M., Miller, A. J. M., Holland, P. L., et al. (2020). Potential economic feasibility of direct electrochemical nitrogen reduction as a route to ammonia. *ACS Sustain. Chem. Eng.* 8 (24), 8938–8948. doi:10.1021/acssuschemeng.0c01206
- Hongda Li, H., Gu, S., Sun, Z., Guo, F., Xie, Y., Tao, B., et al. (2020). The in-built bionic “MoFe cofactor” in Fe-doped two-dimensional MoTe₂ nanosheets for boosting the photocatalytic nitrogen reduction performance. *J. Mat. Chem. A* 8 (26), 13038–13048. doi:10.1039/d0ta04251j
- Horn, M. R., Singh, A., Alomari, S., Goberna-Ferrón, S., Benages-Vilau, R., Chodankar, N., et al. (2021). Polyoxometalates (POMs): From electroactive clusters to energy materials. *Energy Environ. Sci.* 14 (4), 1652–1700. doi:10.1039/D0EE03407J
- Hou, T. T., Xiao, Y., Cui, P. X., Huang, Y., Tan, X. P., Zheng, X. S., et al. (2019). Operating oxygen vacancies for enhanced activity and stability toward nitrogen photofixation. *Adv. Energy Mat.* 9 (43), 1902319. doi:10.1002/aenm.201902319
- Hu, K., Huang, Z., Zeng, L., Zhang, Z., Mei, L., Chai, Z., et al. (2022). Recent advances in MOF-based materials for photocatalytic nitrogen fixation. *Eur. J. Inorg. Chem.* 2022 (3), e202100748. doi:10.1002/ejic.202100748
- Huang, L., Wu, J., Han, P., Al-Enizi, A. M., Almutairi, T. M., Zhang, L., et al. (2019). NbO₂ electrocatalyst toward 32% faradaic efficiency for N₂ fixation. *Small Methods* 3 (6), 1800386. doi:10.1002/smt.201800386
- Huang, Y., Zhang, N., Wu, Z., and Xie, X. (2020). Artificial nitrogen fixation over bismuth-based photocatalysts: Fundamentals and future perspectives. *J. Mat. Chem. A* 8 (10), 4978–4995. doi:10.1039/C9TA13589H
- Hui, X., Li, L., Xia, Q., Hong, S., Hao, L., Robertson, A. W., et al. (2022). Interface engineered Sb₂O₃/W₁₈O₄₉ heterostructure for enhanced visible-light-driven photocatalytic N₂ reduction. *Chem. Eng. J.* 438, 135485. doi:10.1016/j.cej.2022.135485
- Huimin Liu, H., Guijarro, N., and Luo, J. (2021). The pitfalls in electrocatalytic nitrogen reduction for ammonia synthesis. *J. Energy Chem.* 61, 149–154. doi:10.1016/j.jechem.2021.01.039
- Jacobsen, C. J., Dahl, S., Clausen, B. S., Bahn, S., Logadottir, A., Nørskov, J. K., et al. (2001). Catalyst design by interpolation in the periodic table: Bimetallic ammonia synthesis catalysts. *J. Am. Chem. Soc.* 123 (34), 8404–8405. doi:10.1021/ja010963d
- Jia, H. P., and Quadrelli, E. A. (2014). Mechanistic aspects of dinitrogen cleavage and hydrogenation to produce ammonia in catalysis and organometallic chemistry: Relevance of metal hydride bonds and dihydrogen. *Chem. Soc. Rev.* 43 (2), 547–564. doi:10.1039/C3CS60206K
- Kitano, M., Inoue, Y., Yamazaki, Y., Hayashi, F., Kanbara, S., Matsuishi, S., et al. (2012). Ammonia synthesis using a stable electride as an electron donor and reversible hydrogen store. *Nat. Chem.* 4 (11), 934–940. doi:10.1038/nchem.1476
- Kong, W., Liu, Z., Han, J., Xia, L., Wang, Y., Liu, Q., et al. (2019). Ambient electrochemical N₂-to-NH₃ fixation enabled by Nb₂O₅ nanowire array. *Inorg. Chem. Front.* 6 (2), 423–427. doi:10.1039/C8QI01049H
- Kramm, U. I., Marschall, R., and Rose, M. (2019). Pitfalls in heterogeneous thermal, electro- and photocatalysis. *ChemCatChem* 11 (11), 2563–2574. doi:10.1002/cctc.201900137
- Lee, J., Tan, L. L., and Chai, S. P. (2021). Heterojunction photocatalysts for artificial nitrogen fixation: Fundamentals, latest advances and future perspectives. *Nanoscale* 13 (15), 7011–7033. doi:10.1039/d1nr00783a
- Lei, W., Xiao, J.-L., Liu, H.-P., Jia, Q.-L., and Zhang, H.-J. (2020). Tungsten disulfide: Synthesis and applications in electrochemical energy storage and conversion. *Tungsten* 2 (3), 217–239. doi:10.1007/s42864-020-00054-6
- Li, X., Sun, X., Zhang, L., Sun, S., and Wang, W. (2018). Efficient photocatalytic fixation of N₂ by KOH-treated g-C₃N₄. *J. Mat. Chem. A* 6 (7), 3005–3011. doi:10.1039/C7TA09762J
- Li, J., Chen, R., Wang, J., Zhou, Y., Yang, G., Dong, F., et al. (2022a). Subnanometric alkaline-earth oxide clusters for sustainable nitrate to ammonia photosynthesis. *Nat. Commun.* 13 (1), 1098. doi:10.1038/s41467-022-28740-8
- Li, J., Lou, Z., and Li, B. (2022b). Nanostructured materials with localized surface plasmon resonance for photocatalysis. *Chin. Chem. Lett.* 33 (3), 1154–1168. doi:10.1016/j.cclet.2021.07.059
- Liang Yang, L., Choi, C., Hong, S., Liu, Z., Zhao, Z., Yang, M., et al. (2020). Single yttrium sites on carbon-coated TiO₂ for efficient electrocatalytic N₂ reduction. *Chem. Commun.* 56 (74), 10910–10913. doi:10.1039/D0CC01136C
- Libo Wang, L., Zhang, Q., Wei, T., Li, F., Sun, Z., Xu, L., et al. (2021). WC and cobalt nanoparticles embedded in nitrogen-doped carbon 3D nanocage derived from H₃PW₁₂O₄₀@ZIF-67 for photocatalytic nitrogen fixation. *J. Mat. Chem. A* 9 (5), 2912–2918. doi:10.1039/D0TA10303A
- Lin Liu, L., Liu, J., Sun, K., Wan, J., Fu, F., Fan, J., et al. (2021). Novel phosphorus-doped Bi₂WO₆ monolayer with oxygen vacancies for superior photocatalytic water detoxification and nitrogen fixation performance. *Chem. Eng. J.* 411, 128629. doi:10.1016/j.cej.2021.128629
- Lin Wang, L., Li, X., Hao, L., Hong, S., Robertson, A. W., Sun, Z., et al. (2022). Integration of ultrafine CuO nanoparticles with two-dimensional MOFs for enhanced electrochemical CO₂ reduction to ethylene. *Chin. J. Catal.* 43 (4), 1049–1057. doi:10.1016/S1872-2067(21)63947-5
- Lineley, B. M., Appel, A. M., Krogh-Jespersen, K., Mayer, J. M., and Miller, A. J. (2016). Evaluating the thermodynamics of electrocatalytic N₂ reduction in acetonitrile. *ACS Energy Lett.* 1 (4), 698–704. doi:10.1021/acsenrgylett.6b00319
- Linsebigler, A. L., Lu, G., and Yates, J. T., Jr (1995). Photocatalysis on TiO₂ surfaces: Principles, mechanisms, and selected results. *Chem. Rev.* 95 (3), 735–758. doi:10.1021/cr00035a013
- Liu, J., Zhang, Y., Lu, L., Wu, G., and Chen, W. (2012). Self-regenerated solar-driven photocatalytic water-splitting by urea derived graphitic carbon nitride with platinum nanoparticles. *Chem. Commun.* 48 (70), 8826. doi:10.1039/C2CC33644H
- Liu, J., Kelley, M. S., Wu, W., Banerjee, A., Douvalis, A. P., Wu, J., et al. (2016). Nitrogenase-mimic iron-containing chalcogenides for photochemical reduction of dinitrogen to ammonia. *Proc. Natl. Acad. Sci. U. S. A.* 113(20), 5530–5535. doi:10.1073/pnas.1605512113
- Liu, Y., Cheng, M., He, Z., Gu, B., Xiao, C., Zhou, T., et al. (2019). Pothole-rich ultrathin WO₃ nanosheets that trigger N≡N bond activation of nitrogen for direct nitrate photosynthesis. *Angew. Chem. Int. Ed.* 58 (3), 731–735. doi:10.1002/anie.201808177
- Liu, X., Luo, Y., Ling, C., Shi, Y., Zhan, G., Li, H., et al. (2022). Rare Earth La single atoms supported MoO_{3-x} for efficient photocatalytic nitrogen fixation. *Appl. Catal. B Environ.* 301, 120766. doi:10.1016/j.apcatb.2021.120766
- Lu, H., Zhao, Y.-M., Sajji, S. E., Yin, X., Wibowo, A., Tang, C. S., et al. (2022). All rooms-temperature synthesis, N₂ photofixation and reactivation over 2D cobalt oxide. *Appl. Catal. B Environ.* 304, 121001. doi:10.1016/j.apcatb.2021.121001
- Luo, J., Bai, X., Li, Q., Yu, X., Li, C., Wang, Z., et al. (2019). Band structure engineering of bioinspired Fe doped SrMoO₄ for enhanced photocatalytic nitrogen reduction performance. *Nano Energy* 66, 104187. doi:10.1016/j.nanoen.2019.104187
- Lv, C., Yan, C., Chen, G., Ding, Y., Sun, J., Zhou, Y., et al. (2018). An amorphous noble-metal-free electrocatalyst that enables nitrogen fixation under ambient conditions. *Angew. Chem. Int. Ed.* 57 (21), 6073–6076. doi:10.1002/anie.201801538
- Mansingh, S., Das, K. K., Sultana, S., and Parida, K. (2021). Recent advances in wireless photofixation of dinitrogen to ammonia under the ambient condition: A review. *J. Photochem. Photobiol. C Photochem. Rev.* 47, 100402. doi:10.1016/j.jphotochemrev.2021.100402
- Mao, Y., Yang, X., Gong, W., Zhang, J., Pan, T., Sun, H., et al. (2020). A dopant replacement-driven molten salt method toward the synthesis of sub-5-nm-sized ultrathin nanowires. *Small* 16 (23), 2001098. doi:10.1002/sml.202001098
- Medford, A. J., and Hatzell, M. C. (2017). Photon-driven nitrogen fixation: Current progress, thermodynamic considerations, and future outlook. *ACS Catal.* 7 (4), 2624–2643. doi:10.1021/acscatal.7b00439
- Meng, Q., Lv, C., Sun, J., Hong, W., Xing, W., Qiang, L., et al. (2019). High-efficiency Fe-mediated Bi₂MoO₆ nitrogen-fixing photocatalyst: Reduced surface work function and ameliorated surface reaction. *Appl. Catal. B Environ.* 256, 117781. doi:10.1016/j.apcatb.2019.117781
- Meng, S.-L., Li, X.-B., Tung, C.-H., and Wu, L.-Z. (2021). Nitrogenase inspired artificial photosynthetic nitrogen fixation. *Chem* 7 (6), 1431–1450. doi:10.1016/j.chempr.2020.11.002
- Meng Yang, M., Huo, R. P., Shen, H. D., Xia, Q. N., Qiu, J. S., Robertson, A. W., et al. (2020). Metal-tuned W₁₈O₄₉ for efficient electrocatalytic N₂ reduction. *ACS Sustain. Chem. Eng.* 8 (7), 2957–2963. doi:10.1021/acssuschemeng.9b07526

- Mingli Zhang, M., Choi, C., Huo, R., Gu, G. H., Hong, S., Yan, C., et al. (2020). Reduced graphene oxides with engineered defects enable efficient electrochemical reduction of dinitrogen to ammonia in wide pH range. *Nano Energy* 68, 104323. doi:10.1016/j.nanoen.2019.104323
- Montoya, J. H., Tsai, C., Vojvodac, A., and Nørskov, J. K. (2015). The challenge of electrochemical ammonia synthesis: A new perspective on the role of nitrogen scaling relations. *ChemSusChem* 8 (13), 2180–2186. doi:10.1002/cssc.201500322
- Mou, H., Wang, J., Yu, D., Zhang, D., Chen, W., Wang, Y., et al. (2019). Fabricating amorphous g-C₃N₄/ZrO₂ photocatalysts by one-step pyrolysis for solar-driven ambient ammonia synthesis. *ACS Appl. Mat. Interfaces* 11 (47), 44360–44365. doi:10.1021/acsami.9b16432
- Mousavi, M., Habibi, M. M., Zhang, G., Pourhakkak, P., moradian, S., Ghasemi, J. B., et al. (2022). *In-situ* construction of ZnO/Sb₂MoO₆ nano-heterostructure for efficient visible-light photocatalytic conversion of N₂ to NH₃. *Surf. Interfaces* 30, 101844. doi:10.1016/j.surfint.2022.101844
- Ning Zhang, N., Jalil, A., Wu, D. X., Chen, S. M., Liu, Y. F., Gao, C., et al. (2018). Refining defect states in W₁₈O₄₉ by Mo doping: A strategy for tuning N₂ activation towards solar-driven nitrogen fixation. *J. Am. Chem. Soc.* 140 (30), 9434–9443. doi:10.1021/jacs.8b02076
- Nunes, B. N., Lopes, O. F., Patrocínio, A. O. T., and Bahnemann, D. W. (2020). Recent advances in niobium-based materials for photocatalytic solar fuel production. *Catalysts* 10 (1), 126. doi:10.3390/catal10010126
- Oshikiri, T., Ueno, K., and Misawa, H. (2016). Selective dinitrogen conversion to ammonia using water and visible light through plasmon-induced charge separation. *Angew. Chem. Int. Ed.* 55 (12), 3942–3946. doi:10.1002/anie.201511189
- Qin, J., Zhao, W., Hu, X., Li, J., Ndokoye, P., and Liu, B. (2021). Exploring the N₂ adsorption and activation mechanisms over the 2H/1T Mixed-phase ultrathin Mo_{1-x}W_xS₂ nanosheets for boosting N₂ photosynthesis. *ACS Appl. Mater. Interfaces* 13 (6), 7127–7134. doi:10.1021/acsami.0c19282
- Qiu, P., Huang, C., Dong, G., Chen, F., Zhao, F., Yu, Y., et al. (2021). Plasmonic gold nanocrystals simulated photocatalytic nitrogen fixation over Mo doped W₁₈O₄₉ nanowires. *J. Mat. Chem. A* 9 (25), 14459–14465. doi:10.1039/D1TA03339E
- Ren, W., Mei, Z., Zheng, S., Li, S., Zhu, Y., Zheng, J., et al. (2020). Wavelength-dependent solar N₂ fixation into ammonia and nitrate in pure water. *Research* 2020, 1–12. doi:10.34133/2020/3750314
- Rong Zhang, R., Guo, H., Yang, L., Wang, Y., Niu, Z., Huang, H., et al. (2019). Electrocatalytic N₂ fixation over hollow VO₂ microspheres at ambient conditions. *ChemElectroChem* 6 (4), 1014–1018. doi:10.1002/celec.201801484
- Schrauzer, G. N., and Guth, T. D. (1977). Photolysis of water and photoreduction of nitrogen on titanium dioxide. *J. Am. Chem. Soc.* 99 (22), 7189–7193. doi:10.1021/ja00464a015
- Schrauzer, G., and Guth, T. (2002). Photolysis of water and photoreduction of nitrogen on titanium dioxide. *J. Am. Chem. Soc.* 99 (22), 7189–7193. doi:10.1021/ja00464a015
- Shen, H., Peppel, T., Strunk, J., and Sun, Z. (2020). Photocatalytic reduction of CO₂ by metal-free-based materials: Recent advances and future perspective. *Sol. RRL* 4 (8), 1900546. doi:10.1002/solr.201900546
- Shen, H., Yang, M., Hao, L., Wang, J., Strunk, J., Sun, Z., et al. (2021). Photocatalytic nitrogen reduction to ammonia: Insights into the role of defect engineering in photocatalysts. *Nano Res.* 15, 2773–2809. doi:10.1007/s12274-021-3725-0
- Shende, A. G., Tiwari, C. S., Bhojar, T. H., Vidyasagar, D., and Umare, S. S. (2019). BWO nano-octahedron coupled with layered g-C₃N₄: An efficient visible light active photocatalyst for degradation of cationic/anionic dyes, and N₂ reduction. *J. Mol. Liq.* 296, 111771. doi:10.1016/j.molliq.2019.111771
- Shi, R., Zhao, Y., Waterhouse, G. I. N., Zhang, S., and Zhang, T. (2019). Defect engineering in photocatalytic nitrogen fixation. *ACS Catal.* 9 (11), 9739–9750. doi:10.1021/acscatal.9b03246
- Shi, L., Yin, Y., Wang, S., and Sun, H. (2020a). Rational catalyst design for N₂ reduction under ambient conditions: Strategies toward enhanced conversion efficiency. *ACS Catal.* 10 (12), 6870–6899. doi:10.1021/acscatal.0c01081
- Shi, L., Li, Z., Ju, L., Carrasco-Pena, A., Orlovskaya, N., Zhou, H., et al. (2020b). Promoting nitrogen photofixation over a periodic WS₂/TiO₂ nanoporous film. *J. Mat. Chem. A* 8 (3), 1059–1065. doi:10.1039/C9TA12743G
- Shipman, M. A., and Symes, M. D. (2017). Recent progress towards the electrosynthesis of ammonia from sustainable resources. *Catal. Today* 286, 57–68. doi:10.1016/j.cattod.2016.05.008
- Shiraishi, Y., Shiota, S., Kofuji, Y., Hashimoto, M., Chishiro, K., Hirakawa, H., et al. (2018). Nitrogen fixation with water on carbon-nitride-based metal-free photocatalysts with 0.1% solar-to-ammonia energy conversion efficiency. *ACS Appl. Energy Mat.* 1 (8), 4169–4177. doi:10.1021/acsaem.8b00829
- Shuai Zhang, S., Zhao, Y., Shi, R., Waterhouse, G. I., and Zhang, T. (2019). Photocatalytic ammonia synthesis: Recent progress and future. *EnergyChem* 1 (2), 100013. doi:10.1016/j.enchem.2019.100013
- Skúlason, E., Bligaard, T., Gudmundsdóttir, S., Studt, F., Rossmeisl, J., Abild-Pedersen, F., et al. (2012). A theoretical evaluation of possible transition metal electro-catalysts for N₂ reduction. *Phys. Chem. Chem. Phys.* 14 (3), 1235–1245. doi:10.1039/C1CP22271F
- Song, J., Huang, Z.-F., Pan, L., Zou, J.-J., Zhang, X., Wang, L., et al. (2015). Oxygen-deficient tungsten oxide as versatile and efficient hydrogenation catalyst. *ACS Catal.* 5 (11), 6594–6599. doi:10.1021/acscatal.5b01522
- Su, S., Li, X., Zhang, X., Zhu, J., Liu, G., Tan, M., et al. (2022). Keggin-type SiW₁₂ encapsulated in MIL-101(Cr) as efficient heterogeneous photocatalysts for nitrogen fixation reaction. *J. Colloid Interface Sci.* 621, 406–415. doi:10.1016/j.jcis.2022.04.006
- Sun, S., Li, X., Wang, W., Zhang, L., and Sun, X. (2017). Photocatalytic robust solar energy reduction of dinitrogen to ammonia on ultrathin MoS₂. *Appl. Catal. B Environ.* 200, 323–329. doi:10.1016/j.apcatb.2016.07.025
- Sun, Z., Talreja, N., Tao, H., Texter, J., Muhler, M., Strunk, J., et al. (2018). Catalysis of carbon dioxide photoreduction on nanosheets: Fundamentals and challenges. *Angew. Chem. Int. Ed.* 57 (26), 7610–7627. doi:10.1002/anie.201710509
- Sun, Z., Huo, R., Choi, C., Hong, S., Wu, T.-S., Qiu, J., et al. (2019). Oxygen vacancy enables electrochemical N₂ fixation over WO₃ with tailored structure. *Nano Energy* 62, 869–875. doi:10.1016/j.nanoen.2019.06.019
- Sun, D., Bai, H., Zhao, Y., Zhang, Q., Bai, Y., Liu, Y., et al. (2020). Amorphous MnCO₃/C double layers decorated on BiVO₄ photoelectrodes to boost nitrogen reduction. *ACS Appl. Mat. Interfaces* 12 (47), 52763–52770. doi:10.1021/acsami.0c16337
- Swain, G., Sultana, S., and Parida, K. (2020). Constructing a novel surfactant-free MoS₂ nanosheet modified MgIn₂S₄ marigold microflower: An efficient visible-light driven 2D-2D p-n heterojunction photocatalyst toward HER and pH regulated NRR. *ACS Sustain. Chem. Eng.* 8 (12), 4848–4862. doi:10.1021/acsschemeng.9b07821
- Tang, C., and Qiao, S.-Z. (2019). How to explore ambient electrocatalytic nitrogen reduction reliably and insightfully. *Chem. Soc. Rev.* 48 (12), 3166–3180. doi:10.1039/C9CS00280D
- Tao, H., Choi, C., Ding, L.-X., Jiang, Z., Han, Z., Jia, M., et al. (2019). Nitrogen fixation by Ru single-atom electrocatalytic reduction. *Chem* 5 (1), 204–214. doi:10.1016/j.chempr.2018.10.007
- Tianyu Wang, T., Feng, C., Liu, J., Wang, D., Hu, H., Hu, J., et al. (2021). Bi₂WO₆ hollow microspheres with high specific surface area and oxygen vacancies for efficient photocatalysis N₂ fixation. *Chem. Eng. J.* 414, 128827. doi:10.1016/j.cej.2021.128827
- Tianyu Wang, T., Liu, J., Wu, P., Feng, C., Wang, D., Hu, H., et al. (2020). Direct utilization of air and water as feedstocks in the photo-driven nitrogen reduction reaction over a ternary Z-scheme SiW₆Co₃/PDA/BWO hetero-junction. *J. Mat. Chem. A* 8 (32), 16590–16598. doi:10.1039/C9TA13902H
- Tong Xu, T., Ma, B., Liang, J., Yue, L., Liu, Q., Li, T., et al. (2021). Recent progress in metal-free electrocatalysts toward ambient N₂ reduction reaction. *Acta Phys.-Chim. Sin.* 37 (7), 2009043. doi:10.3866/pku.Whxb202009043
- Utomo, W. P., Leung, M. K. H., Yin, Z., Wu, H., and Ng, Y. H. (2022). Advancement of bismuth-based materials for electrocatalytic and photo(electro) catalytic ammonia synthesis. *Adv. Funct. Mat.* 32 (4), 2106713. doi:10.1002/adfm.202106713
- van der Ham, C. J. M., Koper, M. T. M., and Hetterscheid, D. G. H. (2014). Challenges in reduction of dinitrogen by proton and electron transfer. *Chem. Soc. Rev.* 43 (15), 5183–5191. doi:10.1039/C4CS00085D
- Vesali-Kermani, E., Habibi-Yangjeh, A., Diarmid-Khalilabad, H., and Ghosh, S. (2020a). Nitrogen photofixation ability of g-C₃N₄ nanosheets/Bi₂MoO₆ heterojunction photocatalyst under visible-light illumination. *J. Colloid Interface Sci.* 563, 81–91. doi:10.1016/j.jcis.2019.12.057
- Vesali-Kermani, E., Habibi-Yangjeh, A., and Ghosh, S. (2020b). Efficiently enhanced nitrogen fixation performance of g-C₃N₄ nanosheets by decorating Ni₃V₂O₈ nanoparticles under visible-light irradiation. *Ceram. Int.* 46 (15), 24472–24482. doi:10.1016/j.ceramint.2020.06.232
- Wen Zhao, W., Qin, J., Teng, W., Mu, J., Chen, C., Ke, J., et al. (2022). Catalytic photo-redox of simulated air into ammonia over bimetallic MOFs nanosheets with oxygen vacancies. *Appl. Catal. B Environ.* 305, 121046. doi:10.1016/j.apcatb.2021.121046
- Wenjie Liu, W., Yin, K., Yuan, K., Zuo, S., Yang, S., Yao, C., et al. (2020). *In situ* synthesis of Bi₂MoO₆@C@attapulgite photocatalyst for enhanced photocatalytic nitrogen fixation ability under simulated solar irradiation. *Colloids Surfaces A Physicochem. Eng. Aspects* 591, 124488. doi:10.1016/j.colsurfa.2020.124488

- Xiao, C., Zhang, L., Wang, K., Wang, H., Zhou, Y., Wang, W., et al. (2018). A new approach to enhance photocatalytic nitrogen fixation performance via phosphate-bridge: A case study of $\text{SiW}_{12}/\text{K}-\text{C}_3\text{N}_4$. *Appl. Catal. B Environ.* 239, 260–267. doi:10.1016/j.apcatb.2018.08.012
- Xiao-Fei Li, X.-F., Li, Q.-K., Cheng, J., Liu, L., Yan, Q., Wu, Y., et al. (2016). Conversion of dinitrogen to ammonia by FeN_3 -embedded graphene. *J. Am. Chem. Soc.* 138 (28), 8706–8709. doi:10.1021/jacs.6b04778
- Xiao-Hong Li, X.-H., Chen, W.-L., Tan, H.-Q., Li, F.-R., Li, J.-P., Li, Y.-G., et al. (2019). Reduced state of the graphene oxide@polyoxometalate nanocatalyst achieving high-efficiency nitrogen fixation under light driving conditions. *ACS Appl. Mat. Interfaces* 11 (41), 37927–37938. doi:10.1021/acsami.9b12328
- Xiao-Hong Li, X.-H., He, P., Wang, T., Zhang, X.-W., Chen, W.-L., Li, Y.-G., et al. (2020). Keggin-type polyoxometalate-based ZIF-67 for enhanced photocatalytic nitrogen fixation. *ChemSusChem* 13 (10), 2769–2778. doi:10.1002/cssc.202000328
- Xiazhang Li, X., He, C., Dai, D., Zuo, S., Yan, X., Yao, C., et al. (2020). Nano-mineral induced nonlinear optical LiNbO_3 with abundant oxygen vacancies for photocatalytic nitrogen fixation: Boosting effect of polarization. *Appl. Nanosci.* 10 (9), 3477–3490. doi:10.1007/s13204-020-01443-6
- Xin Liu, X., Gu, S., Zhao, Y., Zhou, G., and Li, W. (2020). BiVO_4 , Bi_2WO_6 and Bi_2MoO_6 photocatalysis: A brief review. *J. Mat. Sci. Technol.* 56, 45–68. doi:10.1016/j.jmst.2020.04.023
- Xin Wang, X., Feng, Z., Xiao, B., Zhao, J., Ma, H., Tian, Y., et al. (2020). Polyoxometalate-based metal-organic framework-derived bimetallic hybrid materials for upgraded electrochemical reduction of nitrogen. *Green Chem.* 22 (18), 6157–6169. doi:10.1039/D0GC01149E
- Xing, P., Chen, P., Chen, Z., Hu, X., Lin, H., Wu, Y., et al. (2018). Novel ternary $\text{MoS}_2/\text{C}-\text{ZnO}$ composite with efficient performance in photocatalytic NH_3 synthesis under simulated sunlight. *ACS Sustain. Chem. Eng.* 6 (11), 14866–14879. doi:10.1021/acssuschemeng.8b03388
- Xing, P., Wu, S., Chen, Y., Chen, P., Hu, X., Lin, H., et al. (2019). New application and excellent performance of Ag/KNbO_3 nanocomposite in photocatalytic NH_3 synthesis. *ACS Sustain. Chem. Eng.* 7 (14), acssuschemeng.9b01938. doi:10.1021/acssuschemeng.9b01938
- Xing, P., Zhang, W., Chen, L., Dai, X., Zhang, J., Zhao, L., et al. (2020). Preparation of a NiO/KNbO_3 nanocomposite via a photodeposition method and its superior performance in photocatalytic N_2 fixation. *Sustain. Energy Fuels* 4 (3), 1112–1117. doi:10.1039/C9SE01003C
- Xu, T., Ma, D., Li, C., Liu, Q., Lu, S., Asiri, A. M., et al. (2020). Ambient electrochemical NH_3 synthesis from N_2 and water enabled by ZrO_2 nanoparticles. *Chem. Commun.* 56 (25), 3673–3676. doi:10.1039/C9CC10087C
- Xu, H., Ma, Y., Chen, J., Zhang, W., and Yang, J. (2022). Electrocatalytic reduction of nitrate – A step towards a sustainable nitrogen cycle. *Chem. Soc. Rev.* 51, 2710–2758. doi:10.1039/D1CS00857A
- Xu, Y., and Schoonen, M. A. (2000). The absolute energy positions of conduction and valence bands of selected semiconducting minerals. *Am. Mineral.* 85 (3–4), 543–556. doi:10.2138/am-2000-0416
- Xue Chen, X., Li, J.-Y., Tang, Z.-R., and Xu, Y.-J. (2020). Surface-defect-engineered photocatalyst for nitrogen fixation into value-added chemical feedstocks. *Catal. Sci. Technol.* 10 (18), 6098–6110. doi:10.1039/d0cy01227k
- Xue, X., Chen, R., Yan, C., Hu, Y., Zhang, W., Yang, S., et al. (2019). Efficient photocatalytic nitrogen fixation under ambient conditions enabled by the heterojunctions of n-type Bi_2MoO_6 and oxygen-vacancy-rich p-type BiOBr . *Nanoscale* 11 (21), 10439–10445. doi:10.1039/C9NR02279A
- Xuerui Zhang, X., Shi, R., Li, Z., Zhao, J., Huang, H., Zhou, C., et al. (2022). Photothermal-assisted photocatalytic nitrogen oxidation to nitric acid on palladium-decorated titanium oxide. *Adv. Energy Mat.* 12, 2103740. doi:10.1002/aenm.202103740
- Yang, J., Bai, H., Guo, Y., Zhang, H., Jiang, R., Yang, B., et al. (2021). Photodriven disproportionation of nitrogen and its change to reductive nitrogen photofixation. *Angew. Chem. Int. Ed.* 60 (2), 927–936. doi:10.1002/anie.202010192
- Yehuan Li, Y., Chen, X., Zhang, M., Zhu, Y., Ren, W., Mei, Z., et al. (2019). Oxygen vacancy-rich MoO_{3-x} nanobelts for photocatalytic N_2 reduction to NH_3 in pure water. *Catal. Sci. Technol.* 9 (3), 803–810. doi:10.1039/C8CY02357C
- Yi-Fei Zhang, Y.-F., Zhu, Y.-K., Lv, C.-X., Lai, S.-J., Xu, W.-J., Sun, J., et al. (2020). Enhanced visible-light photoelectrochemical performance via chemical vapor deposition of Fe_2O_3 on a WO_3 film to form a heterojunction. *Rare Met.* 39 (7), 841–849. doi:10.1007/s12598-019-01311-5
- Yifu Chen, Y., Liu, H., Ha, N., Licht, S., Gu, S., Li, W., et al. (2020). Revealing nitrogen-containing species in commercial catalysts used for ammonia electrosynthesis. *Nat. Catal.* 3 (12), 1055–1061. doi:10.1038/s41929-020-00527-4
- Yin, S., and Asakura, Y. (2019). Recent research progress on mixed valence state tungsten based materials. *Tungsten* 1 (1), 5–18. doi:10.1007/s42864-019-00001-0
- Yin, Y., Jiang, M., and Liu, C. (2018). DFT study of POM-supported single atom catalyst (M_1/POM , $\text{M} = \text{Ni}, \text{Pd}, \text{Pt}, \text{Cu}, \text{Ag}, \text{Au}$, $\text{POM} = [\text{PW}_{12}\text{O}_{40}]^{3-}$) for activation of nitrogen molecules. *Acta Phys. -Chim. Sin.* 34 (3), 270–277. doi:10.3866/pku.Whxb201707071
- Ying, Z., Chen, S., Zhang, S., Peng, T., and Li, R. (2019). Efficiently enhanced N_2 photofixation performance of sea-urchin-like $\text{W}_{18}\text{O}_{49}$ microspheres with Mn-doping. *Appl. Catal. B Environ.* 254, 351–359. doi:10.1016/j.apcatb.2019.05.005
- Yuan Feng, Y., Zhao, Z., Wang, T., Li, J., Xu, M., Jiao, H., et al. (2022). Magnetic field-enhanced photocatalytic nitrogen fixation over defect-rich ferroelectric Bi_2WO_6 . *Ceram. Int.* 48, 20062–20069. doi:10.1016/j.ceramint.2022.03.282
- Yuan, J., Yi, X., Tang, Y., Liu, M., and Liu, C. (2020). Efficient photocatalytic nitrogen fixation: Enhanced polarization, activation, and cleavage by asymmetrical electron donation to $\text{N}\equiv\text{N}$ bond. *Adv. Funct. Mater.* 30 (4), 1906983. doi:10.1002/adfm.201906983
- Yuhua Wang, Y. H., Liu, T. Y., Li, H. H., Liu, B., and Yang, L. F. (2019). Tungsten-based photocatalysts with UV-Vis-NIR photocatalytic capacity: Progress and opportunity. *Tungsten* 1 (4), 247–257. doi:10.1007/s42864-020-00031-z
- Yuting Wang, Y., Li, H., Zhou, W., Zhang, X., Zhang, B., Yu, Y., et al. (2022). Structurally disordered RuO_2 nanosheets with rich oxygen vacancies for enhanced nitrate electroreduction to ammonia. *Angew. Chem. Int. Ed. Engl.* 61, e202202604. doi:10.1002/anie.202202604
- Yuxin Liu, Y., Xue, Y., Hui, L., Yu, H., Fang, Y., He, F., et al. (2021). Porous graphdiyne loading CoO_x quantum dots for fixation nitrogen reaction. *Nano Energy* 89, 106333. doi:10.1016/j.nanoen.2021.106333
- Zejian Wang, J. H., Ng, Sue-Faye, Wen, Liu, Huang, Junjie, Chen, Pengfei, and Ong, Wee-Jun (2021). Recent progress of perovskite oxide in emerging photocatalysis landscape: Water splitting, CO_2 reduction, and N_2 fixation. *Acta Phys. -Chim. Sin.* 37 (6), 2011033. doi:10.3866/pku.Whxb202011033
- Zhang, Y., Yu, J., Yu, D., Zhou, X., and Lu, W. (2011). Enhancement in the photocatalytic and photoelectrochemical properties of visible-light driven BiVO_4 photocatalyst. *Rare Met.* 30 (1), 192–198. doi:10.1007/s12598-011-0267-8
- Zhang, L., Mohamed, H. H., Dillert, R., and Bahnemann, D. (2012). Kinetics and mechanisms of charge transfer processes in photocatalytic systems: A review. *J. Photochem. Photobiol. C Photochem. Rev.* 13 (4), 263–276. doi:10.1016/j.jphotochemrev.2012.07.002
- Zhang, Y., Dong, N., Tao, H., Yan, C., Huang, J., Liu, T., et al. (2017). Exfoliation of stable 2D black phosphorus for device fabrication. *Chem. Mat.* 29, 66445–66456. doi:10.1021/acs.chemmater.7b01991
- Zhang, G., Meng, Y., Xie, B., Ni, Z., Lu, H., Xia, S., et al. (2021). Precise location and regulation of active sites for highly efficient photocatalytic synthesis of ammonia by facet-dependent BiVO_4 single crystals. *Appl. Catal. B Environ.* 296, 120379. doi:10.1016/j.apcatb.2021.120379
- Zhao, W., Xi, H., Zhang, M., Li, Y., Chen, J., Zhang, J., et al. (2015). Enhanced quantum yield of nitrogen fixation for hydrogen storage with *in situ*-formed carbonaceous radicals. *Chem. Commun.* 51 (23), 4785–4788. doi:10.1039/C5CC00589B
- Zhao, Y., Shi, R., Bian, X., Zhou, C., Zhao, Y., Zhang, S., et al. (2019). Ammonia detection methods in photocatalytic and electrocatalytic experiments: How to improve the reliability of NH_3 production rates? *Adv. Sci.* 6 (8), 1802109. doi:10.1002/advs.201802109
- Zhao, Z. Q., Choi, C., Hong, S., Shen, H. D., Yan, C., Masa, J., et al. (2020). Surface-engineered oxidized two-dimensional Sb for efficient visible light-driven N_2 fixation. *Nano Energy* 78, 105368. doi:10.1016/j.nanoen.2020.105368
- Zhao, Y., Wu, F., Miao, Y., Zhou, C., Xu, N., Shi, R., et al. (2021). Revealing ammonia quantification minefield in photo/electrocatalysis. *Angew. Chem. Int. Ed.* 60 (40), 21728–21731. doi:10.1002/anie.202108769
- Zhen Zhao, Z., Park, J., Choi, C., Hong, S., Hui, X., Zhang, H., et al. (2022). Engineering vacancy and hydrophobicity of two-dimensional TaTe_2 for efficient and stable electrocatalytic N_2 reduction. *Innovation* 3 (1), 100190. doi:10.1016/j.xinn.2021.100190
- Zheng, H., Ou, J. Z., Strano, M. S., Kaner, R. B., Mitchell, A., Kalantar-zadeh, K., et al. (2011). Nanostructured tungsten oxide-properties, synthesis, and applications. *Adv. Funct. Mat.* 21 (12), 2175–2196. doi:10.1002/adfm.201002477
- Zheng, Q., Xu, Y., Wan, Y., Wu, J., Hu, X., Yao, X., et al. (2020). Synthesis of CoFe_2O_4 -modified $\text{g}-\text{C}_3\text{N}_4$ with enhanced photocatalytic performance for nitrogen fixation. *J. Nanopart. Res.* 22 (9), 301. doi:10.1007/s11051-020-05028-w
- Zheng, J., Lu, L., Lebedev, K., Wu, S., Zhao, P., McPherson, I. J., et al. (2021). Fe on molecular-layer MoS_2 as inorganic $\text{Fe}-\text{S}_2$ -Mo motifs for light-driven nitrogen fixation to ammonia at elevated temperatures. *Chem. Catal.* 1 (1), 162–182. doi:10.1016/j.checat.2021.03.002

Zheng Wang, Z., Li, C., and Domen, K. (2019). Recent developments in heterogeneous photocatalysts for solar-driven overall water splitting. *Chem. Soc. Rev.* 48 (7), 2109–2125. doi:10.1039/C8CS00542G

Zhi-Yuan Wang, Z.-Y., Jiang, S.-D., Duan, C.-Q., Wang, D., Luo, S.-H., Liu, Y.-G., et al. (2020). *In situ* synthesis of Co_3O_4 nanoparticles confined in 3D nitrogen-doped porous carbon as an efficient bifunctional oxygen electrocatalyst. *Rare Met.* 39 (12), 1383–1394. doi:10.1007/s12598-020-01581-4

Zhou, S., Zhang, C., Liu, J., Liao, J., Kong, Y., Xu, Y., et al. (2019). Formation of an oriented Bi_2WO_6 photocatalyst induced by *in situ* Bi reduction and its use for efficient nitrogen fixation. *Catal. Sci. Technol.* 9 (20), 5562–5566. doi:10.1039/C9CY00972H

Zhou, X., Liu, H., Xia, B. Y., Ostrikov, K., Zheng, Y., Qiao, S.-Z., et al. (2022). Customizing the microenvironment of CO_2 electrocatalysis via three-

phase interface engineering. *SmartMat* 3 (1), 111–129. doi:10.1002/smm2.1109

Zhu, D., Zhang, L., Ruther, R. E., and Hamers, R. J. (2013). Photo-illuminated diamond as a solid-state source of solvated electrons in water for nitrogen reduction. *Nat. Mat.* 12 (9), 836–841. doi:10.1038/nmat3696

Zhu, J., Chen, X., Thang, A. Q., Li, F.-L., Chen, D., Geng, H., et al. (2022). Vanadium-based metal-organic frameworks and their derivatives for electrochemical energy conversion and storage. *SmartMat.* doi:10.1002/smm2.1091

Ziegenbalg, D., Zander, J., and Marschall, R. (2021). Photocatalytic nitrogen reduction: Challenging materials with reaction engineering. *ChemPhotoChem* 5 (9), 792–807. doi:10.1002/cptc.202100084



OPEN ACCESS

EDITED BY

Honglei Fan,
Chinese Academy of Sciences, China

REVIEWED BY

Sibao Liu,
Tianjin University, China
Yujing Weng,
Henan Polytechnic University, China

*CORRESPONDENCE

Qineng Xia,
xiaoqineng159@163.com
Yanqin Wang,
wangyanqin@ecust.edu.cn

[†]These authors have contributed equally to this work and share first authorship

SPECIALTY SECTION

This article was submitted to Green and Sustainable Chemistry, a section of the journal Frontiers in Chemistry

RECEIVED 27 June 2022

ACCEPTED 11 July 2022

PUBLISHED 22 August 2022

CITATION

Jia H, Lv Q, Xia Q, Hu W and Wang Y (2022), Tailoring the catalytic performance of Cu/SiO₂ for hydrogenolysis of biomass-derived 5-hydroxymethylfurfural to renewable fuels.
Front. Chem. 10:979353.
doi: 10.3389/fchem.2022.979353

COPYRIGHT

© 2022 Jia, Lv, Xia, Hu and Wang. This is an open-access article distributed under the terms of the [Creative Commons Attribution License \(CC BY\)](#). The use, distribution or reproduction in other forums is permitted, provided the original author(s) and the copyright owner(s) are credited and that the original publication in this journal is cited, in accordance with accepted academic practice. No use, distribution or reproduction is permitted which does not comply with these terms.

Tailoring the catalytic performance of Cu/SiO₂ for hydrogenolysis of biomass-derived 5-hydroxymethylfurfural to renewable fuels

Hongyan Jia^{1†}, Qing Lv^{2†}, Qineng Xia^{1*}, Wanpeng Hu¹ and Yanqin Wang^{2*}

¹College of Biological, Chemical Science and Engineering, Jiaying University, Jiaying, China, ²Shanghai Key Laboratory of Functional Materials Chemistry, Research Institute of Industrial Catalysis, School of Chemistry and Molecular Engineering, East China University of Science and Technology, Shanghai, China

Efficient conversion of biomass-derived 5-hydroxymethylfurfural (HMF) to renewable fuels such as 2,5-dimethylfuran (DMF) and 2,5-dimethyltetrahydrofuran (DMTHF) is of significance for sustainable energy supply. For efficient catalyst design, it is important to understand the catalytic behavior and clarify the influence of physico-chemical properties of catalyst on reaction performance. Herein, to study the structure-activity relationships of monometallic Cu catalysts for HMF hydrogenolysis, a series of Cu/SiO₂ catalysts with different physico-chemical properties were prepared and compared for their catalytic performance in HMF hydrogenolysis. It was found that Cu/SiO₂-HT-8.5 catalyst prepared by hydrothermal method showed excellent activity in HMF hydrohydrolysis reaction. Under the optimal reaction condition, the total yield of liquid fuels reaches 91.6% with 57.1% yield of DMF and 34.5% yield of DMTHF in THF solvent. Characterizations such as XRD, H₂-TPR, N₂-adsorption/desorption, TEM and XPS revealed that the Cu particles in the Cu/SiO₂-HT-8.5 catalyst have uniform size and high dispersion. The Cu species and the SiO₂ support have relatively weak interaction and are easy to be reduced to Cu⁰, which makes it show excellent activity in the hydrogenolysis of HMF.

KEYWORDS

5-hydroxymethylfurfural, 2,5-dimethylfuran, renewable fuels, hydrogenolysis, Cu/SiO₂ catalyst

Introduction

Efficient conversion of renewable lignocellulosic biomass to bio-fuels and value-added chemicals is of significance for sustainable energy supply, and reduction of CO₂ emissions, as an alternative strategy to many other ways to solve the energy and environmental issues (Jing et al., 2019; Hao et al., 2021; Qin et al., 2021; Li et al., 2022). 5-hydroxymethylfurfural (HMF) is regarded as one of the most versatile platform molecules that can be converted to a variety of biofuels and chemicals, such as levulinic acid (Yan et al., 2015), liquid alkanes (Xia et al., 2014; Nakagawa et al., 2019), 2,5-furandicarboxylic acid and derivatives (Yang et al., 2020; Nakagawa et al., 2021), 2,5-bis(hydroxymethyl)tetrahydrofuran (BHMTHF) (Nakagawa et al., 2017), 1,6-hexanediol (Xiao et al., 2016) and so forth (Gao et al., 2021). 2,5-dimethylfuran (DMF) and 2,5-dimethyltetrahydrofuran (DMTHF) derived from hydrogenolysis of HMF are not only important chemical intermediates, but also serves as high-grade biofuels with high octane number and high energy density (Roman-Leshkov et al., 2007). Moreover, DMF is also employed as a feedstock for the production of *p*-xylene through the Diels-Alder reaction (Rohling et al., 2018).

The reaction networks for DMF and DMTHF production from HMF contain a series of parallel and consecutive reactions, and therefore it is a challenge to increase the selectivity to the desired products at a complete conversion of HMF (Maki-Arvela et al., 2021). Over the last decade, catalysts based on noble metals (e.g., Pt (Shi et al., 2016), Ru (Zu et al., 2014; Priecel et al., 2018; Feng et al., 2020; Tzeng et al., 2020), Pd (Hu et al., 2021)) and their bimetallics (Requies et al., 2018; Wang et al., 2018; Mhadmhan et al., 2019; Talpade et al., 2019; Pisal & Yadav, 2021) have been extensively explored and proved to be efficient in the hydrogenolysis of HMF to DMF and DMTHF. However, noble metal-based catalysts suffer from the high cost of catalyst preparation, which may limit their large-scale industrial applications.

As an alternative, catalysts based on non-noble transition metals such as Cu, Co and Ni have been widely studied for HMF hydrogenolysis to DMF and DMTHF, with the great majority efforts emphasis on bimetallic catalysts (e.g., Ni-Co (Yang et al., 2015; Yang et al., 2016; Xia et al., 2022), Co-Cu (Guo et al., 2016), Cu-Ni (Zhang Y.-R. et al., 2019; Zhu et al., 2019; Umasankar et al., 2020), Cu-Zn (Zhu et al., 2015; Brzezinska et al., 2020), Ni-Zn (Kong et al., 2017), Co-Fe (Solanki and Rode, 2019) etc.) or bifunctional catalysts that consist of active metal and acidic supports (Shi et al., 2018; Chen N. et al., 2020; Esteves et al., 2020; Guo et al., 2020). For example, Zhu et al. developed an alloyed Cu-Ni encapsulated in carbon catalyst by loading Ni and Cu onto biochar, and the bimetallic Cu-Ni catalyst displayed high catalytic performance for HMF hydrogenolysis to DMF with yield up to 93.5% under the optimized conditions (Zhu et al., 2019). Our group also reported a non-noble bimetallic Ni-Co

catalyst with the uniform dispersion of Ni and Co species on the active carbon for hydrogenolysis of HMF, and an excellent yield (up to 95%) of DMF can be obtained at relatively mild conditions (Yang et al., 2016). Very recently, our group reported a unique core-shell structured Co@CoO catalyst for this reaction and afforded the highest productivity among all catalysts reported to date (Xiang et al., 2022).

Earth-abundant Cu-based catalysts are well known for their hydrogenation ability, especially in the field of CO₂ hydrogenation (Kattel et al., 2017). From the catalyst design point of view, it is important to understand the catalytic behavior and clarify the influence of physico-chemical properties of metal on reaction performance. However, structure-activity relationships of monometallic non-noble metals (Cu, Co, and Ni) on HMF hydrogenolysis have been rarely explored, especially for Cu-based catalysts (Chen S. et al., 2020).

Herein, to study the structure-activity relationships of monometallic Cu catalysts for HMF hydrogenolysis, a series of Cu/SiO₂ catalysts with different physico-chemical properties were prepared and compared for their catalytic performance in HMF hydrogenolysis. The low acidic non-metal oxide SiO₂ was chosen as the support to exclude the effect of the acid sites and metal-support interactions as far as possible.

Experimental

Chemicals and materials

HMF was purchased from Shanghai Mode Pharmaceutical Technology Co., Ltd. Tetrahydrofuran (THF) was purchased from Shanghai Lingfeng Chemical Reagent Co., Ltd. 2,5-dimethylfuran (DMF), tridecane was obtained from Aladdin Reagent (Shanghai) Co., Ltd. SiO₂ was obtained from Afaisha Chemical Co. Ltd. All other chemicals and solvents (analytical grade) were purchased from Sinopharm Chemical Reagent Co., Ltd, China. All the chemicals were used without further purification.

Catalyst preparation

Cu/SiO₂ catalysts were prepared by three different method, namely excessive impregnation (EI), deposition-precipitation (DP) and hydrothermal (HT) method. For a typical EI method, 1.89 g CuNO₃•3H₂O was dissolved in 70 ml deionized water, and then 1.0 g SiO₂ was added into the solution, stirred at room temperature for 12 h. After that, the suspension was dried at 60°C for 12 h. The obtained precursor was then calcined in static air at 450°C for 4 h, and then reduced in flow 10% H₂/Ar mixture at 450°C for 6 h before use. The catalyst was denoted as Cu/SiO₂-EI.

For a typical DP method, 1.89 g $\text{CuNO}_3 \cdot 3\text{H}_2\text{O}$ was dissolved in 70 ml deionized water, and then silica sol (equivalent to 1.0 g SiO_2) was dropped into the solution and stirred for 0.5 h. Then 1.0 mol/L NaOH solution was dropped into the above mixture with stirring, until the pH of the suspension to a set value of 9. Subsequently, the obtained suspension was filtered, washed by deionized water and dried at 60°C for 12 h. The obtained precursor was then calcined and reduced with the same procedure as EI method. The catalysts were denoted as Cu/SiO₂-DP.

For a typical HT method, 1.89 g $\text{CuNO}_3 \cdot 3\text{H}_2\text{O}$ was dissolved in 70 ml deionized water, and then a certain amount of NH_4Cl , $\text{NH}_3 \cdot \text{H}_2\text{O}$ and silica sol (equivalent to 1.0 g SiO_2) were added into the solution to reach a set pH value (6.5 or 8.5) and stirred for 0.5 h. After that, the mixture was placed in ultrasonic bath for 0.5 h, and then transferred into a 100 ml Teflon-lined autoclave and aged at 120°C for 4 h. After cooling to room temperature, the suspension was filtered, washed by deionized water and dried at 60°C for 12 h. The obtained precursor was then calcined and reduced with the same procedure as EI method. The catalysts were denoted as Cu/SiO₂-HT-6.5 or Cu/SiO₂-HT-8.5.

Catalyst characterization

The X-ray diffraction (XRD) patterns of the catalysts were recorded by a Bruker D8 Focus X-ray diffractometer with Cu K α radiation ($\lambda = 0.1541$ nm) operating at 40 kv and 40 mA. The crystal size was calculated using the Scherrer equation through the Cu 111) diffraction peak.

N_2 adsorption-desorption isotherms were measured at -196°C using a Micromeritics ASAP 2020 instrument. The samples were outgassed at 200°C for 6 h before analysis. The specific surface areas were obtained by the Brunauer-Emmett-Teller (BET) method.

H_2 temperature programmed reduction (H_2 -TPR) was performed on a Huasi DAS-7200 automatic chemisorption apparatus. The samples were pretreated with pure Ar at 150°C for 1 h before reduction. After cooling to room temperature, 10% H_2/Ar mixture was introduced and the sample tube was heated to 800°C at a heating rate of 10°C/min. TCD was used as the detector to collect signals.

Transmission electron microscopy (TEM) images were taken using a JEOL 2100F microscope operated at an acceleration voltage of 200 kV. The sample was grinded and dispersed in ethanol under supersonic waves, and then dropped on a copper net and dried before use.

The copper content of the catalyst was determined by Agilent 725ES inductively coupled plasma atomic emission spectrometer (ICP-AES).

X-ray photoelectron spectroscopy (XPS) was tested on a Thermo Scientific Escalab 250Xi X-ray photoelectron spectrometer with a monochromatic Al K α radiation

(1,486.6 eV photons). All of the binding energies were calibrated by C 1s and the binding energy of C-C is 284.6 eV.

Hydrogenolysis reactions

The hydrogenolysis of HMF was carried out in a batch reactor equipped with a magnetic stirrer. Typically, 0.05 g HMF, 0.05 g catalyst, 100 μL tridecane (internal standard) and 5 ml tetrahydrofuran (THF) were put into a Teflon-lined stainless-steel autoclave (50 ml). After purging with H_2 for three times, the reactor was conducted under H_2 pressure at the required condition for a desired time with magnetic stirring. After the reaction, the reactor was cooled with ice-water and depressurized carefully. After centrifugation of the catalyst, the liquid products were identified by GC-MS (Agilent 7,890A-5975C) equipped with an HP-5 capillary column and quantitatively analyzed by GC (Agilent GC7890 B) equipped with a flame ionization detector (FID) and an HP-5 capillary column using tridecane as an internal standard. The injector temperature was set at 270°C, and the column temperature was increased from 50 to 200°C with a ramp rate of 10°C/min.

Results and discussion

Characterization of catalysts

The Cu/SiO₂ catalysts were prepared by impregnation (EI), deposition-precipitation (DP) and hydrothermal (HT) methods at different pH value. Figure 1A shows the XRD patterns of various catalysts after calcination. It can be seen that the Cu/SiO₂-EI and Cu/SiO₂-DP catalysts exhibit diffraction peaks at 35.5°, 38.7°, 48.7°, 53.5°, 61.5° and 66.2°, indexed to (110), (11-1), (111), (20-2), (020) and (11-3) planes of CuO, suggesting the presence of bulk CuO. Interestingly, obvious CuO diffraction peaks were observed for Cu/SiO₂-HT-6.5, but none of them was found for Cu/SiO₂-HT-8.5, which indicates CuO species were highly dispersed on the latter catalyst. The high dispersion of CuO species on Cu/SiO₂-HT-8.5 can be resulted from the calcination of layered copper silicate (Li et al., 2018). These results indicate that the hydrothermal method favors the Cu^{2+} to complex with surface silanol to form layered copper silicate, leading to high dispersed CuO species after calcination.

Figure 1B shows the XRD patterns of various Cu/SiO₂ catalysts after reduction. Evident peaks at 43.4°, 50.5° and 74.1° were observed for Cu/SiO₂-EI catalyst, assigned to (111), (200) and (220) planes of Cu (Dong et al., 2016). The particle size of Cu of Cu/SiO₂-EI was calculated to be ca. 50 nm according to the Cu 111) diffraction peak, which suggests an agglomeration of Cu cluster. The Cu characteristic diffraction peaks can also be clearly found on Cu/SiO₂-DP and Cu/SiO₂-HT-6.5 catalysts,

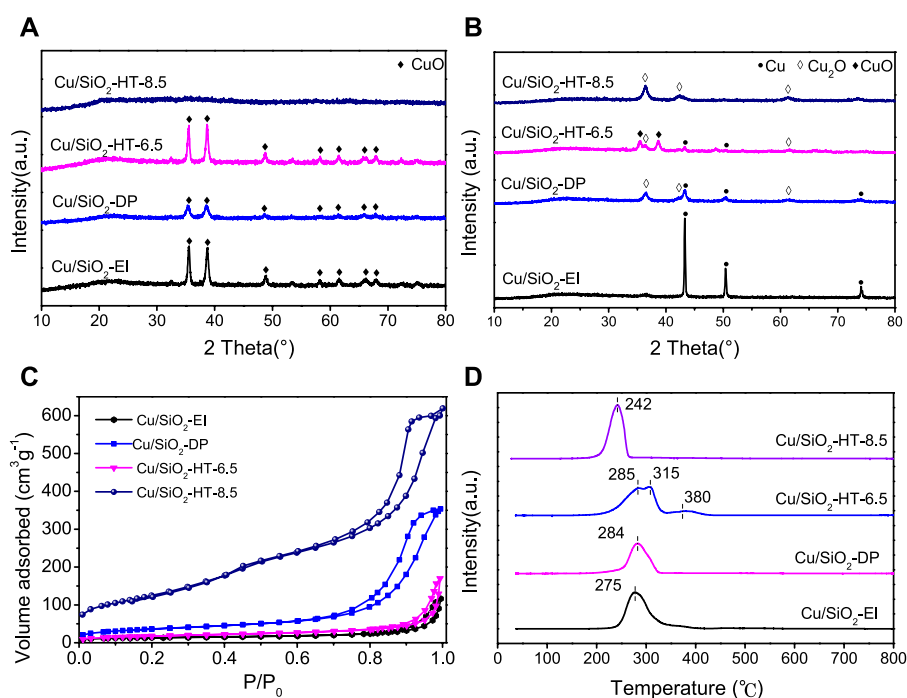


FIGURE 1

Physicochemical characterization of Cu/SiO₂ catalysts prepared by different method. (A) XRD patterns of Cu/SiO₂ catalysts before reduction; (B) XRD patterns of Cu/SiO₂ catalysts after reduction; (C) N₂ adsorption-desorption isotherm of Cu/SiO₂ catalysts; (D) H₂-TPR profiles of Cu/SiO₂ catalysts.

TABLE 1 Cu loading and physical properties of Cu/SiO₂ catalysts prepared by different method.

Catalyst	Cu loading (wt%)	S _{BET} (m ² g ⁻¹)	V _{pore} (cm ³ g ⁻¹)	Pore size (nm)
Cu/SiO ₂ -EI	32	48	0.09	7.6
Cu/SiO ₂ -DP-9	23	132	0.52	15.9
Cu/SiO ₂ -HT-6.5	33	65	0.12	7.5
Cu/SiO ₂ -HT-8.5	31	449	0.92	8.2

while no obvious Cu diffraction peaks observed on Cu/SiO₂-HT-8.5, indicating the high dispersion of Cu nanoparticles on the latter catalyst. Cu/SiO₂-HT-6.5 still exhibits the diffraction peaks at 35.5° (110) and 38.8° (11-1) of CuO, suggesting an incomplete reduction of the catalyst. In addition, Cu/SiO₂-DP and Cu/SiO₂-HT catalysts all exhibit the diffraction peaks at 36.5°, 42.3° and 61.3°, attributed to the (111), (200) and (220) planes of Cu₂O (Wang et al., 2002), indicating the partial reduction of CuO on these catalysts, due to the interactions between CuO_x and SiO₂.

N₂ adsorption/desorption isotherms for the four Cu/SiO₂ catalysts are presented in Figure 1C, and the calculated textural properties as well as ICP-AES results are listed in Table 1. All catalysts present the isotherm shape of type IV (IUPAC classification), indicating the existence of mesoporous

structure in all cases. There are distinct differences of the textural properties in these catalysts. Cu/SiO₂-HT-8.5 possesses the largest BET specific surface area (449 m²g⁻¹) and pore volume (0.92 cm³g⁻¹), while Cu/SiO₂-EI shows the smallest ones (48 m²g⁻¹ and 0.09 cm³g⁻¹, respectively). The large BET specific surface area of Cu/SiO₂-HT-8.5 allows the high dispersion of CuO_x species on the SiO₂ surface, consistent with the XRD results. The Cu contents in Cu/SiO₂-EI and Cu/SiO₂-HT catalysts analyzed by ICP-AES were close to the set value (33 wt%), whereas only 23 wt% Cu was detected in Cu/SiO₂-DP catalyst, which indicates almost a third of Cu content was lost during the DP process.

The reduction features of Cu/SiO₂ catalysts were investigated by H₂-TPR experiments. As shown in Figure 1D, the H₂-TPR

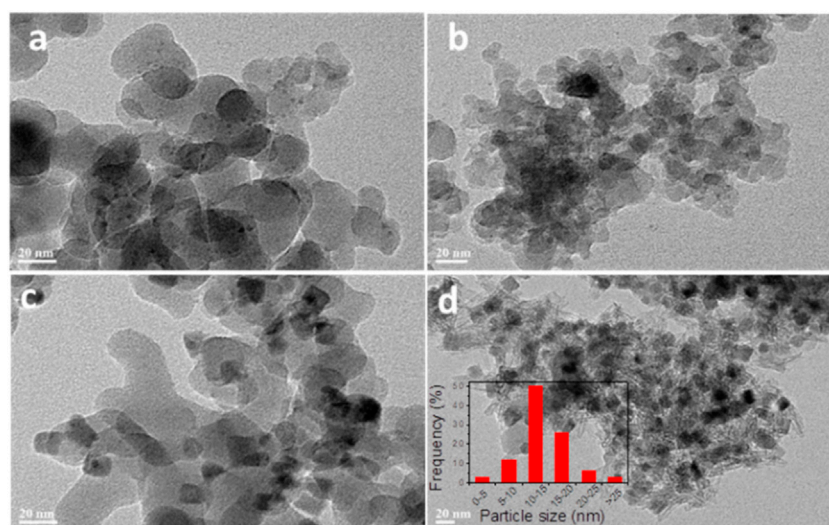


FIGURE 2

Typical TEM images of Cu/SiO₂ catalysts prepared by different method after reduction. (A) Cu/SiO₂-EI, (B) Cu/SiO₂-DP, (C) Cu/SiO₂-HT-6.5, (D) Cu/SiO₂-HT-8.5.

profile of Cu/SiO₂-EI and Cu/SiO₂-DP presents a broad hydrogen consumption peak centered at 275 and 284°C, respectively, which can be attributed to the reduction of bulk CuO (Mo and Kawi, 2014). Significant difference was presented for the reduction peaks of Cu/SiO₂-HT prepared at different pH values. Cu/SiO₂-HT-6.5 catalyst exhibits two adjacent reduction peaks at 250–350°C, assigned to the reduction of bulk CuO with multiple sizes. Generally, the reduction peak at high temperature is caused by the reduction of large bulk CuO, and that at low temperature is caused by the reduction of highly dispersed isolated CuO particles (Mo and Kawi, 2014). Cu/SiO₂-HT-8.5 shows a single symmetrical reduction peak at 242°C. This indicates that there are well-dispersed CuO species with uniform size on the catalyst, which is consistent with the XRD results. Moreover, different reduction temperature can also reflect the strength of the metal-support interactions (Cui et al., 2016). Cu/SiO₂-HT-8.5 exhibit the lowest reduction temperature of CuO, suggesting the weakest interaction between Cu species and SiO₂.

The dispersions of the Cu particles in Cu/SiO₂ catalysts after reduction were further evaluated by TEM (Figure 2). It can be seen from Figures 2A–C that Cu particles were unevenly dispersed on SiO₂ surface for Cu/SiO₂-EI, Cu/SiO₂-DP and Cu/SiO₂-HT-6.5, with the co-existence of both small and large Cu particles. In contrast, it can be clearly seen that Cu particles are uniformly dispersed on the SiO₂ support for Cu/SiO₂-HT-8.5 (Figure 2D). These results are in well agreement with the XRD and H₂-TPR results. Most of the Cu particles are in the range of 10–15 nm for Cu/SiO₂-HT-8.5, as shown in the particle size distribution in Figure 2D. It should be noted that such size (10–15 nm) of Cu particle is relatively small compared to its ultra

high Cu loading of 33 wt%. The results reveal that the metal-support interaction adjusted by different preparation method can affect not only the reduction of CuO, but also the dispersion of Cu particles on SiO₂ surface.

The chemical state of Cu species plays a crucial role on the catalytic performance of Cu/SiO₂ catalysts for HMF hydrogenolysis. The Cu⁰ and Cu⁺ species on the catalyst surface play different roles in catalytic reactions, such as activation of H₂ or adsorption of substrate. There are two steps of reaction in HMF hydrogenolysis to DMF, namely the hydrogenation of the side -CH = O groups and the following hydrogenolysis of -CH₂-OH groups, which both need the activation of H₂ and adsorption of HMF (Zheng et al., 2017). Therefore, XPS and XAES analyses were performed to evaluate the chemical state of Cu species on SiO₂ surface. As XPS spectra shown in Figure 3A, all four catalysts display binding energy peaks of Cu 2p_{3/2} at 932.1–932.5 eV, which can be attributed to the formation of Cu⁰ or Cu⁺ (Liu et al., 2015; Li et al., 2016). In the Cu/SiO₂-EI, Cu/SiO₂-DP and Cu/SiO₂-HT-6.5 catalysts, Cu 2p_{3/2} has both low binding energy (932.1–932.3) and high binding energy (933.7–934.1), indicating that Cu element in these three catalysts exists not only as Cu⁺ or Cu⁰, but also as Cu²⁺ species (Li et al., 2016). In contrast, no high binding energy peak of Cu 2p_{3/2} was observed in Cu/SiO₂-HT-8.5 catalyst, attributed to the disappearance of Cu²⁺ species after reduction. These XPS results indicate the highest reducibility of Cu/SiO₂-HT-8.5, which is in well accordance with H₂-TPR results.

Since it is difficult to distinguish the Cu⁰ and Cu⁺ by XPS spectra, XAES was carried out to determine the surface Cu⁰ and Cu⁺ species of the reduced Cu/SiO₂ catalysts. All the reduced

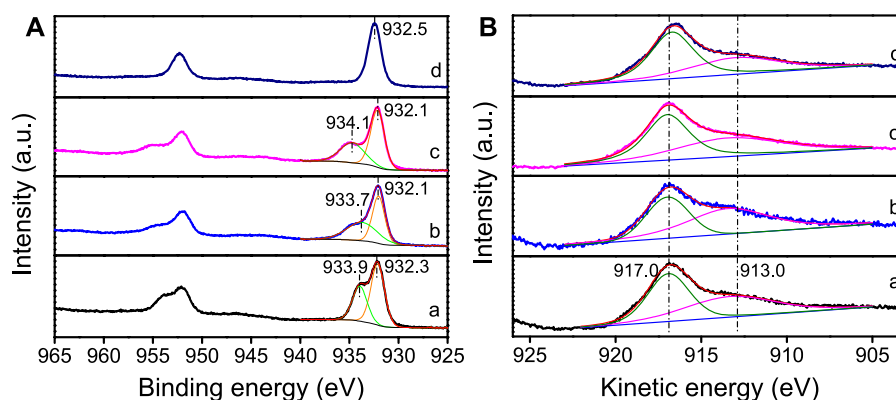


FIGURE 3

Cu 2p XPS (A) and Cu LMM XAFS (B) profiles of Cu/SiO₂ catalysts prepared by different method after reduction. (a) Cu/SiO₂-EI, (b) Cu/SiO₂-DP, (c) Cu/SiO₂-HT-6.5, (d) Cu/SiO₂-HT-8.5.

TABLE 2 Kinetic energy and ratio of Cu⁰/(Cu⁰+ Cu⁺) of Cu/SiO₂ catalysts prepared by different method.

Catalyst	KE ^a (eV)		Cu ⁰ /(Cu ⁰ + Cu ⁺) ^b
	Cu ⁺	Cu ⁰	
Cu/SiO ₂ -EI	913.4	916.9	0.51
Cu/SiO ₂ -DP	913.4	917.0	0.40
Cu/SiO ₂ -HT-6.5	913.4	917.0	0.54
Cu/SiO ₂ -HT-8.5	913.0	916.7	0.59

^aKinetic energy.

^bThe ratio of Cu⁰/(Cu⁰+ Cu⁺) was calculated from Cu LMM XAES spectra.

catalysts exhibit the Auger kinetic energy peaks of Cu LMM at 917.0 and 913.0 eV (Figure 3B), corresponding to Cu⁰ and Cu⁺ species, respectively (Zhang Z. et al., 2019). According to the peak area of the kinetic energy peak of Cu LMM XAES spectra, we can calculate the ratio of Cu⁰/(Cu⁰+ Cu⁺) (Table 2). The peak area ratio of surface Cu⁰/(Cu⁰+ Cu⁺) varies from 0.40 to 0.59 as the different synthetic method of Cu/SiO₂, with the Cu/SiO₂-HT-8.5 catalyst showing the largest proportion of Cu⁰. It is known that the weaker interaction between Cu species and the support leads to the easier reduction of CuO to Cu⁰, while the stronger interaction generates more Cu⁺ species. The largest proportion of Cu⁰ in Cu/SiO₂-HT-8.5 catalyst indicates that the weakest metal-support interaction compared with the other three catalysts, which is consistent with the H₂-TPR results.

Catalytic performances for hydroxymethylfurfural hydrogenolysis

The reaction activity of Cu/SiO₂ catalysts prepared by different methods in HMF hydrogenolysis is shown in

Table 3. HMF was completely converted in all cases, indicating the hydrogenation of HMF to BHMF is easy over Cu-based catalysts. However, the selectivity of the products was obviously different. Among them, the catalyst prepared by over-impregnation method (Cu/SiO₂-EI) and deposition precipitation method (Cu/SiO₂-DP) gave 2,5-dihydroxymethylfuran (BHMF) as a main product with 83.1 and 84.9% yield, respectively, while the total yields of 2,5-dimethylfuran (DMF) and further hydrogenation product 2,5-dimethyltetrahydrofuran (DMTHF) were less than 10%, suggesting a poor hydrogenolysis activity. In contrast, Cu/SiO₂ prepared by hydrothermal method offered a much stronger hydrogenolysis activity with DMF and DMTHF as the majority products, especially for Cu/SiO₂-HT-8.5 which achieving the highest activity in HMF hydrohydrolysis with 57.1% yield of DMF and 34.5% yield of DMTHF. It was reported that the activity of Cu-based catalysts in HMF hydrogenolysis is proportional to the specific surface area of the metallic Cu⁰. The high activity for HMF hydrogenolysis over Cu/SiO₂-HT-8.5 catalyst can be attributed to the high Cu dispersion, small Cu particle size and high proportion of Cu⁰, which is well evidenced by XRD characterization, H₂-TPR, TEM images, XPS and XAES spectra.

Reaction pathway study and reaction optimization for hydroxymethylfurfural hydrogenolysis

The reaction pathway of HMF hydrogenolysis over Cu/SiO₂-HT-8.5 was studied by analyzing the product distribution at different reaction time, as shown in Figure 4. It can be seen that HMF has been completely converted when reaction for 2 h, along with a large number of intermediates BHMF (49.8%) and HMMF (11.2%), as well

TABLE 3 Catalytic performance of HMF hydrogenolysis over Cu/SiO₂ catalysts prepared by different methods.

Catalysts	Conv. of HMF(%)	Yield (%) or selectivity (%)				
		DMF	DMTHF	BHMF	HMMF	Carbon balance
Cu/SiO ₂ -EI	>99.9	5.0	1.6	83.1	7.6	97.3
Cu/SiO ₂ -DP	>99.9	3.4	0.5	84.9	7.8	96.6
Cu/SiO ₂ -HT-6.5	>99.9	42.9	41.4	0	5.0	90.6
Cu/SiO ₂ -HT-8.5	>99.9	57.1	34.5	0	0	93.6

Reaction condition: 0.05 g HMF, 0.05 g catalyst, 100 μ L tridecane, 5 ml THF, 200°C, 8 h.

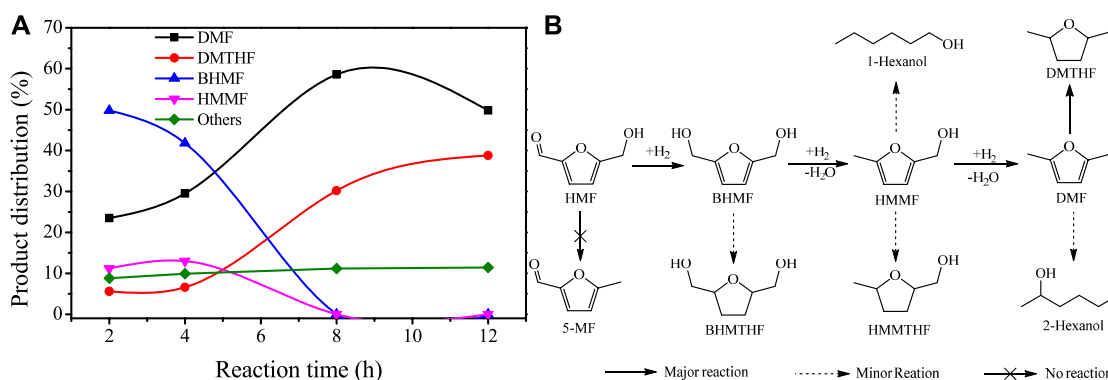


FIGURE 4

Reaction pathway study of HMF hydrogenolysis over Cu/SiO₂-HT-8.5 catalyst. (A) Product distribution of HMF hydrogenolysis at different reaction time; (B) Proposed reaction pathways for HMF hydrogenolysis over Cu/SiO₂-HT-8.5 catalyst. Reaction conditions: 0.05 g HMF, 0.05 g catalyst, 100 μ L tridecane, 5 ml THF, 200°C, 0.6 MPa.

as 23.5% yield of product DMF. This result indicated that the hydrogenation of exocyclic aldehyde group (C=O bond) is a rapid and facile step over Cu/SiO₂-HT-8.5 catalyst, confirming the high hydrogenation activity of Cu species. It is noted that no 5-methylfurfural (5-MF) was detected, revealing that HMF was first undergo hydrogenation of aldehyde group to BHMF rather than hydrogenolysis of hydroxyl group to 5-MF. After reaction for 4 h, the yield of DMF gradually increased to 29.8%, with the decrease of BHMF to 41.8% and slight increase of HMMF to 13.0%. Only trace of DMTHF was produced at this time, indicating that the hydrogenolysis of hydroxyl group is much faster than the hydrogenation of furan ring over Cu/SiO₂-HT-8.5. As the reaction further extended to 8 h, the yield of DMF continued to increase to 58.6%, with the complete conversion of BHMF and HMMF. At the same time, it is noteworthy that the yield of DMTHF also increased rapidly to 30.2%, as well as a small amount of hydration ring opening

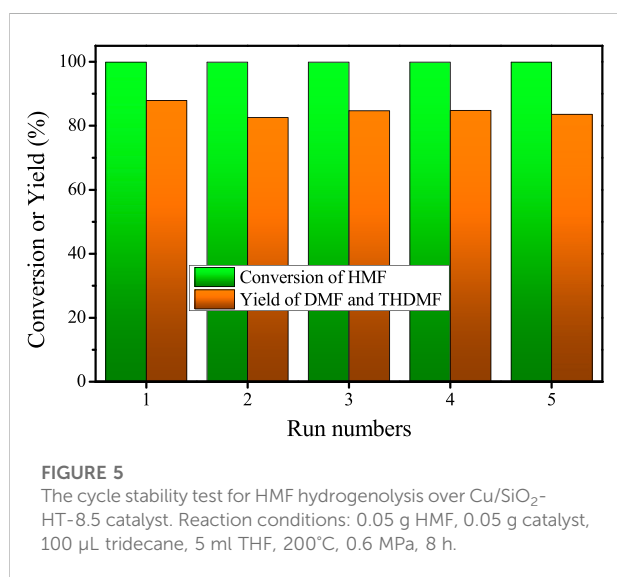
products of DMF. When the reaction was further extended to 12 h, the yield of DMF decreased from 58.6 to 49.8%, and the yield of DMTHF further increased to 38.8%, indicating that the further extension of reaction time would promote the cyclic hydrogenation reaction of DMF to DMTHF. During the reaction period, small amount of other by-products (such as BHMTHF, HMMTHF, hexanols etc., denoted by others) were also detected, totally account for ca. 10%. According to the variation tendency of product distribution versus reaction time, the reaction pathways of HMF hydrogenolysis to DMF and DMTHF over Cu/SiO₂-HT-8.5 was proposed in Figure 4B.

To further tailor the catalytic performance of Cu/SiO₂ for HMF hydrogenolysis, we investigated the influence of reaction temperature and H₂ pressure on the reaction performance, as shown in Table 4. When increase the reaction temperature from 180 to 220°C at 0.6 MPa H₂ pressure, the yield of DMF first increased from 47.5 to 57.1% and then decreased to 51.0%.

TABLE 4 The effects of temperature and pressure on the conversion of HMF over Cu/SiO₂-HT-8.5 catalyst.

Entry	T/°C	P/MPa	Conv. of HMF	Y _{DMF}	Y _{DMTHF}	Y _{DMF+DMTHF}
1	180	0.6	>99.9	47.5	30.7	88.2
2	200	0.6	>99.9	57.1	34.5	91.6
3	220	0.6	>99.9	51.0	36.0	87.0
4	200	0.2	>99.9	66.8	24.3	91.1
5	200	1.0	>99.9	58.1	35.4	93.5
6	200	1.4	>99.9	46.5	34.4	80.9

Reaction conditions: 0.05 g HMF, 0.05 g catalyst, 100 μ L tridecane, 5 ml THF, 8 h.



According to the detection of the product distribution, lower temperature (180°C) led to the incomplete conversion of intermediate HMMF and higher temperature (220°C) resulted in a small amount of side reaction of DMF to hydration by-products. At the same time, the yield of DMTHF continuously increased from 30.7 to 36% with the increase of reaction temperature, indicating that higher temperature accelerated the reaction rate of furan ring hydrogenation and in favor of the production of DMTHF.

When the reaction temperature was fixed at 200°C, the variation of H₂ pressure showed that the H₂ pressure for HMF hydrogenolysis can be as low as 0.2 MPa, at which a high DMF yield of 66.8% was reached, along with 24.3% yield of DMTHF. This result further confirms the high activity of Cu/SiO₂-HT-8.5 catalyst for HMF hydrogenolysis. Increasing of the H₂ pressure from 0.2 to 1.4 MPa led to the decrease of the DMF yield from 66.8 to 46.5% with a slight increase of DMTHF, indicating that high H₂ pressure in favor of the hydrogenation of furan ring, leading to a decline of DMF yield.

Stability test

The stability of a catalyst is an important factor to evaluate its prospect for industrial application. Therefore, the cycle stability of Cu/SiO₂-HT-8.5 catalyst for HMF hydrohydrolysis was also investigated under the optimal reaction conditions (200°C, 0.6 MPa, 8 h). After the first run, the catalyst was separated from the liquid phase by centrifugation, washed with THF, dried and re-used directly for the second run. No obvious activity loss was found after five successive runs and the total yield of DMF and DMTHF maintain close to the values as the first run (Figure 5), revealing the high stability and recyclability of Cu/SiO₂-HT-8.5 catalyst. These results suggest that the high dispersion of Cu species with smaller Cu particle offers not only high activity for HMF hydrogenolysis, but also high catalyst stability.

Conclusion

In summary, we have studied the structure-activity relationships of four Cu/SiO₂ catalysts prepared by different method for HMF hydrogenolysis. It was demonstrated that Cu/SiO₂-HT-8.5 catalyst prepared by hydrothermal method showed the best catalytic activity in HMF hydrohydrolysis reaction. Under the optimal reaction condition, the total yield of liquid fuels reaches 91.6% with 57.1% yield of DMF and 34.5% yield of DMTHF in THF solvent. A combination of multiple characterization revealed that the Cu particles in the Cu/SiO₂-HT-8.5 catalyst have uniform size and high dispersion. The Cu species and the SiO₂ support have relatively weak interaction and are easy to be reduced to Cu⁰, which makes it an excellent catalyst for the hydrogenolysis of HMF. This work provides a new possibility for cheap monometallic catalyst design for biomass valorization.

Data availability statement

The original contributions presented in the study are included in the article/supplementary material, further inquiries can be directed to the corresponding authors.

Author contributions

HJ: Writing-original draft, Writing-review and editing. QL: Data curation, Visualization. QX: Methodology, Writing-review and editing, Funding acquisition. WH: Writing-review and editing. YW: Conceptualization, Supervision, Writing-review and editing, Funding acquisition.

Funding

This work was financially supported by the National Natural Science Foundation of China (No. 21972056 and 21832002),

References

- Brzezinska, M., Keller, N., and Ruppert, A. M. (2020). Self-tuned properties of CuZnO catalysts for hydroxymethylfurfural hydrodeoxygenation towards dimethylfuran production. *Catal. Sci. Technol.* 10 (3), 658–670. doi:10.1039/c9cy01917k
- Chen, N., Zhu, Z., Ma, H., Liao, W., and Lü, H. (2020a). Catalytic upgrading of biomass-derived 5-hydroxymethylfurfural to biofuel 2, 5-dimethylfuran over Beta zeolite supported non-noble Co catalyst. *Mol. Catal.* 486, 110882. doi:10.1016/j.mcat.2020.110882
- Chen, S., Ciotonea, C., De Oliveira Vigier, K., Jérôme, F., Wojcieszak, R., Dumeignil, F., et al. (2020b). Hydroconversion of 5-hydroxymethylfurfural to 2, 5-dimethylfuran and 2, 5-dimethyltetrahydrofuran over non-promoted Ni/SBA-15. *ChemCatChem* 12 (7), 2050–2059. doi:10.1002/cctc.201902028
- Cui, Y., Chen, X., and Dai, W.-L. (2016). Continuous heterogeneous hydrogenation of CO₂-derived dimethyl carbonate to methanol over a Cu-based catalyst. *RSC Adv.* 6 (73), 69530–69539. doi:10.1039/c6ra14447k
- Dong, F., Ding, G. Q., Zheng, H. Y., Xiang, X. M., Chen, L. F., Zhu, Y. L., et al. (2016). Highly dispersed Cu nanoparticles as an efficient catalyst for the synthesis of the biofuel 2-methylfuran. *Catal. Sci. Technol.* 6 (3), 767–779. doi:10.1039/c5cy00857c
- Esteves, L. M., Brijaldo, M. H., Oliveira, E. G., Martinez, J. J., Rojas, H., Caytuero, A., et al. (2020). Effect of support on selective 5-hydroxymethylfurfural hydrogenation towards 2, 5-dimethylfuran over copper catalysts. *Fuel* 270, 117524. doi:10.1016/j.fuel.2020.117524
- Feng, L., Li, X., Lin, Y., Liang, Y., Chen, Y., Zhou, W., et al. (2020). Catalytic hydrogenation of 5-hydroxymethylfurfural to 2, 5-dimethylfuran over Ru based catalyst: Effects of process parameters on conversion and products selectivity. *Renew. Energy* 160, 261–268. doi:10.1016/j.renene.2020.06.123
- Gao, G., Jiang, Z. C., and Hu, C. W. (2021). Selective hydrogenation of the carbonyls in furfural and 5-hydroxymethylfurfural catalyzed by PtNi alloy supported on SBA-15 in aqueous solution under mild conditions. *Front. Chem.* 9, 759512. doi:10.3389/fchem.2021.759512
- Guo, D., Liu, X., Cheng, F., Zhao, W., Wen, S., Xiang, Y., et al. (2020). Selective hydrogenolysis of 5-hydroxymethylfurfural to produce biofuel 2, 5-dimethylfuran over Ni/ZSM-5 catalysts. *Fuel* 274, 117853. doi:10.1016/j.fuel.2020.117853
- Guo, W., Liu, H., Zhang, S., Han, H., Liu, H., Jiang, T., et al. (2016). Efficient hydrogenolysis of 5-hydroxymethylfurfural to 2, 5-dimethylfuran over a cobalt and copper bimetallic catalyst on N-graphene-modified Al₂O₃. *Green Chem.* 18 (23), 6222–6228. doi:10.1039/c6gc02630c
- Hao, L., Xia, Q., Zhang, Q., Masa, J., and Sun, Z. (2021). Improving the performance of metal-organic frameworks for thermo-catalytic CO₂ conversion: Strategies and perspectives. *Chin. J. Catal.* 42 (11), 1903–1920. doi:10.1016/s1872-2067(21)63841-x
- Hu, B., Warczinski, L., Li, X., Lu, M., Bitzer, J., Heidelmann, M., et al. (2021). Formic acid-assisted selective hydrogenolysis of 5-hydroxymethylfurfural to 2, 5-dimethylfuran over bifunctional Pd nanoparticles supported on N-doped mesoporous carbon. *Angew. Chem. Int. Ed.* 60 (12), 6807–6815. doi:10.1002/anie.202012816
- Jing, Y., Guo, Y., Xia, Q., Liu, X., and Wang, Y. (2019). Catalytic production of value-added chemicals and liquid fuels from lignocellulosic biomass. *Chem* 5 (10), 2520–2546. doi:10.1016/j.chempr.2019.05.022
- Kattel, S., Ramirez, P. J., Chen, J. G., Rodriguez, J. A., and Liu, P. (2017). Active sites for CO₂ hydrogenation to methanol on Cu/ZnO catalysts. *Science* 355 (6331), 1296–1299. doi:10.1126/science.aal3573
- Kong, X., Zhu, Y., Zheng, H., Zhu, Y., and Fang, Z. (2017). Inclusion of Zn into metallic Ni enables selective and effective synthesis of 2, 5-dimethylfuran from bioderived 5-hydroxymethylfurfural. *ACS Sustain. Chem. Eng.* 5 (12), 11280–11289. doi:10.1021/acssuschemeng.7b01813
- Li, B. L., Li, L. L., Sun, H., and Zhao, C. (2018). Selective deoxygenation of aqueous furfural to 2-methylfuran over Cu-0/Cu₂O center dot SiO₂ sites via a copper phyllosilicate precursor without extraneous gas. *ACS Sustain. Chem. Eng.* 6 (9), 12096–12103. doi:10.1021/acssuschemeng.8b02425
- Li, F., Cao, B., Ma, R., Liang, J., Song, H., Song, H., et al. (2016). Performance of Cu/TiO₂-SiO₂ catalysts in hydrogenation of furfural to furfuryl alcohol. *Can. J. Chem. Eng.* 94 (7), 1368–1374. doi:10.1002/cjce.22503
- Li, X., Li, L., Xia, Q., Hong, S., Hao, L., Robertson, A. W., et al. (2022). Selective electroreduction of CO₂ and CO to C₂H₄ by synergistically tuning nanocavities and the surface charge of copper oxide. *ACS Sustain. Chem. Eng.* 10 (19), 6466–6475. doi:10.1021/acssuschemeng.2c01600
- Liu, H., Huang, Z., Han, Z., Ding, K., Liu, H., Xia, C., et al. (2015). Efficient production of methanol and diols via the hydrogenation of cyclic carbonates using copper-silica nanocomposite catalysts. *Green Chem.* 17 (8), 4281–4290. doi:10.1039/c5gc00810g
- Maki-Arvela, P., Ruiz, D., and Murzin, D. Y. (2021). Catalytic hydrogenation/hydrogenolysis of 5-hydroxymethylfurfural to 2, 5-dimethylfuran. *ChemSusChem* 14 (1), 150–168. doi:10.1002/cssc.202001927
- Mhadmhan, S., Franco, A., Pineda, A., Reubroycharoen, P., and Luque, R. (2019). Continuous flow selective hydrogenation of 5-hydroxymethylfurfural to 2, 5-dimethylfuran using highly active and stable Cu-Pd/reduced graphene oxide. *ACS Sustain. Chem. Eng.* 7 (16), 14210–14216. doi:10.1021/acssuschemeng.9b03017

- Mo, L., and Kawi, S. (2014). An *in situ* self-assembled core-shell precursor route to prepare ultrasmall copper nanoparticles on silica catalysts. *J. Mat. Chem. A* 2 (21), 7837. doi:10.1039/c3ta14592a
- Nakagawa, Y., Tamura, M., and Tomishige, K. (2019). Recent development of production technology of diesel- and jet-fuel-range hydrocarbons from inedible biomass. *Fuel Process. Technol.* 193, 404–422. doi:10.1016/j.fuproc.2019.05.028
- Nakagawa, Y., Tamura, M., and Tomishige, K. (2017). Supported metal catalysts for total hydrogenation of furfural and 5-hydroxymethylfurfural. *J. Jpn. Pet. Inst.* 60 (1), 1–9. doi:10.1627/jpi.60.1
- Nakagawa, Y., Yabushita, M., and Tomishige, K. (2021). Reductive conversion of biomass-derived furancarboxylic acids with retention of carboxylic acid moiety. *Trans. Tianjin Univ.* 27, 165–179. doi:10.1007/s12209-021-00284-w
- Pisal, D. S., and Yadav, G. D. (2021). Production of biofuel 2, 5-dimethylfuran using highly efficient single-step selective hydrogenation of 5-hydroxymethylfurfural over novel Pd-Co/Al-Zr mixed oxide catalyst. *Fuel* 290, 119947. doi:10.1016/j.fuel.2020.119947
- Priecel, P., Endot, N. A., Cara, P. D., and Lopez-Sanchez, J. A. (2018). Fast catalytic hydrogenation of 2, 5-hydroxymethylfurfural to 2, 5-dimethylfuran with ruthenium on carbon nanotubes. *Ind. Eng. Chem. Res.* 57 (6), 1991–2002. doi:10.1021/acs.iecr.7b04715
- Qin, Y., Guo, J., and Zhao, M. (2021). Metal-Organic framework-based solid acid materials for biomass upgrade. *Trans. Tianjin Univ.* 27, 434–449. doi:10.1007/s12209-021-00298-4
- Requies, J. M., Frias, M., Cuezva, M., Iriondo, A., Agirre, I., Viar, N., et al. (2018). Hydrogenolysis of 5-hydroxymethylfurfural to produce 2, 5-dimethylfuran over ZrO₂ supported Cu and RuCu catalysts. *Ind. Eng. Chem. Res.* 57 (34), 11535–11546. doi:10.1021/acs.iecr.8b01234
- Rohling, R. Y., Uslamin, E., Zijlstra, B., Tranca, I. C., Filot, N. A. W., Hensen, E. J. M., et al. (2018). An active alkali-exchanged faujasite catalyst for p-xylene production via the one-pot diels-alder cycloaddition/dehydration reaction of 2, 5-dimethylfuran with ethylene. *ACS Catal.* 8 (2), 760–769. doi:10.1021/acscatal.7b03343
- Roman-Leshkov, Y., Barrett, C. J., Liu, Z. Y., and Dumesic, J. A. (2007). Production of dimethylfuran for liquid fuels from biomass-derived carbohydrates. *Nature* 447 (7147), 982–985. doi:10.1038/nature05923
- Shi, G., Yang, L., Liu, Z., Chen, X., Zhou, J., Yu, Y., et al. (2018). Photocatalytic reduction of CO₂ to CO over copper decorated g-C₃N₄ nanosheets with enhanced yield and selectivity. *Appl. Surf. Sci.* 427, 1165–1173. doi:10.1016/j.apsusc.2017.08.148
- Shi, J., Wang, Y., Yu, X., Du, W., and Hou, Z. (2016). Production of 2, 5-dimethylfuran from 5-hydroxymethylfurfural over reduced graphene oxides supported Pt catalyst under mild conditions. *Fuel* 163, 74–79. doi:10.1016/j.fuel.2015.09.047
- Solanki, B. S., and Rode, C. V. (2019). Selective hydrogenation of 5-HMF to 2, 5-DMF over a magnetically recoverable non-noble metal catalyst. *Green Chem.* 21 (23), 6390–6406. doi:10.1039/c9gc03091c
- Talpade, A. D., Tiwari, M. S., and Yadav, G. D. (2019). Selective hydrogenation of bio-based 5-hydroxymethyl furfural to 2, 5-dimethylfuran over magnetically separable Fe-Pd/C bimetallic nanocatalyst. *Mol. Catal.* 465, 1–15. doi:10.1016/j.mcat.2018.12.009
- Tzeng, T.-W., Lin, C.-Y., Pao, C.-W., Chen, J.-L., Nuguid, R. J. G., Chung, P.-W., et al. (2020). Understanding catalytic hydrogenolysis of 5-hydroxymethylfurfural (HMF) to 2, 5-dimethylfuran (DMF) using carbon supported Ru catalysts. *Fuel Process. Technol.* 199, 106225. doi:10.1016/j.fuproc.2019.106225
- Umasankar, S., Tamizhdurai, P., Santhana krishnan, P., Narayanan, S., Mangesh, V. L., Shanthi, K., et al. (2020). Effect of copper on NiCu bimetallic catalyst supported on SBA-16 for the catalytic hydrogenation of 5-hydroxymethylfurfural to 2, 5-dimethylfuran. *Biomass Bioenergy* 143, 105868. doi:10.1016/j.biombioe.2020.105868
- Wang, W. Z., Wang, G. H., Wang, X. S., Zhan, Y. J., Liu, Y. K., Zheng, C. L., et al. (2002). Synthesis and characterization of Cu₂O nanowires by a novel reduction route. *Adv. Mat.* 14 (1), 67–69. doi:10.1002/1521-4095(20020104)14:1<67::aid-adma67>3.0.co;2-z
- Wang, Y., Huang, N.-Y., Shen, J.-Q., Liao, P.-Q., Chen, X.-M., Zhang, J.-P., et al. (2018). Hydroxide ligands cooperate with catalytic centers in metal-organic frameworks for efficient photocatalytic CO₂ reduction. *J. Am. Chem. Soc.* 140 (1), 38–41. doi:10.1021/jacs.7b10107
- Xia, J., Gao, D., Han, F., Lv, R. F., Waterhouse, G. I. N., Li, Y., et al. (2022). Hydrogenolysis of 5-hydroxymethylfurfural to 2, 5-dimethylfuran over a modified CoAl-hydrotalcite catalyst. *Front. Chem.* 10, 907649. doi:10.3389/fchem.2022.907649
- Xia, Q.-N., Cuan, Q., Liu, X.-H., Gong, X.-Q., Lu, G.-Z., Wang, Y.-Q., et al. (2014). Pd/NbOPO₄ multifunctional catalyst for the direct production of liquid alkanes from aldol adducts of furans. *Angew. Chem. Int. Ed.* 53 (37), 9755–9760. doi:10.1002/anie.201403440
- Xiang, S., Dong, L., Wang, Z.-Q., Han, X., Daeman, L. L., Li, J., et al. (2022). A unique Co@CoO catalyst for hydrogenolysis of biomass-derived 5-hydroxymethylfurfural to 2, 5-dimethylfuran. *Nat. Commun.* 13, 3657. doi:10.1038/s41467-022-31362-9
- Xiao, B., Zheng, M. Y., Li, X. S., Pang, J. F., Sun, R. Y., Wang, H., et al. (2016). Synthesis of 1, 6-hexanediol from HMF over double-layered catalysts of Pd/SiO₂ + Ir-ReOx/SiO₂ in a fixed-bed reactor. *Green Chem.* 18 (7), 2175–2184. doi:10.1039/c5gc02228b
- Yan, K., Jarvis, C., Gu, J., and Yan, Y. (2015). Production and catalytic transformation of levulinic acid: A platform for speciality chemicals and fuels. *Renew. Sustain. Energy Rev.* 51, 986–997. doi:10.1016/j.rser.2015.07.021
- Yang, C. X., Li, X., Zhang, Z. Z., Lv, B. H., Li, J. C., Liu, Z. J., et al. (2020). High efficient catalytic oxidation of 5-hydroxymethylfurfural into 2, 5-furandicarboxylic acid under benign conditions with nitrogen-doped graphene encapsulated Cu nanoparticles. *J. Energy Chem.* 50, 96–105. doi:10.1016/j.jechem.2020.03.003
- Yang, P., Cui, Q., Zu, Y., Liu, X., Lu, G., Wang, Y., et al. (2015). Catalytic production of 2, 5-dimethylfuran from 5-hydroxymethylfurfural over Ni/Co₃O₄ catalyst. *Catal. Commun.* 66, 55–59. doi:10.1016/j.catcom.2015.02.014
- Yang, P., Xia, Q., Liu, X., and Wang, Y. (2016). High-yield production of 2, 5-dimethylfuran from 5-hydroxymethylfurfural over carbon supported Ni-Co bimetallic catalyst. *J. Energy Chem.* 25 (6), 1015–1020. doi:10.1016/j.jechem.2016.08.008
- Zhang, Y.-R., Wang, B.-X., Qin, L., Li, Q., and Fan, Y.-M. (2019a). A non-noble bimetallic alloy in the highly selective electrochemical synthesis of the biofuel 2, 5-dimethylfuran from 5-hydroxymethylfurfural. *Green Chem.* 21 (5), 1108–1113. doi:10.1039/c8gc03689f
- Zhang, Z., Wang, C., Gou, X., Chen, H., Chen, K., Lu, X., et al. (2019b). Catalytic *in-situ* hydrogenation of 5-hydroxymethylfurfural to 2, 5-dimethylfuran over Cu-based catalysts with methanol as a hydrogen donor. *Appl. Catal. A General* 570, 245–250. doi:10.1016/j.apcata.2018.11.029
- Zheng, S., Zhu, K., Li, W., and Ji, Y. (2017). Hydrogenation of dimethyl malonate to 1, 3-propanediol catalyzed by a Cu/SiO₂ catalyst: The reaction network and the effect of Cu⁺/Cu⁰ on selectivity. *New J. Chem.* 41 (13), 5752–5763. doi:10.1039/c6nj03960j
- Zhu, C., Wang, H., Li, H., Cai, B., Lv, W., Cai, C., et al. (2019). Selective hydrodeoxygenation of 5-hydroxymethylfurfural to 2, 5-dimethylfuran over alloyed Cu–Ni encapsulated in biochar catalysts. *ACS Sustain. Chem. Eng.* 7 (24), 19556–19569. doi:10.1021/acssuschemeng.9b04645
- Zhu, Y., Kong, X., Zheng, H., Ding, G., Zhu, Y., Li, Y.-W., et al. (2015). Efficient synthesis of 2, 5-dihydroxymethylfuran and 2, 5-dimethylfuran from 5-hydroxymethylfurfural using mineral-derived Cu catalysts as versatile catalysts. *Catal. Sci. Technol.* 5 (8), 4208–4217. doi:10.1039/c5cy00700c
- Zu, Y., Yang, P., Wang, J., Liu, X., Ren, J., Lu, G., et al. (2014). Efficient production of the liquid fuel 2, 5-dimethylfuran from 5-hydroxymethylfurfural over Ru/Co₃O₄ catalyst. *Appl. Catal. B Environ.* 146, 244–248. doi:10.1016/j.apcatb.2013.04.026



OPEN ACCESS

EDITED BY

Sabarathinam Shanmugam,
Estonian University of Life Sciences,
Estonia

REVIEWED BY

Pengchao Zhang,
Wuhan University of Technology, China
Yahong Zhou,
Technical Institute of Physics and
Chemistry (CAS), China

*CORRESPONDENCE

Hongliang Liu,
liuhongliang@ytu.edu.cn

SPECIALTY SECTION

This article was submitted to Green and
Sustainable Chemistry,
a section of the journal
Frontiers in Chemistry

RECEIVED 28 July 2022

ACCEPTED 29 August 2022

PUBLISHED 12 September 2022

CITATION

Hou B, Ma C, Li S and Liu H (2022),
Modifying the conductive properties of
poly(3,4-ethylenedioxythiophene) thin
films in green solvents.
Front. Chem. 10:1005266.
doi: 10.3389/fchem.2022.1005266

COPYRIGHT

© 2022 Hou, Ma, Li and Liu. This is an
open-access article distributed under
the terms of the [Creative Commons
Attribution License \(CC BY\)](#). The use,
distribution or reproduction in other
forums is permitted, provided the
original author(s) and the copyright
owner(s) are credited and that the
original publication in this journal is
cited, in accordance with accepted
academic practice. No use, distribution
or reproduction is permitted which does
not comply with these terms.

Modifying the conductive properties of poly(3,4-ethylenedioxythiophene) thin films in green solvents

Bin Hou¹, Chuao Ma², Sidi Li² and Hongliang Liu^{1,2*}

¹Shandong Laboratory of Yantai Advanced Materials and Green Manufacturing, Yantai, China, ²School of Chemistry and Chemical Engineering, Yantai University, Yantai, China

With the rapid development of flexible electronic devices, flexible transparent conductive materials acted as the charge transport layer or electrical interconnect in the devices are of great need. As one of the representative conductive materials, poly(3,4-ethylenedioxythiophene) (PEDOT) has received more and more attention due to its high transparency in the visible region, good flexibility, especially the tunable conductivity. In order to achieve high conductivities, various of effective approaches have been adopted to modify the PEDOT thin films. However, some strategies need to be carried out in hazardous solvents, which may pollute the environment and even hinder the application of PEDOT thin films in emerging bioelectronics. Therefore, in this mini review, we focus on the discussion about the modification methods for PEDOT thin films in green solvents. According to the source of PEDOT, the modification methods of PEDOT thin films are mainly described from two aspects: 1) modification of *in-situ* PEDOT, 2) modification of PEDOT complex with poly(styrenesulfonic acid) (PEDOT:PSS). Finally, we conclude with the remaining challenges for future development on the PEDOT thin films prepared by green methods.

KEYWORDS

electronic devices, conductive materials, PEDOT, green solvents, modification methods

Introduction

Flexible transparent conductive films have gained great attractions due to their promising application in electromagnetic shielding (Bora et al., 2019), antistatic layers (Al-Dahoudi et al., 2001), lighting displays (Yu et al., 2011), touch sensors (Worfolk et al., 2015) and bioelectronics (Berggren and Richter-Dahlfors, 2007). In recent years, various types of flexible transparent conductive films have been developed, including metallic oxides (Minami, 2008), metallic nanomaterials (Schneider et al., 2016; Hu et al., 2019), carbon nanomaterials (Kim et al., 2009; Hecht et al., 2011) and conducting polymers (Das and Prusty, 2012). Among them, conducting polymers show the merits of organic polymers with good mechanical properties, which meets the demand for flexible electronic devices. Furthermore, conducting polymers are of good biocompatibility

and their properties can be fine-tuned by modulating the chemical structures and doping, which is essential to be applied in the field of biological systems (Feron et al., 2018). These unique and irreplaceable properties demonstrated that conducting polymers have a good prospect of practical application.

Poly(3,4-ethylenedioxythiophene) (PEDOT) has been one of the most widely-studied conducting polymers since 1988 when the PEDOT was first invented by Bayer AG (Jonas et al., 1988). Up to now some strategies have been developed to synthesize PEDOT, such as oxidative chemical polymerization, electrochemical polymerization and transition-metal-catalyzed polymerization (Jiang et al., 2020). As the first approach to be applied in synthesizing PEDOT, oxidative chemical polymerization is still the dominant method to prepare PEDOT now. Based on the oxidative chemical polymerization, two main types of PEDOT can be obtained. One is *in-situ* PEDOT, which is directly synthesized on the site of application and need not reprocess the PEDOT thin films. The other is PEDOT dispersion, among which PEDOT dispersed with poly(styrenesulfonic acid) (PEDOT:PSS) is the most representative. PEDOT:PSS is usually prepared and dispersed in aqueous solution first, and further processing into films is necessary for application. The properties of the PEDOT thin films are strongly dependent on the polymerization conditions and secondary treatment. Therefore, many efforts have been made to improve the electrical properties of the PEDOT thin films. However, some strategies need to be conducted in hazardous solvents such as *N*-methyl-2-pyrrolidone (NMP) (Gueye et al., 2016) and pyridine (Winther-Jensen et al., 2005), which will be harmful to the environment. Even worse, the toxic solvent residual in the PEDOT thin films may cause cytotoxicity when applied in bioelectronics. Consequently, it is essential to avoid the use of toxic solvents and modify the conductive properties of PEDOT thin films in green and sustainable solvents. In this mini review, we focus on the *in-situ* PEDOT and PEDOT:PSS, and summarize the modification methods for PEDOT thin films in green solvents. Finally, the perspectives and remaining challenges for development of high-quality PEDOT by green methods are proposed.

Modification of PEDOT in green solvents

PEDOT is prepared by polymerization of 3,4-ethylenedioxythiophene (EDOT) monomers. To achieve the synthesis of PEDOT, EDOT monomers are first oxidated from neutral state to cationic radicals by oxidants, and then followed by polymerization. Through changing the solvents used for polymerization, reaction kinetics and PEDOT chain length can be tuned effectively. Consequently, solvents have a great

effect on the conductivity of the resulting PEDOT thin film (Ha et al., 2004). In addition, secondary treatments in green solvents are also the general methods to modify the conductive properties of PEDOT thin films (Shi et al., 2015).

Modification of *in-Situ* PEDOT

In-situ PEDOT is that the EDOT monomers are polymerized *in situ* to form PEDOT under the action of oxidant. Up to now, three synthetic strategies (Figure 1) have been developed to prepare *in-situ* PEDOT: solution-cast polymerization (SCP), vapor phase polymerization (VPP) and oxidative chemical vapor deposition (oCVD). Due to the *in-situ* polymerization, the synthetic processes influence the properties of *in-situ* PEDOT greatly. Therefore, modification of *in-situ* PEDOT thin films with green solvents mainly focuses on the synthetic processes.

SCP is the original and simplest method to be applied in synthesizing PEDOT. In 1988, Bayer AG developed two reagents known as Baytron M (EDOT monomer) and Baytron C (an oxidative solution of iron (III) *p*-toluenesulfonate ($\text{Fe}(\text{OTs})_3$) in butanol) (Jonas et al., 1988). Simply spinning a mixture of these two reagents (pot-life: 10–20 min) on the substrate can obtain the PEDOT thin film. Alcoholic solvents are the common solvents used to synthesize PEDOT for SCP. Alcoholic solvents with high boiling point usually show high viscosity and hinder the reaction kinetics, which is bad for longer chain formation. However, high boiling point solvents are not easy to volatilize, thus affording a longer reaction time to form longer polymer chains, which allow higher conductivities to be achieved. Shashidhar et al. have systematically investigated the influence of the alcoholic solvents (methanol, propanol, *n*-butanol, 2-methoxyethanol, pentanol, hexanol) on the conductivities of SCP PEDOT thin films (Ha et al., 2004). Interestingly, the PEDOT thin films prepared by both high and low boiling point alcoholic solvents exhibit nearly consistent conductivities, which demonstrates that the two competing factors discussed above are balanced. Therefore, it is a little difficult to choose alcoholic solvents with high or low boiling point for the SCP method to prepare PEDOT thin films.

VPP is a general method to prepare conducting polymers, but it was not until 2003 that Kim et al. first used this strategy to synthesize PEDOT (Kim et al., 2003). A typical VPP method could be divided into three steps (Bhattacharyya et al., 2012; Brooke et al., 2017). Firstly, a solution of oxidant (e.g., FeCl_3 (Cho et al., 2014), $\text{Fe}(\text{OTs})_3$ (Fabretto et al., 2012) and iron (III) trifluoromethanesulfonate ($\text{Fe}(\text{OTf})_3$) (Brooke et al., 2018)) with or without additive is deposited on the substrate by a casting or coating process. Then the substrate with oxidant layer is exposed to the EDOT vapor for polymerization. Bottom up (the oxidant mixture diffuses from bottom to up) (Brooke et al., 2014) and top down (the monomer diffuses from top to down) (Nair et al., 2009) are two possible mechanisms for the film growth, which is still controversial up to now. Finally, the

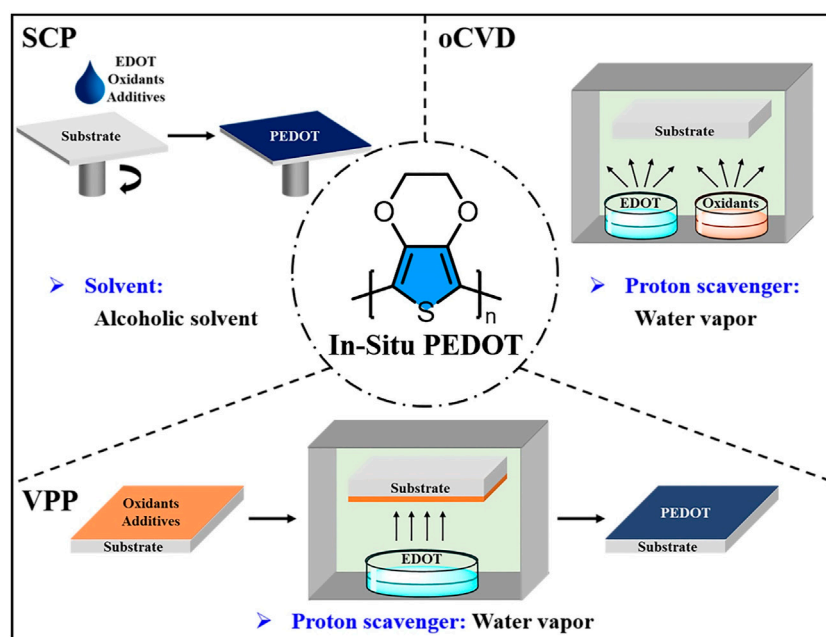


FIGURE 1

Utilization of green solvents to modify the *in-situ* PEDOT thin films prepared by SCP, VPP and oCVD.

deposited film is washed to remove impurities for purification. Water vapor in the reaction environment proved to be an effective proton scavenger and the polymerization will not occur without water vapor (Fabretto et al., 2008). However, Fe(III) oxidants have a propensity for water absorption, which easily lead to crystal formation. Therefore, high humidity during polymerization usually creates holes in the PEDOT thin film, thus decreasing the conductivity of the corresponding PEDOT thin film (Zuber et al., 2008). To overcome this problem, Fabretto et al. use an amphiphilic copolymer polyethylene glycol–polypropylene glycol–polyethylene glycol (PEG–PPG–PEG) to reserve the water and suppress crystal growth of oxidant. In addition to water storage and inhibition of crystal formation, the copolymer can reduce the effective reactivity of the oxidant, which has a similar effect to pyridine (Mueller et al., 2012). But the oxidant layer shows liquid-like state while using PEG–PPG–PEG in the polymerization process, which is different from the gel-like state for pyridine inhibitor (Evans et al., 2012). Because the PEG units have an affinity for “water” (hydrophilic domain) and the PPG moieties show an affinity for “oil” (hydrophobic domain), further studies demonstrate that the PEG/PPG ratio and molecular weight of PEG–PPG–PEG have a great effect on the conductivities of the PEDOT thin films, wherein the PEG–PPG–PEG of 5,800 Da (PEG/PPG ratio = 0.58:1) could afford a sheet-like film with the conductivity of ca. 3400 S cm^{-1} (Fabretto et al., 2012).

oCVD is another vapor deposition method to fabricate *in-situ* PEDOT, which was first developed by Gleason et al. in 2006 (Lock et al., 2006). The synthesis process of oCVD involves only one step in which the vapors of EDOT monomer and volatile oxidant (e.g., FeCl_3 (Gharahcheshmeh and Gleason, 2019), CuCl_2 (Im et al., 2008), SbCl_5 (Nejati et al., 2014), VOCl_3 (Nejati and Lau, 2011) and halogen gases (Chelawat et al., 2010)) meet and immediately undergo oxidative polymerization to obtain the PEDOT thin films on the substrate. Water vapor can also influence the properties of oCVD PEDOT, which is similar with the VPP method. While coevaporating water vapor with EDOT monomer and FeCl_3 oxidant during the oCVD process, the water vapor will assist in dissolving FeCl_3 oxidant. Therefore, Fe^+ and Cl^- ions can be utilized efficiently, thus resulting in a relatively high doping level for PEDOT thin films when compared with the oCVD PEDOT thin films prepared with no water vapor. In addition, water vapor facilitates the stacking of the PEDOT chains perpendicular to the substrate, which is beneficial to the charge transport, thus obtaining a high conductivity of 1042 S cm^{-1} for water-assisted oCVD PEDOT thin film (Goktas et al., 2015).

Modification of PEDOT:PSS

PEDOT:PSS is usually synthesized in an aqueous solution with peroxodisulfates (e.g., $\text{K}_2\text{S}_2\text{O}_8$ and $\text{Na}_2\text{S}_2\text{O}_8$) and Fe(III)

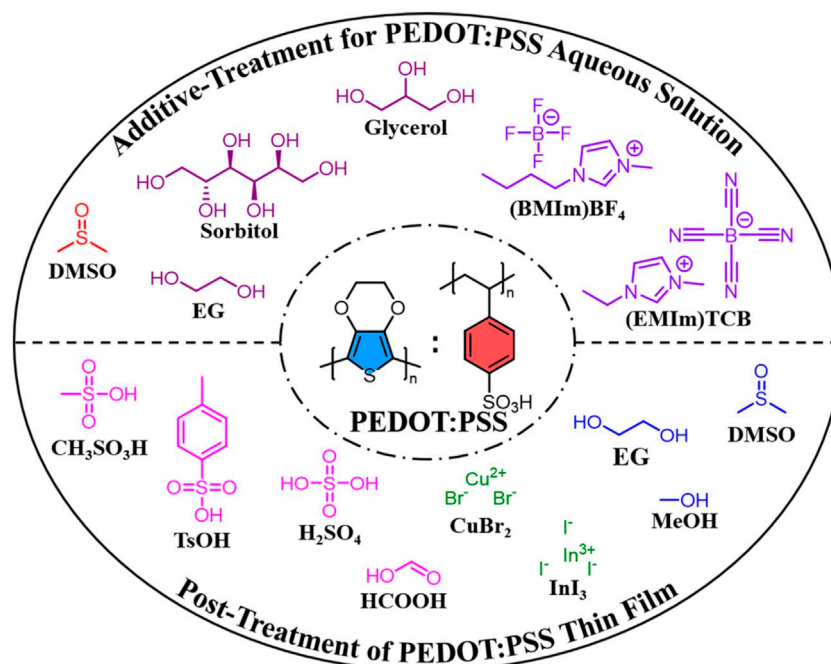


FIGURE 2

Modification of PEDOT:PSS thin films based on additive-treatment for PEDOT:PSS aqueous solution and post-treatment of PEDOT:PSS thin film in green solvents.

salts (e.g., FeCl_3 and $\text{Fe}_2(\text{SO}_4)_3$) as the oxidizing reagents. Compared with aforementioned *in-situ* PEDOT, PEDOT:PSS is commercially available as a stable aqueous dispersion, in which hydrophilic and insulating PSS acts as both a counter-ion and a soluble template for hydrophobic and conducting PEDOT (Lang et al., 2009). Therefore, PEDOT:PSS is a promising conductive material, which can be easy to process by green eco-friendly techniques. Although extremely convenient, this has limited the conductivity optimization of PEDOT:PSS on the synthesis level. Therefore, additive-treatment for PEDOT:PSS aqueous solution and post-treatment of PEDOT:PSS thin film in green solvents have been two common modification methods to improve the conductivities of PEDOT:PSS thin films (Figure 2).

Green solvents such as polar solvents, polyols and ionic liquids have been used as additives for PEDOT:PSS aqueous solution to enhance the conductivities of PEDOT:PSS thin films. In 2002, Kim et al. first studied the effects of polar solvents on conductivity of the PEDOT:PSS thin film (Kim et al., 2002). While adding dimethyl sulfoxide (DMSO) in PEDOT:PSS aqueous solution, the conductivity increased from 0.8 S cm^{-1} to 80 S cm^{-1} , which is more remarkable than addition of *N,N*-dimethylformamide (DMF) and tetrahydrofuran (THF). Since then, DMSO has been widely used as an additive to improve the conductivity of PEDOT:PSS (Lee et al., 2014; Lim et al., 2014). Polyols like ethylene glycol (EG) (Wichiansee and Sirivat, 2009), glycerol (Lee

et al., 2010) and sorbitol (Onorato et al., 2010) are also added into PEDOT:PSS aqueous solution to enhance the conductivity, wherein EG is a widely-used additive. It was proved that addition of EG can increase the carrier mobility and carrier density of PEDOT:PSS thin films, thus increasing the conductivity (Wei et al., 2013). Ionic liquids are another additive for PEDOT:PSS aqueous solution to improve the conductivity of PEDOT:PSS thin films. Due to no volatility, ionic liquids can remain in the PEDOT:PSS thin films, which is different from the high boiling point solvents. In 2007, a series of ionic liquids was first envisaged as additives to enhance the conductivities of PEDOT:PSS thin films, wherein 1-butyl-3-methylimidazolium tetrafluoroborate ((BMIIm)BF₄) afforded the highest conductivity of 136 S cm^{-1} (Döbbelin et al., 2007). When compared with (BMIIm)BF₄ (287 S cm^{-1}), 1-ethyl-3-methylimidazolium tetracyanoborate ((EMIIm)TCB) is a better additive which makes the PEDOT:PSS thin film exhibit a conductivity of 2084 S cm^{-1} (Badre et al., 2012).

Apart from additive-treatment for PEDOT:PSS aqueous solution, post-treatment of PEDOT:PSS thin film in green solvents is also a common modification method to improve the conductivities. Polar solvents such as methanol (Alemu et al., 2012), EG (Okuzaki et al., 2009) and DMSO (Ouyang et al., 2004) have been widely used to post-treat PEDOT:PSS thin film. The hydrophilicity and dielectric constant of the

alcohols have a great effect on the conductivity enhancement. While using methanol for post-treatment of PEDOT:PSS thin film, the conductivity increases from 0.3 to 1362 S cm⁻¹, which is better than using ethanol and propanol (Alemu et al., 2012). Aqueous solutions of salt and zwitterion are also applied in post-treatment of PEDOT:PSS thin film. Ouyang et al. has systematically studied the cation effect of salts on the conductivity of PEDOT:PSS thin film. The result shows that salts with cations of positive soft parameter (Cu²⁺, Ag⁺, and In³⁺) can significantly enhance the conductivity of the PEDOT:PSS thin film, while the ones whose cations have negative soft parameter (Li⁺, Na⁺, Mg²⁺, and Ni²⁺) have negligible effect (Xia and Ouyang, 2009). Further studies on the anions of salts demonstrate that the conductivity enhancement is relevant to the acid dissociation constants of the anions. A salt with higher dissociation can benefit the association of the anions with PEDOT⁺, thus leading to the more significant conductivity enhancement (Xia and Ouyang, 2010). Acid aqueous solution is another choice for post-treatment of PEDOT thin films. Both strong acids like H₂SO₄ (Xia et al., 2012) and weak acids like methanesulfonic acid (Ouyang, 2013) and formic acid (Mengistie et al., 2014) have been studied for conductivity improvement of PEDOT:PSS thin films. For example, Kim et al. have reported the solution-processed crystalline formation in PEDOT:PSS via H₂SO₄ post-treatment (Kim et al., 2014). The concentrated H₂SO₄ treatment induces a significant structural rearrangement in the PEDOT:PSS with the removal of PSS and leads to the formation of crystallized nanofibrils via a charge-separated transition mechanism. Therefore, a conductivity of 4380 S cm⁻¹ is obtained for PEDOT:PSS thin film after post-treatment with concentrated H₂SO₄.

In fact, treatment of PEDOT:PSS is not limited to using only one method or reagent. In order to achieve high conductivities, combination of these strategies has been utilized to treat the PEDOT:PSS. For instance, Kim et al. prepared PEDOT:PSS thin films with the highest conductivity of 1418 S cm⁻¹ through adding EG into the PEDOT:PSS aqueous solution and subsequent post-treatment of PEDOT:PSS thin film with an EG bath (Kim et al., 2011). Subsequently, Pipe et al. adopt the similar method to investigate the PEDOT:PSS (DMSO-mixed) thin films post-treated with an EG bath (Kim et al., 2013). In addition, post-treatment of PEDOT:PSS thin film with a mixture of solvents is also a general method to improve the conductivities of PEDOT:PSS thin films. Luo et al. post-treat PEDOT:PSS thin films with a mixed solution of DMSO and (BMIm)BF₄ (Luo et al., 2013). The results show that all the PEDOT:PSS thin films post-treated with the mixed solution exhibit higher conductivities compared with the pristine films. Kumar et al. find that the conductivity of the PEDOT:PSS thin film post-treated with a mixed solution of *p*-toluenesulfonic acid (TsOH) and DMSO can increase to ca. 3500 S cm⁻¹ (Mukherjee et al., 2014).

Conclusion and perspective

As one of the most widely-studied conducting polymers, PEDOT shows the merits of good flexibility, high transparency in the visible region and tunable conductivity. The conductivities of the PEDOT thin films are strongly dependent on the deposition conditions and secondary treatments. Therefore, many methods have been developed to improve the conductive properties of the PEDOT thin films. In this mini review, we summarize the modification of two types of PEDOT (*in-situ* PEDOT and PEDOT:PSS) in green solvents. The modification methods of *in-situ* PEDOT are mainly introduced from the aspect of synthetic strategies (SCP, VPP and oCVD), while the modifications of PEDOT:PSS are presented according to treatment methods (additive-treatment for PEDOT:PSS aqueous solution and post-treatment of PEDOT:PSS thin film). Although significant progress has been made in the conductivity of PEDOT, there are still some challenges. First, strategies are urgently needed that can afford a PEDOT thin film prepared by dispersion methods with a high conductivity comparable to the *in-situ* PEDOT due to the green eco-friendly process of PEDOT dispersions. In addition, microstructure plays a crucial role on the conductivity of PEDOT, but there is still a lack of effective and green methods to control the stacking orientation of PEDOT chains in the PEDOT thin film. Finally, the conductive mechanism of PEDOT is controversial, which needs further study to guide the modification of PEDOT thin films by green non-pollution approaches.

Author contributions

HL supervised the implementation of the review. BH collected the references and wrote the manuscript. CM and SL discussed and revised the manuscript.

Funding

This work was supported by the National Natural Science Foundation of China (21875268), Taishan Young Scholar Program (tsqn202103053), and Fundamental Research Projects of Science & Technology Innovation and Development Plan in Yantai City (2022YTJC06002541).

Conflict of interest

The authors declare that the research was conducted in the absence of any commercial or financial relationships that could be construed as a potential conflict of interest.

Publisher's note

All claims expressed in this article are solely those of the authors and do not necessarily represent those of their affiliated

organizations, or those of the publisher, the editors and the reviewers. Any product that may be evaluated in this article, or claim that may be made by its manufacturer, is not guaranteed or endorsed by the publisher.

References

- Al-Dahoudi, N., Bisht, H., Göbbert, C., Krajewski, T., and Aegerter, M. A. (2001). Transparent conducting, anti-static and anti-static-glare coatings on plastic substrates. *Thin Solid Films* 392, 299–304. doi:10.1016/S0040-6090(01)01047-1
- Alemu, D., Wei, H.-Y., Ho, K.-C., and Chu, C.-W. (2012). Highly conductive PEDOT:PSS electrode by simple film treatment with methanol for ITO-free polymer solar cells. *Energy Environ. Sci.* 5, 9662–9671. doi:10.1039/C2EE22595F
- Badre, C., Marquant, L., Alsayed, A. M., and Hough, L. A. (2012). Highly conductive poly(3, 4-ethylenedioxythiophene)/poly(styrenesulfonate) films using 1-ethyl-3-methylimidazolium tetracyanoborate ionic liquid. *Adv. Funct. Mat.* 22, 2723–2727. doi:10.1002/adfm.201200225
- Berggren, M., and Richter-Dahlfors, A. (2007). Organic bioelectronics. *Adv. Mat.* 19, 3201–3213. doi:10.1002/adma.200700419
- Bhattacharyya, D., Howden, R. M., Borrelli, D. C., and Gleason, K. K. (2012). Vapor phase oxidative synthesis of conjugated polymers and applications. *J. Polym. Sci. B. Polym. Phys.* 50, 1329–1351. doi:10.1002/polb.23138
- Bora, P. J., Anil, A. G., Vinoy, K. J., and Ramamurthy, P. C. (2019). Outstanding absolute electromagnetic interference shielding effectiveness of cross-linked PEDOT:PSS film. *Adv. Mat. Interfaces* 6, 1901353. doi:10.1002/admi.201901353
- Brooke, R., Cottis, P., Talemi, P., Fabretto, M., Murphy, P., and Evans, D. (2017). Recent advances in the synthesis of conducting polymers from the vapour phase. *Prog. Mat. Sci.* 86, 127–146. doi:10.1016/j.pmatsci.2017.01.004
- Brooke, R., Fabretto, M., Hojati-Talemi, P., Murphy, P., and Evans, D. (2014). Evidence for 'bottom up' growth during vapor phase polymerization of conducting polymers. *Polymer* 55, 3458–3460. doi:10.1016/j.polymer.2014.06.055
- Brooke, R., Franco-Gonzalez, J. F., Wijeratne, K., Pavlopoulou, E., Galliani, D., Liu, X., et al. (2018). Vapor phase synthesized poly(3, 4-ethylenedioxythiophene)-trifluoromethanesulfonate as a transparent conductor material. *J. Mat. Chem. A* 6, 21304–21312. doi:10.1039/C8TA04744H
- Chelawat, H., Vaddiraju, S., and Gleason, K. (2010). Conformal, conducting poly(3, 4-ethylenedioxythiophene) thin films deposited using bromine as the oxidant in a completely dry oxidative chemical vapor deposition process. *Chem. Mat.* 22, 2864–2868. doi:10.1021/cm100092c
- Cho, B., Park, K. S., Baek, J., Oh, H. S., Koo Lee, Y.-E., and Sung, M. M. (2014). Single-crystal poly(3, 4-ethylenedioxythiophene) nanowires with ultrahigh conductivity. *Nano Lett.* 14, 3321–3327. doi:10.1021/nl500748y
- Das, T. K., and Prusty, S. (2012). Review on conducting polymers and their applications. *Polym. Plast. Technol. Eng.* 51, 1487–1500. doi:10.1080/03602559.2012.710697
- Döbelin, M., Marcilla, R., Salsamendi, M., Pozo-Gonzalo, C., Carrasco, P. M., Pomposo, J. A., et al. (2007). Influence of ionic liquids on the electrical conductivity and morphology of PEDOT:PSS films. *Chem. Mat.* 19, 2147–2149. doi:10.1021/cm070398z
- Evans, D., Fabretto, M., Mueller, M., Zuber, K., Short, R., and Murphy, P. (2012). Structure-directed growth of high conductivity PEDOT from liquid-like oxidant layers during vacuum vapor phase polymerization. *J. Mat. Chem.* 22, 14889–14895. doi:10.1039/C2JM32281A
- Fabretto, M. V., Evans, D. R., Mueller, M., Zuber, K., Hojati-Talemi, P., Short, R. D., et al. (2012). Polymeric material with metal-Like conductivity for next generation organic electronic devices. *Chem. Mat.* 24, 3998–4003. doi:10.1021/cm302899v
- Fabretto, M., Zuber, K., Hall, C., and Murphy, P. (2008). High conductivity PEDOT using humidity facilitated vacuum vapour phase polymerisation. *Macromol. Rapid Commun.* 29, 1403–1409. doi:10.1002/marc.200800270
- Feron, K., Lim, R., Sherwood, C., Keynes, A., Brichta, A., and Dastoor, P. C. (2018). Organic bioelectronics: Materials and biocompatibility. *Int. J. Mol. Sci.* 19, 2382. doi:10.3390/ijms19082382
- Gharahcheshmeh, M. H., and Gleason, K. K. (2019). Device fabrication based on oxidative chemical vapor deposition (oCVD) synthesis of conducting polymers and related conjugated organic materials. *Adv. Mat. Interfaces* 6, 1801564. doi:10.1002/admi.201801564
- Goktas, H., Wang, X., Ugur, A., and Gleason, K. K. (2015). Water-assisted vapor deposition of PEDOT thin film. *Macromol. Rapid Commun.* 36, 1283–1289. doi:10.1002/marc.201500069
- Gueye, M. N., Carella, A., Massonnet, N., Yvenou, E., Brenet, S., Faure-Vincent, J., et al. (2016). Structure and dopant engineering in PEDOT thin films: Practical tools for a dramatic conductivity enhancement. *Chem. Mat.* 28, 3462–3468. doi:10.1021/acs.chemmater.6b01035
- Ha, Y. H., Nikolov, N., Pollack, S. K., Mastrangelo, J., Martin, B. D., and Shashidhar, R. (2004). Towards a transparent, highly conductive poly(3, 4-ethylenedioxythiophene). *Adv. Funct. Mat.* 14, 615–622. doi:10.1002/adfm.200305059
- Hecht, D. S., Hu, L., and Irvin, G. (2011). Emerging transparent electrodes based on thin films of carbon nanotubes, graphene, and metallic nanostructures. *Adv. Mat.* 23, 1482–1513. doi:10.1002/adma.201003188
- Hu, H., Wang, S., Wang, S., Liu, G., Cao, T., and Long, Y. (2019). Aligned silver nanowires enabled highly stretchable and transparent electrodes with unusual conductive property. *Adv. Funct. Mat.* 29, 1902922. doi:10.1002/adfm.201902922
- Im, S. G., Kusters, D., Choi, W., Baxamusa, S. H., Van De Sanden, M. C. M., and Gleason, K. K. (2008). Conformal coverage of poly(3, 4-ethylenedioxythiophene) films with tunable nanoporosity via oxidative chemical vapor deposition. *ACS Nano* 2, 1959–1967. doi:10.1021/nn800380e
- Jiang, Y., Liu, T., and Zhou, Y. (2020). Recent advances of synthesis, properties, film fabrication methods, modifications of poly(3, 4-ethylenedioxythiophene), and applications in solution-processed photovoltaics. *Adv. Funct. Mat.* 30, 2006213. doi:10.1002/adfm.202006213
- Jonas, F., Heywang, G., and Schmidtberg, W. (1988). *Novel polythiophenes, process for their preparation, and their use*. German Patent No 3,813,589. München: German Patent and Trade Mark Office.
- Kim, G. H., Shao, L., Zhang, K., and Pipe, K. P. (2013). Engineered doping of organic semiconductors for enhanced thermoelectric efficiency. *Nat. Mat.* 12, 719–723. doi:10.1038/nmat3635
- Kim, J., Kim, E., Won, Y., Lee, H., and Suh, K. (2003). The preparation and characteristics of conductive poly(3, 4-ethylenedioxythiophene) thin film by vapor-phase polymerization. *Synth. Metall.* 139, 485–489. doi:10.1016/S0379-6779(03)00202-9
- Kim, J. Y., Jung, J. H., Lee, D. E., and Joo, J. (2002). Enhancement of electrical conductivity of poly(3, 4-ethylenedioxythiophene)/poly(4-styrenesulfonate) by a change of solvents. *Synth. Metall.* 126, 311–316. doi:10.1016/S0379-6779(01)00576-8
- Kim, K. S., Zhao, Y., Jang, H., Lee, S. Y., Kim, J. M., Kim, K. S., et al. (2009). Large-scale pattern growth of graphene films for stretchable transparent electrodes. *Nature* 457, 706–710. doi:10.1038/nature07719
- Kim, N., Kee, S., Lee, S. H., Lee, B. H., Kahng, Y. H., Jo, Y.-R., et al. (2014). Highly conductive PEDOT:PSS nanofibrils induced by solution-processed crystallization. *Adv. Mat.* 26, 2268–2272. doi:10.1002/adma.201304611
- Kim, Y. H., Sachse, C., Machala, M. L., May, C., Müller-Meskamp, L., and Leo, K. (2011). Highly conductive PEDOT:PSS electrode with optimized solvent and thermal post-treatment for ITO-free organic solar cells. *Adv. Funct. Mat.* 21, 1076–1081. doi:10.1002/adfm.201002290
- Lang, U., Müller, E., Naujoks, N., and Dual, J. (2009). Microscopical investigations of PEDOT:PSS thin films. *Adv. Funct. Mat.* 19, 1215–1220. doi:10.1002/adfm.200801258
- Lee, M.-W., Lee, M.-Y., Choi, J.-C., Park, J.-S., and Song, C.-K. (2010). Fine patterning of glycerol-doped PEDOT:PSS on hydrophobic PVP dielectric with inkjet for source and drain electrode of OTFTs. *Org. Electron.* 11, 854–859. doi:10.1016/j.orgel.2010.01.028
- Lee, S. H., Park, H., Son, W., Choi, H. H., and Kim, J. H. (2014). Novel solution-processable, dedoped semiconductors for application in thermoelectric devices. *J. Mat. Chem. A* 2, 13380–13387. doi:10.1039/C4TA01839G
- Lim, K., Jung, S., Lee, S., Heo, J., Park, J., Kang, J.-W., et al. (2014). The enhancement of electrical and optical properties of PEDOT:PSS using one-step

dynamic etching for flexible application. *Org. Electron.* 15, 1849–1855. doi:10.1016/j.orgel.2014.04.014

Lock, J. P., Im, S. G., and Gleason, K. K. (2006). Oxidative chemical vapor deposition of electrically conducting poly(3, 4-ethylenedioxythiophene) films. *Macromolecules* 39, 5326–5329. doi:10.1021/ma060113o

Luo, J., Billep, D., Waechtler, T., Otto, T., Toader, M., Gordan, O., et al. (2013). Enhancement of the thermoelectric properties of PEDOT:PSS thin films by post-treatment. *J. Mat. Chem. A* 1, 7576–7583. doi:10.1039/C3TA11209H

Mengistie, D. A., Ibrahim, M. A., Wang, P.-C., and Chu, C.-W. (2014). Highly conductive PEDOT:PSS treated with formic acid for ITO-free polymer solar cells. *ACS Appl. Mat. Interfaces* 6, 2292–2299. doi:10.1021/am405024d

Minami, T. (2008). Present status of transparent conducting oxide thin-film development for indium-tin-oxide (ITO) substitutes. *Thin Solid Films* 516, 5822–5828. doi:10.1016/j.tsf.2007.10.063

Mueller, M., Fabretto, M., Evans, D., Hojati-Talemi, P., Gruber, C., and Murphy, P. (2012). Vacuum vapour phase polymerization of high conductivity PEDOT: Role of PEG-PPG-PEG, the origin of water, and choice of oxidant. *Polymer* 53, 2146–2151. doi:10.1016/j.polymer.2012.03.028

Mukherjee, S., Singh, R., Gopinathan, S., Murugan, S., Gawali, S., Saha, B., et al. (2014). Solution-processed poly(3, 4-ethylenedioxythiophene) thin films as transparent conductors: Effect of p-toluenesulfonic acid in dimethyl sulfoxide. *ACS Appl. Mat. Interfaces* 6, 17792–17803. doi:10.1021/am504150n

Nair, S., Hsiao, E., and Kim, S. H. (2009). Melt-welding and improved electrical conductivity of nonwoven porous nanofiber mats of poly(3, 4-ethylenedioxythiophene) grown on electrospun polystyrene fiber template. *Chem. Mat.* 21, 115–121. doi:10.1021/cm8029449

Nejati, S., and Lau, K. K. S. (2011). Chemical vapor deposition synthesis of tunable unsubstituted polythiophene. *Langmuir* 27, 15223–15229. doi:10.1021/la203318f

Nejati, S., Minford, T. E., Smolin, Y. Y., and Lau, K. K. S. (2014). Enhanced charge storage of ultrathin polythiophene films within porous nanostructures. *ACS Nano* 8, 5413–5422. doi:10.1021/nn500007c

Okuzaki, H., Harashina, Y., and Yan, H. (2009). Highly conductive PEDOT/PSS microfibers fabricated by wet-spinning and dip-treatment in ethylene glycol. *Eur. Polym. J.* 45, 256–261. doi:10.1016/j.eurpolymj.2008.10.027

Onorato, A., Invernale, M. A., Berghorn, I. D., Pavlik, C., Sotzing, G. A., and Smith, M. B. (2010). Enhanced conductivity in sorbitol-treated PEDOT-PSS. Observation of an *in situ* cyclodehydration reaction. *Synth. Metall.* 160, 2284–2289. doi:10.1016/j.synthmet.2010.08.021

Ouyang, J. (2013). Solution-processed PEDOT:PSS films with conductivities as indium tin oxide through a treatment with mild and weak organic acids. *ACS Appl. Mat. Interfaces* 5, 13082–13088. doi:10.1021/am404113n

Ouyang, J., Xu, Q., Chu, C.-W., Yang, Y., Li, G., and Shinar, J. (2004). On the mechanism of conductivity enhancement in poly(3, 4-ethylenedioxythiophene): poly(styrene sulfonate) film through solvent treatment. *Polymer* 45, 8443–8450. doi:10.1016/j.polymer.2004.10.001

Schneider, J., Rohner, P., Thureja, D., Schmid, M., Galliker, P., and Poulikakos, D. (2016). Electrohydrodynamic nanodrip printing of high aspect ratio metal grid transparent electrodes. *Adv. Funct. Mat.* 26, 833–840. doi:10.1002/adfm.201503705

Shi, H., Liu, C., Jiang, Q., and Xu, J. (2015). Effective approaches to improve the electrical conductivity of PEDOT:PSS: A review. *Adv. Electron. Mat.* 1, 1500017. doi:10.1002/aelm.201500017

Wei, Q., Mukaida, M., Naitoh, Y., and Ishida, T. (2013). Morphological change and mobility enhancement in PEDOT:PSS by adding co-solvents. *Adv. Mat.* 25, 2831–2836. doi:10.1002/adma.201205158

Wichiansee, W., and Sirivat, A. (2009). Electrorheological properties of poly(dimethylsiloxane) and poly(3, 4-ethylenedioxy thiophene)/poly(styrene sulfonic acid)/ethylene glycol blends. *Mater. Sci. Eng. C* 29, 78–84. doi:10.1016/j.msec.2008.05.018

Winther-Jensen, B., Breiby, D. W., and West, K. (2005). Base inhibited oxidative polymerization of 3, 4-ethylenedioxythiophene with iron(III) tosylate. *Synth. Metall.* 152, 1–4. doi:10.1016/j.synthmet.2005.07.085

Worfolk, B. J., Andrews, S. C., Park, S., Reinsch, J., Liu, N., Toney, M. F., et al. (2015). Ultrahigh electrical conductivity in solution-sheared polymeric transparent films. *Proc. Natl. Acad. Sci. U. S. A.* 112, 14138–14143. doi:10.1073/pnas.1509958112

Xia, Y., and Ouyang, J. (2010). Anion effect on salt-induced conductivity enhancement of poly(3, 4-ethylenedioxythiophene):poly(styrenesulfonate) films. *Org. Electron.* 11, 1129–1135. doi:10.1016/j.orgel.2010.04.007

Xia, Y., and Ouyang, J. (2009). Salt-induced charge screening and significant conductivity enhancement of conducting poly(3, 4-ethylenedioxythiophene): poly(styrenesulfonate). *Macromolecules* 42, 4141–4147. doi:10.1021/ma900327d

Xia, Y., Sun, K., and Ouyang, J. (2012). Solution-processed metallic conducting polymer films as transparent electrode of optoelectronic devices. *Adv. Mat.* 24, 2436–2440. doi:10.1002/adma.201104795

Yu, Z., Niu, X., Liu, Z., and Pei, Q. (2011). Intrinsically stretchable polymer light-emitting devices using carbon nanotube-polymer composite electrodes. *Adv. Mat.* 23, 3989–3994. doi:10.1002/adma.201101986

Zuber, K., Fabretto, M., Hall, C., and Murphy, P. (2008). Improved PEDOT conductivity via suppression of crystallite formation in Fe(III) tosylate during vapor phase polymerization. *Macromol. Rapid Commun.* 29, 1503–1508. doi:10.1002/marc.200800325



OPEN ACCESS

EDITED BY

Honglei Fan,
Institute of Chemistry (CAS), China

REVIEWED BY

Hou Xiufang,
Yan'an University, China
Zhihong Wei,
Shanxi University, China

*CORRESPONDENCE

Wenzuo Li,
liwenzuo2004@126.com
Qingzhong Li,
liqingzhong1990@sina.com
Shaoli Liu,
liushaoli6984@sina.com

[†]These authors have contributed equally
to this work

SPECIALTY SECTION

This article was submitted to Green and
Sustainable Chemistry,
a section of the journal
Frontiers in Chemistry

RECEIVED 25 August 2022

ACCEPTED 06 September 2022

PUBLISHED 26 September 2022

CITATION

Zhao J, Qi L, Li W, Cheng J, Li Q and Liu S
(2022), CH₄ activation by PtX⁺ (X = F, Cl,
Br, I).
Front. Chem. 10:1027465.
doi: 10.3389/fchem.2022.1027465

COPYRIGHT

© 2022 Zhao, Qi, Li, Cheng, Li and Liu.
This is an open-access article
distributed under the terms of the
Creative Commons Attribution License
(CC BY). The use, distribution or
reproduction in other forums is
permitted, provided the original
author(s) and the copyright owner(s) are
credited and that the original
publication in this journal is cited, in
accordance with accepted academic
practice. No use, distribution or
reproduction is permitted which does
not comply with these terms.

CH₄ activation by PtX⁺ (X = F, Cl, Br, I)

Jin Zhao[†], Lingxi Qi[†], Wenzuo Li*, Jianbo Cheng, Qingzhong Li*
and Shaoli Liu*

College of Chemistry and Chemical Engineering, Yantai University, Yantai, China

Reactions of PtX⁺ (X = F, Cl, Br, I) with methane have been investigated at the density functional theory (DFT) level. These reactions take place more easily along the low-spin potential energy surface. For HX (X = F, Cl, Br, I) elimination, the formal oxidation state of the metal ion appears to be conserved, and the importance of this reaction channel decreases in going as the sequence: X = F, Cl, Br, I. A reversed trend is observed in the loss of H₂ for X = F, Cl, Br, while it is not favorable for PtI⁺ in the loss of either HI or H₂. For HX eliminations, the transfer form of H is from proton to atom, last to hydride, and the mechanisms are from PCET to HAT, last to HT for the sequence of X = F, Cl, Br, I. One reason is mainly due to the electronegativity of halogens. Otherwise, the mechanisms of HX eliminations also can be explained by the analysis of Frontier Molecular Orbitals. While for the loss of H₂, the transfer of H is in the form of hydride for all the X ligands. Noncovalent interactions analysis also can be explained the reaction mechanisms.

KEYWORDS

PtX⁺, activation of methane, reaction mechanism, ligand effect, noncovalent interactions

1 Introduction

Catalysts that can convert methane directly into higher-value-added commodities have long been sought, but breaking the thermodynamically strong, kinetically inert C-H bonds in a controlled way under mild conditions remains a central challenge (Geng et al., 2017). Reactivity studies of transition-metal ions in the gas phase, and, in particular, aspects related to the ongoing challenge of selective activation of inert C-H and C-C bonds, have been studied intensely over the past decades (Howell and Burkinshaw, 1983; Dubois, 1989; Eller and Schwarz, 1991; Balcells et al., 2010; Dobereine and Crabtree, 2010; Roithova and Schröder, 2010; Jana et al., 2011). In recent years, how ligation affects the electronic structure at the transition-metal center has been systematically investigated (Howell and Burkinshaw, 1983; Dubois, 1989; Schlangen et al., 2007; Schlangen et al., 2007; Schlangen and Schwarz, 2008; Dede et al., 2009; Li et al., 2016a; Sun et al., 2016; Zhou et al., 2016; Zhou et al., 2017a; Zhou et al., 2017b; Zhou et al., 2017c; Schwarz et al., 2017; Schwarz et al., 2017; Yue et al., 2017). The ligand can change the electronic structure of the metal center through a shift in the electronic state, or provide a more efficient reaction center, so the addition of a single ligand to a metal center has been widely used to

prepare reactants for C-H bonds activation (Chen et al., 1997; Rodgers et al., 2000; Li et al., 2009).

Irikura and Beauchamp (Irikura and Beauchamp, 1989; Irikura and Beauchamp, 1991a; Irikura and Beauchamp, 1991b) discovered that Pt^+ as a 5d transition metal dehydrogenates methane to yield the corresponding carbene complexes $\text{Pt}(\text{CH}_2)^+$. Bare Pt^+ also has been found to catalyze the reaction of methane with molecular oxygen in the gas phase to produce methanol, formaldehyde and other oxidation products (Wesendrup et al., 1994). Subsequently, a series of activation studies around transition metal Pt^+ were carried out (Achatz et al., 2000; Wheeler et al., 2016). Recently, it has been reported that Pt^- is able to selectively activate one C-H bond in methane, which represents the first example of methane activation by atomic anions (Liu et al., 2019).

Open-shell ligands X form a covalent bond with the metal cation and thereby increase the formal oxidation state, for example, X = F, Cl, Br, I, OH, NH, O (Schlangen et al., 2007; Dede et al., 2009), which often increases reactivity. For example, bare Cr^+ is one of the least reactive transition metal cations, whereas CrCl^+ is significantly more reactive (Mandich et al., 1986). Clearly, this example demonstrates that an appropriately chosen ligand can enhance the selectivity of a reagent at the expense of reactivity (Schlangen et al., 2007). Similarly, the naked cations M^+ (M = Fe, Co, Ni, Ru, Rh, Pd) do not bring about thermal C-H bond activation of methane (Halle et al., 1982; Tolbert and Beauchamp, 1986; Tolbert et al., 1986; Schultz et al., 1988; Musaev et al., 1993; Musaev and Morokuma, 1994; Westerberg and Blomberg, 1998), but the corresponding MH^+ cations (Schilling et al., 1986; Elkind and Armentrout, 1987; Schilling et al., 1987; Ohanessian et al., 1990; Zhang and Bowers, 2004; Li et al., 2009; Wang and Andrews, 2009) give rise to efficient H/CH_3 ligand switches.

It is not surprising that the nature of the ligand X controls the outcome of a given ion-molecule reaction, as, for example, demonstrated in a systematic investigation of FeX^+ cations with acetone (Schröder et al., 1993). The number of ligands also affects the reaction activity. With respect to the activation of methane, CrF^+ is not sufficient, and CrF_2^+ does not react with CH_4 , whereas CrF_3^+ and CrF_4^+ are able to activate the C-H bonds of methane (Mazurek et al., 1998).

Schlangen et al. have reported the studies on ligand and substrate effects in gas-phase reactions of NiX^+/RH couples (X = F, Cl, Br, I; R = CH_3 , C_2H_5 , n- C_3H_7 , n- C_4H_9) (Schlangen et al., 2007). The results indicate that NiF^+ is the only Ni^{II} halide complex that brings about thermal activation of methane to eliminate HF, whereas the nickel-halide cations NiCl^+ , NiBr^+ , and NiI^+ react only with large alkanes. In the elimination of HX (X = F, Cl, Br, I), the formal oxidation state of the metal ion appears to be conserved, and the importance of this reaction channel decreased in going from NiF^+ to NiI^+ . A reversed trend is observed in the losses of H_2 , which dominate the gas-phase ion chemistry of Ni^+/RH couples. Schröder and Schwarz (2005)

reported the reactions of methane with PtX^+ (X = H, Cl, Br and CHO) using mass spectrometry and found that these species are able to activate methane.

Here, we report our calculated results for the PtX^+/CH_4 (X = F, Cl, Br, I) systems. The key issues for our study are the mechanistic details of methane catalyzed by ligated transition metal PtX^+/CH_4 (X = F, Cl, Br, I).

2 Computational and technical details

Full optimization of geometries for all stationary points involved in methane dehydrogenation by PtX^+ (X = F, Cl, Br, I) has been calculated using the density functional theory (DFT) method based on the hybrid of Becke's three-parameter exchange functional and the Lee, Yang, and Parr correlation functional (B3LYP) (Becke, 1988; Lee et al., 1988; Becke, 1993), Becke hybrid with correlation functional Perdew (B3P86) (Perdew, 1986a; Perdew, 1986b; Michael et al., 2008) and M06-2X (Zhao and Truhlar, 2008; Zhao and Truhlar, 2008). For carbon and hydrogen, also for F, Cl, and Br, the large 6-311+G** basis set is applied. The Stuttgart/Dresden relativistic effective core potentials (ECP) of SDD were adopted to describe the metal Pt and the halogen I (Andrae et al., 1990). For each optimized stationary point, vibrational analysis was performed at the same level with the geometry optimizations to determine its character (minimum or saddle point). Unscaled harmonic frequencies were employed to obtain entropy corrections and the zero-point vibrational energy (ZPVE) which is included in all relative energies. Furthermore, intrinsic reaction coordinate (IRC) calculations (Gonzalez and Schlegel, 1989) were performed to confirm that the optimized transition states correctly connect the relevant reactants and products. Energies were corrected for (unscaled) zero-point vibrational energy contributions and were given relative to the separated reactant couples PtX^+/CH_4 in the most stable spin state of PtX^+ (Ye and Neese, 2010; Lawson Daku et al., 2012; Vargas et al., 2013). Between two different potential energy surfaces (PES), a configuration that structures are similar with almost the same energy was found, which is called minimum energy crossing point (MECP) (Poli and Harvey, 2003; Harvey, 2007). All computations reported are carried out using the GAUSSIAN 09 program suit (Frisch et al., 2009). The topological parameters of electron density(ρ), its Laplacian ($\nabla^2\rho$), and energy density at the bond critical point (BCP) were analyzed with the AIM2000 program (Bader, 2000). The molecular electrostatic potentials (MEP) of the various monomers were calculated on the 0.001 a. u. isodensity surfaces using the wave function analysis-surface analysis suite (WFA-SAS) program (Bulat et al., 2010).

The geometries were optimized using density functional theory with B3P86, B3LYP, and M06-2X functional. The comparisons show that the results obtained by the three

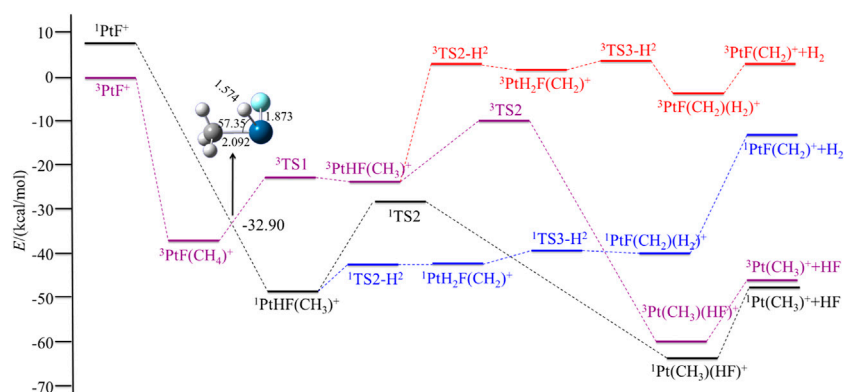


FIGURE 1

Potential energy surfaces of the reaction $\text{PtF}^+ + \text{CH}_4$ in the low- and high-spin states. The structure is the minimum energy crossing point (MECP).

TABLE 1 Calculated relative energies (kcal/mol) of stationary points on the potential energy surfaces of the reaction $\text{PtF}^+ + \text{CH}_4$ in the singlet and triplet states in three methods.

	Singlet			Triplet		
	B3P86	B3LYP	M06-2X	B3P86	B3LYP	M06-2X
PtF^+	0.00	7.48	32.14	1.22	0.00	0.00
$\text{PtF}(\text{CH}_4)^+$				-50.97	-36.92	-48.70
TS1				-37.08	-22.90	
$\text{PtHF}(\text{CH}_3)^+$	-62.23	-48.54	-57.00	-36.98	-23.01	-31.09
TS2	-42.49	-28.17	-39.15		-10.02	-13.73
$\text{Pt}(\text{CH}_3)(\text{HF})^+$	-75.64	-63.91	-89.29		-60.40	-81.57
$\text{Pt}(\text{CH}_3)^+ + \text{HF}$	-58.27	-47.61	-71.10		-45.93	-40.14
TS2-H ₂	-58.17	-42.28	-46.81	-12.36	2.83	-0.25
$\text{PtH}_2\text{F}(\text{CH}_2)^+$	-58.00	-42.43	-46.39	-13.00	1.81	-0.56
TS3-H ₂	-54.65	-39.28	-42.92	-11.46	3.24	1.13
$\text{PtF}(\text{CH}_2)(\text{H}_2)^+$	-54.72	-40.16	-44.52	-14.75	-3.78	-7.71
$\text{PtF}(\text{CH}_2)^+ + \text{H}_2$	-22.32	-12.79	-18.97	-5.80	2.89	-2.22

methods are very similar in terms of geometric optimization, energy, and potential energy surfaces. The data are shown in Table 1 and the Supporting Information. Among them, B3LYP shows a more systematic process in a high-spin state and is also more resource-efficient. Otherwise, we also calculated the single point energy of the reaction at the CCSD(T)/aug-cc-pVTZ (PP) level. The trend of the single point energy is similar to the previous potential energy surface except for the energy of $^1\text{Pt}(\text{CH}_3)^+$ in the last step, which is inconsistent with the experimental results (Schröder and Schwarz, 2005). So, all the data used are obtained based on the B3LYP method.

3 Results and discussions

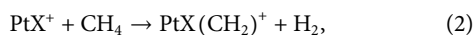
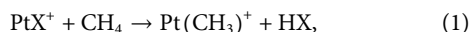
In this section, we discuss the reactivity of the PtX^+ ($\text{X} = \text{F}, \text{Cl}, \text{Br}, \text{I}$) in the activation process of CH_4 and present a brief discussion of the most abundant or interesting processes for the PtX^+/CH_4 systems. Both low- and high-spin states have been considered. The potential energy surfaces of the reaction $\text{PtX}^+ + \text{CH}_4$ in the low- and high-spin states are summarized in Figure 1 and Figure 4, and the energetics (in kcal/mol) of the intermediates and transition states, relative to the ground state PtX^+ plus CH_4 have been summarized in Table 2. Geometries of

TABLE 2 Calculated relative energies (kcal/mol) of stationary points on the potential energy surfaces of the reaction PtX^+ ($\text{X} = \text{F}, \text{Cl}, \text{Br}, \text{I}$) and CH_4 in the singlet and triplet states.

Species	X = F		X = Cl		X = Br		X = I	
	Singlet	Triplet	Singlet	Triplet	Singlet	Triplet	Singlet	Triplet
PtX^+	7.48	0.00	16.40	0.00	23.90	0.00	22.34	0.00
$\text{PtX}(\text{CH}_4)^+$		−36.92		−30.57		−26.39		−23.15
TS1		−22.90		−18.07		−13.60		−11.62
$\text{PtHX}(\text{CH}_3)^+$	−48.54	−23.01	−41.73	−18.43	−35.59	−14.02	−30.93	−12.21
TS2	−28.17	−10.02	−29.62	−2.10	−23.70	0.57	−15.54	6.21
$\text{Pt}(\text{CH}_3)(\text{HX})^+$	−63.91	−60.40	−41.05	−27.47	−31.71	−15.00	−22.80	−4.92
$\text{Pt}(\text{CH}_3)^+ + \text{HX}$	−47.61	−45.93	−10.45	−8.77	7.12	8.81	21.18	22.86
TS2- H_2	−42.28	2.83	−26.52	8.85	−17.20	13.15	−8.94	12.57
$\text{PtH}_2\text{X}(\text{CH}_2)^+$	−42.43	1.81	−26.61	8.57	−15.00	12.76	−9.11	11.28
TS3- H_2	−39.28	3.24	−23.51	11.88	−14.42	16.47	−6.04	16.25
$\text{PtX}(\text{CH}_2)(\text{H}_2)^+$	−40.16	−3.78	−24.84	7.28	−15.84	10.29	−7.56	11.15
$\text{PtX}(\text{CH}_2)^+ + \text{H}_2$	−12.79	2.89	−6.69	10.86	−0.74	14.78	3.97	16.85

these structures, including bond distances and bond angles, are summarized in the [Supporting Information](#).

The reactions observed in [Figure 1](#) can be classified into two different categories: 1) reactions involving Pt-X bond cleavage, namely, the expulsions of HX and 2) bond activation of CH_4 without obvious occurrence of Pt-X bond cleavage, that is, the loss of H_2 (summarized in [Eq. 1](#) and [2](#)).



For the sake of simplicity, each species is labeled with its spin multiplicity as a superscript preceding the formula.

3.1 $\text{PtF}^+ + \text{CH}_4$

For PtF^+ , the ground electronic state has been found to be a triplet, and the singlet electronic excitation state of $^1\text{PtF}^+$ has a relative energy of 7.48 kcal/mol. The reaction starts with the formation of a methane complex $\text{PtF}(\text{CH}_4)^+$. Based on [Figure 1](#), the spin-conserving dehydrogenation of CH_4 along the ground state route $^3\text{PtF}^+ + \text{CH}_4 \rightarrow ^3\text{PtF}(\text{CH}_2)^+ + \text{H}_2$ is endothermic by 2.89 kcal/mol and cannot occur for the high efficiency of the reaction. So, the reaction would obtain HF through the ground route or would be a two-state reaction scenario (TSR) ([Roithova et al., 2010](#)).

In the triplet state, the relative energy of the complex $^3\text{PtF}(\text{CH}_4)^+$ is −36.92 kcal/mol and is found to have a η^2 coordination, the $\theta_{\text{C-Pt-F}} = 179.89^\circ$, which indicates that the carbon atom attacks to Pt along the Pt-F axis. Then, Pt inserts into one of the C-H bonds of methane, resulting in a hydridomethyl complex $^3\text{PtHF}(\text{CH}_3)^+$, which has an energy

of −23.01 kcal/mol. TS1 is the transition state of the oxidative addition of the first C-H bond on the reaction path. On the $^3\text{TS1}$, the activated C-H bond is almost broken with the C-H bond length of 1.775 Å and the Pt-H bond is nearly formed with the Pt-H bond length of 1.565 Å, indicating that $^3\text{TS1}$ is a typical three-centered late transition state, which is 14.02 kcal/mol above the encounter complex $^3\text{PtF}(\text{CH}_4)^+$ but only 0.11 kcal/mol above the $^3\text{PtHF}(\text{CH}_3)^+$.

The low-spin $^1\text{PtF}^+$ with methane tends to form $^1\text{PtHF}(\text{CH}_3)^+$ intermediate directly. No activation transition state has been found on the singlet surface. The results indicate that the first C-H bond is activated spontaneously on the singlet surface. Energetically, the $^1\text{PtHF}(\text{CH}_3)^+$ is 25.53 kcal/mol lower than that of the triplet $^3\text{PtHF}(\text{CH}_3)^+$. A curve crossing is required from the triplet state to the singlet state *via* an MECP. As shown in [Figure 1](#), due to the higher energies of the triplet-spin state in the process of the expulsions of HF, and the processes in the triplet-spin state being similar to the singlet-spin paths, later, the triplet surface is not considered in the expulsion of HF.

In the following pages of this section, we will first discuss the process of the expulsions of HX, namely, HF. On the singlet surface, the next step is a reductive elimination step to form an HF molecule complex; that is, the H and F rearrange to form an HF molecule electrostatically bound to Pt to obtain the $^1\text{Pt}(\text{CH}_3)(\text{HF})^+$ with a barrier of 20.37 kcal/mol. In the last step, HF can be eliminated in an exothermic reaction by 17.98 kcal/mol. This last step leaves $^1\text{Pt}(\text{CH}_3)^+$ in its ground singlet state.

For the elimination of H_2 , a migration of hydrogen from CH_3 to Pt, leading to $^1\text{PtH}_2\text{F}(\text{CH}_2)^+$ with an energy barrier of 6.26 kcal/mol. The transition state $^1\text{TS2-H}^2$ (it represents the transition state in the process of the elimination of H_2) is a

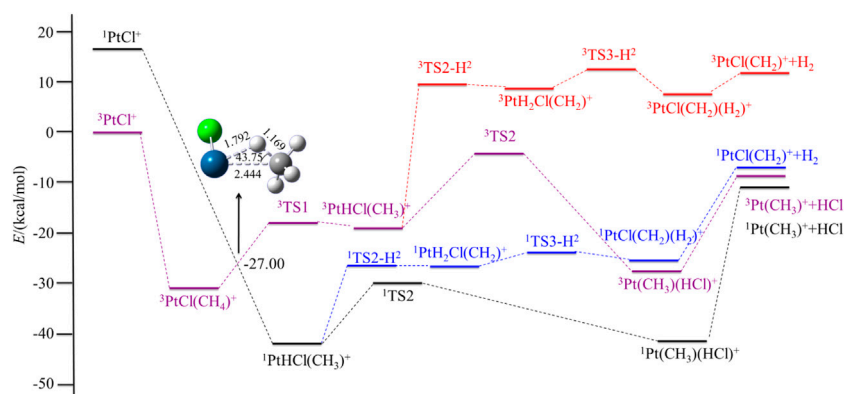


FIGURE 2

Potential energy surfaces of the reaction $\text{PtCl}^+ + \text{CH}_4$ in the low- and high-spin states. The structure is the minimum energy crossing point (MECP).

three-centered late transition state. Then, the two hydrogens rearrange easily to form the $^1\text{PtF}(\text{CH}_2)(\text{H}_2)^+$. Afterward, the molecule H_2 is eliminated. The calculated dissociation energy of H_2 to $^1\text{PtF}(\text{CH}_2)^+$ is 27.38 kcal/mol.

Generally, the energy barrier controls the reaction rate in a channel. Comparing the above two reaction channels, the energy barrier of H_2 elimination is 14.11 kcal/mol lower than that of the HF expulsions. However, in the subsequent steps, the calculated ligand dissociation energy of H_2 to $^1\text{PtF}(\text{CH}_2)^+$ is much higher than any energies of the complexes in the path to produce HF . Namely, the favorable path for the reaction of $\text{PtF}^+ + \text{CH}_4$ is the channel of the elimination of HF .

For the overall process, the energetically most favorable route involves a two-state reactivity scenario. The favorable route is the elimination of HF via the route $^3\text{PtF}^+ + \text{CH}_4 \rightarrow ^3\text{PtF}(\text{CH}_4)^+ \rightarrow \text{MECP} \rightarrow ^1\text{PtHF}(\text{CH}_3)^+ \rightarrow ^1\text{TS2} \rightarrow ^1\text{Pt}(\text{CH}_3)(\text{HF})^+ \rightarrow ^1\text{Pt}(\text{CH}_3)^+ + \text{HF}$.

3.2 PtX^+ ($\text{X} = \text{Cl}, \text{Br}, \text{I}$) + CH_4

As to the CH_4 activation on PtX^+ ($\text{X} = \text{Cl}, \text{Br}, \text{I}$), the mechanisms are very similar to those on PtF^+ , as discussed earlier. Indeed, the critical geometrical parameters in the intermediates and transition state are all very similar to the corresponding structures in the case of PtF^+ , as can be seen clearly by comparing the figures in the [Supporting Information](#). Therefore, we shall not discuss their geometries in further detail but show some differences and their characteristics.

For PtX^+ ($\text{X} = \text{Cl}, \text{Br}, \text{I}$) with CH_4 , as calculated by the results, the ground low-lying state is all the triplet state. The excitation energies to the excited singlet state are 16.40, 23.90, and 22.34 kcal/mol, respectively, for PtX^+ ($\text{X} = \text{Cl}, \text{Br}, \text{I}$). The low-spin $^1\text{PtX}^+$ with methane tends to form a $^1\text{PtHX}(\text{CH}_3)^+$ intermediate directly. No

activation transition state has been found on the singlet surface. The results are similar to the $\text{PtF}^+ - \text{CH}_4$ system and indicate that C-H is activated spontaneously on the singlet surface. Energetically, the $^1\text{PtHX}(\text{CH}_3)^+$ is lower than the triplet $^3\text{PtHX}(\text{CH}_3)^+$. Since the triplet state is the ground state of PtX^+ , the methane activation starting from the ground state again requires an intersystem crossing as described in the case of PtF^+ via a minimum energy crossing point, as shown in [Figures 2–4](#).

Different from PtF^+ , as for the other three PtX^+ ($\text{X} = \text{Cl}, \text{Br}, \text{I}$), on the singlet surface, the next step is the rearrangement of hydrogen and halogen to obtain HX , which has an activation energy of 12.11, 11.89, and 15.39 kcal/mol, respectively, for PtX^+ ($\text{X} = \text{Cl}, \text{Br}, \text{I}$). This activation energy is 3.10, 6.50, and 6.60 kcal/mol lower than that in the path of the elimination of H_2 .

For PtCl^+ , HCl can be eliminated in an exothermic reaction by 10.45 kcal/mol. Due to the path of the expulsions of H_2 always being high-lying compared with the process of elimination of HCl , it is an unfavorable path. Namely, the favorable path of $\text{PtCl}^+/\text{CH}_4$ is the process of HCl elimination. This result is in good agreement with the experimental results as reported by [Schröder and Schwarz \(2005\)](#). They reported the branching ratio of HCl is 100%. For $\text{PtBr}^+/\text{CH}_4$, the favorable path is the process of the elimination of HBr , but the calculated ligand dissociation energy of HBr to $^1\text{Pt}(\text{CH}_3)^+$ is 38.83 kcal/mol, different from PtF^+ , the energy difference between the two processes of the products are only 7.86 kcal/mol, which is lower than others. The activation energy to obtain $^1\text{Pt}(\text{CH}_3)(\text{HBr})^+$ is 6.50 kcal/mol lower than to obtain $^1\text{PtH}_2\text{Br}(\text{CH}_2)^+$. Due to the lower activation energy, the favorable path of the reaction of $\text{PtBr}^+/\text{CH}_4$ probably is the elimination of HBr , but also has some ratio of H_2 in the products, as mentioned in the earlier discussions. As reported by [Schröder and Schwarz \(2005\)](#), the branching ratio of $\text{HBr}:\text{H}_2$ is 85:15. As for PtI^+ , although the

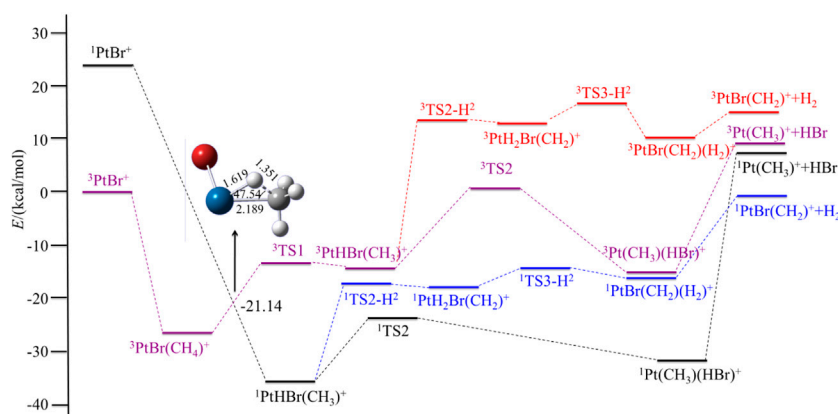


FIGURE 3

Potential energy surfaces of the reaction $\text{PtBr}^+ + \text{CH}_4$ in the low- and high-spin states. The structure is the minimum energy crossing point (MECP).

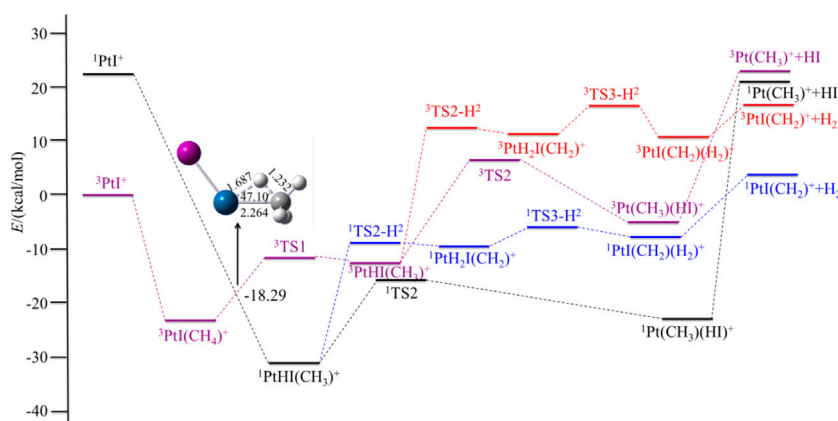


FIGURE 4

Potential energy surfaces of the reaction $\text{PtI}^+ + \text{CH}_4$ in the low- and high-spin states. The structure is the minimum energy crossing point (MECP).

energies in the potential energy surfaces before the loss of HI are lower than that of H_2 , the elimination of HI needs much more energy than H_2 , and it is endothermic at 43.98 kcal/mol, which is not favorable to occur. In the process of the loss of H_2 , there is a barrier height of 21.99 kcal/mol on the singlet state to form the intermediate $^1\text{PtH}_2\text{I}(\text{CH}_2)^+$. After overcoming a small barrier of 3.07 kcal/mol, the complex $^1\text{PtI}(\text{CH}_2)(\text{H}_2)^+$ is formed. The low-spin species $^1\text{PtI}(\text{CH}_2)^+$ has an association energy of 11.53 kcal/mol. This reaction is endothermic of 3.97 kcal/mol, which is also not favorable thermodynamically.

In summary, in the elimination of HX ($\text{X} = \text{F}, \text{Cl}, \text{Br}, \text{I}$), the formal oxidation state of the metal ion appears to be conserved,

and the importance of this reaction channel decreases in going as the sequence: $\text{X} = \text{F}, \text{Cl}, \text{Br}, \text{I}$. A reversed trend is observed in the loss of small closed-shell molecule H_2 for $\text{X} = \text{F}, \text{Cl}, \text{Br}$, while it is not favorable for PtI^+ in the loss of either HI or H_2 . The reason for the reactivity along with the abovementioned trends can be explained by the electronegative character of X; on the other hand, by the corresponding reaction enthalpies, which are mostly related to the formation of HX, that is to say, the halogens are heavier the bond-dissociation energies are much lower (Dede et al., 2009). The results can also be seen by the Natural Bond Orbital (NBO) populations and Natural population analysis (NPA) charge, as shown in the Supporting Information, and the results of part of the key structures are shown in Table 3. The

TABLE 3 Valence NBO populations for the 6s/5d/6p orbitals of Pt and the natural population analysis (NPA) charge of the related atoms in part of the key structures in the reaction of PtX^+ ($\text{X} = \text{F}, \text{Cl}, \text{Br}, \text{I}$) + CH_4 in the singlet state.

	PtF ⁺			PtCl ⁺			PtBr ⁺			PtI ⁺						
NBO																
TS2	0.42/8.73/0.01			0.43/8.93/0.01			0.41/9.01/0.01			0.42/9.07/0.02						
Pt (CH ₃)(HX) ⁺	0.15/9.01/0.01			0.36/9.03/0.01			0.41/9.05/0.01			0.44/9.09/0.02						
TS2-H ₂	0.67/8.52/0.03			0.72/8.69/0.02			0.73/8.72/0.03			0.76/8.77/0.03						
PtX (CH ₂)(H ₂) ⁺	0.57/8.57/0.02			0.62/8.71/0.02			0.64/8.74/0.01			0.67/8.82/0.02						
NPA Charge																
	Pt	F	C		Pt	Cl	C		Pt	Br	C		Pt	I	C	
TS2	0.85	-0.40	-0.52		0.64	-0.02	-0.52		0.57	0.12	-0.54		0.50	0.32	-0.55	
Pt (CH ₃)(HX) ⁺	0.84	-0.54	-0.54		0.60	-0.02	-0.55		0.53	0.13	-0.56		0.46	0.34	-0.56	
TS2-H ₂	0.79	-0.52	-0.13		0.56	-0.25	-0.15		0.51	-0.15	-0.17		0.42	-0.01	-0.19	
PtX (CH ₂)(H ₂) ⁺	0.84	-0.55	0.07		0.64	-0.26	0.02		0.59	-0.16	-0.004		0.48	-0.01	-0.06	
	Pt	F	C	H	Pt	F	C	H	Pt	F	C	H	Pt	F	C	H
PtHX (CH ₃) ⁺	0.99	-0.38	-0.52	0.21	0.68	-0.08	-0.52	0.21	0.53	0.13	-0.56	0.20	0.50	0.17	-0.54	0.19
TS2	0.85	-0.40	-0.52	0.38	0.64	-0.02	-0.52	0.22	0.57	0.12	-0.54	0.19	0.50	0.32	-0.55	0.10
PtH ₂ X (CH ₂) ⁺	0.80	-0.55	-0.10	0.26	0.58	-0.28	-0.12	0.26	0.53	-0.19	-0.14	0.25	0.45	-0.05	-0.18	0.24
TS3-H ₂	0.80	-0.54	0.02	0.14	0.58	-0.27	-0.02	0.14	0.53	-0.18	-0.05	0.14	0.46	-0.06	-0.08	0.13

electronegativity of the halogens decreases gradually from F to I, and the donor properties increase gradually from F to I, so F forms a strongly polarized covalent bond to Pt, and F increases the formal oxidation of Pt.

3.3 Mechanism discussions

Reaction mechanisms of these reactions are elucidated by detailed NPA charge and the Frontier Molecular Orbitals (HOMO and LUMO) of the key structures in the rate controlling step.

In the elimination of HF, as shown in Table 3, the F atom carries a significant negative charge, serving as a good proton acceptor, in which the electron is accepted by the metal center, thus, the NPA charge decreases in Pt. This process can be classified as a conventional proton-coupled electron transfer (PCET (Li et al., 2016b)) mechanism. For HCl and HBr eliminations, the charges of all atoms did not change during hydrogen transforms, and the mechanism can be judged as hydrogen atom transfer (HAT (Dietl et al., 2012)), while for I ligand, the NPA charge of I atom increases and that of H atom decreases, and it can be determined that the process is hydride transfer (HT (Li et al., 2016c)) mechanism.

The mechanisms of HX eliminations also can be explained by the analysis of Frontier Molecular Orbitals, which are shown in Figure 5. In the HOMO orbital, the $\sigma(\text{d}_{x^2-y^2})$ of Pt and $\sigma(\text{p}_y)$ of X occupied the main contribution in Pt-X molecular orbital. The coefficient of Pt ($\sigma(\text{d}_{x^2-y^2})$) becomes smaller and X ($\sigma(\text{p}_y)$) increases in the sequence of $\text{F} < \text{Cl} < \text{Br} < \text{I}$. From $^1\text{PtHX}(\text{CH}_3)^+$ to $^1\text{TS2}$, the increase of electron density (φ^2) on Pt is consistent with the decrease of NPA charge. The decrease of electron density on X also corresponds to the increase of NPA charge. It also can be seen from the LUMO orbital graph of $\text{C}(\sigma(\text{p}_y))\text{-Pt}(\sigma(\text{d}_{xy}))\text{-X}(\sigma(\text{p}_x))$ that the φ^2 of Pt increase and the φ^2 of C and X decrease.

In the course of the formation of H_2 , the positive charge of H diminishes, indicating that it may be an HT mechanism. Corresponding to this, electron density has been transferred from methane to hydrogen, as shown in the HOMO orbital graph in Figure 5. As the transferred electron density takes the same route as that of the concurrently transferred hydrogen atom, it can be described as a hydride transfer mechanism. For different halogens, the change of charges is the same, that is to say, in terms of rate controlling step, different halogen ligands have no significant effect on the process of elimination of H_2 .

In sum, in the eliminations of HX, the mechanisms are different. The transfer form of H is from proton to atom, last

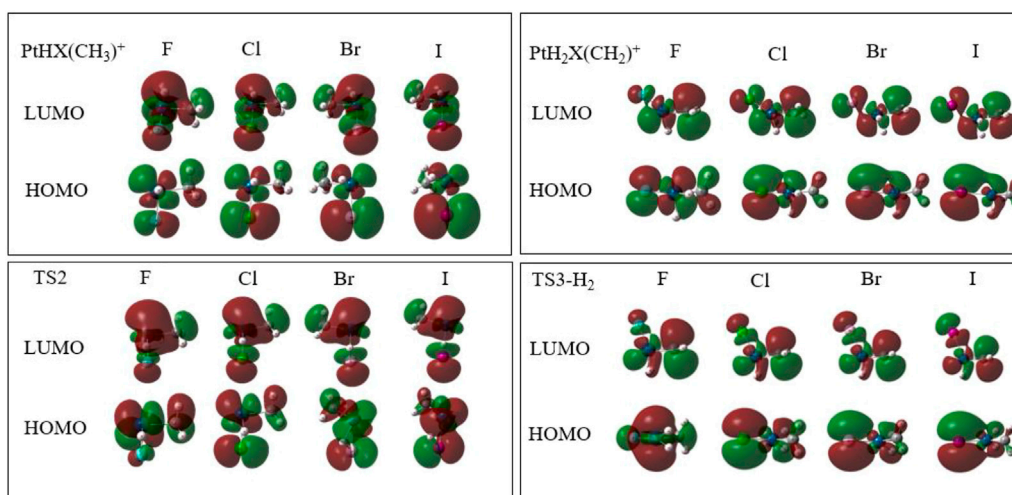


FIGURE 5
HOMO/LUMO orbital graphs in part of the structures of rate controlling step in the reaction of PtX^+ ($\text{X} = \text{F}, \text{Cl}, \text{Br}, \text{I}$) + CH_4 in the singlet state.

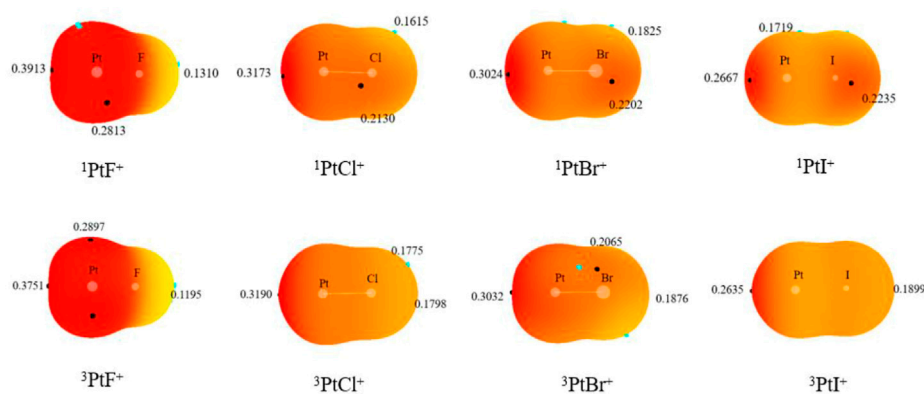


FIGURE 6
Molecular electrostatic potential (MEP) maps on the 0.001 a. u. isodensity surface of the monomers.

TABLE 4 Electron density (ρ , a.u.), Laplacian ($\nabla^2\rho$, a.u.), energy density (H , a.u.), intermolecular distance (R , Å), and charge transfer (CT, e) at the XPt-CH_4 ($\text{X} = \text{F}, \text{Cl}, \text{Br}, \text{I}$) complexes.

Complexes	ρ	$\nabla^2\rho$	H	R	CT
FPt-CH_4	0.0690	0.2009	-0.0143	2.305	0.2101
ClPt-CH_4	0.0727	0.1943	-0.0163	2.284	0.2111
BrPt-CH_4	0.0685	0.1886	-0.0140	2.315	0.1927
IPt-CH_4	0.0671	0.1888	-0.0133	2.327	0.1764

to hydride. The reason is mainly due to the electronegativity of halogens, while for the loss of H_2 , the transfer of H is in the form of hydride for all the X ligands.

3.4 Analysis of interaction between complexes

To further investigate the mechanisms, the interactions between the complexes in the reactions were also discussed. The MEP diagrams of singlet and triplet PtX^+ on the 0.001 a. u. isodensity surface are displayed in Figure 6. Since the complexes have positive charge, the overall electrostatic potential is in the red region. There is a deep red region (σ -hole) along the Pt-F axis around the Pt^+ , which correspond to the site where carbon atoms attack PtX^+ . It is consistent with the previously optimized structure. In addition, the σ -hole strength decreases in the order $\text{PtF}^+ > \text{PtCl}^+ > \text{PtBr}^+ > \text{PtI}^+$ owing to the different electron-withdrawing ability among the halogen.

TABLE 5 Electron density (ρ , a.u.), Laplacian ($\nabla^2\rho$, a.u.), energy density (H, a.u.), and charge transfer (CT, e) in the PtXCH₂-H₂ and PtCH₃-HX (X = F, Cl, Br, I) complexes.

	ρ	$\nabla^2\rho$	H	CT	ρ	$\nabla^2\rho$	H	CT
	Singlet				Triplet			
PtFCH ₂ -H ₂	0.1221	0.3547	-0.0499	0.2136	0.0683	0.2060	-0.0122	0.1537
PtClCH ₂ -H ₂	0.1088	0.3689	-0.0362	0.1873	0.0720	0.2209	-0.0141	0.1451
PtBrCH ₂ -H ₂	0.1037	0.3555	-0.0325	0.1749	0.0621	0.2265	-0.0094	0.1081
PtICH ₂ -H ₂	0.1120	0.3126	-0.0402	0.1923	0.0691	0.2589	-0.0121	0.1132
PtCH ₃ -HF	0.0496	0.2738	-0.0004	0.0655	0.0404	0.2029	0.0002	0.0486
PtCH ₃ -HCl	0.0833	0.2468	-0.0198	0.2990	0.0536	0.1550	-0.0082	0.2091
PtCH ₃ -HBr	0.0866	0.1773	-0.0269	0.3817	0.0574	0.1281	-0.0118	0.2550
PtCH ₃ -HI	0.0690	0.0774	-0.0210	0.4690	0.0489	0.0739	-0.0099	0.3503

In the AIM theory, electron density at the bond critical point (BCP) is one of the indicators of interaction strength. The electron density, Laplacian, and total energy density at the XPt-CH₄ (X = F, Cl, Br, I) complexes are listed in Table 4. The values of the density at the BCP lie in the range around 0.07 a. u., Laplacian is positive and energy density is negative in the methane complexes, which indicates that there exhibits a property of a partially covalent interaction. The charge transfer from CH₄ to PtX⁺ decreases in the order PtF⁺ > PtCl⁺ > PtBr⁺ > PtI⁺, which is consistent with the σ -hole strength of PtX⁺. The charge transfer and the interaction energy of methane complexes in the potential energy surface have similar changes.

Table 5 shows the electron density, Laplacian, and total energy density at the complexes before the expulsions of HX or H₂. It is generally believed that the greater the electron density between two atoms in a composite, the more concentrated the charge between the two atoms, which also means that the bond between these two atoms has a stronger tendency (Kraka and Cremer, 1990; Alkorta et al., 1998). As shown in Table 5, for all the complexes before dissociating the H₂ or HX molecule, Laplacian is positive and energy density is negative, indicating that there exists a partially covalent interaction between H₂ or HX molecule and Pt atom. For the same complex, the values of ρ , $\nabla^2\rho$, and energy density are obviously stronger in the singlet state than those in the triplet state, indicating a stronger interaction between the Pt and the H₂ or HX molecule in the singlet state, and more energy is required to expel H₂ or HX, which is consistent with the energy barrier of the reaction in the potential energy surfaces. Through the analysis of the interaction between atoms in the transition metal-ligand complex, the reaction path can be better explained.

From Table 5, one also can see that for the complexes before H₂ was removed, the values of charge transfer (CT) are between 0.17 e and 0.21 e, and the differences between PtXCH₂-H₂ (X = F,

Cl, Br, I) are small. However, for the complexes before HX was expelled, the values of charge transfer increased from PtCH₃-HF to PtCH₃-HI, which was generally consistent with the interaction energy. Namely, the complexes before the expulsions of HI had larger interaction energy than the others.

3.5 Comparisons with the reactions of NiX⁺ (X = F, Cl, Br, I) + CH₄

The reactions of NiX⁺ (X = F, Cl, Br, I) and methane have been investigated at the B3LYP level of theory by Schlange et al. (Schlange et al., 2007; Schlange and Schwarz, 2008). They reported that NiF⁺ is the only nickel-halide complex capable of activating methane for NiX⁺ (X = F, Cl, Br, I). The driving force of the reaction NiF⁺ with methane is provided by the exceptionally high stability of HF (Schlange et al., 2007). In the present study, we found that the PtX⁺ (X = F, Cl, Br) can bring about thermal activation of methane to loss HX decreasing in going as the sequence X = F, Cl, Br, and to loss H₂ increasing in the reverse sequence.

The reactions of NiF⁺ and their third-row congeners PtX⁺ with methane have many features in common; whereas, fundamental differences exist with regard to the details of the potential energy surfaces and, thus, to actual reaction mechanisms. As reported by Schlange and Schwarz (2008), for the NiF⁺ and methane systems studied, the energetically most favored variant corresponds to an σ -complex-assisted metathesis (σ -CAM). First, the reactions start with the formation of the encounter complex NiF(CH₄)⁺, and then, the molecule HF is directly eliminated via a multicenter transition state to obtain the product complex, Ni(CH₃)(HF)⁺. However, in the PtX⁺/CH₄ systems, oxidative addition/reductive elimination (OA/RE) is operative. After the formation of the complex PtX(CH₄)⁺, the next step is the cleaving of the C-H bond (oxidative addition),

resulting in the insertion product $\text{PtHX}(\text{CH}_3)^+$, and then a reductive elimination step to form an HX molecule complex is obtained, that is, the H and X rearrange to form an HX molecule electrostatically bound to Pt to obtain the $^1\text{Pt}(\text{CH}_3)(\text{HX})^+$.

Another difference in the reaction mechanisms is the potential energy surfaces. In the NiF^+/CH_4 system, the exothermic ligand exchange proceeds adiabatically only on the one potential energy surface, whereas the reaction of PtX^+/CH_4 needs a curve crossing, that is to say, it is a two-state reactivity. Otherwise, the NiF^+/CH_4 system proceeds on the high-spin ground triplet state, while the reaction of PtX^+ with methane takes place more easily along the low-spin potential energy surface. As for the reasons for the differences, Schlangen and Schwarz (2008) have reported that the strongly electron-withdrawing F substituent reduces the electron density at the Ni-center and, thus, decreases the repulsive interaction; therefore, the reaction can proceed on the high-spin ground state. Based on this point, we calculated the Mulliken charges of the M-atom (M = Ni, Pt) in the systems MX^+/CH_4 . The results indicate that the Mulliken charges of the Ni-atom in the NiF^+/CH_4 system increase 0.198, while the Pt-atom in the reaction PtF^+/CH_4 increases only 0.082.

4 Conclusion

The gas-phase ion-molecule reactions of PtX^+ cations (X = F, Cl, Br, I) with methane have been investigated theoretically at the DFT (B3LYP) level, considering both the low- and high-spin potential energy surfaces. All reactions fall into two major categories: 1) reactions involving Pt-X bond cleavage to expulse HX and 2) bond activation of CH_4 without obvious occurrence of Pt-X bond cleavage to loss H_2 . In the elimination of HX (X = F, Cl, Br, I), this reaction channel decreases in going as the sequence: X = F, Cl, Br, I. A reversed trend is observed in the losses of small closed-shell molecule H_2 for X = F, Cl, Br, while it is not favorable for PtI^+ in the loss of either HI or H_2 . The reason for the reactivity along with the abovementioned trends can be explained by the electronegative character of X.

In the eliminations of HX, the transfer form of H is from proton to atom, last to hydride, and the mechanisms are from PECT to HAT, last to HT for the sequence of X = F, Cl, Br, I. One reason is mainly due to the electronegativity of halogens. Otherwise, the mechanisms of HX eliminations also can be explained by the analysis of Frontier Molecular Orbitals, while for the loss of H_2 , the transfer of H is in the form of hydride for all the X ligands.

The charge transfer from CH_4 to PtX^+ decreases in the order $\text{PtF}^+ > \text{PtCl}^+ > \text{PtBr}^+ > \text{PtI}^+$, which is consistent with the σ -hole strength of PtX^+ . For the same complex, the values of ρ , $\nabla^2\rho$, and energy density are obviously stronger in the singlet state than those in the triplet state, indicating a stronger interaction between the Pt and the H_2 or HX molecule in the singlet state, and more energy is required to expel H_2 or HX, which is consistent with the energy barrier of the reaction in the potential energy surfaces. The

differences in charge transfer between $\text{PtXCH}_2\text{-H}_2$ (X = F, Cl, Br, I) for the complexes before H_2 is removed are small. However, for the complexes before HX is expelled, the values of charge transfer increase from $\text{PtCH}_3\text{-HF}$ to $\text{PtCH}_3\text{-HI}$, namely, the complexes before the expulsions of HI have larger interaction energy than the others. Through the analysis of the interaction between atoms in the transition metal ligand complex, the reaction path can be better explained.

Data availability statement

The original contributions presented in the study are included in the article/Supplementary Material; further inquiries can be directed to the corresponding author.

Author contributions

JZ and LQ: structure optimization and data collection; JC and QL: data analysis; WL and SL: data analysis and manuscript writing and revision. All authors read and approved the submitted version.

Acknowledgments

The authors thank the National Natural Science Foundation of China (Grant No. 21803052) and the Natural science foundation of Shandong province, China (Grant No. ZR2018LB017). The grants are gratefully acknowledged.

Conflict of interest

The authors declare that the research was conducted in the absence of any commercial or financial relationships that could be construed as a potential conflict of interest.

Publisher's note

All claims expressed in this article are solely those of the authors and do not necessarily represent those of their affiliated organizations, or those of the publisher, the editors, and the reviewers. Any product that may be evaluated in this article, or claim that may be made by its manufacturer, is not guaranteed or endorsed by the publisher.

Supplementary material

The Supplementary Material for this article can be found online at: <https://www.frontiersin.org/articles/10.3389/fchem.2022.1027465/full#supplementary-material>

References

- Achatz, U., Berg, C., Joos, S., Fox, B. S., Beyer, M. K., Niedner-Schatteburg, G., et al. (2000). Methane activation by platinum cluster ions in the gas phase: Effects of cluster charge on the Pt₄ tetramer. *Chem. Phys. Lett.* 320, 53–58. doi:10.1016/S0009-2614(00)00179-2
- Alkorta, I., Rozas, I., and Elguero, J. (1998). Charge-transfer complexes between dihalogen compounds and electron donors. *J. Phys. Chem. A* 102, 9278–9285. doi:10.1021/jp982251o
- Andrae, D., Haeussermann, U., Dolg, M., Stoll, H., and Preuss, H. (1990). Energy-adjusted *ab initio* pseudopotentials for the second and third row transition elements. *Theor. Chim. Acta* 77, 123–141. doi:10.1007/BF01114537
- Bader, R. F. W. (2000). *AIM2000 Program*. Hamilton, Canada: McMaster University. v. 2.0.
- Balcells, D., Clot, E., and Eisenstein, O. (2010). C-H bond activation in transition metal species from a computational perspective. *Chem. Rev.* 110, 749–823. doi:10.1021/cr900315k
- Becke, A. D. (1988). Density-functional exchange-energy approximation with correct asymptotic behavior. *Phys. Rev. A. Coll. Park.* 38, 3098–3100. doi:10.1103/PhysRevA.38.3098
- Becke, A. D. (1993). Density-functional thermochemistry. III. The role of exact exchange. *J. Chem. Phys.* 98, 5648–5652. doi:10.1063/1.464913
- Bulat, F. A., Toro-Labbé, A., Brinck, T., Murray, J. S., and Politzer, P. (2010). Quantitative analysis of molecular surfaces: Areas, volumes, electrostatic potentials and average local ionization energies. *J. Mol. Model.* 16, 1679–1691. doi:10.1007/s00894-010-0692-x
- Chen, Q., Chen, H. P., Kais, S., and Freiser, B. S. (1997). Gas-phase reactions of Fe(CH₃O)⁺ and Fe(CH₃S)⁺ with small alkanes: An experimental and theoretical study. *J. Am. Chem. Soc.* 119, 12879–12888. doi:10.1021/ja964234n
- Dede, Y., Zhang, X. H., Schlangen, M., Schwarz, H., and Baik, M. H. (2009). A redox non-innocent ligand controls the life time of a reactive quartet excited state: an MCSCF study of [Ni(H)(OH)]⁺. *J. Am. Chem. Soc.* 131, 12634–12642. doi:10.1021/ja902093f
- Dietl, N., Schlangen, M., and Schwarz, H. (2012). Thermal hydrogen-atom transfer from methane: The role of radicals and spin states in oxo-cluster chemistry. *Angew. Chem. Int. Ed.* 51, 5544–5555. doi:10.1002/anie.201108363
- Dobereine, G. E., and Crabtree, R. H. (2010). Dehydrogenation as a substrate-activating strategy in homogeneous transition-metal catalysis. *Chem. Rev.* 110, 681–703. doi:10.1021/cr900202j
- Dubois, M. R. (1989). Catalytic applications of transition-metal complexes with sulfide ligands. *Chem. Rev.* 89, 1–9. doi:10.1021/cr00091a001
- Elkind, J. L., and Armentrout, P. B. (1987). State-specific reactions of atomic transition-metal ions with H₂, HD, and D₂: Effects of d orbitals on chemistry. *J. Phys. Chem.* 91, 2037–2045. doi:10.1021/j100292a012
- Eller, K., and Schwarz, H. (1991). Organometallic chemistry in the gas phase. *Chem. Rev.* 91, 1121–1177. doi:10.1021/cr0006a002
- Frisch, M. J., Trucks, G. W., Schlegel, H. B., Scuseria, G. E., Robb, M. A., Cheeseman, J. R., et al. (2009). *Gaussian 09, revision A. 02*. Wallingford CT: Gaussian, Inc.
- Geng, C. Y., Li, J. L., Weiske, T., Schlangen, M., Shaik, S., and Schwarz, H. (2017). Electrostatic and charge-induced methane activation by a concerted double C-H bond insertion. *J. Am. Chem. Soc.* 139, 1684–1689. doi:10.1021/jacs.6b12514
- Gonzalez, C., and Schlegel, H. B. (1989). An improved algorithm for reaction path following. *J. Chem. Phys.* 90, 2154–2161. doi:10.1063/1.456010
- Halle, L. F., Armentrout, P. B., and Beauchamp, J. L. (1982). Ion beam studies of the reactions of group VIII metal ions with alkanes: Correlation of thermochemical properties and reactivity. *Organometallics* 1, 963–968. doi:10.1021/om00067a012
- Harvey, J. N. (2007). Understanding the kinetics of spin-forbidden chemical reactions. *Phys. Chem. Chem. Phys.* 9, 331–343. doi:10.1039/b614390c
- Howell, J. A. S., and Burkinshaw, P. M. (1983). Ligand substitution reactions at low-valent four-five and six-coordinate transition metal centers. *Chem. Rev.* 83, 557–599. doi:10.1021/cr00057a005
- Irikura, K. K., and Beauchamp, J. L. (1991b). Electronic structure considerations for methane activation by third-row transition-metal ions. *J. Phys. Chem.* 95, 8344–8351. doi:10.1021/j100174a057
- Irikura, K. K., and Beauchamp, J. L. (1991a). Methane oligomerization in the gas phase by third-row transition-metal ions. *J. Am. Chem. Soc.* 113, 2769–2770. doi:10.1021/ja00007a070
- Irikura, K. K., and Beauchamp, J. L. (1989). Osmium tetroxide and its fragment ions in the gas phase: Reactivity with hydrocarbons and small molecules. *J. Am. Chem. Soc.* 111, 75–85. doi:10.1021/ja00183a014
- Jana, R., Pathak, T. P., and Sigman, M. S. (2011). Advances in transition metal (Pd, Ni, Fe)-catalyzed cross-coupling reactions using alkyl-organometallics as reaction partners. *Chem. Rev.* 111, 1417–1492. doi:10.1021/cr100327p
- Kraka, E., and Cremer, D. (1990). Chemical implication of local features of the electron density distribution. *Concept Chem. Bond*, 116, 453–542. Maksic, ZB, Ed. doi:10.1007/978-3-642-61277-0_12
- Lawson Daku, L. M., Aquilante, F., Robinson, T. W., and Hauser, A. (2012). Accurate spin-state energetics of transition metal complexes. 1. CCSD(T), CASPT2, and DFT study of [M(NCH)₆]²⁺ (M = Fe, Co). *J. Chem. Theory Comput.* 8, 4216–4231. doi:10.1021/ct300592w
- Lee, C., Yang, W., and Parr, R. G. (1988). Development of the Colle-Salvetti correlation-energy formula into a functional of the electron density. *Phys. Rev. B* 37, 785–789. doi:10.1103/PhysRevB.37.785
- Li, J. L., Zhou, S. D., Schlangen, M., Weiske, T., and Schwarz, H. (2016a). Hidden hydride transfer as a decisive mechanistic step in the reactions of the unligated gold carbide [AuC]⁺ with methane under ambient conditions. *Angew. Chem. Int. Ed.* 55, 13072–13075. doi:10.1002/anie.201606707
- Li, J. L., Zhou, S. D., Zhang, J., Schlangen, M., Usharani, D., Shaik, S., et al. (2016b). Mechanistic variants in gas-phase metal-oxide mediated activation of methane at ambient conditions. *J. Am. Chem. Soc.* 138, 11368–11377. doi:10.1021/jacs.6b07246
- Li, J. L., Zhou, S. D., Zhang, J., Schlangen, M., Weiske, T., Usharani, D., et al. (2016c). Electronic origins of the variable efficiency of room-temperature methane activation by homo- and heteronuclear cluster oxide cations [XYO₂]⁺ (X, Y = Al, Si, Mg): Competition between proton-coupled electron transfer and hydrogen-atom transfer. *J. Am. Chem. Soc.* 138, 7973–7981. doi:10.1021/jacs.6b03798
- Li, W. Q., Geng, Z. Y., Wang, Y. C., Yan, P. J., Zhang, X., Wang, Z., et al. (2009). Density functional theory studies of thermal activation of methane by MH⁺ (M = Ru, Rh, and Pd). *J. Phys. Chem. A* 113, 1807–1812. doi:10.1021/jp808830c
- Liu, G. X., Zhu, Z. G., Ciborowski, S. M., Ariyaratna, I. R., Miliordos, E., and Bowen, K. H. (2019). Selective activation of the C-H bond in methane by single platinum atomic anions. *Angew. Chem. Int. Ed.* 58, 7773–7777. doi:10.1002/anie.201903252
- Mandich, M. L., Steigerwald, M. L., and Reents, W. D. (1986). The effects of chloro substitution on the electronic structure of ClCr⁺, ClMn⁺, and ClFe⁺ and their reactivity with small alkanes. *J. Am. Chem. Soc.* 108, 6197–6202. doi:10.1021/ja00280a015
- Mazurek, U., Schröder, D., and Schwarz, H. (1998). Generation and reactivity of chromium fluoride cations (CrF_n⁺, n = 0–4) in the gas phase. *Collect. Czech. Chem. Commun.* 63, 1498–1512. doi:10.1135/cccc19981498
- Michael, B., Christoph, R., Dimitrios, A. P., Thomas, B., and Frank, N. (2008). Geometries of third-row transition-metal complexes from density-functional theory. *J. Chem. Theory Comput.* 4, 1449–1459. doi:10.1021/ct800172j
- Musaeu, D. G., Koga, N., and Morokuma, K. (1993). *Ab initio* molecular orbital study of the electronic and geometric structure of RhCH₂⁺ and the reaction mechanism: RhCH₂⁺ + H₂ → Rh⁺ + CH₄. *J. Phys. Chem.* 97, 4064–4075. doi:10.1021/j100118a022
- Musaeu, D. G., and Morokuma, K. (1994). *Ab initio* molecular orbital study of the molecular and electronic structure of FeCH₂⁺ and of the reaction mechanism of FeCH₂⁺ + H₂. *J. Chem. Phys.* 101, 10697–10707. doi:10.1063/1.467883
- Ohanessian, G., Brusich, M. J., and Goddard, W. A., III (1990). Theoretical study of transition-metal hydrides. 5. Hafnium to mercury (HfH⁺ through HgH⁺), barium and lanthanum (BaH⁺ and LaH⁺). *J. Am. Chem. Soc.* 112, 7179–7189. doi:10.1021/ja00176a016
- Perdew, J. P. (1986a). Density-functional approximation for the correlation energy of the inhomogeneous electron gas. *Phys. Rev. B* 33, 8822–8824. doi:10.1103/PhysRevB.33.8822
- Perdew, J. P. (1986b). Erratum: Density-functional approximation for the correlation energy of the inhomogeneous electron gas. *Phys. Rev. B* 34, 7406. doi:10.1103/PhysRevB.34.7406
- Polí, R., and Harvey, J. N. (2003). Spin forbidden chemical reactions of transition metal compounds. New ideas and new computational challenges. *Chem. Soc. Rev.* 32, 1–8. doi:10.1039/b200675h
- Rodgers, M. T., Stanley, J. R., and Amunugama, R. (2000). Periodic trends in the binding of metal ions to pyridine studied by threshold collision-induced dissociation and density functional theory. *J. Am. Chem. Soc.* 122, 10969–10978. doi:10.1021/ja0027923
- Roithova, J., and Schröder, D. (2010). Selective activation of alkanes by gas-phase metal ions. *Chem. Rev.* 110, 1170–1211. doi:10.1021/cr900183p

- Schilling, J. B., Goddard, W. A., III, and Beauchamp, J. L. (1986). Theoretical studies of transition-metal hydrides. 1. Bond energies for MH^+ with $M = Ca, Sc, Ti, V, Cr, Mn, Fe, Co, Ni, Cu,$ and Zn . *J. Am. Chem. Soc.* 108, 582–584. doi:10.1021/ja00264a004
- Schilling, J. B., Goddard, W. A., III, and Beauchamp, J. L. (1987). Theoretical studies of transition-metal hydrides. 2. CaH^+ through ZnH^+ . *J. Phys. Chem.* 91, 5616–5623. doi:10.1021/j100306a024
- Schilling, J. B., Goddard, W. A., III, and Beauchamp, J. L. (1987). Theoretical studies of transition-metal hydrides. 3. SrH^+ through CdH^+ . *J. Am. Chem. Soc.* 109, 5565–5573. doi:10.1021/ja00253a001
- Schlangen, M., Schröder, D., and Schwarz, H. (2007). Ligand and substrate effects in gas-phase reactions of NiX^+/RH couples ($X = F, Cl, Br, I; R = CH_3, C_2H_5, nC_3H_7, nC_4H_9$). *Chem. Eur. J.* 13, 6810–6816. doi:10.1002/chem.200700506
- Schlangen, M., Schröder, D., and Schwarz, H. (2007). Pronounced ligand effects and the role of formal oxidation states in the nickel-mediated thermal activation of methane. *Angew. Chem. Int. Ed.* 46, 1641–1644. doi:10.1002/anie.200603266
- Schlangen, M., and Schwarz, H. (2008). Ligand effects on the mechanisms of thermal bond activation in the gas-phase reactions $NiX^+/CH_4 \rightarrow Ni(CH_3)^+/HX$ ($X = H, CH_3, OH, F$). Short Communication. *Helv. Chim. Acta* 91, 2203–2210. doi:10.1002/hlca.200890238
- Schröder, D., Hrusak, J., and Schwarz, H. (1993). Ligand effects on the reactivity of iron (II) cations FeX^+ in the gas phase. *Berichte Bunsenges. fur Phys. Chem.* 97, 1085–1090. doi:10.1002/bbpc.19930970904
- Schröder, D., and Schwarz, H. (2005). Activation of methane by gaseous platinum (II) ions PtX^+ ($X = H, Cl, Br, CHO$). *Can. J. Chem.* 83, 1936–1940. doi:10.1139/v05-217
- Schultz, R. H., Elkind, J. L., and Armentrout, P. B. (1988). Electronic effects in C-H and C-C bond activation. State-specific reactions of Fe^+ ($^6D, ^4F$) with methane, ethane, and propane. *J. Am. Chem. Soc.* 110, 411–423. doi:10.1021/ja00210a017
- Schwarz, H., Navarrete, P. G., Li, J. L., Schlangen, M., Sun, X. Y., Weiske, T., et al. (2017). Unexpected mechanistic variants in the thermal gas-phase activation of methane. *Organometallics* 36, 8–17. doi:10.1021/acs.organomet.6b00372
- Schwarz, H., Shaik, S., and Li, J. L. (2017). Electronic effects on room-temperature, gas-phase C-H Bond activations by cluster oxides and metal carbides: The methane challenge. *J. Am. Chem. Soc.* 139, 17201–17212. doi:10.1021/jacs.7b10139
- Sun, X. Y., Zhou, S. D., Schlangen, M., and Schwarz, H. (2016). Efficient room-temperature methane activation by the closed-shell, metal-free cluster $[OsIOH]^+$: A novel mechanistic variant. *Chem. Eur. J.* 22, 14257–14263. doi:10.1002/chem.201601981
- Tolbert, M. A., and Beauchamp, J. L. (1986). Homolytic and heterolytic bond dissociation energies of the second row group 8, 9, and 10 diatomic transition-metal hydrides: Correlation with electronic structure. *J. Phys. Chem.* 90, 5015–5022. doi:10.1021/j100412a029
- Tolbert, M. A., Mandich, M. L., Halle, L. F., and Beauchamp, J. L. (1986). Activation of alkanes by ruthenium, rhodium, and palladium ions in the gas phase: Striking differences in reactivity of first- and second-row metal ions. *J. Am. Chem. Soc.* 108, 5675–5683. doi:10.1021/ja00279a003
- Vargas, A., Krivokapic, I., Hauser, A., and Lawson Daku, L. M. (2013). Towards accurate estimates of the spin-state energetics of spin-crossover complexes within density functional theory: A comparative case study of cobalt(II) complexes. *Phys. Chem. Chem. Phys.* 15, 3752–3763. doi:10.1039/c3cp44336a
- Wang, X. F., and Andrews, L. (2009). Infrared spectra and theoretical calculations for Fe, Ru, and Os metal hydrides and dihydrogen complexes. *J. Phys. Chem. A* 113, 551–563. doi:10.1021/jp806845h
- Wesendrup, R., Schroder, D., and Schwarz, H. (1994). Catalytic Pt^+ -mediated oxidation of methane by molecular oxygen in the gas phase. *Angew. Chem. Int. Ed. Engl.* 33, 1174–1176. doi:10.1002/anie.199411741
- Westerberg, J., and Blomberg, M. R. A. (1998). Methane activation by naked Rh^+ atoms. A theoretical study. *J. Phys. Chem. A* 102, 7303–7307. doi:10.1021/jp981291p
- Wheeler, O. W., Michelle, S., Gao, A., Bakker, J. M., and Armentrout, P. B. (2016). Activation of C-H bonds in $Pt^+ + x CH_4$ reactions, where $x = 1-4$: Identification of the platinum dimethyl cation. *J. Phys. Chem. A* 120, 6216–6227. doi:10.1021/acs.jpca.6b05361
- Ye, S., and Neese, F. (2010). Accurate modeling of spin-state energetics in spin-crossover systems with modern density functional theory. *Inorg. Chem.* 49, 772–774. doi:10.1021/ic902365a
- Yue, L., Li, J. L., Zhou, S. D., Sun, X. Y., Schlangen, M., Shaik, S., et al. (2017). Control of product distribution and mechanism by ligation and electric field in the thermal activation of methane. *Angew. Chem. Int. Ed.* 56, 10219–10223. doi:10.1002/anie.201703485
- Zhang, Q., and Bowers, M. T. (2004). Activation of methane by MH^+ ($M = Fe, Co,$ and Ni): A combined mass spectrometric and DFT study. *J. Phys. Chem. A* 108, 9755–9761. doi:10.1021/jp047943t
- Zhao, Y., and Truhlar, D. G. (2008). Density functionals with broad applicability in chemistry. *Acc. Chem. Res.* 41, 157–167. doi:10.1021/ar700111a
- Zhao, Y., and Truhlar, D. G. (2008). The M06 suite of density functionals for main group thermochemistry, thermochemical kinetics, noncovalent interactions, excited states, and transition elements: Two new functionals and systematic testing of four M06-class functionals and 12 other functionals. *Theor. Chem. Acc.* 120, 215–241. doi:10.1007/s00214-007-0310-x
- Zhou, S. D., Firouzbakht, M., Schlangen, M., Kaupp, M., and Schwarz, H. (2017a). On the electronic origin of remarkable ligand effects on the reactivities of $[NiL]^+$ complexes ($L = C_6H_5, C_5H_4N, CN$) towards methane. *Chem. Eur. J.* 23, 14430–14433. doi:10.1002/chem.201703767
- Zhou, S. D., Li, J. L., Firouzbakht, M., Schlangen, M., and Schwarz, H. (2017b). Sequential gas-phase activation of carbon dioxide and methane by $[Re(CO)_2]^+$: The sequence of events matters. *J. Am. Chem. Soc.* 139, 6169–6176. doi:10.1021/jacs.7b01255
- Zhou, S. D., Li, J. L., Schlangen, M., and Schwarz, H. (2016). Thermal dehydrogenation of methane by $[ReN]^+$. *Angew. Chem. Int. Ed.* 55, 14863–14866. doi:10.1002/anie.201607960
- Zhou, S. D., Schlangen, M., and Schwarz, H. (2017c). Spin-Selective, Competitive hydrogen-atom transfer versus CH_2O -generation from the $CH_4/[ReO_4]^+$ couple at ambient conditions. *Chem. Eur. J.* 23, 17469–17472. doi:10.1002/chem.201704892



OPEN ACCESS

EDITED BY

Tiancheng Mu,
Renmin University of China, China

REVIEWED BY

Jun Gao,
Qingdao Institute of Bioenergy and
Bioprocess Technology (CAS), China
Shaoyu Lu,
Lanzhou University, China

*CORRESPONDENCE

Hongliang Liu,
liuhongliang@ytu.edu.cn

SPECIALTY SECTION

This article was submitted to Green and
Sustainable Chemistry,
a section of the journal
Frontiers in Chemistry

RECEIVED 06 September 2022

ACCEPTED 13 September 2022

PUBLISHED 30 September 2022

CITATION

Wei Z, Zhang S, Chang L, Liu H and
Jiang L (2022), Superwetting
membrane-based strategy for high-flux
enrichment of ethanol from ethanol/
water mixture.
Front. Chem. 10:1037828.
doi: 10.3389/fchem.2022.1037828

COPYRIGHT

© 2022 Wei, Zhang, Chang, Liu and
Jiang. This is an open-access article
distributed under the terms of the
[Creative Commons Attribution License](#)
(CC BY). The use, distribution or
reproduction in other forums is
permitted, provided the original
author(s) and the copyright owner(s) are
credited and that the original
publication in this journal is cited, in
accordance with accepted academic
practice. No use, distribution or
reproduction is permitted which does
not comply with these terms.

Superwetting membrane-based strategy for high-flux enrichment of ethanol from ethanol/water mixture

Zhongwei Wei^{1,2}, Shaoqing Zhang³, Li Chang⁴, Hongliang Liu^{3*}
and Lei Jiang^{1,2,3,4}

¹Key Laboratory of Bio-inspired Materials and Interfacial Science, Technical Institute of Physics and Chemistry, Chinese Academy of Sciences, Beijing, China, ²School of Future Technology, University of Chinese Academy of Sciences, Beijing, China, ³School of Chemistry and Chemical Engineering, Yantai University, Yantai, China, ⁴Key Laboratory of Bio-inspired Smart Interfacial Science and Technology of Ministry of Education, School of Chemistry, Beihang University, Beijing, China

Ethanol, which can be scalable produced from fermented plant materials, is a promising candidate to gasoline as the next-generation liquid fuel. As an energy-efficient alternative to distillation, membrane-based strategies including pervaporation and reverse osmosis have been developed to recover ethanol from fermentation broths. However, these approaches suffer the drawback of low separation flux. Herein, we report a superwetting membrane system to enrich ethanol from water in a high-flux manner. By synergistically regulating surface energy of the solid porous membrane and hydration between an additive inorganic potassium salt and water, concentrated ethanol can rapidly wetting and permeate the porous membrane, with the salt solution being blocked. Using this newly developed superwetting membrane system, we can achieve fast enrichment of ethanol from water, with flux of two orders magnitude higher than that of pervaporation and reverse osmosis membranes.

KEYWORDS

superwetting, membrane separation, high flux, ethanol/water separation, bioethanol

1 Introduction

More-sustainable fuels are being intensively searched for to replace non-renewable fossil fuels. In this context, biofuels, such as bioethanol, produced by fermenting plant materials could provide alternative fuels (Frolkova and Raeva, 2010; Baeyens et al., 2015; Singh and Rangaiah, 2017; Khalid et al., 2019). In US and Brazil, it is quite common that ethanol is used in gasohol with 90% gasoline, 10% ethanol (Hartline, 1979). It is estimated that demand for ethanol will grow by 5.2% annually, reaching 14.6 billion gallons by 2030 (Carolan, 2009). Generally, ethanol in the fermentation broth is in the range of 4 wt% to 12 wt% (Singh and Rangaiah, 2017). Therefore, it is necessary to gain ethanol with high purity before it can be used as liquid fuel. Distillation is the most used separation technique, but is energy-consuming (Frolkova and Raeva, 2010; Chávez-Islas et al., 2011;

García-Herreros et al., 2011; Singh and Rangaiah, 2017; Khalid et al., 2019). With the rapid development of membrane separation technology, pervaporation and reverse osmosis membranes are considered to be more cost saving for ethanol purification (Mulder et al., 1983; Choudhury et al., 1985; Lee et al., 1985; Frolkova and Raeva, 2010; Peng et al., 2010; Khalid et al., 2019). For example, polystyrene-grafted cellulose acetate membranes have been used for successful separation of ethanol/water mixture by reverse osmosis (Choudhury et al., 1985). However, pervaporation and reverse osmosis membranes that relying on the solution-diffusion model are inherently limited by their low separation flux. In contrast, superwetting membranes that depending on the capillary force of micrometer pores can efficiently separate immiscible liquids mixture with far higher flux than other membrane-based separations (Feng et al., 2004; Wen et al., 2013; Zhang et al., 2013; Wang et al., 2015; Wang et al., 2017; Tang et al., 2020; Cai et al., 2021; Zhang et al., 2022). However, it has long been a challenging task to separate miscible liquids mixture by using high-flux superwetting membranes, until we recently made a breakthrough by combinational introduction of an extra inductive agent and surface energy regulation of the solid membrane (Chang et al., 2022). Inspired by this idea, could we apply this design principle for high-flux separation of ethanol and water?

Herein, we report a superwetting membrane system (SMS) with the capability to enrich ethanol from ethanol/water mixture in a high-flux manner. An inorganic potassium salt that can form strong hydration with water molecules was introduced to the system. Together with synergistically tuning the surface energy of the porous membrane, ethanol molecules can preferably permeate the porous membrane, with the remaining salt solution being blocked. In this way, diluted ethanol can be efficiently enriched with high flux.

2 Experimental sections

2.1 Materials

Ethanol (Sinopharm Chemical Reagent, 99.5%), acetic acid (Sinopharm Chemical Reagent, 99.5%), tetraethyl orthosilicate (TEOS, TCI (Shanghai) Chemical Trading, 97%), titanium (IV) butoxide (TNTB, J&K Scientific, 99%), polyvinylpyrrolidone (PVP, MW $\sim 1.3 \times 10^6$, J&K Scientific), n-hexyltrimethoxysilane (J&K Scientific, 97%), 1H,1H,2H,2H-perfluorooctyltrimethoxysilane (J&K Scientific, 96%), 3-aminopropyltriethoxysilane (J&K Scientific, 98%), potassium phosphate trihydrate ($K_3PO_4 \cdot 3H_2O$, Sinopharm Chemical Reagent, 99%), dipotassium hydrogen phosphate trihydrate ($K_2HPO_4 \cdot 3H_2O$, J&K Scientific, 99%), potassium citrate monohydrate ($K_3C_6H_5O_7 \cdot H_2O$, J&K Scientific, 99%), Nile red (Rhawn, 95%) and anhydrous copper (II) sulfate (Shanghai Macklin Biochemical, 99%) were used as received. Potassium

pyrophosphate ($K_4P_2O_7$, Sigma-Aldrich, 97%) was dried at 105 °C under a reduced pressure of about 0.03 atm for 4 h prior to use. Potassium carbonate (K_2CO_3 , Sinopharm Chemical Reagent, 99%) and potassium thiosulfate ($K_2S_2O_3$, Sigma-Aldrich, 95%) were dried at 140 °C under a reduced pressure of about 0.03 atm for 4 h prior to use.

2.2 Fabrication of SiO_2 - TiO_2 composite membranes (denoted as STMs)

2.2.1 Fabrication of bare STMs

The fabrication process of bare STMs includes three steps (Wang et al., 2015; Chang et al., 2022).

- 1) Preparation of electrospinning solutions. First, 1 g of acetic acid, 4.6 ~ 5.2 g of ethanol and 0.8 ~ 1.4 g of PVP were mixed and stirred for 0.5 h. The total mass of ethanol and PVP was 6 g. Next, 2.3 g of TEOS and 0.7 g of TNTB were dripped into the mixture with stirring for 24 h at room temperature to achieve homogenous solutions.
- 2) Process of electrospinning. The precursor solution was loaded into a plastic syringe positioned vertically with 24-Gauge blunt stainless nozzle and injected at a flow rate of 1.3 ml h^{-1} via a digital syringe pump. The static electric field was generated by applying positive electrical potential on the metallic needle and negative electrical potential on an aluminum foil-covered metallic rotating roller, with a minimal distance of 11 cm, and the voltage was set at 17 kV.
- 3) Postprocessing electrospun membranes. The finally flexible fibrous membranes were obtained by drying the electrospun membranes at 80 °C for 15 h and then calcining them at 600 °C for 6 h following a heating of 5°C min^{-1} .

2.2.2 Fabrication of STM- C_6 , STM- C_8F_{13} and STM- NH_2

Bare STMs were treated with plasma for 5 min at high RF level under vacuum (PDC-002, HARRICK) to generate hydroxyl groups before surface chemical modifications. The STM- C_6 , STM- C_8F_{13} and STM- NH_2 were prepared by silanization of bare STM with n-hexyltrimethoxysilane, 1H,1H,2H,2H-perfluorooctyltrimethoxysilane and 3-aminopropyltriethoxysilane, respectively. Specifically, the substrates were performed in a closed chamber with concentration of the gaseous reagents about 0.2 g dm^{-3} at 130 °C under a reduced pressure of about 0.1 atm for 4 h.

2.3 Characterization of STM- C_6 , STM- C_8F_{13} and STM- NH_2

The successful modification of bare STM was confirmed by measuring surface elemental composition of the membranes with

an ESCALAB 250Xi X-ray photoelectron spectroscopy (XPS) from ThermoFisher Scientific.

The microstructures of the STM-C₆, STM-C₈F₁₃ and STM-NH₂ were obtained with an SU8010 scanning electron microscope (SEM).

2.4 Contact angle (CA) measurements

The CAs were measured at room temperature with an OCA20 system from DataPhysics. A 0.2–2 µl droplet of measured liquid was deposited with a 24-Gauge blunt stainless syringe onto a chemically modified STM, which was adhered to the glass substrate and under air or another liquid environment. The average CA value was obtained by measuring the CAs at 3 or more different positions on one sample.

2.5 Determination of ternary phase diagrams

The phase diagram for each ethanol/water/salt system was obtained from the binodal curve and eutectic points. The boundary between biphasic and triphasic zone was a line segment, determined by the two eutectic points.

The binodal curve was obtained by cloud point titration at room temperature (Wang et al., 2010; Lu et al., 2013). The salt was weighed with an analytical balance (LE204E, from METTLER TOLEDO) with an uncertainty of $\pm 1 \times 10^{-7}$ kg. Water was added to form a homogeneous mixture, and ethanol was dropwise added to obtain next cloud point, which was repeated until moderate ethanol content. The masses of both liquids were calculated from their densities and volumes recorded by burettes. At high ethanol content, salt solution and water were added into ethanol. Both ethanol and salt solution were defined by the analytical balance, and water was recorded by a burette. The data was correlated by the following equation to form the binodal curve (Hu et al., 2003; Wang et al., 2010):

$$w_{\text{C}_2\text{H}_5\text{OH}}^{0.4} = a + bw_{\text{salt}}^{0.25} + cw_{\text{salt}}^{0.5} + dw_{\text{salt}} + ew_{\text{salt}}^{1.5}.$$

Ethanol was added to concentrated salt solution, forming a triphasic mixture with two liquid phases in equilibrium with a solid phase. The two eutectic points were obtained by the water content and salt content of the liquid phases. Water content was determined by Karl-Fischer titration with a V20 Volumetric KF titrator from METTLER TOLEDO. Salt content was calculated from the mass fraction of potassium, which was determined with an IRIS Intrepid II XSP inductively coupled plasma atomic emission spectroscopy from ThermoFisher Scientific.

2.6 Separation of ethanol/water mixture

The separation of ethanol/water mixture was done with a self-made separation device. In this device, an STM-M was sandwiched between two Teflon flanges, which were installed between two reservoirs. Ethanol/water mixture and salt were added in the upper reservoir, and separated liquid can be collected in the lower reservoir.

The separation efficiency was evaluated by the purity of ethanol in the permeate, calculated from the mass fractions of water and salt as:

$$w_{\text{C}_2\text{H}_5\text{OH}} = 1 - w_{\text{H}_2\text{O}} - w_{\text{salt}}.$$

The flux was determined by measuring the mass of the permeate within certain time, calculated with the formula:

$$q = \frac{m}{\rho At},$$

where q is the flux, m is the mass of permeate within time t , ρ is the density of permeate, and A is the effective area of the STM-M.

3 Results and discussion

3.1 Design of the SMS for enrichment of ethanol from ethanol/water mixture

Porous membranes with proper surface energies were prepared by chemical modification of inorganic STMs generated by electrospinning a viscous precursor solution and subsequent high-temperature calcination. The STMs are composed of entangled nanofibers forming multilayer networks with random pores (left in Figure 1A). Then -CF₃ terminated silane coupling agent 1H,1H,2H,2H-perfluorooctyltrimethoxysilane was introduced onto the STM surface (denoted as STM-C₈F₁₃) (middle in Figure 1A). X-ray photoelectron spectroscopy (XPS) data clearly show the characteristic peak of fluorine (right in Figure 1A), indicating successful modification of the STM.

In initial wetting test, static contact angles (CAs) of the ethanol/water droplets on the STM-C₈F₁₃ are concentration-dependent. For mixed droplets with ethanol concentrations of 10 wt% and 30 wt%, the STM-C₈F₁₃ is lyophobic with CAs of about 120°. For mixed droplets with ethanol percentage of 50 wt% and 70 wt%, the STM-C₈F₁₃ changes to superlyophilic with CAs close to zero (Supplementary Figure S1). Nevertheless, when an inductive agent, concentrated potassium pyrophosphate (K₄P₂O₇) solution was introduced to the system, strong hydration between K₄P₂O₇ and water molecules, together with the high affinity between C₈F₁₃ and ethanol, led to selective

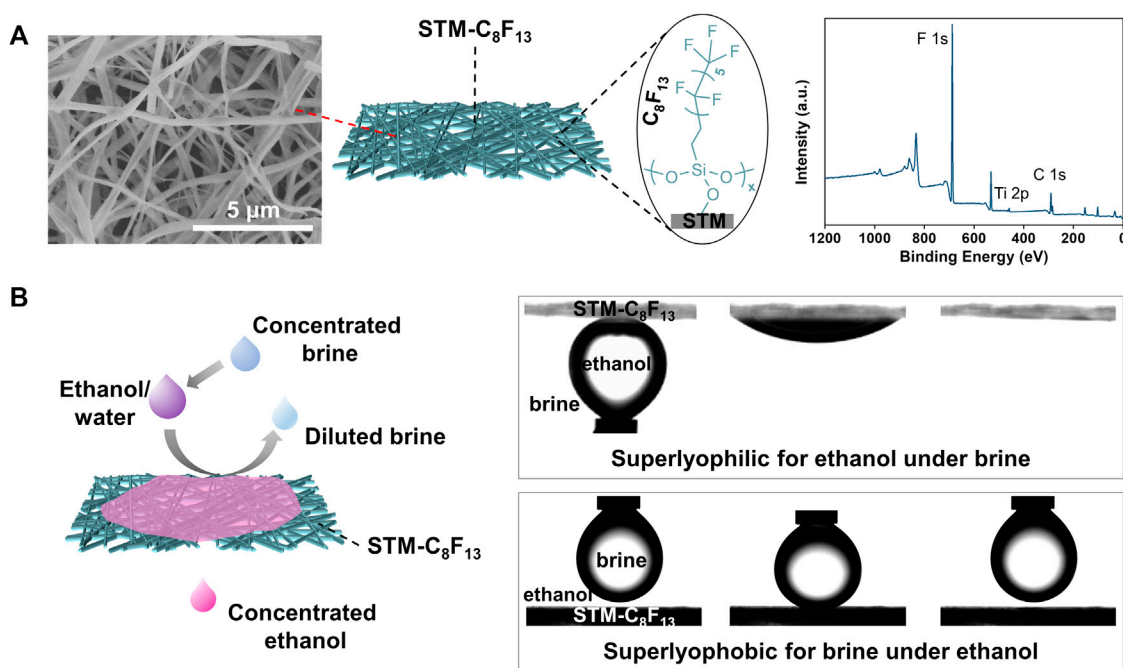


FIGURE 1

Design of SMSs for ethanol/water separation. (A) SEM image, chemical structure and XPS spectrum of the STM-C₈F₁₃. (B) Scheme and dynamic wetting behaviors of superwetting membrane-based separation in the presence of saturated K₄P₂O₇ as an inductive agent.

permeation of ethanol to obtain concentrated ethanol (left in Figure 1B). In this case, the STM-C₈F₁₃ shows superlyophilic for ethanol under K₄P₂O₇ solution and superlyophobic for K₄P₂O₇ solution under ethanol (right in Figure 1B). Thus, STM-C₈F₁₃ can be selectively wetted by concentrated ethanol while concurrently blocking K₄P₂O₇ solution. Specifically, when a feed ethanol/water mixture with 10 wt% of ethanol passes through the STM-C₈F₁₃ membrane in the presence of saturated K₄P₂O₇ solution, the ethanol concentration in the permeate is as high as 90.1 wt%.

3.2 Determination of ternary phase diagram of ethanol/water/salts

In our designed SMSs, the introduction of inorganic salts as inductive agents is significantly important to generate effective phase separation. 18 inorganic salts were used to determine the ternary phase diagram of ethanol/water/salts. The binodal curve was obtained by cloud point titration. The boundary between biphasic and triphasic zone was a line segment, determined by its eutectic points, which were compositions of two liquid phases in equilibrium with a solid phase. With high water content, ethanol and salt both dissolved, forming a homogeneous mixture. With moderate water content, phase separation happened, forming one liquid phase with high ethanol content and the other liquid phase

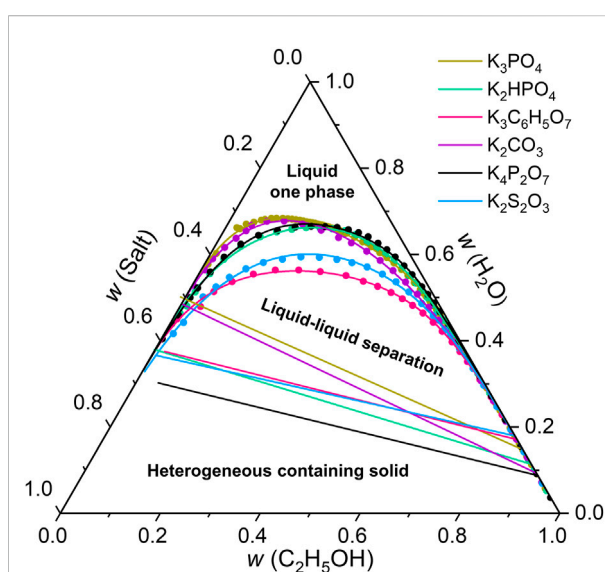
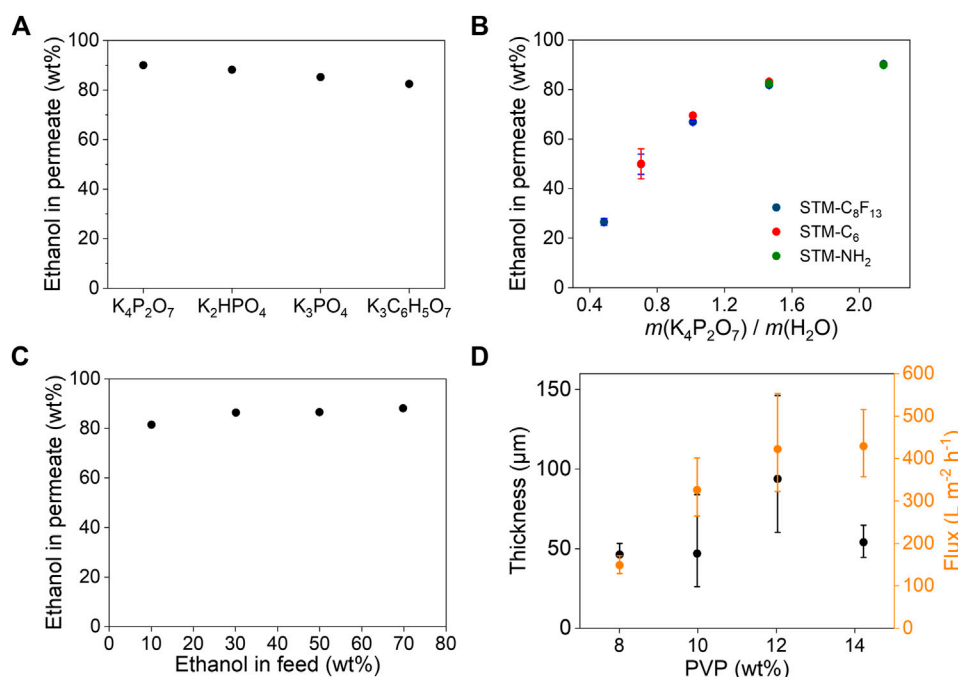


FIGURE 2

Ternary phase diagram of ethanol/water/salts. The binodal curve was obtained by cloud point titration. The boundary between biphasic and triphasic zone was a line segment, determined by its eutectic points, which were compositions of two liquid phases in equilibrium with a solid phase.

with almost no ethanol. The composition of each phase was on the binodal curve. With low water content, solid salt crystallized from the mixture, forming three phases. The

**FIGURE 3**

Separation performance for ethanol/water. (A) Separation efficiencies of SMS-C₈F₁₃ with different saturated potassium salts solutions as the inductive agents. Ethanol in feed is 10 wt%. (B) Separation efficiencies of three different SMSs with different amount of K₄P₂O₇. (C) Separation efficiencies of SMS-C₈F₁₃ for ethanol/water with different compositions in the presence of saturated K₄P₂O₇ solution. (D) Separation fluxes and thicknesses of STM-C₈F₁₃ prepared using different PVP concentrations. Ethanol in feed is 50 wt%. Inductive agent is saturated K₄P₂O₇ solution. The flow was driven by the gravity of 1 cm high liquid. Error bars represent the standard deviation from at least three independent experiments.

composition of each phase was fixed, independent of overall composition.

As shown in Figure 2, the binodal curves and the line segments between biphasic and triphasic zones of 6 potassium salts were obtained by using this method. However, the other 12 salts with weaker salting-out effect, including K₂SO₄, KHSO₄, MgSO₄, (NH₄)₂SO₄, Na₂SO₄, KH₂PO₄, KH₂C₆H₅O₇, KHCO₃, KCl, KBr, KI, KSCN, do not have liquid-liquid equilibrium zone, and thus not suitable for ethanol/water separation.

3.3 Separation performance for ethanol/water

The separation performance of SMSs for ethanol/water was studied by tuning the types of the inductive agents, chemical compositions and pore sizes of the porous membranes. The separation efficiencies depend strongly on the types of inductive agents (Figure 3A). With addition of saturated salt solutions, K₄P₂O₇, K₂HPO₄, K₃C₆H₅O₇ and K₃PO₄ all resulted higher than 80 wt% concentration of ethanol in permeate. K₄P₂O₇ resulted the highest concentration of 90.1% due to the highest thermodynamic limit, consistent with the results showed in phase diagrams

(Figure 2). Therefore, we chose K₄P₂O₇ as the optimal inductive agent for further study.

The amount of K₄P₂O₇ also plays an important role in separation efficiency. As shown in Figure 3B, ethanol in permeate increases obviously with increasing concentration of K₄P₂O₇, independent on the surface chemistry of the porous membranes (Supplementary Figure S2). However, porous membranes with different surface chemistry differ in thresholds of K₄P₂O₇ addition (Supplementary Figure S3). The ethanol/water mixture can be separated by the membrane if more K₄P₂O₇ was added than the threshold, otherwise it cannot. For example, there was a threshold point on ethanol/water/K₄P₂O₇ binodal curve for the STM-C₆. To left of the point, the liquid was blocked by STM-C₆; to right of the point, the liquid would permeate STM-C₆. So, if the composition of biphasic mixture was above the red line, both phases were blocked by STM-C₆, not separated. Only if the composition of biphasic mixture was below the red line, STM-C₆ can separate it. Similarly, for the STM-NH₂, if the composition of biphasic mixture was above the green line, both phases would permeate STM-NH₂, not separated. In contrast, for STM-C₈F₁₃, there is no such threshold and ethanol can be separated from the mixture as long as phase separation occurs. So, STM-C₈F₁₃ was selected for enrichment of ethanol from a wide range of ethanol/water feed compositions. Ethanol concentration in feed slightly affected ethanol concentration

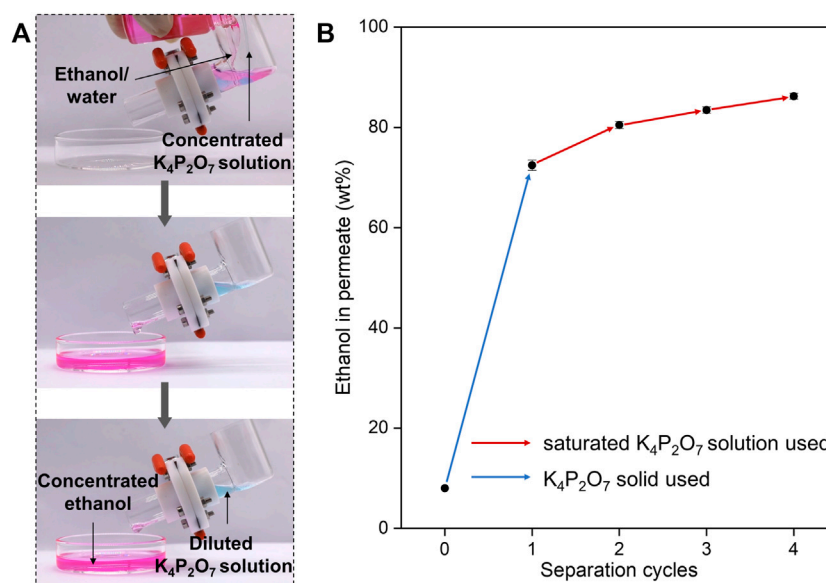


FIGURE 4

Demonstration of the ethanol/water separation. (A) Video captures of separation process using concentrated $K_4P_2O_7$ solution as the inductive agent. Introducing concentrated $K_4P_2O_7$ solution to the ethanol/water results in selective permeation and collection of ethanol with $K_4P_2O_7$ solution being blocked. (B) Cycled separation for ethanol/water. Started ethanol in feed is 8 wt% and equal mass of solid $K_4P_2O_7$ was added for separation. Each cycle takes the permeate of previous cycle as the new feed, and equal mass of saturated $K_4P_2O_7$ solution was added.

in permeate, but all achieved a higher concentration than 80 wt% (Figure 3C).

The separation flux of SMSs was further investigated by regulating the microstructures of the porous membranes (Supplementary Figure S4). By controlling the PVP concentrations during preparation of the porous membranes by electrospinning. As shown in Supplementary Figure S4, with increasing concentration of PVP, diameters of the nanofibers become larger and networks of the porous membranes get looser, which would facilitate permeation of concentrated ethanol and thus lead to higher flux. When PVP concentration is 12 wt%, separation flux for concentrated ethanol is up to $400 \text{ L m}^{-2} \text{ h}^{-1}$ (Figure 3D), nearly 2-3 orders of magnitude higher than that of reverse osmosis and pervaporation.

3.4 Demonstration of the ethanol/water separation process

We demonstrate the enrichment of ethanol from ethanol/water mixtures by a self-made device (Figure 4A). In this device, the STM- C_8F_{13} was sandwiched between two Teflon flanges, which were fixed between two reservoirs. Inductive agent (saturated $K_4P_2O_7$ solution) and ethanol/water mixture (with 10 wt% of ethanol) were added in one reservoir, and concentrated ethanol can be collected in another reservoir. To better monitor the separation process, the ethanol/water mixture and inductive agent were dyed with Nile red and

anhydrous copper (II) sulfate. Pink concentrated ethanol accumulated from the mixture and permeate the STM- C_8F_{13} in time and be collected with blue diluted $K_4P_2O_7$ solution being blocked.

As mentioned above, ethanol concentration in permeate becomes lower with decreasing ethanol concentration in feed. This tendency becomes obvious especially when ethanol concentration in feed is lower than 10 wt%. For example, for ethanol/water mixture with 8 wt% ethanol, under optimal conditions, ethanol concentration in permeate is only 72.4 wt%. Fortunately, we can solve this problem by conducting multiple SMS-based separation processes in series. After 4 separation cycles, 86.2 wt% of ethanol in permeate was obtained (Figure 4B). Moreover, our designed SMS is compatible with traditional reverse osmosis and pervaporation membranes. Composite membrane modules composed of SMS and pervaporation are ongoing in our lab, and ethanol with higher purity could be obtained.

4 Conclusion

In summary, we have designed a superwetting membrane-based strategy for high-flux enrichment of ethanol from ethanol/water mixtures by synergistically tuning the inductive agents and surface energy of the porous membranes. Using this strategy, concentrated ethanol higher than 80 wt%, and separation flux as high as $400 \text{ L m}^{-2} \text{ h}^{-1}$ have been achieved. Moreover, our

designed SMS can be easily assembled with conventional membranes, such as pervaporation membranes, hold the promise for the application of ethanol separation with high purification. It is believed that our work will provide an opportunity for highly efficient separation of ethanol, and would make a step forward for extended application of liquid biofuels.

Data availability statement

The raw data supporting the conclusions of this article will be made available by the authors, without undue reservation.

Author contributions

HL and LJ conceived the original idea; ZW performed experiments and data analysis; ZW and HL wrote the manuscript. All authors discussed and revised the manuscript.

Funding

This work was supported by the National Natural Science Foundation of China (21875268), Taishan Young Scholar Program (tsqn202103053), and Fundamental Research

Projects of Science and Technology Innovation and Development Plan in Yantai City (2022YTJC06002541).

Conflict of interest

The authors declare that the research was conducted in the absence of any commercial or financial relationships that could be construed as a potential conflict of interest.

Publisher's note

All claims expressed in this article are solely those of the authors and do not necessarily represent those of their affiliated organizations, or those of the publisher, the editors and the reviewers. Any product that may be evaluated in this article, or claim that may be made by its manufacturer, is not guaranteed or endorsed by the publisher.

Supplementary material

The Supplementary Material for this article can be found online at: <https://www.frontiersin.org/articles/10.3389/fchem.2022.1037828/full#supplementary-material>

References

- Baeyens, J., Kang, Q., Appels, L., Dewil, R., Lv, Y., and Tan, T. (2015). Challenges and opportunities in improving the production of bio-ethanol. *Prog. Energy Combust. Sci.* 47, 60–88. doi:10.1016/j.pecs.2014.10.003
- Cai, Y., Shi, S. Q., Fang, Z., and Li, J. (2021). Design, development, and outlook of superwettability membranes in oil/water emulsions separation. *Adv. Mat. Interfaces* 8, 2100799. doi:10.1002/admi.202100799
- Carolan, M. S. (2009). Ethanol versus gasoline: the contestation and closure of a socio-technical system in the USA. *Soc. Stud. Sci.* 39 (3), 421–448. doi:10.1177/0306312708101049
- Chang, L., Wang, D., Cao, Z., Liu, C., Yang, J., Zhang, X., et al. (2022). Miscible organic liquid separation of superwetting membrane driven by synergistic polar/nonpolar interactions. *Matter* 5 (4), 1251–1262. doi:10.1016/j.matt.2022.02.011
- Chávez-Islas, L. M., Vásquez-Medrano, R., and Flores-Tlacuahuac, A. (2011). Optimal synthesis of a high purity bioethanol distillation column using ionic liquids. *Ind. Eng. Chem. Res.* 50 (9), 5175–5190. doi:10.1021/ie101801c
- Choudhury, J. P., Ghosh, P., and Guha, B. K. (1985). Separation of ethanol from ethanol–Water mixture by reverse osmosis. *Biotechnol. Bioeng.* 27 (7), 1081–1084. doi:10.1002/bit.260270725
- Feng, L., Zhang, Z., Mai, Z., Ma, Y., Liu, B., Jiang, L., et al. (2004). A super-hydrophobic and super-oleophilic coating mesh film for the separation of oil and water. *Angew. Chem. Int. Ed.* 43 (15), 2012–2014. doi:10.1002/anie.200353381
- Frolkova, A. K., and Raeva, V. M. (2010). Bioethanol dehydration: State of the art. *Theor. Found. Chem. Eng.* 44 (4), 545–556. doi:10.1134/s0040579510040342
- García-Herreros, P., Gómez, J. M., Gil, I. D., and Rodríguez, G. (2011). Optimization of the design and operation of an extractive distillation system for the production of fuel grade ethanol using glycerol as entrainer. *Ind. Eng. Chem. Res.* 50 (7), 3977–3985. doi:10.1021/ie101845j
- Hartline, F. F. (1979). Lowering the cost of alcohol. *Science* 206 (4414), 41–42. doi:10.1126/science.206.4414.41
- Hu, M., Zhai, Q., Liu, Z., and Xia, S. (2003). Liquid–Liquid and Solid–Liquid equilibrium of the ternary system ethanol + cesium sulfate + water at (10, 30, and 50) °C. *J. Chem. Eng. Data* 48 (6), 1561–1564. doi:10.1021/je0301803
- Khalid, A., Aslam, M., Qyyum, M. A., Faisal, A., Khan, A. L., Ahmed, F., et al. (2019). Membrane separation processes for dehydration of bioethanol from fermentation broths: Recent developments, challenges, and prospects. *Renew. Sustain. Energy Rev.* 105, 427–443. doi:10.1016/j.rser.2019.02.002
- Lee, E. K. L., Babcock, W. C., and Bresnahan, P. A. (1985). “Ethanol–water separation by countercurrent reverse osmosis,” in *Materials science of synthetic membranes* (Bend, Oregon, United States: American Chemical Society), 269, 409–428.
- Lu, Y., Hao, T., Hu, S., Han, J., Tan, Z., and Yan, Y. (2013). Measurement and correlation of phase diagram data for acetone and sulfate aqueous two-phase systems at different temperatures. *Thermochim. Acta* 568, 209–217. doi:10.1016/j.tca.2013.07.002
- Mulder, M. H. V., Hendrickman, J. O., Hegeman, H., and Smolders, C. A. (1983). Ethanol–Water separation by pervaporation. *J. Membr. Sci.* 16, 269–284. doi:10.1016/S0376-7388(00)81315-0
- Peng, P., Shi, B., and Lan, Y. (2010). A review of membrane materials for ethanol recovery by pervaporation. *Sep. Sci. Technol.* 46 (2), 234–246. doi:10.1080/01496395.2010.504681
- Singh, A., and Rangaiah, G. P. (2017). Review of technological advances in bioethanol recovery and dehydration. *Ind. Eng. Chem. Res.* 56 (18), 5147–5163. doi:10.1021/acs.iecr.7b00273
- Tang, B., Meng, C., Zhuang, L., Groenewold, J., Qian, Y., Sun, Z., et al. (2020). Field-induced wettability gradients for no-loss transport of oil droplets on slippery surfaces. *ACS Appl. Mat. Interfaces* 12, 38723–38729. doi:10.1021/acsami.0c06389

Wang, L., Zhao, Y., Tian, Y., and Jiang, L. (2015). A general strategy for the separation of immiscible organic liquids by manipulating the surface tensions of nanofibrous membranes. *Angew. Chem. Int. Ed.* 54 (49), 14732–14737. doi:10.1002/anie.201506866

Wang, Y., Di, J., Wang, L., Li, X., Wang, N., Wang, B., et al. (2017). Infused-liquid-switchable porous nanofibrous membranes for multiphase liquid separation. *Nat. Commun.* 8 (1), 575. doi:10.1038/s41467-017-00474-y

Wang, Y., Mao, Y., Han, J., Liu, Y., and Yan, Y. (2010). Liquid–Liquid equilibrium of potassium phosphate/potassium citrate/sodium citrate + ethanol aqueous two-phase systems at (298.15 and 313.15) K and correlation. *J. Chem. Eng. Data* 55 (12), 5621–5626. doi:10.1021/je100501f

Wen, Q., Di, J., Jiang, L., Yu, J., and Xu, R. (2013). Zeolite-coated mesh film for efficient oil–water separation. *Chem. Sci.* 4 (2), 591–595. doi:10.1039/C2SC21772D

Zhang, F., Zhang, W. B., Shi, Z., Wang, D., Jin, J., and Jiang, L. (2013). Nanowire-haired inorganic membranes with superhydrophilicity and underwater ultralow adhesive superoleophobicity for high-efficiency oil/water separation. *Adv. Mat.* 25 (30), 4192–4198. doi:10.1002/adma.201301480

Zhang, L., Kan, X., Huang, T., Lao, J., Luo, K., Gao, J., et al. (2022). Electric field modulated water permeation through laminar Ti3C2Tx MXene membrane. *Water Res.* 219, 118598. doi:10.1016/j.watres.2022.118598



OPEN ACCESS

EDITED BY
Zhenyu Sun,
Beijing University of Chemical
Technology, China

REVIEWED BY
Jiehua Liu,
Hefei University of Technology, China
Feng Han,
Shandong Agricultural University, China

*CORRESPONDENCE
Siqing Cheng,
icnee@whpu.edu.cn

SPECIALTY SECTION
This article was submitted to Green and
Sustainable Chemistry,
a section of the journal
Frontiers in Chemistry

RECEIVED 06 September 2022
ACCEPTED 16 September 2022
PUBLISHED 04 October 2022

CITATION
You J, Qin J, Du C, Fu J and Cheng S
(2022), CO₂-assisted fabrication of silica
gel adsorbent in honeycomb rotary
wheels for air dehumidification.
Front. Chem. 10:1038095.
doi: 10.3389/fchem.2022.1038095

COPYRIGHT
© 2022 You, Qin, Du, Fu and Cheng.
This is an open-access article
distributed under the terms of the
Creative Commons Attribution License
(CC BY). The use, distribution or
reproduction in other forums is
permitted, provided the original
author(s) and the copyright owner(s) are
credited and that the original
publication in this journal is cited, in
accordance with accepted academic
practice. No use, distribution or
reproduction is permitted which does
not comply with these terms.

CO₂-assisted fabrication of silica gel adsorbent in honeycomb rotary wheels for air dehumidification

Junjie You^{1,2}, Junbo Qin¹, Chuanqing Du¹, Jianhua Fu² and
Siqing Cheng^{1,2*}

¹Innovation Centre for Nanomaterials in Energy and Environment (ICNEE), School of Chemical and Environmental Engineering, Wuhan Polytechnic University, Wuhan, Hubei, China, ²Wuhan Coobase Facilities Company Limited, Wuhan, Hubei, China

A honeycomb rotary wheel fabricated from sheet adsorbent of silica gel is a competitive drying facility for air dehumidification in modern drying and air conditioning industries due to its large contacting area (3,000 m²/m³) and the rapid diffusion of the adsorbate compared to silica gel pellets. The delicate preparation procedure of hygroscopic silica gel is paramount for improved adsorption capacity by optimizing the surface area, pore size, and pore volume of silica gel. In this article, silica gel adsorbent in a honeycomb rotary wheel was fabricated by neutralizing the impregnated water glass solution with a modulus of 3.3 on the glass fiber sheet of the honeycomb matrix using CO₂ at different pressure at room temperature instead of corrosive acids. The as-obtained silica gel adsorbent was characterized by XRD, scanning electron microscopy (SEM), specific surface area and pore size analysis, and dynamic vapor/gas sorption analysis. The results showed that the as-obtained silica gel adsorbent is uniform in size and tunable in terms of specific surface area, pore size, pore volume, and adsorption capacity by CO₂ pressure. The typical silica gel fabricated by CO₂ of 0.25 MPa with a specific surface area of 764.86 m²/g, an average micropore size with a diameter of 2.94 nm, and a pore volume of 0.45 ml/g delivers a saturated adsorption capacity of as high as 287.24 mg/g at RH 50%, which is the best in adsorption performance compared to the previously reported results. This provides a new strategy for environment-friendly manufacturing of silica gel adsorbent in honeycomb rotary wheels for air dehumidification.

KEYWORDS

honeycomb rotary wheel, dehumidification, CO₂, silica gel, adsorbent

Introduction

Air humidity has always been drawing a worldwide concern both in our daily life and in various conventional (food, cosmetics, papermaking, pharmaceuticals, etc.) and emerging industries (microelectronics, lithium-related batteries, etc.) due to its role with respect to air quality and its requirement for the manufacture, preservation,

transportation, and further processing of products (Aristov et al., 2002; Wu et al., 2018). Thus, air dehumidification technology has been attracting extensive interest academically and industrially. The traditional direct dehumidification technologies mainly consist of condensing dehumidification, heating dehumidification, membrane dehumidification, and liquid desiccant dehumidification, in which the relevant environmental issues owing to the utilization of a non-environment-friendly refrigerant, the energy-intensive requirement, high-cost membrane fabrication, etc. impede their further development, especially in today's ever-increasing climate deterioration (Cha et al., 2007; Hwang et al., 2007; Bhagat et al., 2008; Iswar et al., 2017). In recent years, an adsorptive dehumidification technology by solid regenerable desiccant to selectively remove and separate the moisture from moist air under ambient conditions shows great promise for future air dehumidification (Kabeel, 2007; Bareschino et al., 2015).

Thus far, four types of solid desiccant dehumidifiers as adsorptive dehumidification technology have been proposed, namely, solid packed beds, rotating horizontal beds, multiple vertical beds, and honeycomb rotary wheels, among which only the honeycomb rotary wheels integrate the dehumidifier and desorption processes into one, demonstrating the lower pressure drop and large surface area for heat and mass transfer with respect to the desirable characteristics, such as high space efficiency, continuous adsorption-desorption cycles, high dehumidification, and utilization of low-grade heat sources, such as solar energy and waste heat, for adsorbent regeneration (Chung et al., 2001; Bhagat et al., 2008; Hindersmann, 2019). As a state-of-the-art solid desiccant dehumidification technology, the honeycomb rotary wheel consists of numerous parallel airflow passageway constructed typically with alternating sinusoidal corrugated fibrous substrate sheets and flat fibrous substrate sheets on whose surface a solid desiccant material is impregnated. As such, the widely dispersed desiccants work based on the famous Kelvin formula which shows the vapor pressure difference between the air and the desiccant to attract the moisture from the air until its vapor pressure is in equilibrium with the air. (Kodama et al., 1993; Jia et al., 2006).

The performance of the solid desiccant honeycomb rotary wheel depends, to a large extent, upon the characteristics of the desiccant materials such as high dehumidification capacity, fast kinetics, high stability, and the ability to regenerate at a low temperature. Silica gel is the most popular solid desiccant usually used in the honeycomb rotary wheel due to its low cost, high porosity, and excellent stability although it has a limited dehumidification capacity of 20%–30% of its initial weight and higher regeneration temperature of 60–100°C (Kuma and Hirose, 1996; La et al., 2010; Lee and Lee, 2012; Li et al., 2016). As we know, desiccant dehumidifies in that desiccants have open empty spaces between the molecules called capillaries. As such, the hygroscopic performance of the silica gel is determined by its

intrinsic physical/chemical properties and the surface porous (capillary) structure including surface area, pore volume, average pore size, and pore size distribution, which are affected by the preparation procedures/variables of silica gel (Kodama et al., 1993; Neti and Wolfe, 2000; Liu, 2003; Manjunatha et al., 2013).

The general manufacturing variables of silica gel are quite complex including the type of starting materials, catalyst, solvent, reaction temperature, gelation schemes, drying temperature, etc. Many research works have investigated in detail the effects of the preparation procedure on the surface characteristics of silica gel. Especially for the silica gel used in the honeycomb rotary wheel with glass fibers as substrate, water glass is generally employed to act as the type of starting material due to its availability, low cost, and environment friendliness (Sarawade et al., 2010; O'Connor et al., 2016; Prasad et al., 2019). The different preparation procedures of silica gel by neutralization using different acids such as HCl, H₃PO₄, H₂SO₄, HNO₃, and HCOOH were investigated to obtain the different surface characteristics of silica gel and thus the different dehumidification properties, which are also adopted to manufacture industrially silica gel desiccant in the honeycomb rotary wheel (Zhang et al., 2003; White et al., 2011; Wu et al., 2018; Yang et al., 2020). However, the usages of strong acids are unfavorable to operation and the environment due to their corrosion or volatility (Wang et al., 2013; Wei et al., 2013; Su et al., 2021). Herein, to our knowledge, it is the first time in this work to report that CO₂ as nontoxic greenhouse gas was employed to neutralize the starting material water glass to prepare silica gel desiccant in the honeycomb rotary wheel and the preparation variables including CO₂ pressure and the reaction time were optimized, the resulting silica gel desiccant in the honeycomb rotary wheel exhibits excellent surface characteristics and thus good dehumidification characteristics.

Experimental

Preparation of honeycomb silica gel

The flat glass fiber paper (Ahlstrom-Munksjo glassfibre Oy, Kotka, Finland) was cut to be 10 × 10 cm square and was rolled down to be corrugated glass fiber paper with colloidal silica (10 wt%, Chemical Engineering Sci. and Tech. Ltd. Company, Henan, China). Then, the flat and the prepared corrugated glass fiber paper were stacked alternately with a thickness of 10 cm to form a honeycomb monolith. The as-obtained honeycomb monolith was impregnated with water glass (ca. 3.3 modulus, 40 wt%, Haobo Chemical Engineering Ltd. Company, Shandong, China) for 2 hours and taken out to dry incompletely. The water glass-impregnated honeycomb monolith was placed in a high-pressure reactor and subjected to CO₂ at different pressure for 3–5 h. After the reaction was complete, the honeycomb monolith was washed to remove the carbonate until the solution is close to

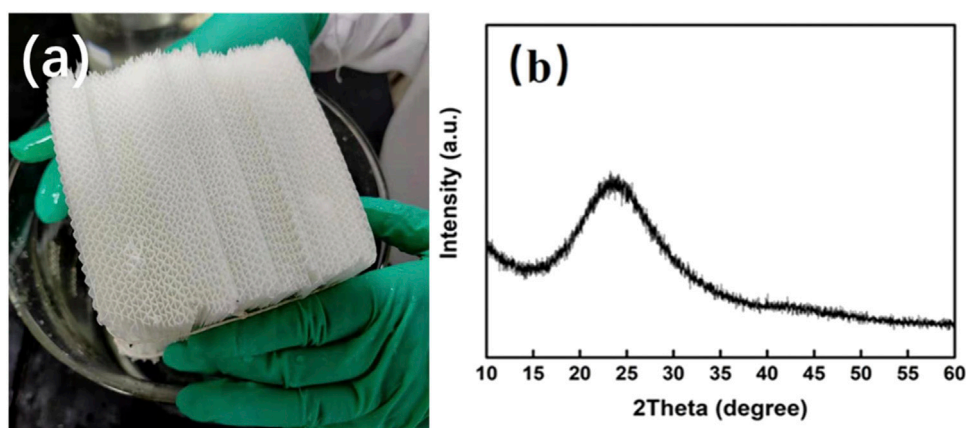


FIGURE 1

(A) Typical photograph of the as-obtained honeycomb silica gel with CO_2 as the neutralized agent; (B) typical XRD pattern of silica gel powder detached from the honeycomb monolith.

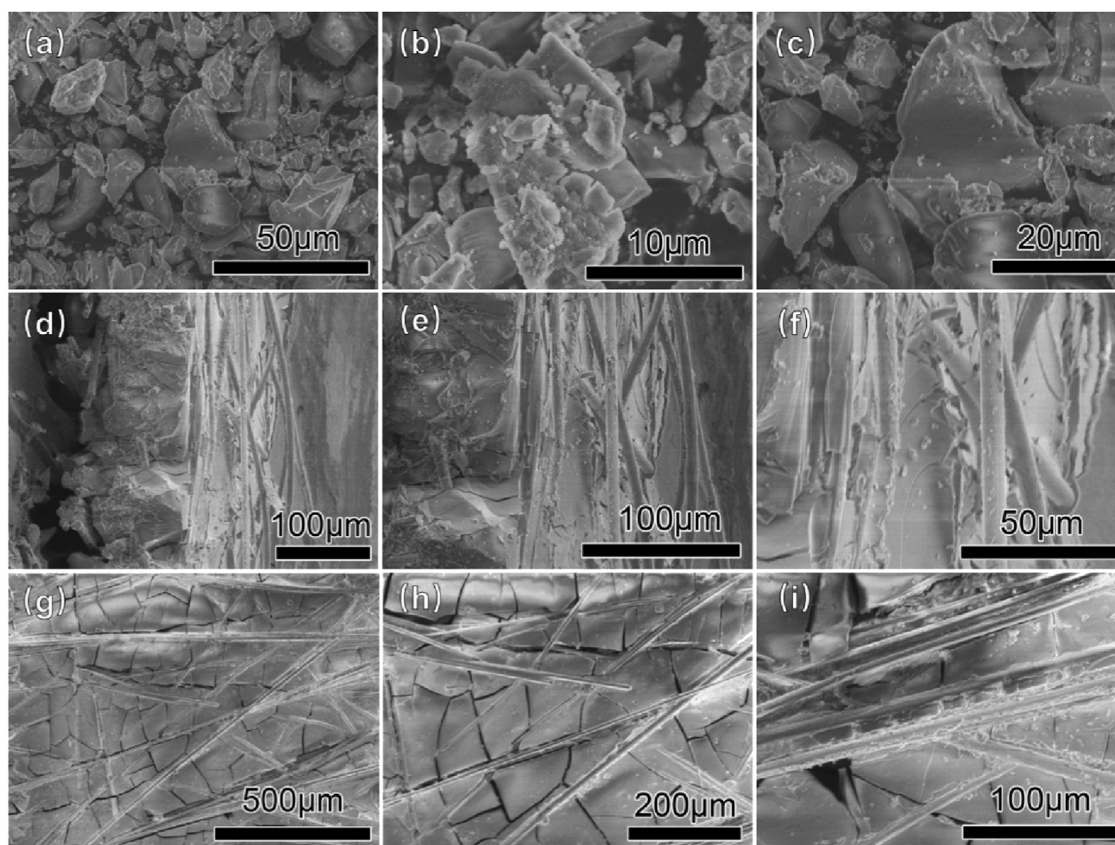


FIGURE 2

Typical SEM images of the as-obtained honeycomb silica gel with CO_2 as the neutralized agent. (A–C) Silica gel powder detached from the honeycomb matrix; (D–F) cross section of honeycomb matrix; and (G–I) surface of the honeycomb matrix.

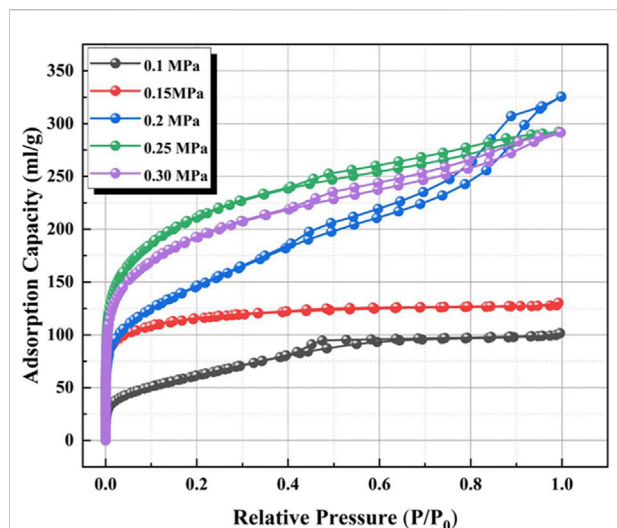


FIGURE 3

Nitrogen adsorption and desorption isotherms of the as-obtained honeycomb silica gel using water glass as the starting material at different CO_2 pressures.

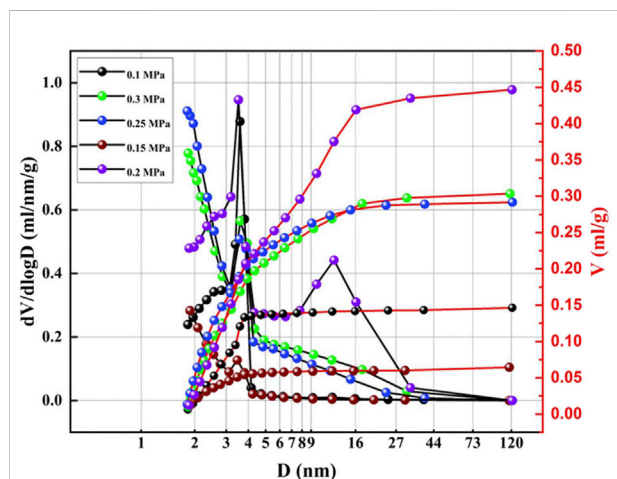


FIGURE 4

BJH (desorption) pore volume and pore size logarithm curves of the as-obtained honeycomb silica gel using water glass as the starting material at different CO_2 pressures.

being neutral followed by the aging in the deionized water for 2 h at 40°C . Finally, the honeycomb monolith with silica gel was completed by drying and calcination.

Characterization of honeycomb silica gel

The powder X-ray diffraction (XRD) patterns were collected on a Japan Shimadzu DX-7000 advanced X-ray diffractometer

using the Cu K α radiation with $\lambda = 0.15418$ nm over 2θ degree from 10° to 70° at a scan rate of 4° min^{-1} . Scanning electron microscopy (SEM) images were performed on a JEOL JSM-6700M scanning electron microscopy. Nitrogen physisorption was carried out at -196°C on a Micromeritics BeishiDe PS2-1529-B specific surface area and pore size analyzer. The Brunauer-Emmett-Teller (BET) surface area, pore volume, and pore size distribution were obtained. The samples were pretreated at 150°C under a high vacuum for 12 h prior to the nitrogen adsorption-desorption test. The pore volume was calculated from the adsorbed nitrogen after complete pore condensation at the relative pressure of $P/P_0 = 0.995$. The pore size was estimated from the desorption branch *via* the Barrett-Joyner-Halenda (BJH) method.

Adsorption/desorption kinetics and isotherms of water vapor

The adsorption/desorption kinetics and isotherms of the water vapor on the silica gel were measured on a gravity dynamic vapor system (BSD-VVS, BeiShiDe Instrument). Before the measurement of vapor adsorption, the samples were dried at 200°C for 2 h. Nitrogen was used as the dry carrier gas and the concentration of vapor was precisely controlled with a mass flow controller and real-time vapor concentration monitor. The sample weight change during water vapor sorption/desorption can be measured by an ultra-microbalance module. With the mass change to < 0.002 mass %/min, the samples were considered to reach the kinetic equilibrium. Based on the equilibrium moisture content at different relative humidity, water vapor isotherms can be plotted. The adsorption kinetics was obtained by measuring the weight change of the samples with time at 25°C at different relative humidity (RH). The adsorption isotherms were plotted based on the equilibrium adsorption capacity at various RHs. The desorption kinetics was obtained by measuring the weight change of the samples with time at 87°C . Regeneration of silica gel in multiple adsorption-desorption cycles was also obtained in the system.

Results and discussion

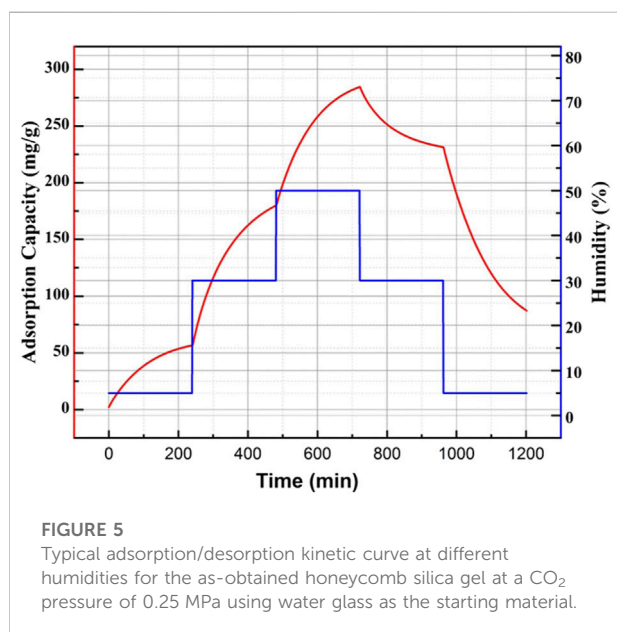
Silica gel as a solid desiccant in a honeycomb rotary wheel is thought to be environmentally friendly and its desiccant capacity is dependent on its surface structure including specific surface area, pore volume, pore size, etc. As such, it is vital to choose a suitable and clean fabrication procedure to tune the surface structure of the silica gel solid desiccant in a honeycomb rotary wheel. Indeed, the surface structure of silica gel is affected by many preparation variables consisting of starting materials, catalyst, reaction temperature and time, aging

TABLE 1 Surface parameters of the prepared silica gel at different CO₂ pressures.

CO ₂ pressure (MPa)	Specific area (m ² /g)	Pore volume (ml/g)	Average pore diameter (nm)
0.10	224.260	0.147	2.817
0.15	431.483	0.0644	2.563
0.20	523.207	0.292	4.088
0.25	764.862	0.447	2.938
0.30	695.765	0.303	3.316

TABLE 2 Adsorption capacity and time for saturated adsorption of silica gel prepared at different CO₂ pressures at a relative humidity of 50%

CO ₂ pressure (MPa)	Adsorption capacity (mg/g)	Time for saturated adsorption (min)
0.10	127.801	517.20
0.15	194.121	712.67
0.20	238.286	722.03
0.25	287.244	721.6
0.30	264.386	721.25



temperature and time, etc. So, it is difficult to control elaborately the preparation procedure to obtain the desirable silica gel with excellent desiccant capacity (Zhang et al., 2006; Zheng et al., 2014). In this work, water glass was used as a green and low-cost raw material for the preparation of silica gel desiccant in a honeycomb rotary by the neutralization of acids. Although it is more difficult to result in the good surface structure of silica gel than organic silicon as a starting material because inorganic salt

yielded during the neutralization in the solution impacts greatly the gelatinization of the silica sol, water glass could be used as an adhesive agent for the formation of honeycomb monolith without any other organic adhesive introduction. More importantly, CO₂ gas as the neutralized acid should be able to relieve the salt effect in the solution due to the usage of liquid acid on the gelation of silica sol. As demonstrated in Figure 1 for the monolith and the XRD pattern of the as-obtained honeycomb silica gel by the reaction of water glass and CO₂, it can be seen that there is a weak broadening band at about 23° without any diffraction peaks of impurity, revealing the typical amorphous nature of SiO₂ and thus a feasible preparation approach.

Figure 2 shows the SEM images of the obtained honeycomb silica gel at a different state. From Figures 2A–C, it can be seen that the prepared silica gel is gelatinized well with a smooth and uniform surface, which could be further verified by the SEM images of the cross section of honeycomb silica gel monolith in Figures 2D–F, illustrating the complete reaction of water glass with CO₂ to implement the polymerization between SiO₂ molecules during gelatinization. From Figures 2G–I, it is indicated that the prepared silica gel is dispersed evenly between the networks of glass fiber paper, allowing the available maximal exposed surface, which is favorable to promote the adsorption capacity. Although it is not observed obviously the surface microstructure of the prepared silica gel by glass fiber paper as a substrate, the texture of the monolith is indicated to disperse widely the silica gel on fiber gel paper so that the pretty large contact area of the silica gel with vapor for desiccant is obtained, which shall be verified further by the

following characterized surface structure including specific surface area, pore volume, pore diameters.

To optimize the effect of CO₂ pressure on the surface structure, the preparation of the honeycomb silica gel using water glass as starting material was investigated at different CO₂ pressure at ambient temperature. The nitrogen adsorption and desorption isotherms of the as-obtained honeycomb silica gel are shown in Figure 3. As indicated in Figure 3, all isotherms are identified as the typical Type IV, which are the characteristic isotherms of mesoporous materials at any pressure of CO₂, preferably used as a desiccant as well. Nonetheless, the different isotherms at different pressure of CO₂ demonstrate the different surface structures of the prepared honeycomb silica gel, displaying the regularity of CO₂ on the surface structure of silica gel with the exception of the acid effect for the neutralization of water glass. As shown in Figure 4 for the changed surface structure with CO₂ pressure including the pore size distribution, pore size, and pore volume, it could be seen that the most probable pore size between 2 and 10 nm is further evidence of the above typical Type IV BET isotherms of mesoporous materials although the pore size difference with CO₂ pressure is markable, which should be embodied from the accumulative pore volume change with CO₂ pressure. As known generally, the reaction of CO₂ with water glass should be the neutralization of water glass by carbonic acid generated by CO₂ and H₂O, thus, CO₂ pressure affects the reaction rate due to CO₂ pressure dependence of CO₂ concentration so that the surface structure of the generated silica gel is varied. All the detailed surface structure data of the prepared honeycomb silica gel at different CO₂ were compiled in Table 1. From Table 1, it is clear that the surface structure of the prepared honeycomb silica gel is varied greatly with CO₂ pressure, which could be explained by the famous Kelvin formula, as shown in the following equation:

$$RT \ln \frac{P_2}{P_1} = \frac{2\sigma M}{\rho} \left(\frac{1}{R_2} - \frac{1}{R_1} \right), \quad (1)$$

where R is the gas constant, T is the thermodynamic temperature of the system, P_2 and P_1 are the saturated vapor pressure at different curved diameters R_2 and R_1 , respectively, M is the molar mass of water, ρ is the density of water.

From Eq. 1, it is clear that the saturated vapor pressure at constant temperature is dependent on the pore diameter, and the larger the pore diameter, the larger the saturated vapor pressure. Thus, the adsorption capacity of desiccant is directly related to the pore volume and the specific surface area of desiccant with the average pore diameter of the mesopore (2–50 nm). Thus, the optimized CO₂ pressure for the preparation of the honeycomb silica gel is about 0.25 MPa, which might be contributed to the unique gas acid effect with rapid diffusion.

To investigate the adsorptive characteristic of the prepared honeycomb silica gel, the adsorption/desorption kinetics was carried out at different humidity, as shown in Figure 5 for the

typical adsorption/desorption kinetics at different humidity for the as-obtained honeycomb silica gel at CO₂ pressure of 0.25 MPa. From Figure 5, it can be seen that the prepared silica gel at CO₂ pressure of 0.25 MPa exhibits adsorptive ability at different relative humidity, which is indispensable for desiccant dehumidification used in industry due to the hash requirement of products to air humidity. Moreover, it could be further desorpted after saturated adsorption, exhibiting the cycling adsorption/desorption characteristics. The comparative adsorption capacity and time for saturated adsorption of different silica gels prepared at different CO₂ pressure at a relative humidity of 50% were compiled in Table 2. In comparison, the silica gel prepared at CO₂ pressure of 0.25 MPa shows the best high adsorption capacity and the suitable time for saturated adsorption at the relative humidity of 50%, which is attributed to the optimized surface structure, as shown above.

Conclusion

The honeycomb silica gel in a solid desiccant rotary wheel is fabricated environmentally friendly using water glass as starting material and CO₂ as neutralized acid. Water glass is used as an adhesive agent as well allowing the formation of the honeycomb monolith without any additional organic adhesive agent and guarantees a clean manufacturing procedure. CO₂ could tune the surface structure of silica gel including the specific surface area, pore volume, and pore size due to its rapid diffusion and pressure. The results indicate that the prepared honeycomb silica gel has a large specific surface area of as much as 760 m²/g, a large pore volume of 0.45 ml/g, and suitable mesoporous size of 2.94 nm at a CO₂ pressure of 0.25 MPa, which allows the excellent performance of the prepared honeycomb silica gel as a solid desiccant with an adsorption capacity of 287.24 mg/g at a relative humidity of 50%. Therefore, the proposed green preparation procedure of the honeycomb silica gel as a solid desiccant is feasible and promising in the manufacturing of honeycomb rotary wheels for dehumidification.

Data availability statement

The original contributions presented in the study are included in the article/supplementary material; further inquiries can be directed to the corresponding author.

Author contributions

JY: writing and experiment design. JQ: experiment. JF: experiment design. CD: experiment. SC: writing and experiment.

Acknowledgments

The authors are pleased to acknowledge the funding support by the Wuhan Science and Technology Plan Project (No. 2020020602012123).

Conflict of interest

JY, JF, and SC were employed by Wuhan Coobase Facilities Company Limited.

The remaining authors declare that the research was conducted in the absence of any commercial or financial

relationships that could be construed as a potential conflict of interest.

Publisher's note

All claims expressed in this article are solely those of the authors and do not necessarily represent those of their affiliated organizations, or those of the publisher, the editors, and the reviewers. Any product that may be evaluated in this article, or claim that may be made by its manufacturer, is not guaranteed or endorsed by the publisher.

References

- Aristov, Y. I., Restuccia, G., Cacciola, G., and Parmon, V. N. (2002). A family of new working materials for solid sorption air conditioning systems. *Appl. Therm. Eng.* 22, 191–204. doi:10.1016/s1359-4311(01)00072-2
- Bareschino, P., Diglio, G., Pepe, F., Angrisani, G., Roselli, C., and Sasso, M. (2015). Modelling of a rotary desiccant wheel: Numerical validation of a variable properties model. *Appl. Therm. Eng.* 78, 640–648. doi:10.1016/j.applthermaleng.2014.11.063
- Bhagat, S. D., Park, K.-T., Kim, Y.-H., Kim, J.-S., and Han, J.-H. (2008). A continuous production process for silica aerogel powders based on sodium silicate by fluidized bed drying of wet-gel slurry. *Solid State Sci.* 10, 1113–1116. doi:10.1016/j.solidstatesciences.2007.11.016
- Cha, Y. C., Kim, C. E., Lee, S. H., Hwang, H. J., Moon, J. W., Han, I. S., et al. (2007). Synthesis of silica aerogel thin film from waterglass. *Solid State Phenom.* 124–126, 671–674. doi:10.4028/www.scientific.net/ssp.124-126.671
- Chung, T.-W., Yeh, T.-S., and Yang, T. C. K. (2001). Influence of manufacturing variables on surface properties and dynamic adsorption properties of silica gels. *J. Non-Crystalline Solids* 279, 145–153. doi:10.1016/s0022-3093(00)00411-7
- Hindersmann, A. (2019). Experimental investigation of a method to avoid channel marks during vacuum infusion. *J. Compos. Mater.* 54, 2147–2158. doi:10.1177/0021998319889120
- Hwang, H. J., Kim, C. E., and Cha, Y. C. (2007). Strengthening of water glass based aerogel by TEOS. *Mater. Sci. Forum* 544–545, 1053–1056. doi:10.4028/www.scientific.net/msf.544-545.1053
- Iswar, S., Malfait, W. J., Balog, S., Winnefeld, F., Lattuada, M., and Koebel, M. M. (2017). Effect of aging on silica aerogel properties. *Microporous Mesoporous Mater.* 241, 293–302. doi:10.1016/j.micromeso.2016.11.037
- Jia, C. X., Dai, Y. J., Wu, J. Y., and Wang, R. Z. (2006). Experimental comparison of two honeycombed desiccant wheels fabricated with silica gel and composite desiccant material. *Energy Convers. Manag.* 47, 2523–2534. doi:10.1016/j.enconman.2005.10.034
- Kabeel, A. E. (2007). Solar powered air conditioning system using rotary honeycomb desiccant wheel. *Renew. Energy* 32, 1842–1857. doi:10.1016/j.renene.2006.08.009
- Kodama, A., Goto, M., Hirose, T., and Kuma, T. (1993). Experimental study of optimal operation for a honeycomb adsorber operated with thermal swing. *J. Chem. Eng. Jpn.* 26, 530–535. doi:10.1252/jcej.26.530
- Kuma, T., and Hirose, T. (1996). Performance of honeycomb rotor dehumidifiers in improved methods of adsorbent preparation. *J. Chem. Eng. Jpn.* 29, 376–378. doi:10.1252/jcej.29.376
- La, D., Dai, Y. J., Li, Y., Wang, R. Z., and Ge, T. S. (2010). Technical development of rotary desiccant dehumidification and air conditioning: A review. *Renew. Sustain. Energy Rev.* 14, 130–147. doi:10.1016/j.rser.2009.07.016
- Lee, J., and Lee, D.-Y. (2012). Sorption characteristics of a novel polymeric desiccant. *Int. J. Refrig.* 35, 1940–1949. doi:10.1016/j.ijrefrig.2012.07.009
- Li, Y., Cheng, X., Cao, W., Gong, L., Zhang, R., and Zhang, H. (2016). Development of adiabatic foam using sodium silicate modified by boric acid. *J. Alloys Compd.* 666, 513–519. doi:10.1016/j.jallcom.2016.01.139
- Liu, Y. (2003). Pore structure of new composite adsorbent $\text{SiO}_2\text{-xH}_2\text{O-yCaCl}_2$ with high uptake of water from air. *Sci. China Ser. E* 46, 551–559. doi:10.1360/02ye0480
- Manjunatha, C. M., Bojja, R., Jagannathan, N., Kinloch, A. J., and Taylor, A. C. (2013). Enhanced fatigue behavior of a glass fiber reinforced hybrid particles modified epoxy nanocomposite under WISPERX spectrum load sequence. *Int. J. Fatigue* 54, 25–31. doi:10.1016/j.ijfatigue.2013.04.008
- Neti, S., and Wolfe, E. I. (2000). Measurements of effectiveness in a silica gel rotary exchanger. *Appl. Therm. Eng.* 20, 309–322. doi:10.1016/s1359-4311(99)00031-9
- O'Connor, D., Calautit, J. K., and Hughes, B. R. (2016). A novel design of a desiccant rotary wheel for passive ventilation applications. *Appl. Energy* 179, 99–109. doi:10.1016/j.apenergy.2016.06.029
- Prasad, A. K., Yadav, L., and Yadav, A. (2019). Comparative analysis of different design of rotary dehumidifier. *Heat. Trans. Asian. Res.* 48, 2193–2215. doi:10.1002/htj.21480
- Sarawade, P. B., Kim, J.-K., Hilonga, A., and Kim, H. T. (2010). Influence of aging conditions on textural properties of water-glass-based silica aerogels prepared at ambient pressure. *Korean J. Chem. Eng.* 27, 1301–1309. doi:10.1007/s11814-010-0173-z
- Su, M., Han, X., Chong, D., Wang, J., Liu, J., and Yan, J. (2021). Experimental study on the performance of an improved dehumidification system integrated with precooling and recirculated regenerative rotary desiccant wheel. *Appl. Therm. Eng.* 199, 117608. doi:10.1016/j.applthermaleng.2021.117608
- Wang, W., Wu, L., Li, Z., Fang, Y., Ding, J., and Xiao, J. (2013). An overview of adsorbents in the rotary desiccant dehumidifier for air dehumidification. *Dry. Technol.* 31, 1334–1345. doi:10.1080/07373937.2013.792094
- Wei, X., Wang, W., Xiao, J., Zhang, L., Chen, H., and Ding, J. (2013). Hierarchically porous aluminosilicates as the water vapor adsorbents for dehumidification. *Chem. Eng. J.* 228, 1133–1139. doi:10.1016/j.cej.2013.05.062
- White, S. D., Goldsworthy, M., Reece, R., Spillmann, T., Gorur, A., and Lee, D.-Y. (2011). Characterization of desiccant wheels with alternative materials at low regeneration temperatures. *Int. J. Refrig.* 34, 1786–1791. doi:10.1016/j.ijrefrig.2011.06.012
- Wu, X. N., Ge, T. S., Dai, Y. J., and Wang, R. Z. (2018). Review on substrate of solid desiccant dehumidification system. *Renew. Sustain. Energy Rev.* 82, 3236–3249. doi:10.1016/j.rser.2017.10.021
- Yang, F., Wu, X. N., Peng, J. J., Ge, T. S., Dai, Y. J., and Wang, R. Z. (2020). Investigation on humidification performance of silica gel rotary wheel system in winter. *Build. Environ.* 183, 107064. doi:10.1016/j.buildenv.2020.107064
- Zhang, X. J., Dai, Y. J., and Wang, R. Z. (2003). A simulation study of heat and mass transfer in a honeycombed rotary desiccant dehumidifier. *Appl. Therm. Eng.* 23, 989–1003. doi:10.1016/s1359-4311(03)00047-4
- Zhang, X. J., Sumathy, K., Dai, Y. J., and Wang, R. Z. (2006). Dynamic hygroscopic effect of the composite material used in desiccant rotary wheel. *Sol. Energy* 80, 1058–1061. doi:10.1016/j.solener.2005.07.008
- Zheng, X., Ge, T. S., and Wang, R. Z. (2014). Recent progress on desiccant materials for solid desiccant cooling systems. *Energy* 74, 280–294. doi:10.1016/j.energy.2014.07.027



OPEN ACCESS

EDITED BY

Ivanhoe Leung,
The University of Melbourne, Australia

REVIEWED BY

Xiqi Zhang,
Technical Institute of Physics and
Chemistry (CAS), China
Jun-Bing Fan,
Southern Medical University, China
Amal Narayanan,
Howard Hughes Medical Institute
(HHMI), United States

*CORRESPONDENCE

Hongliang Liu,
liuhongliang@ytu.edu.cn

SPECIALTY SECTION

This article was submitted to Green and
Sustainable Chemistry,
a section of the journal
Frontiers in Chemistry

RECEIVED 30 July 2022

ACCEPTED 17 October 2022

PUBLISHED 31 October 2022

CITATION

Li S, Ma C, Hou B and Liu H (2022),
Rational design of adhesives for
effective underwater bonding.
Front. Chem. 10:1007212.
doi: 10.3389/fchem.2022.1007212

COPYRIGHT

© 2022 Li, Ma, Hou and Liu. This is an
open-access article distributed under
the terms of the [Creative Commons
Attribution License \(CC BY\)](#). The use,
distribution or reproduction in other
forums is permitted, provided the
original author(s) and the copyright
owner(s) are credited and that the
original publication in this journal is
cited, in accordance with accepted
academic practice. No use, distribution
or reproduction is permitted which does
not comply with these terms.

Rational design of adhesives for effective underwater bonding

Sidi Li¹, Chuao Ma¹, Bin Hou² and Hongliang Liu^{1,2*}

¹College of Chemistry and Chemical Engineering, Yantai University, Yantai, Shandong, China,

²Shandong Laboratory of Yantai Advanced Materials and Green Manufacturing, Yantai, Shandong, China

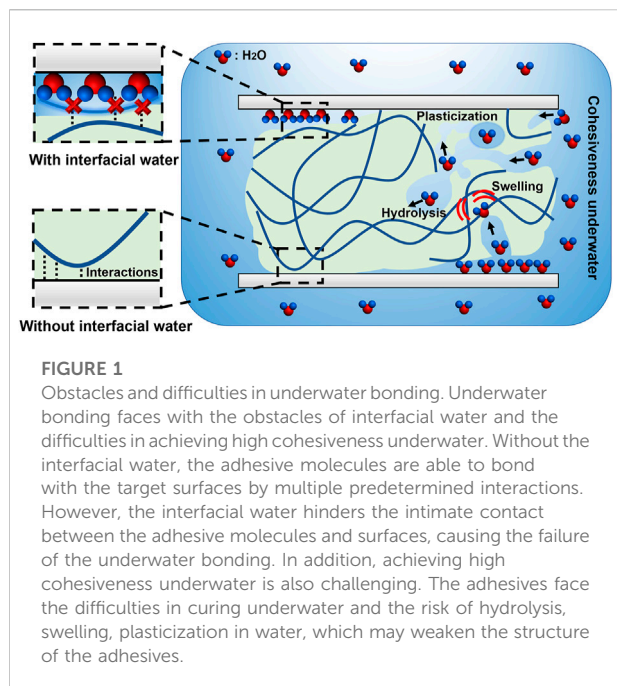
Underwater adhesives hold great promises in our daily life, biomedical fields and industrial engineering. Appropriate underwater bonding can reduce the huge cost from removing the target substance from water, and greatly lift working efficiency. However, different from bonding in air, underwater bonding is quite challenging. The existence of interfacial water prevents the intimate contact between the adhesives and the submerged surfaces, and water environment makes it difficult to achieve high cohesiveness. Even so, in recent years, various underwater adhesives with macroscopic adhesion abilities were emerged. These smart adhesives can ingeniously remove the interfacial water, and enhance cohesion by utilizing their special physicochemical properties or functional groups. In this mini review, we first give a detail introduction of the difficulties in underwater bonding. Further, we overview the recent strategies that are used to construct underwater adhesives, with the emphasis on how to overcome the difficulties of interfacial water and achieve high cohesiveness underwater. In addition, future perspectives of underwater adhesives from the view of practical applications are also discussed. We believe the review will provide inspirations for the discovery of new strategies to overcome the obstacles in underwater bonding, and therefore may contribute to designing effective underwater adhesives.

KEYWORDS

underwater bonding, underwater adhesives, interfacial water, interfacial adhesion, cohesiveness

Introduction

Underwater bonding is highly demand in wide range of areas (Cui et al., 2017; Fan and Gong, 2021; Wang Z. M., et al., 2021; Wu J. et al., 2022). For example, in our daily life and industrial field, it often requires to directly repair the water pipeline leakage, attach the underwater sensor, or even repair the broken hull in water. In medical applications, doctors usually need to seal the wounds in moisture environment or even under blood. Efficient underwater bonding can greatly simplify the working procedures with no need for creating dry surfaces, thereby lifting working efficiency and reducing cost (Xia et al., 2021). However, achieving underwater bonding is commonly challenging (Ahn et al., 2015; Narayanan et al., 2021). And commercial man-made adhesives, such as cyanoacrylate (Super glue), vinyl acetate (Elmer's glue), as well as most epoxy and polyurethane glue, cannot perform well in underwater



adhesion (Li et al., 2017; White and Wilker, 2011; North et al., 2017; Cheng et al., 2022).

The challenges in underwater bonding mainly result from the interfacial water on the submerged surfaces, and the difficulties in achieving high cohesiveness underwater (Kamino, 2008; Kamino, 2013; Waite, 2017; Fan and Gong, 2021; Narayanan et al., 2021; Cheng et al., 2022). In recent years, researchers have proposed various strategies to overcome these obstacles, and therefore developed new types of adhesives that were capable of underwater bonding. In this mini review, we first introduced the difficulties in underwater bonding, and then overviewed the main discovered strategies that are used to realize underwater macroscopical adhesion. In this part, we mainly focused on the strategies of creating underwater adhesives with macroscopical underwater bonding capacities. In the last part, the future perspectives of adhesives according to practical applications were discussed.

Obstacles in underwater bonding

Water and adhesives are in conflict (Akdogan et al., 2014; Myslicki et al., 2020), and achieving efficient underwater bonding is challenging (Figure 1). One reason is that interfacial water disrupts the adhesion of the adhesives on submerged surfaces (Petrone et al., 2015; Narayanan et al., 2021). Especially for hydrophilic submerged surfaces, such as most minerals, metals, oxides, some fabrics and biological surfaces (Rapp et al., 2016), water molecules and salts (if any) can strongly bind to the surfaces and form hydration layers, thereby

preventing intimate contact between the adhesives and surfaces. For example, in saline solution, a hydration layer with the thickness of about 13 Å forms on the surface of anionic mica (Maier et al., 2015; Rapp et al., 2016), which is a substantial molecular barrier for adhesion. Another obstacle is the difficulties in achieving high cohesiveness in water. On one hand, some adhesives that rely on volatilization of solvent, such as polyvinyl alcohol and vinyl acetate-based glues (White and Wilker, 2011; North et al., 2017), are unable to cure underwater. On the other hand, water may weaken the cured structure of adhesives through hydrolytic degradation, plasticization or swelling over time (Narayanan et al., 2021). For example, it has been reported that the cured structures of some epoxy and polyurethane glues are prone to being broken by water molecules, leading to the decrease of adhesive strength over time (Li et al., 2018; Lee et al., 2020). All of these cases impede the long-term underwater adhesive strength.

Strategies to remove interfacial water

Removing interfacial water is the essential step in underwater bonding. In recent years, researchers have proposed various strategies to remove interfacial water, and achieved macroscopical underwater adhesion (Figure 2). In the following, we systematically overviewed these elaborate strategies.

Hydrophobicity

Hydrophobic interactions have been recently used in the design of underwater adhesives to overcome the barrier of interfacial water (Xu et al., 2017; Kaur et al., 2018; Cui et al., 2019; Wang Z. M. et al., 2021; Wu Y. C. et al., 2022; Liu et al., 2022). The hydrophobic segments were introduced into the adhesives through multiple reactions, such as Michael addition (Cui et al., 2019), polyesterification (Xu et al., 2017; Wang Z. M. et al., 2021), and free radical polymerization (Wu Y. C. et al., 2022). A representative example is the hyperbranched polymer (HBP) universal adhesive developed by Liu and coworkers (Cui et al., 2019). HBP with a hydrophobic backbone and hydrophilic catechol side branches was synthesized through Michael addition between multi-vinyl monomers and dopamine, and exhibited underwater adhesion performance. The authors proposed that upon contacting water, the hydrophobic segments were able to aggregate, thereby displacing the interfacial water molecules. Other typical examples were showed by Dhinojwala and coworkers who designed polyesters-based adhesives with hydrophobic aliphatic pendant groups (Xu et al., 2017; Kaur et al., 2018). In their study, the hydrophobic aliphatic chains were proposed to remove the bound water from the interface. In addition, directly

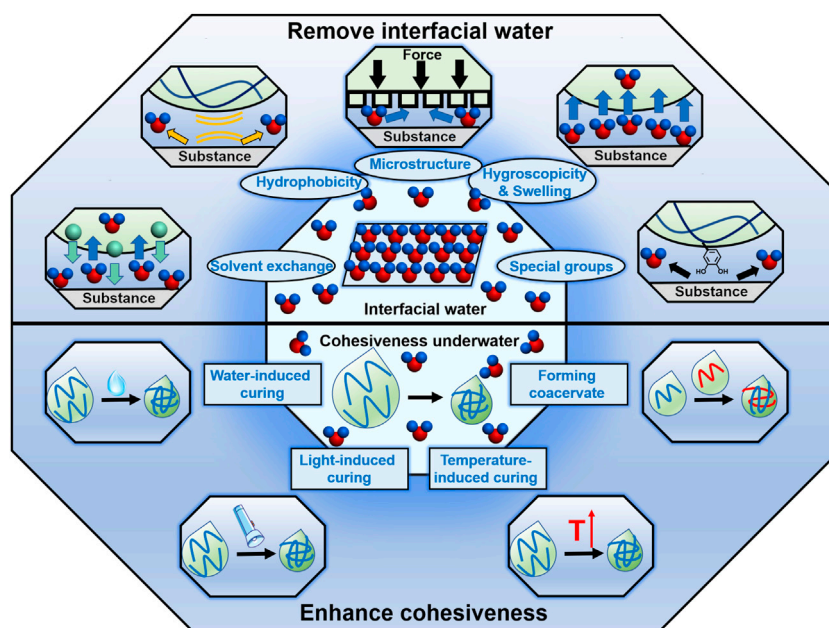


FIGURE 2

Strategies of removing interfacial water and enhancing cohesiveness underwater. Utilization of the hydrophobicity, hygroscopicity and swelling property, special groups of the adhesives, solvent exchange and bioinspired microstructures are the mainly reported strategies to remove the interfacial water. And there are also many strategies to enhance the cohesiveness of the underwater adhesives, including water-induced curing, light-induced curing, temperature-induced curing and forming coacervate.

utilizing the inner hydrophobic characteristic of natural polymer was another way to remove interfacial water. For example, Wang and coworkers reported a natural sericin protein-based self-hydrophobized adhesive (rSer-TA), whose hydrophobic chains were exposed by tris(2-carboxyethyl) phosphine (TCEP) reduction. It was proposed that after the adhesive was exposed to water, the hydrophobic chains can self-aggregate and therefore repel the interfacial water, after which the underwater interfacial adhesion was enhanced by hydrogen bonding or electrostatic interactions provided by catechol (Liu et al., 2022).

Hygroscopicity and swelling property

Some underwater adhesives are inherent hydrophilic, and can remove the interfacial water (Pan et al., 2020; Wang et al., 2020). For example, Wang and coworkers developed an anthracenyl-functionalized polyethylenimine (anth-PEI) based adhesive, whose main polymer component PEI was hydrophilic. After the adhesive was applied underwater, it removed the interfacial water, benefiting for the intimate contact between the adhesive and the submerged surfaces (Wang et al., 2020). In addition, the swelling properties of hydrogels matrix were used to remove the interfacial water as reported by Zhang and coworkers (Pan et al., 2020). In their work, inorganic $\text{Ca}_4(\text{AlO}_2)_6\text{SO}_3$ -filled poly(acrylic amide) precursor solution was utilized as an

adhesive. The authors proposed that after the adhesive was injected onto the substance underwater, the *in situ* formed hydrophilic poly(acrylic amide)-based matrix swelled and thus removed the interfacial water.

Solvent exchange

The solvent exchange concept in underwater adhesion was developed by Waite and coworkers (Zhao et al., 2016). In this concept, the solvent of an adhesive, dimethylsulfoxide (DMSO), for example, was miscible with water. When the adhesive was extruded into water, the solvent exchange happened. As a result, the interfacial water entered into the adhesive, and the adhesive therefore well contacted with the submerged substance. This strategy was also illustrated by Dan and coworkers, who also utilized DMSO as the solvent (Song et al., 2021).

Special functional groups

The functional groups of adhesives have also been reported to contribute to overcoming the barriers of interfacial water. A representative group was catechol, the special functional group that worked excellently in marine mussel's adhesion (Lee et al., 2011; Hofman et al., 2018; Li S. D. et al., 2020). Due to its multiple

interactions with various substance such as H bonds, covalent bonds, coordination interaction and π - π stacking (Moulay, 2014; Saiz-Poseu et al., 2019), catechol group has been introduced into the design of man-made adhesives through polymerization (Matos-Perez et al., 2012; Meredith et al., 2014; North et al., 2017; Tang et al., 2021), coupling reaction (Ryu et al., 2015; Shin et al., 2015; Li S. D. et al., 2020), Michael addition (Zhang et al., 2014; Cui et al., 2019), *in vivo* residue-specific incorporation strategy (Yang et al., 2014), etc. Even catechol group endowed the adhesives with considerable adhesive performance, only a few catechol-based adhesives that exhibited excellent underwater adhesion properties were reported (North et al., 2017; Zhan et al., 2017). A famous example was the poly(catechol-styrene) adhesive which was developed by Wilker and coworkers (North et al., 2017). This adhesive can strongly bond aluminum (Al) substance underwater with the maximal adhesive strength about 3 MPa. It was proposed that the surface water was broken by the “drilling down” properties of the incorporated catechol groups.

Another functional group is the isocyanate. This group is highly reactive, and widely used in the synthesis of polyurethane (PU) materials (Tseng et al., 2021; Xia et al., 2021; Yan et al., 2022). Due to the high reactivity, the isocyanate-containing adhesives can react with the interfacial water, and then form multiple bonds or interactions with the underwater substance, achieving strong underwater adhesion. For example, Huang and coworkers developed a hexamethylene diisocyanate-incorporated, polydimethylsiloxane-based adhesive (HDI-PDMS) by the addition reaction (Yan et al., 2022). It was proposed that the surface water molecules were removed by the reaction with the residual isocyanate groups in the adhesive. The underwater adhesion of isocyanate-containing adhesives was also verified by Wan and coworkers (Xia et al., 2021). In their work, the adhesive was synthesized by the reaction between tolylene diisocyanate (TDI) and diol, and the TDI was a little excessive to ensure the existence of diisocyanate in the adhesives. The results indicated that the adhesive exhibited strong adhesive properties to various submerged surfaces, including glass, Al, stainless steel (SS), et al.

Structural underwater adhesives

Many natural organisms exhibited unique underwater adhesive performance. In recent years, learning from nature, researchers have designed numerous bioinspired structural underwater adhesives that are also capable of removing the interfacial water (Lee et al., 2007; Iturri et al., 2015; Baik et al., 2017; Ma et al., 2018; Yi et al., 2018; Lee et al., 2019; Wang and Hensel, 2021; Cui and Liu, 2021). For example, Pang and coworkers developed an octopus-inspired adhesive patch which contains dome-like protuberances that are similar to the suction cups of octopuses. It was proposed that after applying pressure, the interfacial water was removed into the

upper chambers of the adhesives, and the pressure difference thus generated for underwater adhesion (Baik et al., 2017). Similarly, Kwak and coworkers developed a remora-inspired adhesive (RIA) that contains microstructures similar to the suction disk of remoras (Lee et al., 2019). The pressure difference was also produced by deformation of the adhesive after external forces, and the underwater adhesion was therefore achieved. In addition, other creatures, such as torrent frog (Iturri et al., 2015), mussels and geckos (Lee et al., 2007; Ma et al., 2018) also inspired researchers to design structural underwater adhesives recently. Compared with other adhesives, the structural underwater adhesives usually required elaborate structure design and complex fabrication process (Fan and Gong, 2021).

Strategies of enhancing cohesion of underwater adhesives

In addition to the high interfacial adhesion, achieving macroscopical underwater bonding also requires the adhesives to possess high cohesion strength. Nowadays, researchers have developed numerous strategies to enhance the cohesiveness of underwater adhesives (Figure 2).

Water-induced underwater curing

The adhesives that cure directly when encountering with water are convenient and easy-to-use in practical applications. Nowadays, various methods have been proposed to design this type of adhesives. A relatively simple method is to use facile chemical reactions to crosslink the adhesive. The solidification of epoxy-based adhesives is in this type. Typically, epoxy and curing agents, Mannich base, diamine for example (Choi et al., 2013; Zhou et al., 2018), are mixed before they are applied underwater, and then the mixture is able to cure underwater due to the crosslinking between epoxy groups and curing agents.

In addition, the curing process can be initiated when the adhesive encounters with water. There are several ways to achieve this type of curing, such as hydrophobicity-induced aggregation (Cui et al., 2019), water-incorporated chain extension reactions (Xia et al., 2021; Yan et al., 2022), solvent exchange-induced electrostatic complexation or hydrogen bond (H bond) crosslinking (Zhao et al., 2016; Song et al., 2021), etc. For example, the core of hydrophobic pentaerythritol tetraacrylate (PETEA) in a hyperbranched polymer with hydrophilic branches can self-aggregate upon encountering water (Cui et al., 2019), and the residual isocyanate in adhesive can react with water, thus extending chains and enhancing cohesiveness (Xia et al., 2021; Yan et al., 2022). The polyanion and polycation-mixed adhesive with the solvent of DMSO can solidify after it was applied underwater due to the production of electrostatic complexation caused by the exchange of DMSO and water

(Zhao et al., 2016; Song et al., 2021). Besides, water can also be utilized to accelerate the curing process. The nanocomposite hydrogel-based adhesive developed by Zhang and coworkers was an example (Pan et al., 2020). In their work, the inorganic filters-incorporated hydrogel precursor slurry with initiator was used as an adhesive. After it was applied underwater, the inorganic $\text{Ca}_4(\text{AlO}_2)_6\text{SO}_3$ absorbed water, and then released heat, which further accelerated the free radical polymerization process.

Light or temperature induced underwater curing

When exposed to light, anthracene undergoes dimerization reaction (Claus et al., 2017; Truong et al., 2017; Van Damme and Du Prez, 2018), thus forming crosslinking structures. Therefore, the adhesive polymer chains that contain anthracene can proceed photo-induced underwater crosslinking. One impressive example was the anthracenyl-functionalized polyethylenimine (anth-PEI)-based adhesives developed by Wang and coworker (Wang et al., 2020). In their work, LED blue light ($\lambda > 400 \text{ nm}$) was utilized as the light source, and the curing of the anth-PEI adhesive happened within 2 min underwater, as shown by the fast increase of adhesive strength. In addition, the alkoxyphenacyl group or coumarin-contained materials can also be crosslinked upon light irradiation as illustrated by Joy and coworkers (Xu et al., 2017; Kaur et al., 2018; Tseng et al., 2021). For example, they developed alkoxyphenacyl-based polyurethane adhesives, and the changes in T_g , rheology behaviors, and the peel strength all demonstrated the occurrence of crosslinking reactions after UV irradiating (Tseng et al., 2021).

The temperature change of an adhesive was also utilized to cure the adhesive. For example, Dong and coworkers reported a type of supramolecular adhesive (P1) from low-molecular-weight monomer that is formed by incorporating dibenzo-24-crown-8 to four-armed pentaerythritol. P1 exhibited a relatively low melting point (52°C), and can cure underwater by heating-cooling process (Li X. et al., 2020).

Forming coacervate

Coacervate is a dense, highly concentrated, relatively low-viscosity, water-immiscible fluid with low interfacial energy, which has been reported to possess potentials to wet target surfaces and contribute to the following adhesion (Kaur et al., 2011; Wei et al., 2014). Forming coacervate was also an effective way to enhance the cohesiveness due to the generation of multiple interactions inside the adhesives in the coacervate formation process (Lee et al., 2020; Peng et al., 2020; Peng et al., 2021). Some coacervate-based adhesives, even showed no obvious liquid-solid transition underwater,

can exhibit underwater adhesive capacities. The widely reported coacervate adhesive was formed through electrostatic interactions (Vahdati et al., 2020), as the sandcastle worms mainly use this interaction to produce glues (Shao and Stewart, 2010; Stewart et al., 2011a; Stewart et al., 2011b; Zhang et al., 2016). In addition, H bond can also be used to form coacervate-based underwater adhesives. For example, Lee and coworkers reported a coacervate adhesive, namely VATA, which is formed by mixing the poly(vinyl alcohol) (PVA) polymer and tannin (TA). The H bonds between the PVA and TA enhance the cohesiveness of the adhesive, achieving the macroscopical underwater bonding, though the adhesive did not cure underwater (Lee et al., 2020). Similarly, Zeng and coworkers directly mixed polyethylene glycol (PEG) and silicotungstic acid (SiW), and developed the SiW-PEG coacervate-based adhesive through H bonds. This coacervate adhesive was able to bond various wet surfaces, and treat bleeding (Peng et al., 2020). Through the combination of multiple interactions, the coacervate adhesives can also be formed. For example, Zeng and coworkers utilized hydrophobic interactions within poly(ethylene glycol)₇₇-b-poly(propylene glycol)₂₉-b-poly(ethylene glycol)₇₇ (F68) and the H bonds between F68 and tannin forming a coacervate adhesive. It was able to exhibit underwater bonding capacities under the circumstances of coacervate state, even without curing (Peng et al., 2021).

Some types of coacervate-based adhesives can cure underwater. Commonly, the changes of water environment, such as temperature or pH, can induce curing (Shao and Stewart, 2010; Dompe et al., 2019). For example, Stewart and coworkers reported a sandcastle worms-mimetic coacervate-based adhesive consisting of aminated collagen, phosphodopa copolymer and some ions (Ca^{2+} and Mg^{2+}). At a specific ions and polymer ratio, tuning the pH or increasing the temperature leads to curing of the coacervate (Shao and Stewart, 2010). Another example was reported by Kamperman and coworkers (Dompe et al., 2019). In their work, a complex coacervate based adhesive that consists of poly(N-isopropylacrylamide) (PNIPAM)-grafted oppositely charged polyelectrolytes was constructed. When the temperature of water environment was elevated higher than the lower critical solution temperature of PNIPAM, this adhesive can transform to non-flowing hydrogels underwater. In addition, the covalent crosslinking that happened within the coacervate, such as the oxidation of catechol groups-induced crosslinking (Shao and Stewart, 2010), azetidinium-induced crosslinking in base condition or over long time (Wei et al., 2019; Zhu et al., 2019; Wang Z. et al., 2021) and [2 + 2] cycloaddition reaction of coumarin-induced crosslinking (Narayanan et al., 2020) also result in the curing of the coacervate-based adhesives. For these coacervate-based adhesives, the underwater adhesive strength was often higher than those of uncured coacervate-based adhesive, probably due to their stronger cohesiveness.

Conclusion and perspectives

Realizing efficient underwater bonding is challenging due to the obstacles of interfacial water and difficulties in enhancing cohesiveness underwater. In this review, we summarized and overviewed the proposed strategies for overcoming these obstacles and difficulties. Despite that much progress has been made in underwater bonding, current underwater adhesives still have much space to made from the view of practical use. First, many adhesives require complex synthesis process or rigorous synthesis conditions (Pan et al., 2020). Although some adhesives showed high underwater bonding performance, the large production is also urgently needed (Li et al., 2022) for the commercialization. Second, the storability and usability of the adhesives should be carefully considered. Finally, current adhesives mainly focus on the underwater adhesive performance in static water environment, but the practical waters, such as lakes, rivers, and ocean are mainly dynamic. In dynamic water, the diffusion of the adhesive molecules accelerates, and the efficient bonding is more difficult to realize. Future works can focus on the dynamic environment of the water, thus developing underwater adhesives suitable for practical dynamic water environment.

Author contributions

SL: outline of the review and principal writer. CM, BH and HL: article revision and review before submission.

References

- Ahn, B. K., Das, S., Linstadt, R., Kaufman, Y., Martinez-Rodriguez, N. R., Mirshafian, R., et al. (2015). High-performance mussel-inspired adhesives of reduced complexity. *Nat. Commun.* 6, 8663. doi:10.1038/ncomms9663
- Akdogan, Y., Wei, W., Huang, K. Y., Kageyama, Y., Danner, E. W., Miller, D. R., et al. (2014). Intrinsic surface-drying properties of bioadhesive proteins. *Angew. Chem. Int. Ed.* 53 (42), 11253–11256. doi:10.1002/anie.201406858
- Baik, S., Kim, D. W., Park, Y., Lee, T. J., Bhang, S. H., and Pang, C. (2017). A wet-tolerant adhesive patch inspired by protuberances in suction cups of octopi. *Nature* 546 (7658), 396–400. doi:10.1038/nature22382
- Cheng, B. H., Yu, J. H., Arisawa, T., Hayashi, K., Richardson, J. J., Shibuta, Y., et al. (2022). Ultrastrong underwater adhesion on diverse substrates using non-canonical phenolic groups. *Nat. Commun.* 13 (1), 1892. doi:10.1038/s41467-022-29427-w
- Choi, S., Maul, S., Stewart, A., Hamilton, H. R., and Douglas, E. P. (2013). Effect of silane coupling agent on the durability of epoxy adhesion for structural strengthening applications. *Polym. Eng. Sci.* 53 (2), 283–294. doi:10.1002/pen.23261
- Claus, T. K., Telitel, S., Welle, A., Bastmeyer, M., Vogt, A. P., Delaitre, G., et al. (2017). Light-driven reversible surface functionalization with anthracenes: Visible light writing and mild UV erasing. *Chem. Commun.* 53 (10), 1599–1602. doi:10.1039/c6cc09897e
- Cui, C. Y., Fan, C. C., Wu, Y. H., Xiao, M., Wu, T. L., Zhang, D. F., et al. (2019). Water-triggered hyperbranched polymer universal adhesives: From strong underwater adhesion to rapid sealing hemostasis. *Adv. Mat.* 31 (49), 1905761. doi:10.1002/adma.201905761
- Cui, C. Y., and Liu, W. G. (2021). Recent advances in wet adhesives: Adhesion mechanism, design principle and applications. *Prog. Polym. Sci.* 116, 101388. doi:10.1016/j.progpolymsci.2021.101388
- Cui, M. K., Ren, S. S., Wei, S. C., Sun, C. J., and Zhong, C. (2017). Natural and bio-inspired underwater adhesives: Current progress and new perspectives. *Apl. Mat.* 5 (11), 116102. doi:10.1063/1.4985756
- Dompe, M., Cedano-Serrano, F. J., Heckert, O., van den Heuvel, N., van der Gucht, J., Tran, Y., et al. (2019). Thermoresponsive complex coacervate-based underwater adhesive. *Adv. Mat.* 31 (21), 1808179. doi:10.1002/adma.201808179
- Fan, H. L., and Gong, J. P. (2021). Bioinspired underwater adhesives. *Adv. Mat.* 33 (44), 2102983. doi:10.1002/adma.202102983
- Hofman, A. H., van Hees, I. A., Yang, J., and Kamperman, M. (2018). Bioinspired underwater adhesives by using the supramolecular toolbox. *Adv. Mat.* 30 (19), 1704640. doi:10.1002/adma.201704640
- Iturri, J., Xue, L. J., Kappl, M., Garcia-Fernandez, L., Barnes, W. J. P., Butt, H. J., et al. (2015). Torrent frog-inspired adhesives: Attachment to flooded surfaces. *Adv. Funct. Mat.* 25 (10), 1499–1505. doi:10.1002/adfm.201403751
- Kamino, K. (2013). Mini-review: Barnacle adhesives and adhesion. *Biofouling* 29 (6), 735–749. doi:10.1080/08927014.2013.800863
- Kamino, K. (2008). Underwater adhesive of marine organisms as the vital link between biological science and material science. *Mar. Biotechnol.* 10, 111–121. doi:10.1007/s10126-007-9076-3
- Kaur, S., Narayanan, A., Dalvi, S., Liu, Q. H., Joy, A., and Dhinojwala, A. (2018). Direct observation of the interplay of catechol binding and polymer hydrophobicity in a mussel-inspired elastomeric adhesive. *ACS Cent. Sci.* 4 (10), 1420–1429. doi:10.1021/acscentsci.8b00526
- Kaur, S., Weerasekare, G. M., and Stewart, R. J. (2011). Multiphase Adhesive coacervates inspired by the sandcastle worm. *ACS Appl. Mat. Interfaces* 3 (4), 941–944. doi:10.1021/am200082v
- Lee, B. P., Messersmith, P. B., Israelachvili, J. N., and Waite, J. H. (2011). Mussel-inspired adhesives and coatings. *Annu. Rev. Mat. Res.* 41, 99–132. doi:10.1146/annurev-matsci-062910-100429

Funding

The work is supported by grants from the National Natural Science Foundation of China (52203280, 21875268), Natural Science Foundation of Shandong Province (ZR2022QE040), Young Doctoral Research Fund of Yantai University (2222005), Taishan Young Scholar Program (tsqn202103053), and Fundamental Research Projects of Science and Technology Innovation and Development Plan in Yantai City (2022YTJC06002541).

Conflict of interest

The authors declare that the research was conducted in the absence of any commercial or financial relationships that could be construed as a potential conflict of interest.

The reviewer XZ declared a past co-authorship with the author CM, HL to the handling editor.

Publisher's note

All claims expressed in this article are solely those of the authors and do not necessarily represent those of their affiliated organizations, or those of the publisher, the editors and the reviewers. Any product that may be evaluated in this article, or claim that may be made by its manufacturer, is not guaranteed or endorsed by the publisher.

- Lee, D., Hwang, H., Kim, J. S., Park, J., Youn, D., Kim, D., et al. (2020). Vata: A poly(vinyl alcohol)- and tannic acid-based nontoxic underwater adhesive. *ACS Appl. Mat. Interfaces* 12 (18), 20933–20941. doi:10.1021/acsami.0c02037
- Lee, H., Lee, B. P., and Messersmith, P. B. (2007). A reversible wet/dry adhesive inspired by mussels and geckos. *Nature* 448, 338–341. doi:10.1038/nature05968
- Lee, S. H., Song, H. W., Kang, B. S., and Kwak, M. K. (2019). Remora-inspired reversible adhesive for underwater applications. *ACS Appl. Mat. Interfaces* 11 (50), 47571–47576. doi:10.1021/acsami.9b16350
- Li, G. M., Wu, Y. P., Chen, Z. T., Chen, M., Xiao, P. S., Li, X. T., et al. (2022). Biomimetic epoxy adhesive capable of large-scale preparation: From structural underwater bonding to hydrothermal durability. *Chem. Eng. J.* 431 (1), 134011. doi:10.1016/j.cej.2021.134011
- Li, J., Celiz, A. D., Yang, J., Yang, Q., Wamala, I., Whyte, W., et al. (2017). Tough adhesives for diverse wet surfaces. *Science* 357 (6349), 378–381. doi:10.1126/science.aah6362
- Li, S. D., Chen, N., Li, X. P., Li, Y., Xie, Z. P., Ma, Z. Y., et al. (2020). Bioinspired double-dynamic-bond crosslinked bioadhesive enables post-wound closure care. *Adv. Funct. Mat.* 30 (17), 2000130. doi:10.1002/adfm.202000130
- Li, X., Deng, Y., Lai, J. L., Zhao, G., and Dong, S. Y. (2020). Tough, long-term, water-resistant, and underwater adhesion of low-molecular-weight supramolecular adhesives. *J. Am. Chem. Soc.* 142 (11), 5371–5379. doi:10.1021/jacs.0c00520
- Li, X., Li, W., Liu, Z. Q., Wang, X. L., Guo, H. L., Wang, R. J., et al. (2018). Underwater polyurethane adhesive with enhanced cohesion by postcrosslinking of glycerol monomethacrylate. *J. Appl. Polym. Sci.* 135 (32), 46579. doi:10.1002/app.46579
- Liu, H., Qin, S. M., Liu, J., Zhou, C., Zhu, Y. Y., Yuan, Y., et al. (2022). Bio-inspired self-hydrophobized sericin adhesive with tough underwater adhesion enables wound healing and fluid leakage sealing. *Adv. Funct. Mat.* 32, 2201108. doi:10.1002/adfm.202201108
- Ma, Y. F., Ma, S. H., Wu, Y., Pei, X. W., Gorb, S. N., Wang, Z. K., et al. (2018). Remote control over underwater dynamic attachment/detachment and locomotion. *Adv. Mat.* 30 (30), 1801595. doi:10.1002/adma.201801595
- Maier, G. P., Rapp, M. V., Waite, J. H., Israelachvili, J. N., and Butler, A. (2015). Adaptive synergy between catechol and lysine promotes wet adhesion by surface salt displacement. *Science* 349 (6248), 628–632. doi:10.1126/science.aab0556
- Matos-Perez, C. R., White, J. D., and Wilker, J. J. (2012). Polymer composition and substrate influences on the adhesive bonding of a biomimetic, cross-linking polymer. *J. Am. Chem. Soc.* 134 (22), 9498–9505. doi:10.1021/ja303369p
- Meredith, H. J., Jenkins, C. L., and Wilker, J. J. (2014). Enhancing the adhesion of a biomimetic polymer yields performance rivaling commercial glues. *Adv. Funct. Mat.* 24 (21), 3259–3267. doi:10.1002/adfm.201303536
- Moulay, S. (2014). Dopa/catechol-tethered polymers: Bioadhesives and biomimetic adhesive materials. *Polym. Rev. Phila. Pa.* 54 (3), 436–513. doi:10.1080/15583724.2014.881373
- Myslicki, S., Kordy, H., Kaufmann, M., Creac'hcadec, R., and Vallee, T. (2020). Under water glued stud bonding fasteners for offshore structures. *Int. J. Adhes. Adhes.* 98, 102533. doi:10.1016/j.ijadhadh.2019.102533
- Narayanan, A., Dhinojwala, A., and Joy, A. (2021). Design principles for creating synthetic underwater adhesives. *Chem. Soc. Rev.* 50 (23), 13321–13345. doi:10.1039/d1cs00316j
- Narayanan, A., Menefee, J. R., Liu, Q. H., Dhinojwala, A., and Joy, A. (2020). Lower critical solution temperature-driven self-coacervation of nonionic polyester underwater adhesives. *ACS Nano* 14 (7), 8359–8367. doi:10.1021/acsnano.0c02396
- North, M. A., Del Grosso, C. A., and Wilker, J. J. (2017). High strength underwater bonding with polymer mimics of mussel adhesive proteins. *ACS Appl. Mat. Interfaces* 9 (8), 7866–7872. doi:10.1021/acsami.7b00270
- Pan, F., Ye, S. X., Wang, R. X., She, W., Liu, J. P., Sun, Z. M., et al. (2020). Hydrogel networks as underwater contact adhesives for different surfaces. *Mat. Horiz.* 7 (8), 2063–2070. doi:10.1039/d0mh00176g
- Peng, Q. Y., Chen, J. S., Zeng, Z. C., Wang, T., Xiang, L., Peng, X. W., et al. (2020). Adhesive coacervates driven by hydrogen-bonding interaction. *Small* 16 (43), 2004132. doi:10.1002/smll.202004132
- Peng, Q. Y., Wu, Q. Q., Chen, J. S., Wang, T., Wu, M., Yang, D. L., et al. (2021). Coacervate-based instant and repeatable underwater adhesive with anticancer and antibacterial properties. *ACS Appl. Mat. Interfaces* 13 (40), 48239–48251. doi:10.1021/acsami.1c13744
- Petrone, L., Kumar, A., Sutanto, C. N., Patil, N. J., Kannan, S., Palaniappan, A., et al. (2015). Mussel adhesion is dictated by time-regulated secretion and molecular conformation of mussel adhesive proteins. *Nat. Commun.* 6, 8737. doi:10.1038/ncomms9737
- Rapp, M. V., Maier, G. P., Dobbs, H. A., Higdon, N. J., Waite, J. H., Butler, A., et al. (2016). Defining the catechol-cation synergy for enhanced wet adhesion to mineral surfaces. *J. Am. Chem. Soc.* 138 (29), 9013–9016. doi:10.1021/jacs.6b03453
- Ryu, J. H., Hong, S., and Lee, H. (2015). Bio-inspired adhesive catechol-conjugated chitosan for biomedical applications: A mini review. *Acta Biomater.* 27, 101–115. doi:10.1016/j.actbio.2015.08.043
- Saiz-Poseu, J., Mancebo-Aracil, J., Nador, F., Busque, F., and Ruiz-Molina, D. (2019). The Chemistry behind catechol-based adhesion. *Angew. Chem. Int. Ed.* 58 (3), 696–714. doi:10.1002/anie.201801063
- Shao, H., and Stewart, R. J. (2010). Biomimetic underwater adhesives with environmentally triggered setting mechanisms. *Adv. Mat.* 22 (6), 729–733. doi:10.1002/adma.200902380
- Shin, J., Lee, J. S., Lee, C., Park, H. J., Yang, K., Jin, Y., et al. (2015). Tissue adhesive catechol-modified hyaluronic acid hydrogel for effective, minimally invasive cell therapy. *Adv. Funct. Mat.* 25 (25), 3814–3824. doi:10.1002/adfm.201500006
- Song, Q. T., Chen, Y. N., Huang, Y. P., Dan, W. H., Wang, M., and Dan, N. H. (2021). Adhesive capable of underwater adhesion and wound hemostasis prepared based on solvent exchange. *Adv. Mat. Technol.* 7 (1), 2100852. doi:10.1002/admt.202100852
- Stewart, R. J., Ransom, T. C., and Hlady, V. (2011a). Natural underwater adhesives. *J. Polym. Sci. B. Polym. Phys.* 49 (11), 757–771. doi:10.1002/polb.22256
- Stewart, R. J., Wang, C. S., and Shao, H. (2011b). Complex coacervates as a foundation for synthetic underwater adhesives. *Adv. Colloid Interface Sci.* 167 (1–2), 85–93. doi:10.1016/j.cis.2010.10.009
- Tang, Z. W., Bian, S., Lin, Z. W., Xiao, H., Zhang, M., Liu, K., et al. (2021). Biocompatible catechol-functionalized cellulose-based adhesives with strong water resistance. *Macromol. Mat. Eng.* 306 (9), 2100232. doi:10.1002/mame.202100232
- Truong, V. X., Li, F., and Forsythe, J. S. (2017). Versatile bioorthogonal hydrogel platform by catalyst-free visible light initiated photodimerization of anthracene. *ACS Macro Lett.* 6 (7), 657–662. doi:10.1021/acsmacrolett.7b00312
- Tseng, Y. M., Narayanan, A., Mishra, K., Liu, X. H., and Joy, A. (2021). Light-activated adhesion and debonding of underwater pressure-sensitive adhesives. *ACS Appl. Mat. Interfaces* 13 (24), 29048–29057. doi:10.1021/acsami.1c04348
- Vahdati, M., Cedano-Serrano, F. J., Creton, C., and Hourdet, D. (2020). Coacervate-based underwater adhesives in physiological conditions. *ACS Appl. Polym. Mat.* 2 (8), 3397–3410. doi:10.1021/acscapm.0c00479
- Van Damme, J., and Du Prez, F. (2018). Anthracene-containing polymers toward high-end applications. *Prog. Polym. Sci.* 82, 92–119. doi:10.1016/j.progpolymsci.2018.02.002
- Waite, J. H. (2017). Mussel adhesion - essential footwork. *J. Exp. Biol.* 220 (4), 517–530. doi:10.1242/jeb.134056
- Wang, Y., and Hensel, R. (2021). Bioinspired underwater adhesion to rough substrates by cavity collapse of cupped microstructures. *Adv. Funct. Mat.* 31 (31), 2101787. doi:10.1002/adfm.202101787
- Wang, Z., Guo, L. F., Xiao, H. Y., Cong, H., and Wang, S. T. (2020). A reversible underwater glue based on photo- and thermo-responsive dynamic covalent bonds. *Mat. Horiz.* 7 (1), 282–288. doi:10.1039/c9mh01148j
- Wang, Z. M., Zhao, J., Tang, W. Z., He, T. Z., Wang, S., He, X. Q., et al. (2021). Robust underwater adhesives based on dynamic hydrophilic and hydrophobic moieties to diverse surfaces. *ACS Appl. Mat. Interfaces* 13 (2), 3435–3444. doi:10.1021/acsami.0c20186
- Wang, Z., Zhang, S. F., Zhao, S. J., Kang, H. J., Wang, Z. K., Xia, C. L., et al. (2021). Facile biomimetic self-coacervation of tannic acid and polycation: Tough and wide pH range of underwater adhesives. *Chem. Eng. J.* 404, 127069. doi:10.1016/j.cej.2020.127069
- Wei, C. Y., Zhu, X. W., Peng, H. Y., Chen, J. J., Zhang, F., and Zhao, Q. (2019). Facile preparation of lignin-based underwater adhesives with improved performances. *ACS Sustain. Chem. Eng.* 7 (4), 4508–4514. doi:10.1021/acscuschemeng.8b06731
- Wei, W., Tan, Y. P., Rodriguez, N. R. M., Yu, J., Israelachvili, J. N., and Waite, J. H. (2014). A mussel-derived one component adhesive coacervate. *Acta Biomater.* 10 (4), 1663–1670. doi:10.1016/j.actbio.2013.09.007
- White, J. D., and Wilker, J. J. (2011). Underwater bonding with charged polymer mimics of marine mussel adhesive proteins. *Macromolecules* 44 (13), 5085–5088. doi:10.1021/ma201044x
- Wu, J., Lei, H. D., Fang, X. Z., Wang, B., Yang, G., O'Reilly, R. K., et al. (2022). Instant strong and responsive underwater adhesion manifested by bioinspired supramolecular polymeric adhesives. *Macromolecules* 55 (6), 2003–2013. doi:10.1021/acs.macromol.1c02361
- Wu, Y. C., Chen, Y. Z., Zeng, Y., Li, C., Qiu, R. H., and Liu, W. D. (2022). Photocuring preparation of biobased underwater adhesives with hydrophobic chain-ring

interlace structure for protecting adhesion. *Appl. Mat. Today* 27, 101436. doi:10.1016/j.apmt.2022.101436

Xia, G. Z., Lin, M., Jiayu, Y., Jinkang, H., Bowen, L., Mu, Y. B., et al. (2021). Solvent-free mussel-inspired adhesive with rapid underwater curing capability. *Adv. Mat. Interfaces* 8 (32), 2101544. doi:10.1002/admi.202101544

Xu, Y., Liu, Q. H., Narayanan, A., Jain, D., Dhinojwala, A., and Joy, A. (2017). Mussel-inspired polyesters with aliphatic pendant groups demonstrate the importance of hydrophobicity in underwater adhesion. *Adv. Mat. Interfaces* 4 (22), 1700506. doi:10.1002/admi.201700506

Yan, Y. G., Huang, J., Qiu, X. Y., Zhuang, D. X., Liu, H. L., Huang, C. Z., et al. (2022). A strong underwater adhesive that totally cured in water. *Chem. Eng. J.* 431 (4), 133460. doi:10.1016/j.cej.2021.133460

Yang, B., Ayyadurai, N., Yun, H., Choi, Y. S., Hwang, B. H., Huang, J., et al. (2014). *In vivo* residue-specific dopa-incorporated engineered mussel bioglue with enhanced adhesion and water resistance. *Angew. Chem. Int. Ed.* 53 (49), 13360–13364. doi:10.1002/anie.201406099

Yi, H., Lee, S. H., Seong, M., Kwak, M. K., and Jeong, H. E. (2018). Bioinspired reversible hydrogel adhesives for wet and underwater surfaces. *J. Mat. Chem. B* 6 (48), 8064–8070. doi:10.1039/c8tb02598c

Zhan, K., Kim, C., Sung, K., Ejima, H., and Yoshie, N. (2017). Tunicate-inspired gallol polymers for underwater adhesive: A comparative study of catechol and gallol. *Biomacromolecules* 18 (9), 2959–2966. doi:10.1021/acs.biomac.7b00921

Zhang, H., Bre, L. P., Zhao, T. Y., Zheng, Y., Newland, B., and Wang, W. X. (2014). Mussel-inspired hyperbranched poly(amino ester) polymer as strong wet tissue adhesive. *Biomaterials* 35 (2), 711–719. doi:10.1016/j.biomaterials.2013.10.017

Zhang, L. H., Lipik, V., and Miserez, A. (2016). Complex coacervates of oppositely charged Co-polypeptides inspired by the sandcastle worm glue. *J. Mat. Chem. B* 4 (8), 1544–1556. doi:10.1039/c5tb02298c

Zhao, Q., Lee, D. W., Ahn, B. K., Seo, S., Kaufman, Y., Israelachvili, J. N., et al. (2016). Underwater contact adhesion and microarchitecture in polyelectrolyte complexes actuated by solvent exchange. *Nat. Mat.* 15 (4), 407–412. doi:10.1038/NMAT4539

Zhou, J. J., Wan, Y., Liu, N., Yin, H., Li, B., Sun, D. W., et al. (2018). Epoxy adhesive with high underwater adhesion and stability based on low viscosity modified Mannich bases. *J. Appl. Polym. Sci.* 135 (3), 45688. doi:10.1002/app.45688

Zhu, X. W., Wei, C. Y., Zhang, F., Tang, Q. Q., and Zhao, Q. (2019). A robust salty water adhesive by counterion exchange induced coacervate. *Macromol. Rapid Commun.* 40 (7), 1800758. doi:10.1002/marc.201800758

Advantages of publishing in Frontiers



OPEN ACCESS

Articles are free to read
for greatest visibility
and readership



FAST PUBLICATION

Around 90 days
from submission
to decision



HIGH QUALITY PEER-REVIEW

Rigorous, collaborative,
and constructive
peer-review



TRANSPARENT PEER-REVIEW

Editors and reviewers
acknowledged by name
on published articles

Frontiers

Avenue du Tribunal-Fédéral 34
1005 Lausanne | Switzerland

Visit us: www.frontiersin.org

Contact us: frontiersin.org/about/contact



REPRODUCIBILITY OF RESEARCH

Support open data
and methods to enhance
research reproducibility



DIGITAL PUBLISHING

Articles designed
for optimal readership
across devices



FOLLOW US

@frontiersin



IMPACT METRICS

Advanced article metrics
track visibility across
digital media



EXTENSIVE PROMOTION

Marketing
and promotion
of impactful research



LOOP RESEARCH NETWORK

Our network
increases your
article's readership